

GEOPHYSICAL METHODS FOR ENVIRONMENTAL STUDIES

GUEST EDITORS: UMBERTA TINIVELLA, MICHELA GIUSTINIANI, AND GIORGIO CASSIANI





Geophysical Methods for Environmental Studies

International Journal of Geophysics

Geophysical Methods for Environmental Studies

Guest Editors: Umberta Tinivella, Michela Giustiniani,
and Giorgio Cassiani



Copyright © 2013 Hindawi Publishing Corporation. All rights reserved.

This is a special issue published in “International Journal of Geophysics.” All articles are open access articles distributed under the Creative Commons Attribution License, which permits unrestricted use, distribution, and reproduction in any medium, provided the original work is properly cited.

Editorial Board

José Badal, Spain
Andrea Bizzarri, Italy
Jean-Pierre Burg, Switzerland
John F. Cassidy, Canada
Ping Chang, USA
Yun-tai Chen, China
Gordon Cooper, South Africa
Robin Crockett, UK
Gary Egbert, USA
Semih Ergintav, Turkey
Fabrizio Galadini, Italy
Marek Grad, Poland
Hans-Gert Kahle, Switzerland

Masao Kanamitsu, USA
Honn Kao, Canada
Shuichi Kodaira, Japan
Libo Liu, China
Francisco Luzon Martinez, Spain
Zdenek Martinec, Czech Republic
Philip Meredith, UK
Steve Milan, UK
Marco Mucciarelli, Italy
Michael Nicolls, USA
Salvatore Piro, Italy
Ruey-Juin Rau, Taiwan
Ahmed Salem, UK

Wouter Schellart, Australia
Joerg Schleicher, Brazil
Sheng-Rong Song, Taiwan
Alexey Stovas, Norway
Sndor Szalai, Hungary
P. Talwani, USA
Robert Tenzer, China
Rudolf A. Treumann, Germany
Filippos Vallianatos, Greece
Petr Vaníček, Canada
Michael S. Zhdanov, USA
Sergej Zilitinkevich, Finland

Contents

Geophysical Methods for Environmental Studies, Umberta Tinivella, Michela Giustiniani,
and Giorgio Cassiani
Volume 2013, Article ID 950353, 2 pages

Fundamentals of the Thermohydrogravodynamic Theory of the Global Seismotectonic Activity of the Earth, Sergey V. Simonenko
Volume 2013, Article ID 519829, 39 pages

Metrological Analysis of Geopotential Gravity Field for Harbor Waterside Management and Water Quality Control, Osvaldo Faggioni, Maurizio Soldani, and Davide Andrea Leoncini
Volume 2013, Article ID 398956, 12 pages

Relationship of Worldwide Rocket Launch Crashes with Geophysical Parameters, N. Romanova,
N. Crosby, and V. Pilipenko
Volume 2013, Article ID 297310, 15 pages

Removing Regional Trends in Microgravity in Complex Environments: Testing on 3D Model and Field Investigations in the Eastern Dead Sea Coast (Jordan), A. Al-Zoubi, L. Eppelbaum, A. Abueladas,
M. Ezersky, and E. Akkawi
Volume 2013, Article ID 341797, 13 pages

3D Imaging of Dead Sea Area Using Weighted Multipath Summation: A Case Study, Shemer Keydar,
Benjamin Medvedev, Abdallah Al-Zoubi, Michael Ezersky, and Emad Akkawi
Volume 2013, Article ID 692452, 7 pages

Environmental Geophysical Study of the Groundwater Mineralization in a Plot of the Cotonou Littoral Zone (South Benin), Yalo Nicaise, Desclotres Marc, Alassane Abdoukarim, Mama Daouda,
and Boukari Moussa
Volume 2012, Article ID 329827, 10 pages

Editorial

Geophysical Methods for Environmental Studies

Umberta Tinivella,¹ Michela Giustiniani,¹ and Giorgio Cassiani²

¹ *Istituto Nazionale di Oceanografia e di Geofisica Sperimentale, Borgo Grotta Gigante 42C, 34010 Trieste, Italy*

² *University of Padua, via Gradenigo 6, 35127 Padua, Italy*

Correspondence should be addressed to Umberta Tinivella; utinivella@ogs.trieste.it

Received 2 May 2013; Accepted 2 May 2013

Copyright © 2013 Umberta Tinivella et al. This is an open access article distributed under the Creative Commons Attribution License, which permits unrestricted use, distribution, and reproduction in any medium, provided the original work is properly cited.

Geophysical methods are powerful tools to explore the subsoil for environmental investigations. Among the possible fields of application are hydrological and hydrogeological characterization and monitoring, slope stability assessments, archaeological surveys, locating voids and karstic features, soil characterization, contamination assessment, and so forth. Ground-penetrating radar (GPR), seismics, DC resistivity, electromagnetic induction, gravity, and magnetic methods are the most used, whilst the use of other technologies has grown over the past decades. The available techniques are characterised by different penetration and resolution capabilities, from few centimeters to kilometers. For this reason, there is drive in the scientific community towards the integration of several geophysical methods in order to detect and characterize the subsoil from the analysis of different physical properties.

A paper in this special issue presents an original use of the gravity field to model the sea level oscillations. The analysis of the gravity field leads to the forecast of sea level variation due to meteorological tide events. This analysis defines a compensation in the inverse hydrobarometric factor to be taken into account for a correct compensation of the atmospheric pressure variations in basins. This phenomenon has several consequence in Harbor Water Side Management and in Water Quality Control as shown by the reported case studies and introduces a new reference parameter (the so-called Water 1000).

The main topic of the paper authored by Y. Nicaise et al. is the use of electrical resistivity and electromagnetic conductivity methods to demonstrate that geophysical methods can greatly contribute to the study of the water table mineralization in the littoral zone for a sustainable

management of water resources. In fact, this study allows the determination of the spatial extent of the water table mineralization by direct measurements of water conductivity in wells and the depth of the fresh/saline water interface in the coastal aquifer by means of geophysical measurements. Moreover, the electromagnetic measurements allow to map a gradient of water salinity in the North West direction. On the environmental level, they have demonstrated that these methods can be used in the zones where drilling of the wells is difficult even impossible or useless in order to delimit the zones where the water resource is exploitable.

The paper of A. Al-Zoubi et al. is focused on microgravity investigations that are a powerful tool for subsurface imaging and especially for the localization of underground karsts. Several geological, technical, and environmental factors, such as the influence of regional trends, interfere with microgravity survey processing and interpretation. A. Al-Zoubi et al. observe that the most effective methods for regional trend removal are the bilinear saddle and local polynomial regressions. Application of these methods makes it possible to detect the anomalous gravity effects from buried targets and to extract the local gravity anomaly at the study site. Consequently, the 3D gravity field modeling led to the identification of the parameters of a physical-geological model in the Eastern Dead Sea coast (Jordan).

The study area of S. Keydar et al. is again the Dead Sea area. In particular, the authors investigate the fast decline of the Dead Sea level, as a possible result of extensive human activities. The authors analyse 3D high resolution seismic data. The method is based on a spatial summation of seismic waves along time surfaces using recently proposed multipath summation with proper weights. This approach

does not require any explicit information on parameters, since the involved multipath summation is performed for all possible parameter values within a wide specified range. The results from processed 3D time volume show subhorizontal coherent reflectors at an approximate depth of 50–80 m which show dip changes in proximity to outcropping sinkholes and suggest a possible link between revealed fault and the sinkholes.

The paper by Simonenko proposes a possible cosmic energy gravitational genesis of the strong Chinese 2008 and the strong Japanese 2011 earthquakes, based on the established generalized differential formulation of the first law of thermodynamics.

Finally, Romanova et al. examine all worldwide launch crashes occurring at all major 31 launching sites from 1957 to 2008. The authors have developed a comprehensive database, which includes 50 years of information from the beginning of the space age in 1957. The authors analyze correlations with the geomagnetic indices as indirect indicators of the space weather condition. In view of the high costs associated with delaying launch and possibly missing launch windows, only a nowcast could provide a sufficiently reliable service. Thus, space weather real-time monitoring and prediction could become an important issue in the optimization of launch procedures.

In conclusion, the papers reported in this special issue contribute to highlight the role of integrated geophysical methods, illustrating technologies and methods of data analysis that can be applied and developed in various areas of public interest. Moreover, the papers set the stage for emerging future topics in this important interdisciplinary field.

We would like to dedicate this special issue to Ilaria Sanvenero, a brilliant physics student at the University of Pisa, who passed away far too soon at the age of twenty-two. Here, we wish to remember Ilaria by paying a public homage to her brief but precious work. Her thesis has been part of a paper in this special issue presented by Faggioni et al., who will preserve the memory of this wonderful girl in their heart.

*Umberta Tinivella
Michela Giustiniani
Giorgio Cassiani*

Research Article

Fundamentals of the Thermohydrogravodynamic Theory of the Global Seismotectonic Activity of the Earth

Sergey V. Simonenko

*V.I. Il'ichev Pacific Oceanological Institute, Far Eastern Branch of Russian Academy of Sciences,
43 Baltiyskaya Street, Vladivostok 690041, Russia*

Correspondence should be addressed to Sergey V. Simonenko; sergeysimonenko@mail.ru

Received 7 November 2012; Accepted 10 April 2013

Academic Editor: Umberta Tinivella

Copyright © 2013 Sergey V. Simonenko. This is an open access article distributed under the Creative Commons Attribution License, which permits unrestricted use, distribution, and reproduction in any medium, provided the original work is properly cited.

The article presents the fundamentals of the cosmic geophysics (representing the deterministic thermohydrogravodynamic theory intended for earthquakes prediction) based on the author's generalized differential formulation of the first law of thermodynamics extending the classical Gibbs' formulation by taking into account (along with the classical infinitesimal change of heat δQ and the classical infinitesimal change of the internal energy dU_τ) the infinitesimal increment of the macroscopic kinetic energy dK_τ , the infinitesimal increment of the gravitational potential energy $d\pi_\tau$, the generalized expression for the infinitesimal work $\delta A_{np,\partial\tau}$ done by the nonpotential terrestrial stress forces (determined by the symmetric stress tensor \mathbf{T}) acting on the boundary of the continuum region τ , and the infinitesimal increment dG of energy due to the cosmic and terrestrial nonstationary energy gravitational influence on the continuum region τ during the infinitesimal time dt . Based on the established generalized differential formulation of the first law of thermodynamics, the author explains the founded cosmic energy gravitational genesis of the strong Chinese 2008 and the strong Japanese 2011 earthquakes.

1. Introduction

The problem of the long-term predictions of the strong earthquakes [1, 2] is the significant problem of the modern geophysics. The analysis of the period 1977–1985 revealed [3] the strongly nonrandom tendencies in the earthquake-induced geodetic changes (owing to the mass redistribution of material inside the Earth) related to the change of the Earth's rotation and the Earth's gravitational field. The analysis of the period 1977–1993 (characterized by 11015 major earthquakes) revealed [4] the strong earthquakes' tendency to increase the Earth's spin (rotational) energy. The analysis of the same period 1977–1993 revealed [5] “an extremely strong tendency for the earthquakes to decrease the global gravitational energy” confirming the inherent relation of the earthquakes with the transformation of the Earth's gravitational energy into the seismic wave energy and frictional heat. The previous analysis of the principal geological features of the past 400×10^6 years revealed [6] the geological evidence for a pulsating gravitation related to periodic variation of the Earth's radius during the geological evolution of the Earth. The combination

of satellite and gravimetric data revealed [7] the free-air anomalies of the Earth's gravitational field.

It is well known that “the deterministic prediction of the time of origin, hypocentral (or epicentral) location, and magnitude of an impending earthquake is an open scientific problem” [8]. It was conjectured [8] that the possible earthquake prediction and warning must be carried out on a deterministic basis. However, it was pointed out [8] with some regret that the modern “study of the physical conditions that give rise to an earthquake and the processes that precede a seismic rupture of an ordinary event are at a very preliminary stage and, consequently, the techniques of prediction of time of origin, epicentre, and magnitude of an impending earthquake now available are below standard”. The authors [8] argued that “a new strong theoretical scientific effort is necessary to try to understand the physics of the earthquake”. It was conjectured [8] that the present level of knowledge of the geophysical processes “is unable to achieve the objective of a deterministic prediction of an ordinary seismic event, but it certainly will in a more or less distant future tackle the problem with seriousness and avoiding scientifically incorrect, wasteful, and

inconclusive shortcuts, as sometimes has been done". Sgrigna and Conti conjectured [8] that "it will take long time (may be years, tens of years, or centuries) because this approach requires a great cultural, financial, and organizational effort on an international basis". It was conjectured [8] that a possible contribution to a deterministic earthquake prediction approach is related to observations and physical modelling of earthquake precursors to formulate, in perspective, "a unified theory able to explain the causes of its genesis, and the dynamics, rheology, and microphysics of its preparation, occurrence, postseismic relaxation, and interseismic phases". It was conjectured [8] that "the study of the physical conditions that give rise to an earthquake and of the processes that precede a seismic rupture is at a very preliminary stage and, consequently, the techniques of prediction available at the moment are below standard". However, Sgrigna and Conti believe [8] that "it should be better to pursue the deterministic prediction approach even if a reliable deterministic method of earthquake prediction will presumably be available only in the more distant future".

It was pointed out [9] that the gravity changes (derived from regional gravity monitoring data in China from 1998 to 2005) exhibited noticeable variations before the occurrence of two large earthquakes in 2008 in the areas surrounding Yutian (Xinjiang) and Wenchuan (Sichuan). A recent research [10] by Zhan and his colleagues demonstrated that significant gravity changes were observed before all nine large earthquakes that ruptured within or near mainland China from 2001 to 2008. It was pointed out [9] that the past experience and empirical data showed that "earthquakes typically occur within one to two years after a period of significant gravity changes in the region in question". It was concluded [9] that the "additional research is needed to remove the subjective nature in the determination of the timeframe of a forecasted earthquake".

The need of the thermohydrogravidynamic approach [11, 12] is confirmed by previous studies [3–5, 13] and by noticeable variations of gravitational field identified [9, 10] before strong earthquakes in China from 2001 to 2008. The necessity to consider the gravitational field (during the strong earthquakes) is also related to the observations of the slow gravitational [14, 15] ground waves resulting from strong earthquakes and spreading out from the focal regions [16, 17] of earthquakes. Lomnitz pointed out [16] that the gravitational ground waves (related to great earthquakes) "have been regularly reported for many years and remain a controversial subject in earthquake seismology". Richter presented [18] the detailed analysis of these observations and made the conclusion that "there is almost certainly a real phenomenon of progressing or standing waves seen on soft ground in the meizoseismal areas of great earthquakes". Lomnitz presented [17] the real evidence of the existence of the slow gravitational waves in sedimentary layers during strong earthquakes. The fundamental connections of the geodynamics, seismicity, and volcanism with gravitation (and the slow gravitational ground waves resulting from strong earthquakes) are presented in the works [19–22].

It was conjectured [23] that the recent destructive earthquakes occurred in Sichuan (China, 2008), Italy (2009), Haiti

(2010), Chile (2010), New Zealand (2010), and Japan (2011) "have shown that, in present state, scientific researchers have achieved little or almost nothing in the implementation of short- and medium-term earthquake prediction, which would be useful for disaster mitigation measures". It was conjectured [23] that "this regrettable situation could be ascribed to the present poor level of achievements in earthquake forecast". It was pointed out [23] that "although many methods have been claimed to be capable of predicting earthquakes (as numerous presentations on earthquake precursors regularly show at every international meeting), the problem of formulating such predictions in a quantitative, rigorous, and repeatable way is still open". It was formulated [23] that "another problem of practical implementation of earthquake forecasting could be due to the lack of common understanding and exchange of information between the scientific community and the governmental authorities that are responsible for earthquake damage mitigation in each country: they operate in two different environments, they aim at different tasks, and they generally speak two different languages". It was pointed out [23] that "the way how seismologists should formulate their forecasts and how they should transfer them to decision-makers and to the public is still a tricky issue". It was clearly formulated [23] that "the formulation of probabilistic earthquake forecasts with large uncertainties in space and time and very low probability levels is still difficult to be used by decision-making people". It was conjectured [23] that "in real circumstances the authorities deal with critical problems related to the high cost of evacuating the population from an area where the scientific methods estimate an expected rate of destructive earthquake as one in many thousand days, while they require much more deterministic statements". In the special issue [23] of the International Journal of Geophysics, Console et al. assessed the status of the art of earthquake forecasts and their applicability. They invited authors "to report methods and case studies that could concretely contribute or, at least seemed promising, to improve the present frustrating situation, regarding the practical use of earthquake forecasts" [23].

In this article, by accepting with gratitude the personal invitation from Dr. Reem Ali and Dr. Radwa Ibrahim (representing the Editorial Office of the International Journal of Geophysics) to submit an article to the special issue on "Geophysical Methods for Environmental Studies", the author presents the fundamentals of the thermohydrogravidynamic theory intended for deterministic prediction of earthquakes. The thermohydrogravidynamic theory is based on the established generalized differential formulation [11, 12, 24–26] of the first law of thermodynamics (for moving rotating deforming compressible heat-conducting stratified macroscopic continuum region τ subjected to the nonstationary Newtonian gravity):

$$dU_{\tau} + dK_{\tau} + d\pi_{\tau} = \delta Q + \delta A_{np, \partial\tau} + dG \quad (1)$$

extending the classical formulation [27] by taking into account (along with the classical infinitesimal change of heat δQ and the classical infinitesimal change of the internal energy dU_{τ}) the infinitesimal increment of the macroscopic

kinetic energy dK_τ , the infinitesimal increment of the gravitational potential energy $d\pi_\tau$, the generalized expression for the infinitesimal work $\delta A_{np,\partial\tau}$ done by the nonpotential terrestrial stress forces (determined by the symmetric stress tensor \mathbf{T}) acting on the boundary of the continuum region τ , and the infinitesimal increment dG of energy due to the cosmic and terrestrial nonstationary energy gravitational influence on the continuum region τ during the infinitesimal time dt .

In Section 2 we begin by considering the inherent physical incompleteness of the classical expression [28, 29] for the macroscopic kinetic energy per unit mass ε_k defined (in classical nonequilibrium thermodynamics) as the sum of the macroscopic translational kinetic energy per unit mass $\varepsilon_t = (1/2)\mathbf{v}^2$ of the mass center of a continuum region and the macroscopic internal rotational kinetic energy per unit mass $\varepsilon_r = (1/2)\theta\omega^2$, where \mathbf{v} is the speed of the mass center of a small continuum region, ω is an angular velocity of internal rotation [29, 30], and θ is an inertia moment per unit mass of a small continuum region [28]. The classical de Groot and Mazur expression has inherent physical incompleteness [24, 31] related to the questionable assumption about the rigid-like rotation of a small continuum region. The classical de Groot and Mazur expression [28] does not consider the nonequilibrium component of the macroscopic velocity field related to the velocity shear defined by the rate of strain tensor e_{ij} . In Section 2 the macroscopic kinetic energy per unit mass ε_k is presented [31] as a sum of the macroscopic translational kinetic energy per unit mass $\varepsilon_t = (1/2)\mathbf{v}^2$ of the mass center of a continuum region, the classical macroscopic internal rotational kinetic energy per unit mass ε_r [28], the new macroscopic internal shear kinetic energy per unit mass ε_s [31], and the new macroscopic internal kinetic energy of shear-rotational coupling per unit mass $\varepsilon_{s,r}^{\text{coup}}$ [31] with a small correction. The presented expression for ε_k and its particular form for homogeneous continuum regions of spherical and cubical shapes generalized [31] the classical de Groot and Mazur expression in classical nonequilibrium thermodynamics [28, 29] by taking into account the new macroscopic internal shear kinetic energy per unit mass ε_s , which expresses the kinetic energy of irreversible dissipative shear motion, and also the new macroscopic internal kinetic energy of shear-rotational coupling per unit mass $\varepsilon_{s,r}^{\text{coup}}$, which expresses the kinetic energy of local coupling between irreversible dissipative shear and reversible rigid-like rotational macroscopic continuum motions.

Following the “Statistical thermohydrodynamics of irreversible strike-slip-rotational processes” [11] and the “Thermohydrogravidynamics of the Solar System” [12], in Section 2.2 we present the generalized differential formulation of the first law of thermodynamics (in the Galilean frame of reference) for nonequilibrium shear-rotational states of the deformed finite one-component individual continuum (characterized by the symmetric stress tensor \mathbf{T}) region τ moving in the nonstationary gravitational field. In Section 2.3 we present the generalized differential formulation [11, 12] of the first law of thermodynamics (in the Galilean frame of reference) for nonequilibrium shear-rotational states of the deformed finite individual region τ of the compressible

viscous Newtonian one-component continuum moving in the nonstationary gravitational field. We present the generalization [11, 12] of the classical [27] expression $\delta A_{np,\partial\tau} = -\delta W = -pdV$ by taking into account (for Newtonian continuum) the infinitesimal works δA_c and δA_s , respectively, of acoustic and viscous Newtonian forces acting during the infinitesimal time interval dt on the boundary surface $\partial\tau$ of the individual continuum region τ bounded by the continuum boundary surface $\partial\tau$. Based on the generalized differential formulation of the first law of thermodynamics, in Section 2.4 we present the analysis [11, 12] of the gravitational energy mechanism of the gravitational energy supply into the continuum region τ owing to the local time increase of the potential ψ of the gravitational field inside the continuum region τ subjected to the nonstationary Newtonian gravitational field.

Following the “Statistical thermohydrodynamics of irreversible strike-slip-rotational processes” [11] and the “Thermohydrogravidynamics of the Solar System” [12], in Section 3 we present the fundamentals of the cosmic energy gravitational genesis of earthquakes. Using the evolution equation of the total mechanical energy of the macroscopic continuum region τ (of the compressible viscous Newtonian continuum), we demonstrate the physical adequacy [11, 12] of the rotational model [2] of the earthquake focal region for the seismic zone of the Pacific Ring. We present the thermodynamic foundation [11, 12] of the classical deformational (shear) model [1] of the earthquake focal region for the quasi-uniform medium of the Earth’s crust characterized by practically constant viscosity. We present the generalized thermohydrogravidynamic shear-rotational model [11, 12] of the earthquake focal region by taking into account the classical macroscopic rotational kinetic energy [28, 29], the macroscopic nonequilibrium kinetic energies [24, 31], and the external cosmic energy gravitational influences [12, 25, 26] on the focal region of earthquakes.

In Section 4 we present the fundamentals of the cosmic geophysics [12] applicable for the planets of the Solar System. In Section 4.1 we consider the energy gravitational influences on the Earth of the inner planets and the outer planets of the Solar System. In Section 4.1.1 we present the relation for the energy gravitational influences (on the Earth) of the inner and the outer planets in the second approximation of the elliptical orbits of the planets of the Solar System. In Section 4.1.2 we present the evaluation of the relative maximal planetary instantaneous energy gravitational influences on the Earth in the approximation of the circular orbits of the planets of the Solar System. In Section 4.1.3 we present the evaluation of the relative maximal planetary integral energy gravitational influences on the Earth in the approximation of the circular orbits of the planets of the Solar System. In Section 4.2 we consider the energy gravitational influences on the Earth of the Moon. In Section 4.2.1 we present the evaluation of the relative maximal instantaneous energy gravitational influence of the Moon on the Earth in the second approximation of the elliptical orbits of the Earth and the Moon around the combined mass center $C_{3,MOON}$ of the Earth and the Moon. In Section 4.2.2. we present the evaluation of the maximal integral energy gravitational influence of

the Moon on the Earth in the approximation of the elliptical orbits of the Earth and the Moon around the combined mass center $C_{3,MOON}$ of the Earth and the Moon. In Section 4.3 we demonstrate the reality of the cosmic energy gravitational genesis of preparation and triggering of earthquakes owing to the energy gravitational influence on the Earth of the Moon and the planets of the Solar System. In Section 4.3.1 we demonstrate the real cosmic energy gravitational genesis of preparation of earthquakes by considering the energy gravitational influence on the Earth of Venus. In Section 4.3.2 we demonstrate the real cosmic energy gravitational genesis of triggering of the preparing earthquakes. In Section 4.4 we demonstrate the cosmic energy gravitational genesis of the seismotectonic activity induced by the nonstationary cosmic energy gravitational influences on the Earth of the Sun, the Moon, Venus, Jupiter, and Mars. In Section 4.4.1 we present the evaluations of the time periodicities of the maximal (instantaneous and integral) energy gravitational influences on the Earth of the Sun-Moon system, Venus, Jupiter, and Mars. In Section 4.4.2 we present the empirical time periodicities of the seismotectonic activity for various regions of the Earth. In Section 4.4.3 we present the set of the time periodicities of the periodic global seismotectonic (and volcanic) activity and the global climate variability of the Earth induced by the different combinations of the cosmic energy gravitational influences on the Earth of the Sun and the Moon, Venus, Jupiter, and Mars. In Section 4.5 we present the evidence of the cosmic energy gravitational genesis of the strong Chinese 2008 earthquakes. In Section 4.6 we present the evidence of the cosmic energy gravitational genesis of the strongest Japanese earthquakes near the Tokyo region. In Section 5 we present the summary of main results and conclusion.

2. The Generalized Formulation of the First Law of Thermodynamics for Moving Rotating Deforming Compressible Heat-Conducting Macroscopic Individual Continuum Region τ Subjected to the Nonstationary Newtonian Gravitational Field

2.1. The Generalized Expression for the Macroscopic Kinetic Energy of a Small Continuum Region in Nonequilibrium Thermodynamics. De Groot and Mazur defined the macroscopic kinetic energy per unit mass ε_k as [28] the sum of the macroscopic translational kinetic energy per unit mass $\varepsilon_t = (1/2)\mathbf{v}^2$ of a continuum region (particle) mass center and the macroscopic internal rotational kinetic energy per unit mass $\varepsilon_r = (1/2)\theta\omega^2$:

$$\varepsilon_k = \varepsilon_t + \varepsilon_r = \frac{1}{2}\mathbf{v}^2 + \frac{1}{2}\theta\omega^2, \quad (2)$$

where \mathbf{v} is the speed of the mass center of a small continuum region, ω is an angular velocity of internal rotation [29], and θ is an inertia moment per unit mass of a small continuum region [28]. Gyarmati's definition [29] of the macroscopic

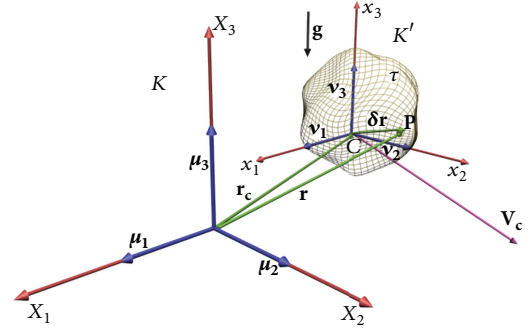


FIGURE 1: Cartesian coordinate system K of a Galilean frame of reference and the continuum region mass center-affixed Lagrangian coordinate system K' .

kinetic energy per unit mass is analogous to de Groot and Mazur's one. The classical de Groot and Mazur's and Gyarmati's definition (2) of the macroscopic kinetic energy per unit mass for a shear flows has some inherent physical incompleteness associated with the assumption about the rigid-like rotation of the continuum region with the angular velocity vector ω . This definition is based on the assumption of local thermodynamic equilibrium since it does not consider the nonequilibrium shear component of the macroscopic continuum motion related to the rate of strain tensor e_{ij} . However, the assumption of local thermodynamic equilibrium, as noted by de Groot and Mazur [28], may be justified only by reasonable agreement of the experimental results with the theoretical deductions based on this assumption.

Landau and Lifshitz defined [32] the macroscopic internal energy of a small macroscopic continuum region as the difference between the total kinetic energy of the continuum region and kinetic energy of the translational macroscopic motion of the continuum region. According to Landau and Lifshitz's definition [32] of the macroscopic internal energy, the term $(1/2)\theta\omega^2$ in the expression (2) is the internal energy of the macroscopic (hydrodynamic) continuum motion. The classical definition [28, 29] of the macroscopic internal rotational kinetic energy per unit mass $(1/2)\theta\omega^2$ is consistent with the Landau and Lifshitz's definition of the macroscopic internal energy. We shall use further the Landau and Lifshitz's definition [32] of the macroscopic internal energy.

Following the works [11, 12, 24–26], we shall present the foundation of the generalized expression for the macroscopic kinetic energy in nonequilibrium thermodynamics. We shall assume that τ is a small individual continuum region (domain) bounded by the closed continual boundary surface $\partial\tau$ considered in the three-dimensional Euclidean space with respect to a Cartesian coordinate system K . We shall consider the small continuum region τ in a Galilean frame of reference with respect to a Cartesian coordinate system K centred at the origin O and determined by the axes X_1 , X_2 , and X_3 (see Figure 1).

The unit normal K -basis coordinate vectors triad μ_1 , μ_2 , and μ_3 is taken in the directions of the axes X_1 , X_2 , and X_3 ,

respectively. The K -basis vector triad is taken to be right-handed in the order $\boldsymbol{\mu}_1$, $\boldsymbol{\mu}_2$, and $\boldsymbol{\mu}_3$; see Figure 1. \mathbf{g} is the local gravity acceleration.

An arbitrary point P in three-dimensional physical space will be uniquely defined by the position vector $\mathbf{r} = X_i \boldsymbol{\mu}_i \equiv (X_1, X_2, \text{ and } X_3)$ originating at the point O and terminating at the point P . The continuum region-affixed Lagrangian coordinate system K' (with the axes x_1, x_2 , and x_3) is centered to the mass center C of the continuum region τ . The axes x_1, x_2 , and x_3 are taken parallel to the axes X_1, X_2 , and X_3 , respectively: the axis x_i parallel to the axis X_i , where $i = 1, 2, 3$. The unit normal K' -basis coordinate vector triad $\boldsymbol{\nu}_1, \boldsymbol{\nu}_2$, and $\boldsymbol{\nu}_3$ is taken in the directions of the axes x_1, x_2 , and x_3 , respectively. The K' -basis vector triad is taken to be right-handed in the order $\boldsymbol{\nu}_1, \boldsymbol{\nu}_2$, and $\boldsymbol{\nu}_3$. The mathematical differential of the position vector \mathbf{r} , $\delta \mathbf{r} \equiv x_i \boldsymbol{\nu}_i \equiv (x_1, x_2, \text{ and } x_3)$, expressed in terms of the coordinates x_i ($i = 1, 2, 3$) in the K' -coordinate system, originates at the mass center C of the continuum region τ and terminates at the arbitrary point P of the continuum region.

The position vector \mathbf{r}_c of the mass center C of the continuum region τ in the K -coordinate system is given by the following expression:

$$\mathbf{r}_c = \frac{1}{m_\tau} \iiint_{\tau} \mathbf{r} \rho dV, \quad (3)$$

where

$$m_\tau = \iiint_{\tau} \rho dV \quad (4)$$

is the mass of the continuum region τ , dV is the mathematical differential of physical volume of the continuum region, $\rho \equiv \rho(\mathbf{r}, t)$ is the local macroscopic density of mass distribution, \mathbf{r} is the position vector of the continuum volume dV , and t is the time. The speed of the mass center C of the continuum region τ is defined by the following expression:

$$\mathbf{v}_c = \frac{d\mathbf{r}_c}{dt} = \frac{\iiint_{\tau} \mathbf{v} \rho dV}{m_\tau}, \quad (5)$$

where $\mathbf{v} = d\mathbf{r}/dt$ is the hydrodynamic velocity vector and the operator $d/dt = (\partial/\partial t) + \mathbf{v} \cdot \nabla$ denotes the total derivative following the continuum substance [33]. The relevant three-dimensional fields such as the velocity and the local mass density (and also the first and the second derivatives of the relevant fields) are assumed to vary continuously throughout the entire continuum bulk of the continuum region τ . The instantaneous macroscopic kinetic energy of the continuum region τ (bounded by the continuum boundary surface $\partial\tau$) is the sum of the kinetic energies of small parts constituting the continuum region τ when the number of the parts, n , tends to infinity and the maximum from their volumes tends to zero [33]:

$$K_\tau \equiv \iiint_{\tau} \frac{\rho \mathbf{v}^2}{2} dV, \quad (6)$$

where \mathbf{v} is the local hydrodynamic velocity vector, ρ is the local mass density, and dV is the mathematical differential of

physical volume of the continuum region. We use the common Riemann's integral here and everywhere.

For the analysis of the relative continuum motion in the physical space in the vicinity of the position vector \mathbf{r}_c of the mass centre C we have the Taylor series expansion (consistent with the Helmholtz's theorem [30, 34]) of the hydrodynamic velocity vector $\mathbf{v}(\mathbf{r})$ for each time moment t :

$$\begin{aligned} \mathbf{v}(\mathbf{r}_c + \delta \mathbf{r}) &= \mathbf{v}(\mathbf{r}_c) + \boldsymbol{\omega}(\mathbf{r}_c) \times \delta \mathbf{r} \\ &+ \sum_{i,j=1}^3 e_{ij}(\mathbf{r}_c) \delta r_j \boldsymbol{\mu}_i \\ &+ \frac{1}{2} \sum_{i,j,k=1}^3 \frac{\partial^2 v_i}{\partial X_j \partial X_k} \delta r_j \delta r_k \boldsymbol{\mu}_i + \mathbf{v}_{\text{res}}, \end{aligned} \quad (7)$$

where $\mathbf{v}(\mathbf{r}) \equiv (v_1(\mathbf{r}), v_2(\mathbf{r}), v_3(\mathbf{r}))$ is the hydrodynamic velocity vector at the position vector \mathbf{r} , $\delta \mathbf{r} \equiv \mathbf{r} - \mathbf{r}_c \equiv (\delta r_1, \delta r_2, \delta r_3) \equiv (x_1, x_2, x_3)$ is the differential of the position vector \mathbf{r} ,

$$\boldsymbol{\omega}(\mathbf{r}) \equiv \frac{1}{2} (\nabla \times \mathbf{v}(\mathbf{r})) = (\omega_1, \omega_2, \omega_3) \quad (8)$$

is the angular velocity of internal rotation (a half of the vorticity vector) in the K -coordinate system at the position vector \mathbf{r} ,

$$\boldsymbol{\omega}_v(\mathbf{r}) \equiv (\nabla \times \mathbf{v}(\mathbf{r})) \quad (9)$$

is the local vorticity in the K -coordinate system at the position vector \mathbf{r} ,

$$e_{ij}(\mathbf{r}) = \frac{1}{2} \left(\frac{\partial v_i(\mathbf{r})}{\partial X_j} + \frac{\partial v_j(\mathbf{r})}{\partial X_i} \right) \quad (10)$$

is the rate of strain tensor in the K -coordinate system at the position vector \mathbf{r} , ($i, j = 1, 2, 3$),

$$\nabla \equiv \boldsymbol{\mu}_1 \frac{\partial}{\partial X_1} + \boldsymbol{\mu}_2 \frac{\partial}{\partial X_2} + \boldsymbol{\mu}_3 \frac{\partial}{\partial X_3} \quad (11)$$

is the gradient operator, and

$$\mathbf{v}_{\text{res}} = \sum_{i=1}^3 w_i \boldsymbol{\mu}_i \quad (12)$$

is the small residual part of the Taylor series expansion (7), where $w_i = O(d_\tau^3)$, ($i = 1, 2, 3$), $d_\tau = \sup_{A, B \in \partial\tau} \sqrt{(\mathbf{r}(A, B))^2}$ is the diameter of the continuum region τ and the vector $\mathbf{r}(A, B)$ originates at point A and terminates at point B of the surface $\partial\tau$. The linear of $\delta \mathbf{r}$ terms of the Taylor series expansion (7) is presented in the classical form [33].

Substituting formula (7) into the formula (6) and integrating by parts, then we obtain the following expression [24, 31]:

$$\begin{aligned}
K_\tau &= K_t + K_r + K_s + K_{s,r}^{\text{coup}} + K_{\text{res}} \\
&= \frac{1}{2} m_\tau \mathbf{V}_c^2 + \frac{1}{2} \sum_{i,k=1}^3 I_{ik} \omega_i(\mathbf{r}_c) \omega_k(\mathbf{r}_c) \\
&\quad + \frac{1}{2} \sum_{i,j,k=1}^3 J_{jk} e_{ij}(\mathbf{r}_c) e_{ik}(\mathbf{r}_c) \\
&\quad + \sum_{i,j,k,m=1}^3 \varepsilon_{ijk} J_{jm} \omega_i(\mathbf{r}_c) e_{km}(\mathbf{r}_c) + K_{\text{res}},
\end{aligned} \tag{13}$$

where m_τ is the mass of the continuum region τ and I_{ik} is the ik -component of the classical inertia tensor depending on the mass distribution in the continuum region τ under consideration:

$$I_{ik} = \iiint_{\tau, K'} \left(\delta_{ik} \left(\sum_{j=1}^3 x_j^2 \right) - x_i x_k \right) \rho dV, \tag{14}$$

where x_i, x_k are the i, k -components of the vector $\delta \mathbf{r}$, respectively, in the K' -coordinate system, δ_{ik} is the Kronecker delta tensor, ε_{ijk} is the third-order permutation symbol, and J_{jk} is the j, k -component classical centrifugal tensor depending on the mass distribution in the continuum region τ under consideration:

$$J_{jk} = \iiint_{\tau, K'} x_j x_k \rho dV, \tag{15}$$

$K_{\text{res}} = O(d_\tau^7)$ is a small residual part of the macroscopic kinetic energy after substituting the Taylor series expansion (7) into formula (6).

Formula (13) states that the macroscopic kinetic energy K_τ of the small continuum region τ is the sum of the macroscopic translational kinetic energy K_t of the continuum region τ

$$K_t = \frac{1}{2} m_\tau \mathbf{V}_c^2, \tag{16}$$

the macroscopic internal rotational kinetic energy K_r of the continuum region τ

$$\begin{aligned}
K_r &= \frac{1}{2} \sum_{i,k=1}^3 I_{ik} \omega_i(\mathbf{r}_c) \omega_k(\mathbf{r}_c) \\
&\equiv \frac{1}{2} I_{ik} \omega_i(\mathbf{r}_c) \omega_k(\mathbf{r}_c),
\end{aligned} \tag{17}$$

the macroscopic internal shear kinetic energy K_s of the continuum region τ

$$\begin{aligned}
K_s &= \frac{1}{2} \sum_{i,j,k=1}^3 J_{jk} e_{ij}(\mathbf{r}_c) e_{ik}(\mathbf{r}_c) \\
&\equiv \frac{1}{2} J_{jk} e_{ij}(\mathbf{r}_c) e_{ik}(\mathbf{r}_c),
\end{aligned} \tag{18}$$

and the macroscopic kinetic energy of shear-rotational coupling $K_{s,r}^{\text{coup}}$ of the continuum region τ

$$\begin{aligned}
K_{s,r}^{\text{coup}} &= \sum_{i,j,k,m=1}^3 \varepsilon_{ijk} J_{jm} \omega_i(\mathbf{r}_c) e_{km}(\mathbf{r}_c) \\
&\equiv \varepsilon_{ijk} J_{jm} \omega_i(\mathbf{r}_c) e_{km}(\mathbf{r}_c).
\end{aligned} \tag{19}$$

The macroscopic internal rotational kinetic energy K_r is the classical [28, 29] kinetic energy of reversible (equilibrium) rigid-like macroscopic rotational continuum motion. The macroscopic internal shear kinetic energy K_s expresses the kinetic energy of irreversible (nonequilibrium) shear continuum motion related to the rate of strain tensor e_{ij} . The macroscopic internal kinetic energy of the shear-rotational coupling $K_{s,r}^{\text{coup}}$ expresses the kinetic energy of the local coupling between irreversible deformation and reversible rigid-like rotation.

The deduced expression (13) for K_τ confirms the postulate [35] that the velocity shear ($e_{ij} \neq 0$) represents an additional energy source taking into account the Evans, Hanley, and Hess's extended formulation [35] of the first law of thermodynamics for nonequilibrium deformed states of continuum motion. The energies $K_r, K_s, K_{s,r}^{\text{coup}}$, and K_{res} are the Galilean invariants with respect to different inertial K -coordinate systems.

We obtained [31] from (13) the following expression for the macroscopic kinetic energy per unit mass $\varepsilon_k = K_\tau/m_\tau$:

$$\begin{aligned}
\varepsilon_k &= \varepsilon_t + \varepsilon_r + \varepsilon_s + \varepsilon_{s,r}^{\text{coup}} + \varepsilon_{\text{res}} \\
&= \frac{1}{2} \mathbf{V}_c^2 + \frac{1}{2} \sum_{i,k=1}^3 \theta_{ik} \omega_i \omega_k + \frac{1}{2} \sum_{i,j,k=1}^3 \beta_{jk} e_{ij} e_{ik} \\
&\quad + \sum_{i,j,k,m=1}^3 \varepsilon_{ijk} \beta_{jm} \omega_i e_{km} + \varepsilon_{\text{res}},
\end{aligned} \tag{20}$$

where

$$\theta_{ik} = \frac{I_{ik}}{m_\tau} = \frac{I_{ik}}{\iiint_{\tau} \rho dV} \quad (i, k = 1, 2, 3) \tag{21}$$

is the ik -component of the classical inertia tensor per unit mass of the continuum region τ ,

$$\beta_{ik} = \frac{J_{ik}}{m_\tau} = \frac{J_{ik}}{\iiint_{\tau} \rho dV} \quad (i, k = 1, 2, 3) \tag{22}$$

is the ik -component of the classical centrifugal tensor per unit mass of the continuum region τ ,

$$\varepsilon_t = \frac{K_t}{m_\tau} = \frac{1}{2} \mathbf{V}_c^2 \tag{23}$$

is the macroscopic translational kinetic energy per unit mass of the continuum region τ (moving as a whole at speed \mathbf{V}_c of the mass center of the continuum region τ),

$$\varepsilon_r = \frac{K_r}{m_\tau} = \frac{1}{2} \theta_{ik} \omega_i \omega_k \tag{24}$$

is the macroscopic internal rotational kinetic energy per unit mass of the continuum region τ ,

$$\varepsilon_s = \frac{K_s}{m_\tau} = \frac{1}{2}\beta_{jk}e_{ij}e_{ik} \quad (25)$$

is the macroscopic internal shear kinetic energy per unit mass of the continuum region τ ,

$$\varepsilon_{s,r}^{\text{coup}} = \frac{K_{s,r}^{\text{coup}}}{m_\tau} = \varepsilon_{ijk}\beta_{jm}\omega_i e_{km} \quad (26)$$

is the macroscopic internal kinetic energy of the shear-rotational coupling per unit mass (of the continuum region τ), and $\varepsilon_{\text{res}} = O(d_\tau^4)$ is the residual correction. The energies ε_r , ε_s , $\varepsilon_{s,r}^{\text{coup}}$, and ε_{res} are the Galilean invariants with respect to different inertial K -coordinate systems. We have $\varepsilon_r = O(d_\tau^2)$, $\varepsilon_s = O(d_\tau^2)$, $\varepsilon_{s,r}^{\text{coup}} = O(d_\tau^2)$, and $\varepsilon_{\text{res}} = O(d_\tau^4)$, when $d_\tau \rightarrow 0$, where d_τ is the defined diameter of the continuum region τ .

For a homogeneous continuum region of simple form (sphere or cube) we have

$$I_{ik} = I\delta_{ik}, \quad J_{jk} = J\delta_{jk}. \quad (27)$$

Formula (17) for the macroscopic internal rotational kinetic energy K_r is reduced to the classical expression [29]

$$K_r = \frac{1}{2}I\omega^2, \quad (28)$$

where $\omega^2 = \omega_1^2 + \omega_2^2 + \omega_3^2$. Formula (18) for the macroscopic internal shear kinetic energy K_s is reduced to the expression [24, 31]

$$K_s = \frac{1}{2}J e_{ij}e_{ij} \equiv \frac{1}{2}J(e_{ij})^2, \quad (29)$$

which is proportional to the local kinetic energy dissipation rate per unit mass $\varepsilon_{\text{dis}} = 2\nu(e_{ij})^2$ in an incompressible viscous Newtonian continuum, where ν is the molecular viscosity. The macroscopic internal kinetic energy of shear-rotational coupling $K_{s,r}^{\text{coup}}$ vanishes for the homogeneous continuum region τ of the form of the sphere or cube. The macroscopic kinetic energy K_τ for the homogeneous continuum region τ of the shape of sphere or cube is given by following expression [24, 31]

$$K_\tau = \frac{1}{2}m_\tau \mathbf{V}_c^2 + \frac{1}{2}I\omega^2 + \frac{1}{2}J(e_{ij})^2 + K_{\text{res}}. \quad (30)$$

Hence, the macroscopic kinetic energy per unit mass ε_k for the homogeneous continuum sphere or cube τ is expressed as the sum of explicit terms [24, 31]

$$\varepsilon_k = \frac{1}{2}\mathbf{V}_c^2 + \frac{1}{2}\theta\omega^2 + \frac{1}{2}\beta(e_{ij})^2 + \varepsilon_{\text{res}}, \quad (31)$$

where $\varepsilon_t = (1/2)\mathbf{V}_c^2$ is the macroscopic translational kinetic energy per unit mass of the continuum region τ ; $\theta = I/m_\tau$; $\beta = J/m_\tau$; $\varepsilon_r = (1/2)\theta\omega^2$ is the classical [28, 29] macroscopic internal rotational kinetic energy per unit mass of the continuum region τ ; $\varepsilon_s = (1/2)\beta(e_{ij})^2$ is the macroscopic internal

shear kinetic energy per unit mass of the homogeneous continuum sphere or cube τ [24, 31].

We have the following expression for the macroscopic internal kinetic energy K_{int} of the homogeneous continuum region τ of the shape of sphere or cube [24, 31]

$$K_{\text{int}} = \frac{1}{2}I\omega^2 + \frac{1}{2}J(e_{ij})^2 + K_{\text{res}}. \quad (32)$$

The macroscopic internal kinetic energy per unit mass ε_{int} for the homogeneous continuum region τ of the shape of sphere or cube is given by the sum of explicit terms [24, 31]:

$$\varepsilon_{\text{int}} = \frac{1}{2}\theta\omega^2 + \frac{1}{2}\beta(e_{ij})^2 + \varepsilon_{\text{res}}. \quad (33)$$

Compare formula (31) with the de Groot and Mazur's definition (2). Expression (31) is reduced to de Groot and Mazur's definition (2) under condition

$$e_{ij} = 0 \quad (i, j = 1, 2, 3) \quad (34)$$

of local thermodynamic equilibrium. Therefore, we can conclude that the definition (2) of the macroscopic kinetic energy per unit mass ε_k in classical nonequilibrium thermodynamics [28, 29] is based on the assumption $e_{ij} = 0$ of local thermodynamic equilibrium [24, 31, 35].

The obtained formula (20) for ε_k and its particular form (31) (obtained for homogeneous continuum regions of spherical and cubical shapes) generalized [24, 31] the classical de Groot and Mazur expression (2) in classical nonequilibrium thermodynamics [28, 29] by taking into account the irreversible dissipative shear component of the macroscopic continuum motion related to the rate of strain tensor e_{ij} . The expression (20) for ε_k contains the new macroscopic internal shear kinetic energy per unit mass ε_s , which expresses the kinetic energy of irreversible dissipative shear motion, and also the new macroscopic internal kinetic energy of the shear-rotational coupling per unit mass $\varepsilon_{s,r}^{\text{coup}}$, which expresses the kinetic energy of local coupling between irreversible dissipative shear and reversible rigid-like rotational macroscopic continuum motions.

The macroscopic internal shear kinetic energy per unit mass (for homogeneous continuum regions of spherical and cubical shapes)

$$\varepsilon_s = \frac{1}{2}\beta(e_{ij})^2 \quad (35)$$

is proportional to the kinetic energy viscous dissipation rate per unit mass

$$\varepsilon_{\text{dis},s} = 2\nu(e_{ij})^2 \quad (36)$$

in an incompressible viscous Newtonian continuum characterized by the kinematic viscosity ν . We have shown [24] that the proportionality

$$\varepsilon_s \sim \varepsilon_{\text{dis},s} = 2\nu(e_{ij})^2 \quad (37)$$

is the basis of the established association [36, 37] between a structure and an order (and, hence, the associated macroscopic kinetic energy), on the one hand, and irreversible dissipation, on the other hand, for the dissipative structures of turbulence in viscous Newtonian fluids.

2.2. *The Generalized Differential Formulation of the First Law of Thermodynamics (in the Galilean Frame of Reference) for Nonequilibrium Shear-Rotational States of the Deformed One-Component Individual Finite Continuum Region (Characterized by the Symmetric Stress Tensor \mathbf{T}) Moving in the Nonstationary Newtonian Gravitational Field.* Following the works [11, 12, 25, 26], we shall present the foundation of the generalized differential formulation of the first law of thermodynamics (in the Galilean frame of reference) for nonequilibrium shear-rotational states of the deformed finite one-component individual continuum region (characterized by the symmetric stress tensor \mathbf{T}) moving in the nonstationary Newtonian gravitational field. We shall consider the deformed finite one-component individual continuum region in nonequilibrium shear-rotational states characterized by the following condition:

$$e_{ij} \neq 0 \quad (i, j = 1, 2, 3). \quad (38)$$

Considering the graphical methods in the thermodynamics of fluids, Gibbs [27] formulated the first law of thermodynamics for the fluid body (fluid region) as follows (in Gibbs' designations):

$$d\varepsilon = dH - dW, \quad (39)$$

where $d\varepsilon$ is the differential of the internal thermal energy of the fluid body, dH is the differential change of heat across the boundary of the fluid body related to the thermal molecular conductivity (associated with the corresponding external or internal heat fluxes), and $dW = p dV$ is the differential work produced by the considered fluid body on its surroundings (surrounding fluid) under the differential change dV of the fluid region (of volume V) characterized by the thermodynamic pressure p .

The formulation [32] of the first law of thermodynamics for the general thermodynamic system (material region) is given by the equivalent form (in Landau's and Lifshitz's designations [32])

$$dE = dQ - p dV, \quad (40)$$

where $dA = -p dV$ is the differential work produced by the surroundings (surroundings of the thermodynamic system) on the thermodynamic system under the differential change dV of volume V of the thermodynamic system characterized by the thermodynamic pressure p ; dQ is the differential heat transfer (across the boundary of the thermodynamic system) related to the thermal interaction of the thermodynamic system and the surroundings (surrounding environment); E is the energy of the thermodynamic system, which should contain (as supposed [32]) the kinetic energy of the macroscopic continuum motion.

We shall use the differential formulation of the first law of thermodynamics [28] for the specific volume $\vartheta = 1/\rho$ of the compressible viscous one-component deformed continuum with no chemical reactions:

$$\frac{du}{dt} = \frac{dq}{dt} - p \frac{d\vartheta}{dt} - \vartheta \mathbf{\Pi} : \text{Grad } \mathbf{v}, \quad (41)$$

where u is the specific (per unit mass) internal thermal energy, p is the thermodynamic pressure, $\mathbf{\Pi}$ is the viscous stress tensor, \mathbf{v} is the hydrodynamic velocity of the continuum macrodifferential element [28], and dq is the differential change of heat across the boundary of the continuum region (of unit mass) related to the thermal molecular conductivity described by the heat equation [28]:

$$\rho \frac{dq}{dt} = -\text{div } \mathbf{J}_q, \quad (42)$$

where \mathbf{J}_q is the heat flux [28]. The viscous stress tensor $\mathbf{\Pi}$ is taken from the decomposition of the pressure tensor \mathbf{P} [28]:

$$\mathbf{P} = p\boldsymbol{\delta} + \mathbf{\Pi}, \quad (43)$$

where $\boldsymbol{\delta}$ is the Kronecker delta tensor.

Considering the Newtonian viscous stress tensor $\mathbf{P}^v \equiv \mathbf{\Pi}$ of the compressible viscous Newtonian continuum with the components [29]

$$\Pi_{ij} = \left\{ \left(\frac{2}{3} \nu \rho - \eta_v \right) \text{div } \mathbf{v} \right\} \delta_{ij} - 2\nu \rho e_{ij}, \quad (44)$$

the differential formulation (41) of the first law of thermodynamics (for the continuum region (of unit mass) of the compressible viscous Newtonian one-component deformed continuum with no chemical reactions) can be rewritten as follows:

$$\frac{du}{dt} = \frac{dq}{dt} - p \frac{d\vartheta}{dt} + \left(\nu_2 - \frac{2}{3} \nu \right) (\text{div } \mathbf{v})^2 + 2\nu (e_{ij})^2, \quad (45)$$

where $\nu = \eta/\rho$ is the coefficient of the molecular kinematic (first) viscosity and $\nu_2 = \eta_v/\rho$ is the coefficient of the molecular volume (second) viscosity [38]. The first and the second terms in the right-hand side of relation (45) are analogous to the corresponding respective first and second terms in the right-hand side of the classical formulations (39) and (40). The third term in the right-hand side of relation (45)

$$dq_{i,c} = \left(\frac{\eta_v}{\rho} - \frac{2}{3} \nu \right) (\text{div } \mathbf{v})^2 dt \quad (46)$$

is related to the "internal" heat induced during the time interval dt by viscous-compressible irreversibility [24]. The fourth term in the right-hand side of relation (45)

$$dq_{i,s} = 2\nu (e_{ij})^2 dt \quad (47)$$

is related to the "internal" heat induced during the time interval dt by viscous-shear irreversibility [24]. The differential formulation (45) of the first law of thermodynamics (for the continuum element of the compressible viscous Newtonian one-component deformed continuum with no chemical reactions) takes into account (in addition to the classical terms) the viscous-compressible irreversibility and viscous-shear irreversibility inside the continuum element of the compressible viscous Newtonian one-component deformed continuum with no chemical reactions.

Using the differential formulation (41) of the first law of thermodynamics [28] for the total derivative du/dt (following the liquid substance) of the specific (per unit mass) internal thermal energy u of a compressible viscous one-component deformed continuum with no chemical reactions, the heat equation (42) [28], the general equation of continuum movement [29]

$$\frac{d\mathbf{v}}{dt} = \frac{1}{\rho} \operatorname{div} \mathbf{T} + \mathbf{g} \quad (48)$$

for the deformed continuum characterized by the symmetric stress tensor \mathbf{T} of general form (in particular, with the components [29])

$$T_{ij} = - \left\{ p + \left(\frac{2}{3} \nu \rho - \eta_v \right) \operatorname{div} \mathbf{v} \right\} \delta_{ij} + 2\nu \rho e_{ij} \quad (49)$$

for the compressible viscous Newtonian one-component continuum) and taking into account the time variations of the potential ψ of the nonstationary gravitational field (characterized by the local gravity acceleration vector $\mathbf{g} = -\nabla\psi$) inside an arbitrary finite macroscopic individual continuum region τ , we derived [11, 12] the generalized differential formulation (for the Galilean frame of reference) of the first law of thermodynamics (for moving rotating deforming compressible heat-conducting stratified macroscopic continuum region τ subjected to the nonstationary Newtonian gravitational field):

$$\begin{aligned} & d(K_\tau + U_\tau + \pi_\tau) \\ &= dt \iint_{\partial\tau} (\mathbf{v} \cdot \mathbf{n} \cdot \mathbf{T}) d\Omega_{\mathbf{n}} \\ & - dt \iint_{\partial\tau} (\mathbf{J}_q \cdot \mathbf{n}) d\Omega_{\mathbf{n}} + dt \iiint_{\tau} \frac{\partial\psi}{\partial t} \rho dV, \end{aligned} \quad (50)$$

where

$$\delta A_{\text{np},\partial\tau} = dt \iint_{\partial\tau} (\mathbf{v} \cdot \mathbf{n} \cdot \mathbf{T}) d\Omega_{\mathbf{n}} \quad (51)$$

is the differential work done during the infinitesimal time interval dt by nonpotential stress forces (pressure, compressible, and viscous forces for Newtonian continuum) acting on the boundary surface $\partial\tau$ of the continuum region τ ; $d\Omega_{\mathbf{n}}$ is the differential element (of the boundary surface $\partial\tau$ of the continuum region τ) characterized by the external normal unit vector \mathbf{n} ; $\mathbf{t} = \mathbf{n} \cdot \mathbf{T}$ is the stress vector [29], $\mathbf{T} = -\mathbf{P}$ [29], where \mathbf{P} is the pressure tensor characterized (in particular, for the model of the compressible viscous Newtonian continuum characterized by the coefficients of kinematic viscosity ν and the volume viscosity η_v) by components (obtained from (49))

$$\begin{aligned} P_{ij} &= \left\{ p + \left(\frac{2}{3} \nu \rho - \eta_v \right) \operatorname{div} \mathbf{v} \right\} \delta_{ij} - 2\nu \rho e_{ij}; \\ \delta Q &= -dt \iint_{\partial\tau} (\mathbf{J}_q \cdot \mathbf{n}) d\Omega_{\mathbf{n}} \end{aligned} \quad (52)$$

is the differential change of heat of the macroscopic individual continuum region τ related to the thermal molecular conductivity of heat across the boundary $\partial\tau$ of the continuum region

τ , where \mathbf{J}_q is the heat flux [28] (across the element $d\Omega_{\mathbf{n}}$ of the continuum boundary surface $\partial\tau$);

$$\pi_\tau \equiv \iiint_{\tau} \psi \rho dV \quad (53)$$

is the macroscopic potential energy (of the macroscopic individual continuum region τ) related to the nonstationary potential ψ of the gravitational field;

$$U_\tau \equiv \iiint_{\tau} u \rho dV \quad (54)$$

is the classical microscopic internal thermal energy of the macroscopic individual continuum region τ ;

$$K_\tau = \iiint_{\tau} \frac{\rho \mathbf{v}^2}{2} dV \quad (55)$$

is the instantaneous macroscopic kinetic energy of the macroscopic individual continuum region τ . The instantaneous macroscopic kinetic energy K_τ is given by the relation (13) [24, 31] for the small macroscopic individual continuum region τ .

The generalized differential formulation (50) of the first law of thermodynamics can be rewritten as follows [11, 12]:

$$dU_\tau + dK_\tau + d\pi_\tau = \delta Q + \delta A_{\text{np},\partial\tau} + dG \quad (56)$$

extending the classical [12] formulations (39) and (40)

$$dU = \delta Q - pdV, \quad (d\varepsilon \equiv dU, -\delta W = -pdV) \quad (57)$$

by taking into account (along with the classical infinitesimal change of heat δQ and the classical infinitesimal change of the internal energy $dU_\tau \equiv dU$) the infinitesimal increment of the macroscopic kinetic energy dK_τ , the infinitesimal increment of the gravitational potential energy $d\pi_\tau$, the generalized infinitesimal work $\delta A_{\text{np},\partial\tau}$ done on the continuum region τ by the surroundings of τ , and the infinitesimal amount dG of energy [11, 12]

$$dG = dt \iiint_{\tau} \frac{\partial\psi}{\partial t} \rho dV \quad (58)$$

added (or lost) as the result of the Newtonian nonstationary gravitational energy influence on the continuum region τ during the infinitesimal time interval dt .

The generalized differential formulation (50) of the first law of thermodynamics can be rewritten as follows [11, 12]:

$$\begin{aligned} \frac{dE_\tau}{dt} &= \frac{d}{dt} (K_\tau + U_\tau + \pi_\tau) \\ &= \iiint_{\tau} \left(\frac{1}{2} \mathbf{v}^2 + u + \psi \right) \rho dV \\ &= \iint_{\partial\tau} (\mathbf{v} \cdot \mathbf{n} \cdot \mathbf{T}) d\Omega_{\mathbf{n}} \\ & - \iint_{\partial\tau} (\mathbf{J}_q \cdot \mathbf{n}) d\Omega_{\mathbf{n}} + \iiint_{\tau} \frac{\partial\psi}{\partial t} \rho dV. \end{aligned} \quad (59)$$

The equivalent generalized differential formulations (50), (56), and (59) of the first law of thermodynamics take into account the following factors:

- (1) the classical heat thermal molecular conductivity (across the boundary $\partial\tau$ of the macroscopic continuum region τ) related to the classical infinitesimal change of heat δQ :

$$\delta Q = -dt \iint_{\partial\tau} (\mathbf{J}_q \cdot \mathbf{n}) d\Omega_{\mathbf{n}}, \quad (60)$$

- (2) the classical infinitesimal change of the internal energy dU_{τ} of the macroscopic continuum region τ :

$$dU_{\tau} \equiv d \iiint_{\tau} u \rho dV, \quad (61)$$

- (3) the established [11, 12] infinitesimal increment of the macroscopic kinetic energy dK_{τ} of the macroscopic continuum region τ :

$$dK_{\tau} = d \iiint_{\tau} \frac{\rho \mathbf{v}^2}{2} dV, \quad (62)$$

- (4) the established [11, 12] infinitesimal increment of the gravitational potential energy $d\pi_{\tau}$ of the macroscopic continuum region τ :

$$d\pi_{\tau} = d \iiint_{\tau} \psi \rho dV, \quad (63)$$

- (5) the established [11, 12] generalized infinitesimal work $\delta A_{np,\partial\tau}$ done on the macroscopic continuum region τ by the surroundings of τ :

$$\delta A_{np,\partial\tau} = dt \iint_{\partial\tau} (\mathbf{v} \cdot (\mathbf{n} \cdot \mathbf{T})) d\Omega_{\mathbf{n}}, \quad (64)$$

- (6) the established [11, 12] infinitesimal amount dG of energy added (or lost) as the result of the Newtonian nonstationary gravitational energy influence on the macroscopic continuum region τ during the infinitesimal time interval dt :

$$dG = dt \iiint_{\tau} \frac{\partial\psi}{\partial t} \rho dV. \quad (65)$$

The generalized differential formulations (50), (56), and (59) of the first law of thermodynamics (given for the Galilean frame of reference) are valid for nonequilibrium shear-rotational states of the deformed finite individual continuum region (characterized by the symmetric stress tensor \mathbf{T} in the general equation (48) of continuum movement [29]) moving in the nonstationary gravitational field. The generalized differential formulations (50) and (56) of the first law of thermodynamics [11, 12] are the generalizations of the classical formulations (39) and (40) of the first law of thermodynamics taking into account: (1) the generalized expression (51) for the differential work $\delta A_{np,\partial\tau}$ done during the infinitesimal time interval dt by nonpotential stress forces acting on the boundary surface $\partial\tau$ of the individual continuum region τ and (2)

the time variations of the potential ψ of the nonstationary gravitational field inside the individual continuum region τ due to the deformation of the individual continuum region τ and due to the external (terrestrial and cosmic) gravitational influence on the individual continuum region τ moving in the total (internal + external) nonstationary gravitational field.

2.3. The Generalized Differential Formulation of the First Law of Thermodynamics (in the Galilean Frame of Reference) for Nonequilibrium Shear-Rotational States of the Deformed Finite Individual Region of the Compressible Viscous Newtonian One-Component Continuum Moving in the Nonstationary Gravitational Field. There is evidence [39] that the rocks of the Earth's crust at protracted loadings may be considered as fluids characterized by the very high viscosity. According to the classical viewpoint [39], the local mechanism of creation of the earthquakes is related to the release of the accumulated potential energy of the elastic deformation during the sudden local break (i.e., the discontinuous shear) of the Earth's crust (or the sudden increase of fluidity in the local region of the Earth's crust) accompanied by viscous relaxation and generation of seismic waves. It was conjectured [40] that "more punctual and refined methods of the mathematical analysis are obligatory" for "the practical assessment of the seismic hazard".

Taking into account the established [31] conception of the macroscopic internal shear kinetic energy (per unit mass) ε_s related to the rate of medium deformation (i.e., with the rate of strain tensor $e_{ij} = d\varepsilon_{ij}/dt$, where ε_{ij} is the deformation tensor [30]), we have elucidated [41] from the viewpoint of nonequilibrium thermodynamics the mechanism of generation of seismic waves from the separate deformed finite zone of the Earth's crust. The proportionality (37) takes place also for deformed compressible finite region of the Earth's crust for sudden rise of fluidity (in a local region of the Earth's crust) related to the local sudden medium deformation in the separate seismic zones of the seismic activity. Taking into account the established [31] proportionality (37), we have assumed [31] that the accumulated potential energy of the elastic deformation (related to the deformation tensor ε_{ij}) converts to the macroscopic internal shear kinetic energy K_s (related to the rate of strain tensor e_{ij}) in the seismic zone simultaneously with the damping of K_s by viscous dissipation and radiation of seismic waves during several oscillations. In Section 3 we shall evaluate this mechanism on the basis of the generalized differential formulation (50) of the first law of thermodynamics for nonequilibrium shear-rotational states of the deformed finite individual continuum region (characterized by the symmetric stress tensor \mathbf{T}) moving in the nonstationary gravitational field.

Following the works [11, 12, 25, 26], we shall present the foundation of the generalized differential formulation of the first law of thermodynamics for nonequilibrium shear-rotational states of the deformed finite individual region of the compressible viscous Newtonian one-component continuum moving in the nonstationary gravitational field. The generalized differential formulation (50) of the first law of thermodynamics (formulated for the Galilean frame of

reference) is valid for arbitrary symmetric stress tensor \mathbf{T} , in particular for nonequilibrium shear-rotational states of the deformed finite individual region of the compressible viscous Newtonian one-component continuum moving in the nonstationary gravitational field. The coefficient of molecular kinematic (first, shear) viscosity $\nu = \eta/\rho$ and the coefficient of molecular volume (second) viscosity $\nu_2 = \eta_v/\rho$ are assumed to vary for each time moment t as an arbitrary continuous functions of the Cartesian space (three-dimensional) coordinates.

The differential work $\delta A_{np,\partial\tau}$ for the Newtonian symmetric stress tensor \mathbf{T} (characterized by the components (49)) is presented by three explicit terms [11, 12]:

$$\begin{aligned}\delta A_{np,\partial\tau} &= \delta A_p + \delta A_c + \delta A_s \\ &= -dt \iint_{\partial\tau} p(\mathbf{v} \cdot \mathbf{n}) d\Omega_n \\ &\quad - dt \iint_{\partial\tau} \left(\frac{2}{3}\eta - \eta_v \right) \operatorname{div} \mathbf{v}(\mathbf{v} \cdot \mathbf{n}) d\Omega_n \\ &\quad + dt \iint_{\partial\tau} 2\eta \nu_\beta n_\alpha e_{\alpha\beta} d\Omega_n,\end{aligned}\quad (66)$$

where

$$\delta A_p = -dt \iint_{\partial\tau} p(\mathbf{v} \cdot \mathbf{n}) d\Omega_n \quad (67)$$

is the differential work of the hydrodynamic pressure forces acting on the boundary surface $\partial\tau$ of the individual continuum region τ (bounded by the continuum boundary surface $\partial\tau$) during the infinitesimal time interval dt ;

$$\delta A_c = -dt \iint_{\partial\tau} \left(\frac{2}{3}\eta - \eta_v \right) \operatorname{div} \mathbf{v}(\mathbf{v} \cdot \mathbf{n}) d\Omega_n \quad (68)$$

is the differential work (related to the combined effects of the acoustic compressibility, molecular kinematic viscosity, and molecular volume viscosity) of the acoustic (compressible) pressure forces acting on the boundary surface $\partial\tau$ of the individual continuum region τ during the infinitesimal time interval dt ;

$$\delta A_s = dt \iint_{\partial\tau} 2\eta \nu_\beta n_\alpha e_{\alpha\beta} d\Omega_n \quad (69)$$

is the differential work of the viscous Newtonian forces (related to the combined effect of the velocity shear, that is, the deformation of the continuum region τ , and the molecular kinematic viscosity) acting on the boundary surface $\partial\tau$ of the individual continuum region τ during the infinitesimal time interval dt .

Along with (45) the differential formulation of the first law of thermodynamics [28] for the total derivative du/dt (following the continuum substance) of the internal thermal energy per unit mass u of the one-component deformed continuum with no chemical reactions, the thermodynamic theory [28] contains additionally the equations of the mass and momentum balances:

$$\frac{\partial \rho}{\partial t} = -\operatorname{div} \rho \mathbf{v}, \quad (70)$$

$$\rho \frac{d\mathbf{v}}{dt} = -\operatorname{Grad} p + \eta \Delta \mathbf{v} + \left(\frac{1}{3}\eta + \eta_v \right) \operatorname{Grad} \operatorname{div} \mathbf{v}. \quad (71)$$

The generalized differential formulation (50) of the first law of thermodynamics (together with the generalized differential work $\delta A_{np,\partial\tau}$ given by the expression (66)) is valid for nonequilibrium shear-rotational states of the deformed finite individual region of the compressible viscous Newtonian one-component continuum moving in the nonstationary gravity field. The coefficient of molecular kinematic (first, shear) viscosity $\nu = \eta/\rho$ and the coefficient of molecular volume (second) viscosity $\nu_2 = \eta_v/\rho$ are assumed to vary for each time moment t as an arbitrary continuous functions of Cartesian space (three-dimensional) coordinates.

The generalized differential formulation (50) takes into account the dependences of the hydrodynamic pressure on the hydrodynamic vorticity $\boldsymbol{\omega}$, and on the rate of strain tensor e_{ij} by means of the component δA_p (in the expression (66) for $\delta A_{np,\partial\tau}$) given by the expression (67). The presence of the third term δA_s (given by the expression (69) and related to the combined effect of the molecular kinematic viscosity and the deformation of the continuum region τ defined by the rate of strain tensor $e_{\alpha\beta}$) in the expression (66) for $\delta A_{np,\partial\tau}$ generalizes essentially the classical formulations (39) and (40) of the first law of thermodynamics by taking into account the differential work of the viscous Newtonian forces acting on the boundary continuum surface $\partial\tau$ of the individual continuum region τ .

The general equation (48) of continuum movement [29] for the compressible viscous Newtonian one-component continuum is reduced to the following equation:

$$\begin{aligned}\rho \frac{d\mathbf{v}}{dt} &= -\operatorname{Grad} p + \eta \Delta \mathbf{v} \\ &\quad + \left(\frac{1}{3}\eta + \eta_v \right) \operatorname{Grad} \operatorname{div} \mathbf{v} \\ &\quad + (\operatorname{Grad} \eta) \cdot \mathbf{e} \\ &\quad - \operatorname{div} \mathbf{v} \operatorname{Grad} \left(\frac{2}{3}\eta - \eta_v \right) + \mathbf{g},\end{aligned}\quad (72)$$

where $(\operatorname{Grad} \eta) \cdot \mathbf{e}$ is the internal multiplication of the vector $(\operatorname{Grad} \eta)$ and the rate of strain tensor \mathbf{e} in accordance with the corresponding definition [29]. Equation (72) generalizes the Navier-Stokes equation (71) (given for $\mathbf{g} = 0$) by taking into account the dependences of the coefficient of molecular kinematic viscosity $\nu = \eta/\rho$ and the coefficient of molecular volume viscosity $\nu_2 = \eta_v/\rho$ on the space (three-dimensional) Cartesian coordinates.

The relevant example for illustration of the significance of the term δA_s (in the expression (66) for the differential work $\delta A_{np,\partial\tau}$) is related to the thermodynamic consideration [12] of the processes of the energy exchange [42] between the oceans and the lithosphere of the Earth. According to the expression (69) for the term δA_s , the energy exchange between the oceans (and the atmosphere) and the lithosphere of the Earth is possible only under the presence of the medium acoustic compressibility (i.e., $\operatorname{div} \mathbf{v} \neq 0$) and the medium deformations (i.e., $e_{\alpha\beta} \neq 0$) in the boundary regions of fluid (in the oceans), air (in the atmosphere), and the compressible deformed lithosphere of the Earth. According to the generalized expression (66) for the differential work $\delta A_{np,\partial\tau}$,

the energy exchange between the oceans (and the atmosphere) and the lithosphere of the Earth is impossible for nondeformed ($e_{\alpha\beta} = 0$) and noncompressible ($\text{div } \mathbf{v} = 0$) lithosphere.

We have the evolution equation for the total mechanical energy ($K_\tau + \pi_\tau$) of the deformed finite individual macroscopic continuum region τ [11, 12]:

$$\begin{aligned} \frac{d}{dt} (K_\tau + \pi_\tau) &= \frac{d}{dt} \iiint_\tau \left(\frac{1}{2} \mathbf{v}^2 + \psi \right) \rho dV \\ &= \iiint_\tau p \text{div } \mathbf{v} dV \\ &\quad + \iiint_\tau \left(\frac{2}{3} \eta - \eta_v \right) (\text{div } \mathbf{v})^2 dV \\ &\quad - \iiint_\tau 2\nu (e_{ij})^2 \rho dV \\ &\quad + \iint_{\partial\tau} (\mathbf{v} \cdot (\mathbf{n} \cdot \mathbf{T})) d\Omega_{\mathbf{n}} \\ &\quad + \iiint_\tau \frac{\partial\psi}{\partial t} \rho dV \end{aligned} \quad (73)$$

obtained from the generalized differential formulation (50) for the compressible viscous Newtonian one-component continuum moving in the nonstationary gravitational field. In Section 3 we shall use the evolution equation (73) of the total mechanical energy to found the rotational, shear, and the shear-rotational models of the earthquake focal region.

2.4. Cosmic and Terrestrial Energy Gravitational Genesis of the Seismotectonic (and Volcanic) Activity of the Earth Induced by the Combined Cosmic and Terrestrial Nonstationary Energy Gravitational Influences on an Arbitrary Individual Continuum Region τ (of the Earth) and by the Nonpotential Terrestrial Stress Forces Acting on the Boundary Surface $\partial\tau$ of the Individual Continuum Region τ . Following the works [11, 12], we shall present the physical mechanisms of the energy fluxes to the continuum region τ related to preparation of earthquakes. The equivalent generalized differential formulations (50) and (59) of the first law of thermodynamics show that the nonstationary gravitational field (related to the nonstationary gravitational potential ψ) gives the following gravitational energy power:

$$W_{\text{gr}}(\tau) = \iiint_\tau \frac{\partial\psi}{\partial t} \rho dV = \frac{dG}{dt} \quad (74)$$

associated with the gravitational energy power of the total combined (external cosmic and terrestrial and internal related to the macroscopic continuum region τ) gravitational field. If the macroscopic continuum region τ is not very large, consequently, it cannot induce the significant time variations to the potential ψ of the gravity field inside the continuum region τ . According to the equivalent generalized differential formulations (50) and (59) of the first law of thermodynamics and to the evolution equation (73) for the total mechanical

energy ($K_\tau + \pi_\tau$) of the deformed finite individual macroscopic continuum region τ , the energy power of the gravitational field may produce the fractures in the continuum region τ . We shall consider this aspect in Section 3.

The generalized differential formulation (59) of the first law of thermodynamics and the expression (74) for the gravitational energy power $W_{\text{gr}}(\tau)$ show that the local time increase of the potential ψ of the gravitational field is the gravitational energy mechanism of the gravitational energy supply into the continuum region τ . Really, the local time increase of the potential ψ of the gravitational field inside the continuum region τ ($\partial\psi/\partial t > 0$) supplies the gravitational energy into the continuum region τ . Consequently, according to the generalized differential formulation (59) and to the evolution equation (73), the total energy ($K_\tau + U_\tau + \pi_\tau$) of the continuum region τ and the total mechanical energy ($K_\tau + \pi_\tau$) of the continuum region τ are increased if $\partial\psi/\partial t > 0$.

According to the generalized differential formulation (59) of the first law of thermodynamics and to the evolution equation (73), the gravitational energy supply into the continuum region τ may induce the formation of fractures in the continuum region τ related to the production of earthquake. This conclusion corresponds to the observations [1, 3–5, 9, 10, 13] of the identified anomalous variations of the gravitational field before strong earthquakes.

According to the generalized differential formulation (59) of the first law of thermodynamics and to the evolution equation (73), the supply of energy into the continuum region τ may occur also by means of the work

$$A_{\text{np},\partial\tau} = \int_{t_0}^t dt \iint_{\partial\tau} (\mathbf{v} \cdot (\mathbf{n} \cdot \mathbf{T})) d\Omega_{\mathbf{n}} \quad (75)$$

done by nonpotential stress forces (pressure, compressible, and viscous forces for Newtonian continuum) acting on the boundary surface $\partial\tau$ of the continuum region τ during the time interval $(t - t_0)$.

The considered mechanisms of the energy supply to the Earth's macroscopic continuum region τ should result in the irreversible process of the splits formation in the rocks related to the generation of the high-frequency acoustic waves from the focal continuum region τ before the earthquake. Taking this into account, the sum $\delta A_c + \delta A_s$ in the expression (45) is interpreted [11, 12] as the energy flux (related to the compressible and viscous forces acting on the boundary surface $\partial\tau$ of the continuum region τ) [38]

$$\delta F_{\text{vis},c} = \delta A_c + \delta A_s \quad (76)$$

directed across the boundary $\partial\tau$ (see Figures 2 and 3) of the continuum region τ .

The considered mechanisms of the energy supply to the Earth's macroscopic continuum region τ should result in the significant increase of the energy flux $\delta F_{\text{vis},c}$ of the geo-acoustic energy from the focal region τ before the earthquake. The deduced conclusion is in a good agreement with the results of the detailed experimental studies [43].

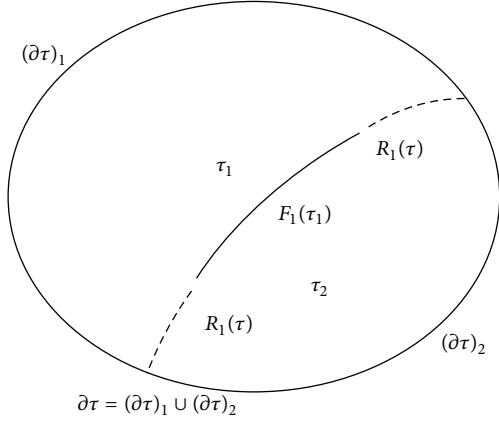


FIGURE 2: The macroscopic continuum region τ containing two subsystems τ_1 and τ_2 interacting on the surface $F_1(\tau)$ of the tangential jump of the continuum velocity.

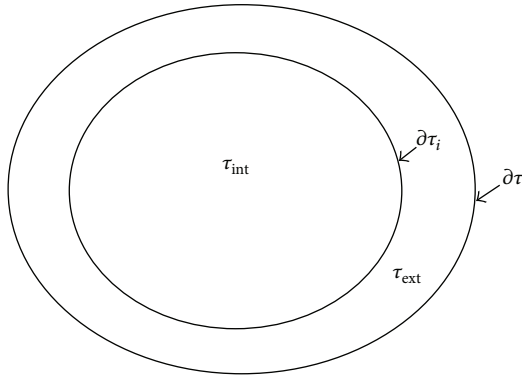


FIGURE 3: The macroscopic continuum region τ consisting of the subsystems τ_{int} and τ_{ext} interacting on the surface $\partial\tau_i$ of the continuum velocity jump.

3. Generalized Thermohydrodynamic Shear-Rotational and Classical Shear and Rotational Models of the Earthquake Focal Region

3.1. *The Generalized Thermohydrodynamic Shear-Rotational and the Classical Shear (Deformational) Models of the Earthquake Focal Region Based on the Generalized Differential Formulation of the First Law of Thermodynamics.* Following the works [11, 12], we shall present the foundation of the generalized thermohydrodynamic shear-rotational model of the earthquake focal region based on the generalized differential formulation (59) of the first law of thermodynamics. Using the evolution equation (73) of the total mechanical energy of the subsystem τ (the macroscopic continuum region τ) of the Earth, we shall show now that the formation of fractures (modeling by the jumps of the continuum velocity on some surfaces) is related to irreversible dissipation of the macroscopic kinetic energy and the corresponding increase of entropy. We consider at the beginning the analysis of formation of the main line flat fracture (associated

with the surface $F_1(\tau)$ of the continuum velocity jump) inside the macroscopic continuum region τ (bounded by the closed surface $\partial\tau$). The macroscopic continuum region τ may be divided into two subsystems τ_1 and τ_2 by continuing mentally the surface $F_1(\tau)$ by means of surface $R_1(\tau)$ crossing the surface $\partial\tau$ of the macroscopic region τ . The surface of the subsystem τ_1 consists of the surface $(\partial\tau)_1$ (which is the part of the surface $\partial\tau$) and the surfaces $F_1(\tau)$ and $R_1(\tau)$. The surface of the subsystem τ_2 consists of the surface $(\partial\tau)_2$ (which is the part of the surface $\partial\tau$) and the surfaces $F_1(\tau)$ and $R_1(\tau)$.

Using the formulation (73), we have the evolution equations for the total mechanical energy of the macroscopic subsystems τ_1 and τ_2 :

$$\begin{aligned}
 & \frac{d}{dt} (K_{\tau_1} + \pi_{\tau_1}) \\
 &= \frac{d}{dt} \iiint_{\tau_1} \left(\frac{1}{2} \mathbf{v}^2 + \psi \right) \rho dV \\
 &= \iiint_{\tau_1} \rho \operatorname{div} \mathbf{v} dV \\
 &+ \iiint_{\tau_1} \left(\frac{2}{3} \eta - \eta_v \right) (\operatorname{div} \mathbf{v})^2 dV \\
 &- \iiint_{\tau_1} 2\nu (e_{ij})^2 \rho dV \\
 &+ \iint_{(\partial\tau)_1} (\mathbf{v} \cdot \mathbf{n} \cdot \mathbf{T}) d\Omega_{\mathbf{n}} \\
 &+ \iint_{F_1(\tau)} (\mathbf{v}_1(\tau_1) \cdot \boldsymbol{\zeta}_1 \cdot \mathbf{T}) d\Sigma_{\boldsymbol{\zeta}_1} \\
 &+ \iint_{R_1(\tau)} (\mathbf{v}_1(\tau_1) \cdot \boldsymbol{\zeta}_1 \cdot \mathbf{T}) d\Sigma_{\boldsymbol{\zeta}_1} \\
 &+ \iiint_{\tau_1} \frac{\partial\psi}{\partial t} \rho dV, \\
 & \frac{d}{dt} (K_{\tau_2} + \pi_{\tau_2}) \\
 &= \frac{d}{dt} \iiint_{\tau_2} \left(\frac{1}{2} \mathbf{v}^2 + \psi \right) \rho dV \\
 &= \iiint_{\tau_2} \rho \operatorname{div} \mathbf{v} dV \\
 &+ \iiint_{\tau_2} \left(\frac{2}{3} \eta - \eta_v \right) (\operatorname{div} \mathbf{v})^2 dV \\
 &- \iiint_{\tau_2} 2\nu (e_{ij})^2 \rho dV \\
 &+ \iint_{(\partial\tau)_2} (\mathbf{v} \cdot \mathbf{n} \cdot \mathbf{T}) d\Omega_{\mathbf{n}} \\
 &- \iint_{F_1(\tau)} (\mathbf{v}_1(\tau_2) \cdot \boldsymbol{\zeta}_1 \cdot \mathbf{T}) d\Sigma_{-\boldsymbol{\zeta}_1} \\
 &- \iint_{R_1(\tau)} (\mathbf{v}_1(\tau_2) \cdot \boldsymbol{\zeta}_1 \cdot \mathbf{T}) d\Sigma_{-\boldsymbol{\zeta}_1} \\
 &+ \iiint_{\tau_2} \frac{\partial\psi}{\partial t} \rho dV, \tag{77}
 \end{aligned}$$

where ζ_1 is the external unit normal vector of the surface (of the subsystem τ_1) presented by surfaces $F_1(\tau)$ and $R_1(\tau)$ and $-\zeta_1$ is the external unit normal vector of the surface (of the subsystem τ_2) presented also by surfaces $F_1(\tau)$ and $R_1(\tau)$. Adding (77) (by using the equality $d\Sigma_{\zeta_1} = d\Sigma_{-\zeta_1}$ of the elements of area of surfaces $F_1(\tau)$ and $R_1(\tau)$) we get the evolution equation for the total mechanical energy $(K_\tau + \pi_\tau) = (K_{\tau_1} + K_{\tau_2} + \pi_{\tau_1} + \pi_{\tau_2})$ of the macroscopic region τ consisting of subsystems τ_1 and τ_2 interacting on the surface $F_1(\tau)$ of the tangential jump of the continuum velocity:

$$\begin{aligned}
& \frac{d}{dt} (K_\tau + \pi_\tau) \\
&= \frac{d}{dt} \iiint_\tau \left(\frac{1}{2} \mathbf{v}^2 + \psi \right) \rho dV \\
&= \iiint_\tau p \operatorname{div} \mathbf{v} dV \\
&+ \iiint_\tau \left(\frac{2}{3} \eta - \eta_v \right) (\operatorname{div} \mathbf{v})^2 dV \\
&- \iiint_\tau 2\nu (e_{ij})^2 \rho dV \\
&+ \iint_{\partial\tau} (\mathbf{v} \cdot (\mathbf{n} \cdot \mathbf{T})) d\Omega_{\mathbf{n}} \\
&+ \iint_{F_1(\tau)} ((\mathbf{v}_1(\tau_1) - \mathbf{v}_1(\tau_2)) \cdot (\zeta_1 \cdot \mathbf{T})) d\Sigma_{\zeta_1} \\
&+ \iiint_\tau \frac{\partial\psi}{\partial t} \rho dV,
\end{aligned} \tag{78}$$

where $\mathbf{v}_1(\tau_1)$ is the vector of the continuum velocity on the surface $F_1(\tau)$ in the subsystem τ_1 , and $\mathbf{v}_1(\tau_2)$ is the vector of the continuum velocity on the surface $F_1(\tau)$ in the subsystem τ_2 .

The evolution equation (78) takes into account the total mechanical energy $(K_\tau + \pi_\tau)$ of the macroscopic region τ consisting of subsystems τ_1 and τ_2 interacting on the surface $F_1(\tau)$ of the tangential jump of the continuum velocity. The first term in the right-hand side (of (78)) describes the evolution of the total mechanical energy of the macroscopic continuum region τ due to the continuum reversible compressibility; the second and third terms express the dissipation of the macroscopic kinetic energy by means of the irreversible continuum compressibility and the velocity shear. The forms of three primary terms in the right-hand side (of (78)) are related to the considered model of the compressible viscous Newtonian continuum. The fourth, fifth, and sixth terms in the right-hand side (of (78)) are the universal terms for arbitrary model of continuum characterized by symmetrical stress tensor \mathbf{T} . The fourth term expresses the power

$$W_{\text{np},\partial\tau} = \frac{\delta A_{\text{np},\partial\tau}}{dt} = \iint_{\partial\tau} (\mathbf{v} \cdot (\mathbf{n} \cdot \mathbf{T})) d\Omega_{\mathbf{n}} \tag{79}$$

of external (for the continuum region τ) nonpotential stress forces acting on the boundary surface $\partial\tau$ of the macroscopic continuum region τ . The fifth term expresses the power of external (for the continuum region τ) forces on different sides

of the surface $F_i(\tau)$ characterized by the velocity jump during the fracture formation. The sixth term in (78) presents the power of the total mechanical energy added (or lost) as the result of the Newtonian nonstationary gravitational energy influence on the macroscopic continuum region τ related to variations of the potential ψ of the combined gravitational field in the continuum region τ .

Consider (78) for one continuum velocity jump on the nonstationary surface $F_1(\tau)$ during the time interval $(t, t + \Delta t)$. Taking into account the form of the fifth term on the right-hand side of the evolution equation (78), we obtained [11, 12] the expression for the work $\delta A_{\text{np},F_1(\tau)}$ (done during the time interval $(t, t + \Delta t)$ by the external (for the continuum region τ) nonpotential stress forces acting on different sides of the velocity jump on the surface $F_1(\tau)$):

$$\begin{aligned}
& \delta A_{\text{np},F_1(\tau)} \\
&= \int_t^{t+\Delta t} \left(\iint_{F_1(\tau)} ((\mathbf{v}_1(\tau_1) - \mathbf{v}_1(\tau_2)) \cdot (\zeta_1 \cdot \mathbf{T})) d\Sigma_{\zeta_1} \right) dt,
\end{aligned} \tag{80}$$

which is reduced to the following expression:

$$\begin{aligned}
& \delta A_{\text{np},F_1(\tau)} \\
&= \iint_{F_1(\tau)} \left(\int_t^{t+\Delta t} (\mathbf{v}_1(\tau_1) - \mathbf{v}_1(\tau_2)) \cdot (\zeta_1 \cdot \mathbf{T}) dt \right) d\Sigma_{\zeta_1}.
\end{aligned} \tag{81}$$

To test the formula (81), let us calculate the energy $\delta A_{\text{np},\Delta\Sigma}$, which dissipates during formation of the surface dislocation on the small surface $\Delta\Sigma$ during the time interval $(t, t + \Delta t)$. Using the theorem about the average value and integrating the internal integral on time, we obtained from relation (81) for $F_1(\tau) = \Delta\Sigma$ the following relation [11, 12]:

$$\begin{aligned}
& \delta A_{\text{np},\Delta\Sigma} \\
&= \iint_{\Delta\Sigma} (\mathbf{w}(\zeta_1, t + \Delta t) - \mathbf{w}(-\zeta_1, t + \Delta t)) \cdot \langle (\zeta_1 \cdot \mathbf{T}) \rangle d\Sigma_{\zeta_1},
\end{aligned} \tag{82}$$

where $\langle (\zeta_1 \cdot \mathbf{T}) \rangle$ is the average value of the stress vector for the element of area $d\Sigma_{\zeta_1}$ of the two-side surface $\Delta\Sigma$, and $\mathbf{w}(\zeta_1, t + \Delta t)$ and $\mathbf{w}(-\zeta_1, t + \Delta t)$ are the vectors of the continuum displacement on different sides of the element of area $d\Sigma_{\zeta_1}$ of the two-side surface $\Delta\Sigma$ in the points characterized by normal unit vectors ζ_1 and $-\zeta_1$. Using the obvious expression for "linear" time average $\langle (\zeta_1 \cdot \mathbf{T}) \rangle$

$$\langle (\zeta_1 \cdot \mathbf{T}) \rangle = \frac{1}{2} (\mathbf{p}(\zeta_1, t) - \mathbf{p}(-\zeta_1, t + \Delta t)) \tag{83}$$

as the arithmetical average of the values of the stress vectors \mathbf{p} on the different sides from the surface of the jump of the continuum velocity, we obtained [11, 12] the expression for

the elementary work of the external nonpotential stress forces on the two-side surface $\Delta\Sigma$ of dislocation:

$$\begin{aligned} \delta A_{\text{np},\Delta\Sigma} &= \frac{1}{2} \iint_{\Delta\Sigma} (\mathbf{w}(\boldsymbol{\zeta}_1, t + \Delta t) - \mathbf{w}(-\boldsymbol{\zeta}_1, t + \Delta t)) \\ &\quad \cdot (\mathbf{p}(\boldsymbol{\zeta}_1, t) + \mathbf{p}(-\boldsymbol{\zeta}_1, t + \Delta t)) d\Sigma_{\boldsymbol{\zeta}_1}. \end{aligned} \quad (84)$$

This expression was obtained [44] in the frame of the classical linear approach to formation of surface dislocations in rigid compressible continuum on the small area of surface $\Delta\Sigma$. It is clear that the assumption (83) is valid only for weak tangential jumps of the continuum displacement. Consequently, we can consider the expression (80) as the natural nonlinear generalization of expression (84) for arbitrary surface $F_1(\tau)$ of dislocation and for strong tangential jumps of the continuum displacement on the surface $F_1(\tau)$ of dislocation. The work (80) of the external (for the continuum region τ) nonpotential stress forces should be negative. The sufficient energy $\delta E_{d,F_1(\tau)}$ needed for formation of the surface $F_1(\tau)$ of dislocation is equal to the work of the internal forces in the macroscopic continuum region τ . The energy $\delta E_{d,F_1(\tau)}$ should be positive and equal to the expression (80) with the sign “-”:

$$\begin{aligned} \delta E_{d,F_1(\tau)} &= -\delta A_{\text{np},F_1(\tau)} \\ &= -\int_t^{t+\Delta t} \left(\iint_{F_1(\tau)} ((\mathbf{v}_1(\tau_1) - \mathbf{v}_1(\tau_2)) \cdot \boldsymbol{\zeta}_1 \cdot \mathbf{T}) d\Sigma_{\boldsymbol{\zeta}_1} \right) dt \\ &> 0. \end{aligned} \quad (85)$$

The formulae (80), (84), and (85) are obtained (taking into account the generalized differential formulation (50) of the first law of thermodynamics) for the model of continuum characterized by an arbitrary symmetrical stress tensor \mathbf{T} .

The macroscopic internal shear kinetic energy $(K_s)_{\tau_1}$ (of the subsystem τ_1), the macroscopic internal rotational kinetic energy $(K_r)_{\tau_1}$ (of the subsystem τ_1), and the macroscopic kinetic energy of shear-rotational coupling $(K_{s,r}^{\text{coup}})_{\tau_1}$ (of the subsystem τ_1) are the significant components of the macroscopic internal shear-rotational kinetic energy $(K_{s-r})_{\tau_1}$ [11, 12, 24, 31]:

$$(K_{s-r})_{\tau_1} = (K_r)_{\tau_1} + (K_s)_{\tau_1} + (K_{s,r}^{\text{coup}})_{\tau_1}, \quad (86)$$

taken into account (along with the classical internal thermal energy U_{τ_1} of the macroscopic continuum region τ_1 , the macroscopic potential energy π_{τ_1} of the macroscopic continuum region τ_1 , and the macroscopic translational kinetic energy $(K_t)_{\tau_1} = (1/2)m_{\tau_1}(\mathbf{V}_c)_{\tau_1}^2$ of the continuum region τ_1 (of a mass m_{τ_1}) moving as a whole at speed equal to the speed $(\mathbf{V}_c)_{\tau_1}$ of the center of mass of the continuum region τ_1) in the generalized differential formulation (50) of the first law of thermodynamics for the macroscopic continuum region τ_1 .

The macroscopic internal shear kinetic energy $(K_s)_{\tau_2}$ (of the subsystem τ_2), the macroscopic internal rotational kinetic

energy $(K_r)_{\tau_2}$, and the macroscopic kinetic energy of shear-rotational coupling $(K_{s,r}^{\text{coup}})_{\tau_2}$ are the significant components of the macroscopic internal shear-rotational kinetic energy $(K_{s-r})_{\tau_2}$ [11, 12, 24, 31]:

$$(K_{s-r})_{\tau_2} = (K_r)_{\tau_2} + (K_s)_{\tau_2} + (K_{s,r}^{\text{coup}})_{\tau_2}, \quad (87)$$

taken into account (along with the classical internal thermal energy U_{τ_2} , the macroscopic potential energy π_{τ_2} , and the macroscopic translational kinetic energy $(K_t)_{\tau_2} = (1/2)m_{\tau_2}(\mathbf{V}_c)_{\tau_2}^2$ of the continuum region τ_2 (of a mass m_{τ_2}) moving as a whole at the speed $(\mathbf{V}_c)_{\tau_2}$ of the center of mass of the continuum region τ_2) in the generalized differential formulation (50) of the first law of thermodynamics for the macroscopic continuum region τ_2 .

The macroscopic internal shear kinetic energy $(K_s)_{\tau_1}$ (of the subsystem τ_1), the macroscopic internal rotational kinetic energy $(K_r)_{\tau_1}$, the macroscopic kinetic energy of shear-rotational coupling $(K_{s,r}^{\text{coup}})_{\tau_1}$, the macroscopic translational kinetic energy $(K_t)_{\tau_1} = (1/2)m_{\tau_1}(\mathbf{V}_c)_{\tau_1}^2$, the macroscopic potential energy π_{τ_1} , the macroscopic internal shear kinetic energy $(K_s)_{\tau_2}$ (of the subsystem τ_2), the macroscopic internal rotational kinetic energy $(K_r)_{\tau_2}$, the macroscopic kinetic energy of shear-rotational coupling $(K_{s,r}^{\text{coup}})_{\tau_2}$, the macroscopic translational kinetic energy $(K_t)_{\tau_2} = (1/2)m_{\tau_2}(\mathbf{V}_c)_{\tau_2}^2$, and the macroscopic potential energy π_{τ_2} are the significant energy components taken into account in the presented thermo-hydrogravodynamic shear-rotational model described by the evolution equation (78) for the total mechanical energy $(K_t + \pi_\tau)$ of the macroscopic region τ consisting of interacting subsystems τ_1 and τ_2 .

3.2. The Rotational Model of the Earthquake Focal Region Based on the Generalized Differential Formulation of the First Law of Thermodynamics. Following the works [11, 12], we shall present the foundation of the rotational model [2] of the earthquake focal region for the seismic zone of the Pacific Ring. It was noted [2] that the studies of the dislocation models of the focal regions of strong earthquakes showed the bad correspondence with the model of flat endless dislocation in the uniform continuum [45–47]. The analysis [2] showed that the conditions exist to realize the rotational mechanism related to the rotation of the geoblocks by means of the stress forces related to the Earth rotation in the vicinity of the seismic zone of the Pacific Ring. It was noted [2] that the rotational mechanism can be more real compared to the conventional mechanism related to the formation of the main line flat fracture inside the focal region.

Let us consider the energy thermodynamic analysis of the rotational mechanism [2] of the earthquake focal region, related to formation of the circular continuum velocity jump revealed in the form of circular dislocation after relaxation of the seismic process in the earthquake focal region. The developed and tested (in this section) mathematical formalism of description of the main line flat fracture may be generalized on the closed surfaces of the continuum velocity jumps. Following the rotational model [2] of the earthquake focal

region, we consider the separate geoblock τ_{int} of the seismic zone. If the external influences of the nonstationary gravitational forces (on the geoblock τ_{int}) and the nonpotential stress forces (on the boundary $\partial\tau_i$ of the geoblock τ_{int}) exceed the certain critical value then the geoblock may rotate and slip relative to the surrounding fine plastic layer (subsystem) τ_{ext} with the tangential continuum velocity jump on the boundary surface $\partial\tau_i$ of the geoblock τ_{int} . We assume that fine plastic layer (subsystem) τ_{ext} is limited by external surface $\partial\tau$ of the considered thermodynamic system τ consisting of the macroscopic subsystems τ_{int} and τ_{ext} .

Using the evolution equation (73) of the total mechanical energy of the subsystem τ , we obtained [11, 12] the evolution equations for the total mechanical energy of the macroscopic subsystems τ_{int} and τ_{ext} :

$$\begin{aligned}
& \frac{d}{dt} (K_{\tau_{\text{int}}} + \pi_{\tau_{\text{int}}}) \\
&= \frac{d}{dt} \iiint_{\tau_{\text{int}}} \left(\frac{1}{2} \mathbf{v}^2 + \psi \right) \rho dV \\
&= \iiint_{\tau_{\text{int}}} p \operatorname{div} \mathbf{v} dV \\
&+ \iiint_{\tau_{\text{int}}} \left(\frac{2}{3} \eta - \eta_v \right) (\operatorname{div} \mathbf{v})^2 dV \\
&- \iiint_{\tau_{\text{int}}} 2\nu (e_{ij})^2 \rho dV \\
&+ \iint_{\partial\tau_i} (\mathbf{v}_{\text{int}}(\partial\tau_i) \cdot (\mathbf{m} \cdot \mathbf{T})) d\Sigma_{\mathbf{m}} \\
&+ \iiint_{\tau_{\text{int}}} \frac{\partial\psi}{\partial t} \rho dV, \\
& \frac{d}{dt} (K_{\tau_{\text{ext}}} + \pi_{\tau_{\text{ext}}}) \\
&= \frac{d}{dt} \iiint_{\tau_{\text{ext}}} \left(\frac{1}{2} \mathbf{v}^2 + \psi \right) \rho dV \\
&= \iiint_{\tau_{\text{ext}}} p \operatorname{div} \mathbf{v} dV \\
&+ \iiint_{\tau_{\text{ext}}} \left(\frac{2}{3} \eta - \eta_v \right) (\operatorname{div} \mathbf{v})^2 dV \\
&- \iiint_{\tau_{\text{ext}}} 2\nu (e_{ij})^2 \rho dV \\
&+ \iint_{\partial\tau} (\mathbf{v} \cdot (\mathbf{n} \cdot \mathbf{T})) d\Omega_{\mathbf{n}} \\
&- \iint_{\partial\tau_i} (\mathbf{v}_{\text{ext}}(\partial\tau_i) \cdot (\mathbf{m} \cdot \mathbf{T})) d\Sigma_{-\mathbf{m}} \\
&+ \iiint_{\tau_{\text{ext}}} \frac{\partial\psi}{\partial t} \rho dV, \tag{88}
\end{aligned}$$

where \mathbf{m} is the external unit normal vector of the surface $\partial\tau_i$ of the subsystem τ_{int} , $-\mathbf{m}$ is the internal unit normal vector

of the surface $\partial\tau_i$, \mathbf{n} is the external unit normal vector of the surface $\partial\tau$, $\mathbf{v}_{\text{int}}(\partial\tau_i)$ are the velocities vectors on the inner side of the surface $\partial\tau_i$ in the subsystem τ_{int} , and $\mathbf{v}_{\text{ext}}(\partial\tau_i)$ are the velocities vectors on the outer side of the surface $\partial\tau_i$ in the subsystem τ_{ext} .

Adding the evolution equation (88) and using the condition of equality $d\Sigma_{\mathbf{m}} = d\Sigma_{-\mathbf{m}}$ of the area elements of the surface $\partial\tau_i$, we get the evolution equation for the total mechanical energy of the macroscopic continuum region τ consisting of the subsystems τ_{int} and τ_{ext} interacting on the surface $\partial\tau_i$ of the continuum velocity jump:

$$\begin{aligned}
& \frac{d}{dt} (K_{\tau} + \pi_{\tau}) \\
&= \frac{d}{dt} \iiint_{\tau} \left(\frac{1}{2} \mathbf{v}^2 + \psi \right) \rho dV \\
&= \iiint_{\tau} p \operatorname{div} \mathbf{v} dV \\
&+ \iiint_{\tau} \left(\frac{2}{3} \eta - \eta_v \right) (\operatorname{div} \mathbf{v})^2 dV \\
&- \iiint_{\tau} 2\nu (e_{ij})^2 \rho dV \\
&+ \iint_{\partial\tau} (\mathbf{v} \cdot (\mathbf{n} \cdot \mathbf{T})) d\Omega_{\mathbf{n}} \\
&+ \iint_{\partial\tau_i} ((\mathbf{v}_{\text{int}}(\partial\tau_i) - \mathbf{v}_{\text{ext}}(\partial\tau_i)) \cdot (\mathbf{m} \cdot \mathbf{T})) d\Sigma_{\mathbf{m}} \\
&+ \iiint_{\tau} \frac{\partial\psi}{\partial t} \rho dV. \tag{89}
\end{aligned}$$

Equation (89) is analogous to (78). The energy needed for formation of the continuum velocities jumps (on the surfaces $F_1(\tau)$ and $\partial\tau_i$) is related to the penultimate terms in the right-hand sides of (78) and (89). Similar to expression (85), we have the expression for the sufficient energy $\delta E_{d,\partial\tau_i}$ needed to rotate and slip (for the subsystem τ_{int}) during the time interval $(t, t + \Delta t)$ relative to the surrounding fine plastic layer (subsystem) τ_{ext} (with the tangential continuum fine velocity jump $(\mathbf{v}_{\text{int}}(\partial\tau_i) - \mathbf{v}_{\text{ext}}(\partial\tau_i))$ on the boundary surface $\partial\tau_i$ of the geoblock τ_{int}):

$$\begin{aligned}
\delta E_{d,\partial\tau_i} &= -\delta A_{\text{np},\partial\tau_i} \\
&= -\int_t^{t+\Delta t} \left(\iint_{\partial\tau_i} ((\mathbf{v}_{\text{int}}(\partial\tau_i) - \mathbf{v}_{\text{ext}}(\partial\tau_i)) \cdot (\mathbf{m} \cdot \mathbf{T})) d\Sigma_{\mathbf{m}} \right) dt > 0. \tag{90}
\end{aligned}$$

Taking into account the information [2] that the critical continuum stresses (required for rotation of the geoblock τ_{int} weakly coupled with the surrounding plastic layer τ_{ext}) are less than the critical continuum stresses required to split the mountain rock by forming the main line flat fracture, we concluded [11, 12] that the required energy $\delta E_{d,\partial\tau_i}$ (given by the expression (90)) is less than the required energy $\delta E_{d,F_1(\tau)}$

(given by the expression (85)) if the displacements of the rock continuum on different sides of the analyzed different jumps of the continuum displacements (the closed dislocation and the main line flat fracture) have the same order of magnitude and the ratio of the surfaces area of the closed dislocation to the surfaces area of the main line flat fracture does not exceed 10.

This thermodynamic energy consideration showed [11, 12] the preferable realization of the rotational motion of the geoblock τ_{int} (under condition that exists the surrounding plastic layer around the geoblock τ_{int}) as compared with formation of the of the main line flat fracture inside the geoblock τ_{int} . This result explains the rotational motions of the geoblocks in the seismic zone of the Pacific Ring [2] and the vortical structures of the lithosphere of Earth [48] and the lithospheres of the planets [49] of the Solar System.

Using of the generalized differential formulation (50) of the first law of thermodynamics for the macroscopic continuum region τ of the quasi-uniform medium of the Earth's crust characterized by practically constant viscosity, we obtained [11, 12] the thermodynamic foundation of the classical deformational (shear) model [1] of the earthquake focal region for the quasi-uniform medium of the Earth's crust characterized by practically constant viscosity.

4. Fundamentals of the Cosmic Geophysics

4.1. The Energy Gravitational Influences on the Earth of the Planets of the Solar System

4.1.1. *The Instantaneous Energy Gravitational Influences on the Earth of the Planets of the Solar System in the Approximation of the Elliptical Orbits of the Planets.* We shall consider the movements of the Earth τ_3 and the outer (or inner) planet τ_i in the ecliptic plane XZ (see Figure 4) around the Sun τ_0 in the approximation of the elliptical orbits of the planets. The mass center C_3 of the Earth τ_3 , the mass center O of the Sun, and the mass center C_i of the inner ($i = 1, 2$) and the outer ($i = 4, 5, 6, 7, 8, 9$) planet τ_i are located on the direct coordinate axis X at a certain initial time moment $t = 0$ characterized by the minimal distance between the mass center C_i of the inner ($i = 1, 2$) and the outer ($i = 4, 5, 6, 7, 8, 9$) planet τ_i and the mass center C_3 of the Earth τ_3 . The fixed mass center O of the Sun is considered as the right focus of the elliptical orbits of the inner ($i = 1, 2$) planet τ_i , the outer ($i = 4, 5, 6, 7, 8, 9$) planet τ_i , and the Earth τ_3 .

We have the following relations:

$$r_i(\varphi_i(t)) = \frac{P_i}{(1 + e_i \cos \varphi_i(t))}, \quad (i = 1, 2, 4, 5, 6, 7, 8, 9), \quad (91)$$

$$r_3(\varphi_3(t)) = \frac{P_3}{(1 + e_3 \cos \varphi_3(t))} \quad (92)$$

for the distance $r_i(\varphi_i(t))$ between the mass center O of the Sun and the mass center C_i of the inner ($i = 1, 2$) or the outer ($i = 4, 5, 6, 7, 8, 9$) planet τ_i and for the distance $r_3(\varphi_3(t))$

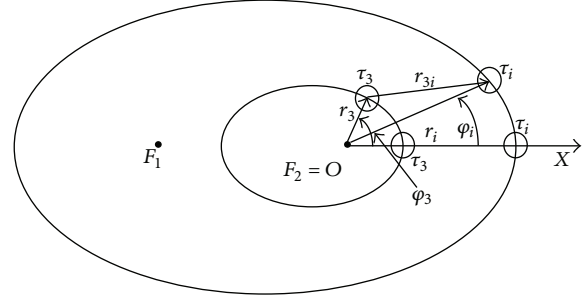


FIGURE 4: The geometric sketch of circulation of the outer planet τ_i (Mars or Jupiter, Saturn, Uranus, Neptune, and Pluto) and the Earth τ_3 around the mass center O of the Sun.

between the mass center O of the Sun and the mass center C_3 of the Earth τ_3 . Here p_i and e_i are the focal parameters and the eccentricity, respectively, of the elliptical orbit of the inner ($i = 1, 2$) and the outer ($i = 4, 5, 6, 7, 8, 9$) planet τ_i and p_3 and e_3 are the focal parameters and the eccentricity, respectively, of the elliptical Earth's orbit. We have $\varphi_i(0) = 0$ ($i = 1, 2, 3, 4, 5, 6, 7, 8, 9$) for the initial time moment $t = 0$.

We shall consider the gravitational potential $\psi_{3i}(C_3, \text{int, ext, } t, r_3(\varphi_3(t)))$ created by the inner ($i = 1, 2$) or the outer ($i = 4, 5, 6, 7, 8, 9$) planet τ_i in the mass center C_3 (of the Earth τ_3):

$$\psi_{3i}(C_3, \text{int, ext, } t, r_3(\varphi_3(t))) = -\gamma \frac{M_i}{r_{3i}(C_3, C_i, t)}, \quad (93)$$

where $r_{3i}(C_3, C_i, t)$ is the distance between the mass center C_3 of the Earth τ_3 and the mass center C_i of the inner ($i = 1, 2$) or the outer ($i = 4, 5, 6, 7, 8, 9$) planet τ_i . We find the distance $r_{3i}(C_3, C_i, t)$ for the outer ($i = 4, 5, 6, 7, 8, 9$) planet τ_i from the following relation:

$$\begin{aligned} (r_{3i}(C_3, C_i, t))^2 &= (r_3(\varphi_3(t)))^2 + (r_i(\varphi_i(t)))^2 \\ &\quad - r_3(\varphi_3(t)) r_i(\varphi_i(t)) \cos(\varphi_3(t) - \varphi_i(t)), \end{aligned} \quad (94)$$

which is valid also for the inner planet τ_i ($i = 1, 2$). The relation (93) can be rewritten as follows:

$$\begin{aligned} \psi_{3i}(C_3, \text{int, ext, } t, r_3(\varphi_3(t))) &= -(\gamma M_i) \\ &\quad \times \left((r_3(\varphi_3(t)))^2 + (r_i(\varphi_i(t)))^2 \right. \\ &\quad \left. - 2r_3(\varphi_3(t)) r_i(\varphi_i(t)) \cos(\varphi_3(t) - \varphi_i(t)) \right)^{-1/2}. \end{aligned} \quad (95)$$

We obtained [25, 26] the expression for the partial derivative of the gravitational potential (95):

$$\begin{aligned} & \frac{\partial}{\partial t} \psi_{3i}(C_3, \text{int, ext, } t, r_3(\varphi_3(t))) \\ &= \left(\gamma M_i r_i(\varphi_i(t)) \frac{d\varphi_i(t)}{dt} \right) \\ & \times \left((r_3(\varphi_3(t)))^2 + (r_i(\varphi_i(t)))^2 \right. \\ & \quad \left. - 2r_3(\varphi_3(t)) r_i(\varphi_i(t)) \cos(\varphi_3(t) - \varphi_i(t)) \right)^{-3/2} \\ & \times \left\{ r_3(\varphi_3(t)) \sin(\varphi_i(t) - \varphi_3(t)) + \frac{e_i r_i(\varphi_i(t)) \sin \varphi_i(t)}{(1 + e_i \cos \varphi_i(t))} \right. \\ & \quad \left. - \frac{e_i r_3(\varphi_3(t)) \sin \varphi_i(t) \cos(\varphi_i(t) - \varphi_3(t))}{(1 + e_i \cos \varphi_i(t))} \right\}, \end{aligned} \quad (96)$$

where the distances $r_i(\varphi_i(t))$ and $r_3(\varphi_3(t))$ are given by the relations (91) and (92), respectively.

The expression (96) is reduced to the following expression [12]:

$$\begin{aligned} & \frac{\partial}{\partial t} \psi_{3i}(C_3, \text{int}) \\ &= \frac{\partial}{\partial t} \psi_{3i}(C_3, \text{ext}) \\ &= \frac{\gamma M_i R_{O_3} R_{O_i} \omega_i \sin(\omega_i - \omega_3) t}{[R_{O_3}^2 + R_{O_i}^2 - 2R_{O_3} R_{O_i} \cos(\omega_i - \omega_3) t]^{3/2}} \end{aligned} \quad (97)$$

under the following conditions: $e_i = 0$, $e_3 = 0$, and $d\varphi_i(t)/dt = \omega_i$ corresponding to the circular orbits of the planet τ_i ($i = 1, 2, 4, 5, 6, 7, 8, 9$) and the Earth τ_3 .

The first term in the figured brackets of the expression (96) gives the principal contribution to the partial derivative $(\partial/\partial t)\psi_{3i}(C_3, \text{int, ext, } t, r_3(\varphi_3(t)))$. The expression (96) contains the additional two small terms (vanishing at $e_i \rightarrow 0$ and $e_3 \rightarrow 0$) related to the eccentricities e_i and e_3 of the elliptical orbits of the planet τ_i ($i = 1, 2, 4, 5, 6, 7, 8, 9$) and the Earth τ_3 , respectively.

The combined maximal contribution of these additional two terms is of the order

$$O(e_i, e_3) \left(\max \frac{\partial}{\partial t} \psi_{3i}(C_3, \text{int}) \right) \quad (98)$$

for the inner ($i = 1, 2$) planet τ_i and of the order

$$O(e_i, e_3) \left(\max \frac{\partial}{\partial t} \psi_{3i}(C_3, \text{ext}) \right) \quad (99)$$

for the outer ($i = 4, 5, 6, 7, 8, 9$) planet τ_i . Consequently, the contribution of the first term in the figured brackets of the expression (96) is $O(1/e_i, 1/e_3)$ times larger than the contribution of the additional two new terms related to the eccentricities e_i and e_3 . Using the maximal eccentricity $e_1 = 0.206$ of Mercury's orbit, we have that the contribution of the first term in the figured brackets of the expression (96) is approximately 5 times larger than the contribution of the additional two new terms (in the figured brackets of the expression (96))

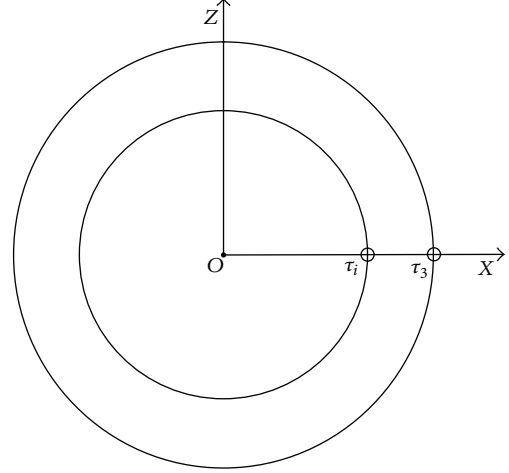


FIGURE 5: The initial ($t = 0$) planetary configuration characterized by the opposition of the inner planet τ_i (Mercury or Venus) and the Earth τ_3 .

related to the eccentricities $e_1 = 0.206$ and $e_3 = 0.017$ of the elliptical orbits of Mercury τ_1 and the Earth τ_3 , respectively. We have that the first term (in the figured brackets of the expression (96)) is significantly larger than the contribution of the additional two new terms for the other planets (of the Solar System) having the small eccentricities of the elliptical orbits.

Thus, the obtained [12, 25, 26] evaluation (97) (for the circular orbits of the planets) of the relative maximal energy gravitational influences on the Earth (of the planets of the Solar System) may be considered as the first sound approximation for the evaluation of the relative maximal energy gravitational influences of the inner ($i = 1, 2$) and the outer ($i = 4, 5, 6, 7, 8, 9$) planets on the Earth.

4.1.2. The Evaluation of the Relative Maximal Planetary Instantaneous Energy Gravitational Influences on the Earth in the Approximation of the Circular Orbits of the Planets of the Solar System. Following the monograph [12], we shall consider the movement of the Earth τ_3 and the inner planet τ_i around the Sun $\tau_{0,0}$ in the first approximation of the circular orbits of the planets. The planets revolve in the ecliptic plane XZ (see Figures 5 and 6). The mass center of the Sun is located at the fixed point O of the origin of the coordinate system. The mass center C_3 of the Earth, the mass center O of the Sun, and the mass center C_i of the inner planet τ_i are located on the direct coordinate axis X at a certain initial time moment $t = 0$ characterized by the minimal distance between the Earth and the inner planet τ_i (see Figure 5).

We have the following expressions for the angles φ_i and φ_3 :

$$\begin{aligned} \varphi_i(t) &= \omega_i t = \frac{2\pi}{T_i} t, \\ \varphi_3(t) &= \omega_3 t = \frac{2\pi}{T_3} t, \end{aligned} \quad (100)$$

which describe the positions of the mass centers of the planet τ_i and the Earth τ_3 during the time t .

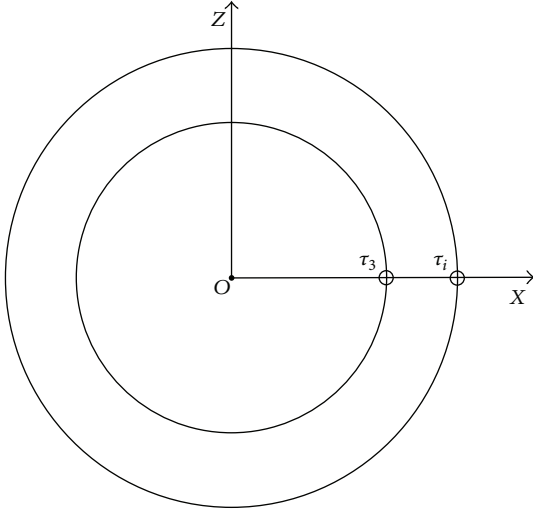


FIGURE 6: The initial planetary configuration of the outer planet τ_i (Mars or Jupiter, Saturn, Uranus, Neptune, and Pluto) and the Earth τ_3 .

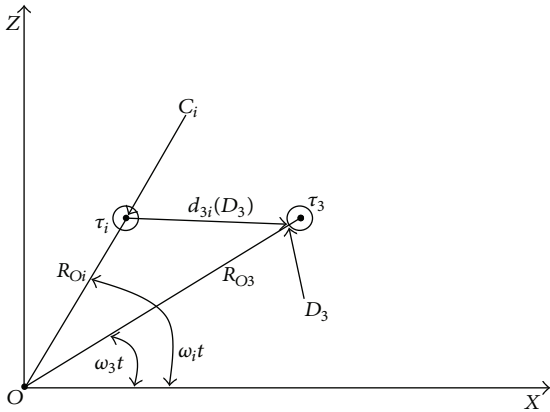


FIGURE 7: The geometric sketch of circulations of the Earth τ_3 and the inner planet τ_i (Mercury or Venus) around the mass center O of the Sun.

We shall consider the gravitational potential $\psi_{3i}(C_3, \text{int})$

$$\psi_{3i}(C_3, \text{int}) = -\gamma \frac{M_i}{d_{3i}(C_3)} \quad (101)$$

created by the inner planet τ_i in the mass center C_3 of the Earth. We have the distance $d_{3i}(C_3)$ between the mass center C_i of the inner planet τ_i and the mass center C_3 of the Earth (see Figure 7):

$$d_{3i}^2(C_3) = R_{O3}^2 + R_{Oi}^2 - 2R_{O3}R_{Oi} \cos(\omega_i t - \varphi_3). \quad (102)$$

The relation (101) can be rewritten as follows [12]:

$$\psi_{3i}(C_3, \text{int}) = -\frac{\gamma M_i}{\sqrt{R_{O3}^2 + R_{Oi}^2 - 2R_{O3}R_{Oi} \cos(\omega_i t - \varphi_3)}}. \quad (103)$$

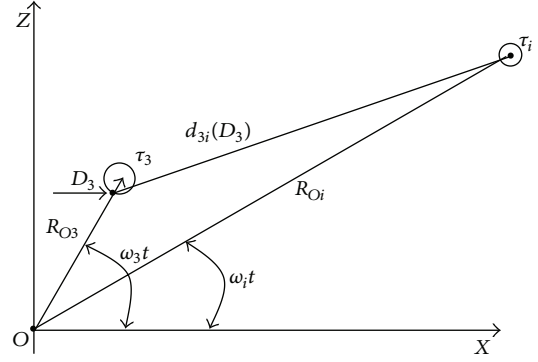


FIGURE 8: The geometric sketch of circulation of the outer planet τ_i (Mars or Jupiter, Saturn, Uranus, Neptune, and Pluto) and Earth τ_3 around the mass center O of the Sun.

We derived [12] the expression for the partial derivative $(\partial/\partial t)\psi_{3i}(C_3, \text{int})$:

$$\begin{aligned} \frac{\partial}{\partial t} \psi_{3i}(C_3, \text{int}) &= \frac{\gamma M_i R_{O3} R_{Oi} \omega_i \sin(\omega_i - \omega_3) t}{[R_{O3}^2 + R_{Oi}^2 - 2R_{O3}R_{Oi} \cos(\omega_i - \omega_3) t]^{3/2}}, \end{aligned} \quad (104)$$

which is reduced to zero for the time moments $t_n^*(i, 3) = (1/2)(T_i T_3 / (T_3 - T_i))n$ (for $i = 1, 2; n = 0, 1, 2, \dots$), when the mass centers of the Sun, the Earth, and the inner planet τ_i are located on the direct line.

We have (for configuration of the Earth and the outer planet τ_i shown on Figure 8) the distance $d_{i3}(C_3)$ between the mass center C_i of the planet τ_i and the mass center C_3 of the Earth:

$$d_{i3}^2(C_3) = R_{O3}^2 + R_{Oi}^2 - 2R_{O3}R_{Oi} \cos(\omega_3 - \omega_i) t. \quad (105)$$

The gravitational potential created by the outer planet τ_i at the point C_3 (for configuration shown on Figure 8) is given by the following expression:

$$\begin{aligned} \psi_{3i}(C_3, \text{ext}) &= -\frac{\gamma M_i}{d_{i3}(C_3)} \\ &= -\frac{\gamma M_i}{\sqrt{R_{O3}^2 + R_{Oi}^2 - 2R_{O3}R_{Oi} \cos(\varphi_3 - \omega_i t)}}. \end{aligned} \quad (106)$$

We derived [12] the expression of the partial derivative $(\partial/\partial t)\psi_{3i}(C_3, \text{ext})$ for the expression (106):

$$\begin{aligned} \frac{\partial}{\partial t} \psi_{3i}(C_3, \text{ext}) &= -\frac{\gamma M_i R_{O3} R_{Oi} \omega_i \sin(\omega_3 - \omega_i) t}{[R_{O3}^2 + R_{Oi}^2 - 2R_{O3}R_{Oi} \cos(\omega_3 - \omega_i) t]^{3/2}}. \end{aligned} \quad (107)$$

We used [25, 26] the maximal positive value $\max(\partial/\partial t)\psi_{3M}(C_3, \text{int})$ (of the partial derivative $(\partial/\partial t)\psi_{3M}(C_3, \text{int})$)

of the gravitational potential $\psi_{3M}(C_3, \text{int})$ created by Mercury at the mass center C_3 of the Earth) as a scale of the energy gravitational influence of the planets of the Solar System on the Earth in the considered first approximation of the circular orbits of the planets. To evaluate the relative energy gravitational influence of the inner planet τ_i (Mercury or Venus) at the mass center C_3 of the Earth, we considered [25, 26] the ratio $f(i, C_3)$ of the maximal positive value $\max(\partial/\partial t)\psi_{3i}(C_3, \text{int})$ (of the partial derivative $(\partial/\partial t)\psi_{3i}(C_3, \text{int})$ of the gravitational potential $\psi_{3i}(C_3, \text{int})$ created by the inner planet τ_i at the point C_3) and the maximal positive value $\max(\partial\psi_{31}(C_3, \text{int})/\partial t)$ (of the partial derivative $\partial\psi_{31}(C_3, \text{int})/\partial t$ of the gravitational potential $\psi_{31}(C_3, \text{int}) \equiv \psi_{3M}(C_3, \text{int})$ created by Mercury at the mass center C_3 of the Earth):

$$f(i, C_3) = \frac{\max(\partial\psi_{3i}(C_3, \text{int})/\partial t)}{\max(\partial\psi_{3M}(C_3, \text{int})/\partial t)}, \quad (i = 1, 2). \quad (108)$$

We obtained [25, 26] from expression (108) the obvious value $f(1, C_3) = 1$ for Mercury τ_1 . Using the formula (108) for Venus ($i = 2$), we calculated [25, 26] the numerical value $f(2, C_3) = 37.69807434$ for the following numerical values [35]: the mass $M_M = 0.06M_3$ of Mercury, where M_3 is the mass of the Earth, the mass $M_V = M_2 = 0.82M_3$ of Venus, the time period $T_3 = 365.3$ days of the Earth's circulation around the Sun, the time period $T_M = 88$ days of Mercury's circulation around the Sun, the time period $T_V = T_2 = 224.7$ days of the Venusian circulation around the Sun, the average radius $R_{OM} = R_{O1} = 57.85 \cdot 10^6$ km of Mercury's orbit, around the Sun, the average radius $R_{O3} = 149.6 \cdot 10^6$ km of the Earth's orbit, and the average radius $R_{OV} = R_{O2} = 108.1 \cdot 10^6$ km of Venusian orbit around the Sun. The power of the maximal energy gravitational Venusian influence (on the unit mass at the mass center C_3 of the Earth) is $f(2, C_3) = 37.69807434$ times larger than the power of the maximal energy gravitational influence of Mercury (on the unit mass at the mass center C_3 of the Earth).

To evaluate the relative energy gravitational influence on the Earth of the outer planet τ_i at the mass center C_3 of the Earth, we considered [25, 26] the ratio $f(i, C_3)$ (for $i = 4, 5, 6, 7, 8, 9$) of the maximal value $\max(\partial/\partial t)\psi_{3i}(C_3, \text{ext})$ of the partial derivative of the gravitational potential $\psi_{3i}(C_3, \text{ext})$ (created by the outer planet τ_i at the mass center C_3 of the Earth) and the maximal value $\max(\partial/\partial t)\psi_{3M}(C_3, \text{int})$ of the partial derivative of the gravitational potential $\psi_{3M}(D_3, \text{int})$ (created by Mercury at the mass center C_3 of the Earth):

$$f(i, C_3) = \frac{\max(\partial\psi_{3i}(C_3, \text{ext})/\partial t)}{\max(\partial\psi_{3M}(C_3, \text{int})/\partial t)}, \quad (i = 4, 5, 6, 7, 8, 9). \quad (109)$$

Using the formula (109), we calculated [25, 26] the following numerical values: $f(4, C_3) = 0.67441034$ (for Mars τ_4 , $i = 4$), $f(5, C_3) = 7.41055774$ (for Jupiter τ_5 , $i = 5$), $f(6, C_3) = 0.24601009$ (for Saturn τ_6 , $i = 6$), $f(7, C_3) = 0.00319056$ (for Uranus τ_7 , $i = 7$), $f(8, C_3) = 0.00077565$ (for Neptune τ_8 , $i = 8$), and $f(9, C_3) = 3.4813 \cdot 10^{-8}$ (for Pluto τ_9 , $i = 9$). We used the following additional planetary numerical values [50]: the mass $M_{MARS} = M_4 = 0.11M_3$ of Mars, the time

period $T_{MARS} = T_4 = 687$ days of Mars' circulation around the Sun, the average radius $R_{OMARS} = R_{O4} = 227.7 \cdot 10^6$ km of Mars' orbit, the mass $M_J = M_5 = 318M_3$ of Jupiter, the time period $T_J = T_5 = 4332$ days of Jupiter's circulation around the Sun, and the average radius $R_{OJ} = R_{O5} = 777.6 \cdot 10^6$ km of Jupiter's orbit, the time period $T_{SAT} = T_6 = 10759$ days of Saturn's circulation around the Sun, the mass $M_{SAT} = M_6 = 95.2M_3$ of Saturn, and the average radius $R_{OSAT} = R_{O6} = 1426 \cdot 10^6$ km of Saturn's orbit, the mass $M_U = M_7 = 14.6M_3$ of Uranus, the time period $T_U = T_7 = 30685$ days of Uranus' circulation around the Sun, and the average radius $R_{OU} = R_{O7} = 2868 \cdot 10^6$ km of Uranus' orbit, the mass $M_N = M_8 = 17.2M_3$ of Neptune, the average radius $R_{ON} = R_{O8} = 4497 \cdot 10^6$ km of Neptune's orbit, and the time period $T_N = T_8 = 60189$ days of Neptune's circulation around the Sun, the mass $M_P = M_9 = 0.002M_3$ of Pluto, the time period $T_P = T_9 = 90465$ days of Pluto's circulation around the Sun, and the average radius $R_{OP} = R_{O9} = 5900 \cdot 10^6$ km of Pluto's orbit.

Taking into account the calculated powers of the maximal energy gravitational influences of the planets on the unit mass of the Earth (at the mass center C_3 of the Earth), we obtained [25, 26] the following numerical sequence of the nondimensional relative maximal powers of the planetary energy gravitational influences on the unit mass of the Earth (at the mass center C_3 of the Earth): $f(2, C_3) = 37.69807434$ (for Venus), $f(5, C_3) = 7.41055774$ (for Jupiter), $f(1, C_3) = 1$ (for Mercury), $f(4, C_3) = 0.67441034$ (for Mars), $f(6, C_3) = 0.24601009$ (for Saturn), $f(7, C_3) = 0.00319056$ (for Uranus), $f(8, C_3) = 0.00077565$ (for Neptune), and $f(9, C_3) = 3.4813 \cdot 10^{-8}$ (for Pluto).

To evaluate the relative energy gravitational influence of the inner planets τ_i (Mercury and Venus) and the outer planets τ_i (Mars, Jupiter, Saturn, Uranus, Neptune, and Pluto) at the surface point D_3 (which is the intersection of the direct line (connecting the mass center O of the Sun and the mass center C_3 of the Earth) with the surface of the Earth), we obtained [12] the gravitational potential $\psi_{3i}(D_3, \text{int})$:

$$\begin{aligned} \psi_{3i}(D_3, \text{int}) &= - \frac{\gamma M_i}{\sqrt{(R_{O3} - R_3)^2 + R_{O_i}^2 - 2(R_{O3} - R_3)R_{O_i} \cos(\omega_i t - \varphi_3)}} \end{aligned} \quad (110)$$

created by the inner planet τ_i in the surface point D_3 of the Earth. We derived the expression for the partial derivative $(\partial/\partial t)\psi_{3i}(D_3, \text{int})$ of the gravitational potential (110):

$$\begin{aligned} \frac{\partial}{\partial t} \psi_{3i}(D_3, \text{int}) &= \frac{\gamma M_i (R_{O3} - R_3) R_{O_i} \omega_i \sin(\omega_i - \omega_3) t}{\left[(R_{O3} - R_3)^2 + R_{O_i}^2 - 2(R_{O3} - R_3) R_{O_i} \cos(\omega_i - \omega_3) t \right]^{3/2}}. \end{aligned} \quad (111)$$

The gravitational potential created by the outer planet τ_i at the surface point D_3 (for configuration shown on Figure 8) is given by the following expression [12]:

$$\begin{aligned} \psi_{3i}(D_3, \text{ext}) &= -\frac{\gamma M_i}{d_{3i}(D_3)} \\ &= -\frac{\gamma M_i}{\sqrt{(R_{O3} - R_3)^2 + R_{O_i}^2 - 2(R_{O3} - R_3)R_{O_i} \cos(\varphi_3 - \omega_i t)}}. \end{aligned} \quad (112)$$

We derived [12] the expression of the partial derivative $(\partial/\partial t)\psi_{3i}(D_3, \text{ext})$ of the gravitational potential (112):

$$\begin{aligned} \frac{\partial}{\partial t}\psi_{3i}(D_3, \text{ext}) &= -(\gamma M_i (R_{O3} - R_3) R_{O_i} \omega_i \sin(\omega_3 - \omega_i) t) \\ &\quad \times \left(\left[(R_{O3} - R_3)^2 + R_{O_i}^2 - 2(R_{O3} - R_3) R_{O_i} \cos(\omega_3 - \omega_i) t \right]^{3/2} \right)^{-1}, \end{aligned} \quad (113)$$

which is reduced to the relation (111) owing to the equalities $\sin(\omega_i - \omega_3)t = -\sin(\omega_3 - \omega_i)t$ and $\cos(\omega_i - \omega_3)t = \cos(\omega_3 - \omega_i)t$. However, we take into account that the expression (113) is given for the outer planet τ_i , but the expression (111) is given for the inner planet τ_i .

We used [12, 25, 26] the maximal positive value $\max(\partial/\partial t)\psi_{3M}(D_3, \text{int})$ (of the partial derivative $(\partial/\partial t)\psi_{3M}(D_3, \text{int})$ of the gravitational potential $\psi_{3M}(D_3, \text{int})$ created by Mercury at the surface point D_3 of the Earth) as a scale of the energy gravitational influence of the planets of the Solar System on the Earth in the considered first approximation of the circular orbits of the planets.

To evaluate the relative energy gravitational influence of the inner planet τ_i ($i = 1, 2$) at the surface point D_3 , we considered [12, 25, 26] the ratio $f(i, D_3)$ of the maximal positive value $\max(\partial/\partial t)\psi_{3i}(D_3, \text{int})$ (of the partial derivative $(\partial/\partial t)\psi_{3i}(D_3, \text{int})$ of the gravitational potential $\psi_{3i}(D_3, \text{int})$ created by the inner planet τ_i at the point D_3) and the maximal positive value $\max(\partial/\partial t)\psi_{3M}(D_3, \text{int})$ (of the partial derivative $(\partial/\partial t)\psi_{3M}(D_3, \text{int})$ of the gravitational potential $\psi_{3M}(D_3, \text{int}) \equiv \psi_{3M}(D_3, \text{int})$ created by Mercury at the surface point D_3 of the Earth):

$$f(i, D_3) = \frac{\max(\partial\psi_{3i}(D_3, \text{int})/\partial t)}{\max(\partial\psi_{3M}(D_3, \text{int})/\partial t)}, \quad (i = 1, 2). \quad (114)$$

To evaluate the relative energy gravitational influence of the outer planet τ_i ($i = 4, 5, 6, 7, 8, 9$) on the surface point D_3 of the Earth, we considered [12, 25, 26] the ratio $f(i, D_3)$ (for $i = 4, 5, 6, 7, 8, 9$) of the maximal positive value $\max(\partial/\partial t)\psi_{3i}(D_3, \text{ext})$ (of the partial derivative $(\partial/\partial t)\psi_{3i}(D_3, \text{ext})$ of the gravitational potential $\psi_{3i}(D_3, \text{ext})$ created by the outer planet τ_i at the surface point D_3) and the maximal positive value $\max(\partial/\partial t)\psi_{3M}(D_3, \text{int})$ (of the partial derivative

$(\partial/\partial t)\psi_{3M}(D_3, \text{int})$ of the gravitational potential $\psi_{3M}(D_3, \text{int})$ created by Mercury at surface point D_3):

$$f(i, D_3) = \frac{\max(\partial\psi_{3i}(D_3, \text{ext})/\partial t)}{\max(\partial\psi_{3M}(D_3, \text{int})/\partial t)}, \quad (i = 4, 5, 6, 7, 8, 9). \quad (115)$$

Using the formulae (114) and (115), we calculated [25, 26] (for the average radius $R_3 = 6371$ km of the Earth and the planetary numerical values [50]) the following numerical values (corrected slightly the previous numerical values of $f(i, D_3)$ [9]): $f(2, D_3) = 37.70428085$ (for Venus), $f(5, D_3) = 7.40926122$ (for Jupiter), $f(1, D_3) = 1$ (for Mercury), $f(4, D_3) = 0.67420160$ (for Mars), $f(6, D_3) = 0.24596865$ (for Saturn), $f(7, D_3) = 0.00319004$ (for Uranus), $f(8, D_3) = 0.00077552$ (for Neptune), and $f(9, D_3) = 3.4807 \cdot 10^{-8}$ (for Pluto).

Taking into account the calculated powers of the maximal energy gravitational influences of the planets on the unit mass of the Earth (at the mass center C_3 of the Earth and at the surface point D_3 of the Earth), we obtained [12, 25, 26] the following order of signification of the planets of the Solar System (Venus, Jupiter, Mercury, Mars, Saturn, Uranus, Neptune, and Pluto) with respect to the planetary power of the maximal energy gravitational influences on the unit mass of the Earth.

To evaluate the relative energy gravitational influence of the inner planet τ_i at the surface point D_3 and at the mass center C_3 of the Earth, we considered [25, 26] the ratio $q_i(D_3, C_3)$:

$$q_i(D_3, C_3) = \frac{\max(\partial\psi_{3i}(D_3, \text{int})/\partial t)}{\max(\partial\psi_{3i}(C_3, \text{int})/\partial t)}, \quad (i = 1, 2). \quad (116)$$

To evaluate the relative energy gravitational influence of the outer planet τ_i at the surface point D_3 and at the mass center C_3 of the Earth, we considered [25, 26] the ratio $q_i(D_3, C_3)$:

$$q_i(D_3, C_3) = \frac{\max(\partial\psi_{3i}(D_3, \text{ext})/\partial t)}{\max(\partial\psi_{3i}(C_3, \text{ext})/\partial t)}, \quad (i = 4, 5, 6, 7, 8, 9). \quad (117)$$

Using the formula (116), we calculated [25, 26] the following numerical values: $q_1(D_3, C_3) = 1.000123023$ (for Mercury) and $q_2(D_3, C_3) = 1.000287771$ (for Venus). Using the formula (117), we calculated [25, 26] the following numerical values: $q_4(D_3, C_3) = 0.999813318$ (for Mars), $q_5(D_3, C_3) = 0.999948084$ (for Jupiter), $q_6(D_3, C_3) = 0.999954640$ (for Saturn), $q_7(D_3, C_3) = 0.999956727$ (for Uranus), $q_8(D_3, C_3) = 0.999957084$ (for Neptune), and $q_9(D_3, C_3) = 0.999957263$ (for Pluto).

The revealed [25, 26] small difference of the maximal energy gravitational influence of each planet at the surface point D_3 and at the mass center C_3 of the Earth must lead to the small difference of the combined maximal energy gravitational influences of the planets of the Solar System at the points C_3 and D_3 of the Earth. It was recognized [25, 26] that the small difference of the combined planetary maximal energy gravitational influences at the surface point D_3 and at the mass center C_3 of the Earth can contribute to the following related geophysical phenomena: the small oscillatory

motion of the rigid kernel of the Earth relative to the fluid kernel of the Earth; the small oscillation of the Earth's pole (i.e., the Chandler's wobble of the Earth's pole); the small oscillations of the boundary of the Pacific Ocean (i.e., the seismic zone of the Pacific Ring); the oscillations, rotations, and deformations of the geoblocks weakly coupled with the surrounding plastic layers in all seismic zones of the Earth and the formation of fractures related to the strong earthquakes and the planetary cataclysms.

4.1.3. The Evaluation of the Relative Maximal Planetary Integral Energy Gravitational Influences on the Earth in the Approximation of the Circular Orbits of the Planets of the Solar System. We assume that φ_{03} and φ_{0i} are the initial phases of the Earth τ_3 and the planet τ_i , respectively. Consequently, the positions of the center of the Earth τ_3 and the center of the planet τ_i (inner or outer) for the time moment t are given (instead of the relation (100)) by the following expressions:

$$\begin{aligned}\varphi_i(t) &= \omega_i t = \frac{2\pi}{T_i} t + \varphi_{0i}, \\ \varphi_3(t) &= \omega_3 t = \frac{2\pi}{T_3} t + \varphi_{03}.\end{aligned}\quad (118)$$

Taking into account the initial phases φ_{03} and φ_{0i} , the expressions (104), (107), (111), and (113) can be generalized as follows:

$$\begin{aligned}& \frac{\partial}{\partial t} \psi_{3i}(C_3, \text{int}) \\ &= \frac{\partial}{\partial t} \psi_{3i}(C_3, \text{ext}) = \frac{\partial}{\partial t} \psi_{3i}(C_3) \\ &= \frac{\gamma M_i R_{O3} R_{Oi} \omega_i \sin \{(\omega_i - \omega_3) t + \varphi_{0i} - \varphi_{03}\}}{[R_{O3}^2 + R_{Oi}^2 - 2R_{O3} R_{Oi} \cos \{(\omega_i - \omega_3) t + \varphi_{0i} - \varphi_{03}\}]^{3/2}},\end{aligned}\quad (119)$$

$$\begin{aligned}& \frac{\partial}{\partial t} \psi_{3i}(D_3, \text{int}) \\ &= \frac{\partial}{\partial t} \psi_{3i}(D_3, \text{ext}) = \frac{\partial}{\partial t} \psi_{3i}(D_3) \\ &= (\gamma M_i (R_{O3} - R_3) R_{Oi} \omega_i \\ & \quad \times \sin \{(\omega_i - \omega_3) t + \varphi_{0i} - \varphi_{03}\}) \\ & \quad \times \left([(R_{O3} - R_3)^2 + R_{Oi}^2 - 2(R_{O3} - R_3) R_{Oi} \right. \\ & \quad \left. \times \cos \{(\omega_i - \omega_3) t + \varphi_{0i} - \varphi_{03}\}]^{3/2} \right)^{-1}.\end{aligned}\quad (120)$$

We obtained [12] the integral energy gravitational influence $\Delta_g E_3(\tau_i, \varphi_{0i}, \varphi_{03}, t, t_0)$ on the Earth τ_3 owing to

the nonstationary instantaneous energy gravitational influence of the planet τ_i (inner or outer) during the time interval (t_0, t) :

$$\begin{aligned}\Delta_g E_3(\tau_i, \varphi_{0i}, \varphi_{03}, t, t_0) \\ &= \int_{t_0}^t \left(\iiint_{\tau_3} \left(\frac{\partial \psi_{3i}(C_3)}{\partial t'} \right) \rho dV \right) dt' \\ &\approx M_3 \int_{t_0}^t \left(\frac{\partial \psi_{3i}(C_3)}{\partial t'} \right) dt',\end{aligned}\quad (121)$$

where M_3 is the mass of the Earth. Substituting (119) into (121), we obtained [12]

$$\begin{aligned}\Delta_g E_3(\tau_i, \varphi_{0i}, \varphi_{03}, t, t_0) \\ &= M_3 \int_{t_0}^t \left(\gamma M_i R_{O3} R_{Oi} \omega_i \sin \{(\omega_i - \omega_3) t' + \varphi_{0i} - \varphi_{03}\} \right. \\ & \quad \times \left([(R_{O3})^2 + R_{Oi}^2 - 2R_{O3} R_{Oi} \right. \\ & \quad \left. \left. \times \cos \{(\omega_i - \omega_3) t' + \varphi_{0i} - \varphi_{03}\}]^{3/2} \right)^{-1} dt'.\end{aligned}\quad (122)$$

The result of integration of the expression (122) is given by the relation [12]:

$$\begin{aligned}\Delta_g E_3(\tau_i, \varphi_{0i}, \varphi_{03}, t, t_0) \\ &= \frac{2\alpha_i}{(\omega_i - \omega_3) \chi_i} \left[\frac{1}{[\beta_i - \chi_i \cos \{(\omega_i - \omega_3) t_0 + \varphi_{0i} - \varphi_{03}\}]^{1/2}} \right. \\ & \quad \left. - \frac{1}{[\beta_i - \chi_i \cos \{(\omega_i - \omega_3) t + \varphi_{0i} - \varphi_{03}\}]^{1/2}} \right],\end{aligned}\quad (123)$$

characterized by the following coefficients:

$$\begin{aligned}\alpha_i &= \gamma M_3 M_i R_{O3} R_{Oi} \omega_i, \\ \beta_i &= (R_{O3})^2 + (R_{Oi})^2, \\ \chi_i &= 2R_{O3} R_{Oi}.\end{aligned}\quad (124)$$

Using the initial phases $\varphi_{03} = 0$ and $\varphi_{0i} = 0$ for the initial time moment $t_0 = 0$, the expression (123) gives the more simple relation [12]:

$$\begin{aligned}\Delta_g E_3(\tau_i, 0, 0, t, 0) \\ &= \frac{2\alpha_i}{(\omega_i - \omega_3) \chi_i} \left[\frac{1}{[\beta_i - \chi_i]^{1/2}} \right. \\ & \quad \left. - \frac{1}{[\beta_i - \chi_i \cos \{(\omega_i - \omega_3) t\}]^{1/2}} \right]\end{aligned}\quad (125)$$

used for calculation of the maximal integral energy gravitational influence of the planet τ_i (inner or outer) on the Earth

τ_3 . Consider the expression (125) by taking into account that the mass center C_i of the inner planet τ_i , the mass center C_3 of the Earth τ_3 , and the mass center O of the Sun are located on the axis X for the initial time moment $t_0 = 0$ as it is shown on Figure 6. Considering the time duration

$$t_1^*(i, 3) = \frac{1}{2} \frac{T_i T_3}{(T_3 - T_i)}, \quad (i = 1, 2) \quad (126)$$

we obtain that the mass center C_i of the inner planet τ_i , the mass center C_3 of the Earth τ_3 , and the mass center O of the Sun will be localized again on the same straight line and the distance between the mass centers of the inner planet τ_i , and the Earth τ_3 will be maximal. We have from relation (125) the positive integral energy gravitational influence on the Earth's continuum during the time $t_1^*(i, 3)$:

$$\begin{aligned} \Delta_g E_3(\tau_i, 0, 0, t_1^*(i, 3), 0) \\ = \frac{2\alpha_i}{(\omega_i - \omega_3) \chi_i} \left[\frac{1}{[R_{O3} - R_{Oi}]} - \frac{1}{[R_{O3} + R_{Oi}]} \right] > 0. \end{aligned} \quad (127)$$

We obtained [12] from relation (125) that the integral energy gravitational influence on the Earth of the inner planet τ_i is equal to the zero

$$\Delta_g E_3(\tau_i, 0, 0, t_2^*(i, 3), 0) = 0 \quad (128)$$

during the time duration

$$t_2^*(i, 3) = \frac{T_i T_3}{(T_3 - T_i)}, \quad (i = 1, 2) \quad (129)$$

when the distance between the mass centers of the inner planet τ_i and the Earth τ_3 will be minimal.

We tested [12] the relation (125) for the outer planet τ_i and the Earth τ_3 assuming that the mass centers of the outer planet τ_i and the Earth τ_3 and the mass center O of the Sun are located on the axis X for the initial time moment $t_0 = 0$ as it is shown on Figure 6. Considering the time duration

$$t_1^*(3, i) = \frac{1}{2} \frac{T_i T_3}{(T_i - T_3)}, \quad (i = 4, 5, 6, 7, 8, 9) \quad (130)$$

we have that the mass center of the outer planet τ_i , the mass center C_3 of the Earth τ_3 , and the mass center O of the Sun will again be located on the same straight line, and the distance between the mass centers of the outer planet τ_i and the Earth τ_3 will be maximal. We obtained [12] from relation (125) the negative integral energy gravitational influence on the Earth of outer planet τ_i during the time $t_1^*(3, i)$:

$$\begin{aligned} \Delta_g E_3(\tau_i, 0, 0, t_1^*(3, i), 0) \\ = \frac{2\alpha_i}{(\omega_i - \omega_3) \chi_i} \left[\frac{1}{[R_{Oi} - R_{O3}]} - \frac{1}{[R_{Oi} + R_{O3}]} \right] < 0. \end{aligned} \quad (131)$$

Considering the time duration

$$t_2^*(3, i) = \frac{T_i T_3}{(T_i - T_3)}, \quad (132)$$

we obtained [12] from relation (125) the zero integral energy gravitational influence on the Earth from the outer planet τ_i during the time $t_2^*(3, i)$:

$$\Delta_g E_3(\tau_i, 0, 0, t_2^*(3, i), 0) = 0. \quad (133)$$

Using the expression (124), we established [12] that the expressions (127) and (131) give the following extreme values:

$$\begin{aligned} \max_t \Delta_g E_3(\tau_i, 0, 0, t, 0) \\ = \Delta_g E_3(\tau_i, 0, 0, t_1^*(i, 3), 0) \\ = 2\gamma M_3 M_i \frac{R_{Oi} T_3}{(R_{O3}^2 - R_{Oi}^2)(T_3 - T_i)} > 0, \end{aligned} \quad (134)$$

$(i = 1, 2),$

$$\begin{aligned} \min_t \Delta_g E_3(\tau_i, 0, 0, t, 0) \\ = \Delta_g E_3(\tau_i, 0, 0, t_1^*(3, i), 0) \\ = 2\gamma M_3 M_i \frac{R_{O3} T_3}{(R_{Oi}^2 - R_{O3}^2)(T_3 - T_i)} < 0, \end{aligned} \quad (135)$$

$(i = 4, 5, 6, 7, 8, 9)$

of the integral energy gravitational influences (respectively, the positive maximal integral energy gravitational influence from the inner planet τ_i and the negative minimal integral energy gravitational influence from the outer planet τ_i) for the given initial phases $\varphi_{03} = 0$ and $\varphi_{0i} = 0$ (for the initial time moment $t_0 = 0$) corresponding to the initial configurations shown on Figures 5 and 6.

Using relation (134), we obtained [12] for Mercury ($i = 1$) and for Venus ($i = 2$) the following expressions of the maximal positive integral energy gravitational influences on the Earth:

$$\begin{aligned} \max_t \Delta_g E_3(\tau_1, 0, 0, t, 0) \\ = \Delta_g E_3(\tau_1, 0, 0, t_1^*(1, 3), 0) \\ = 2\gamma M_3 M_1 \frac{R_{O1} T_3}{(R_{O3}^2 - R_{O1}^2)(T_3 - T_1)} > 0, \quad i = 1, \end{aligned} \quad (136)$$

$$\begin{aligned} \max_t \Delta_g E_3(\tau_2, 0, 0, t, 0) \\ = \Delta_g E_3(\tau_2, 0, 0, t_1^*(2, 3), 0) \\ = 2\gamma M_3 M_2 \frac{R_{O2} T_3}{(R_{O3}^2 - R_{O2}^2)(T_3 - T_2)} > 0, \quad i = 2. \end{aligned} \quad (137)$$

Considering the mass m_τ of the macroscopic continuum region near the surface point D_3 (instead of the mass M_3 of the Earth) in relations (136) and (137), we obtained [12] the following expressions for the positive integral energy gravitational influences of Mercury ($i = 1$) and Venus ($i = 2$) on

the macroscopic continuum region of the mass m_τ near the surface point D_3 of the Earth:

$$\begin{aligned} & \max_t \Delta_g E_3 (\tau_1, D_3, m_\tau, 0, 0, t, 0) \\ &= \Delta_g E_3 (\tau_1, D_3, m_\tau, 0, 0, t_1^* (1, 3), 0) \\ &= 2\gamma m_\tau M_1 \frac{R_{O1} T_3}{(R_{O3}^2 - R_{O1}^2)(T_3 - T_1)} > 0, \quad i = 1, \end{aligned} \quad (138)$$

$$\begin{aligned} & \max_t \Delta_g E_3 (\tau_2, D_3, m_\tau, 0, 0, t, 0) \\ &= \Delta_g E_3 (\tau_2, D_3, m_\tau, 0, 0, t_1^* (2, 3), 0) \\ &= 2\gamma m_\tau M_2 \frac{R_{O2} T_3}{(R_{O3}^2 - R_{O2}^2)(T_3 - T_2)} > 0, \quad i = 2. \end{aligned} \quad (139)$$

We shall use the expression (136) as a measuring unit for evaluations of the maximal absolute values of the integral energy gravitational influences on the Earth of the planets of the Solar System and the Moon.

Considering the ratio of the extreme value $\max_t \Delta_g E_3 (\tau_i, 0, 0, t, 0)$ (given by expression (134)) and the maximal positive integral energy gravitational influence $\max_t \Delta_g E_3 (\tau_1, 0, 0, t, 0)$ (given by the expression (136)) of Mercury on the Earth, we obtained [12] the relative values $s(i)$ of the maximal integral energy gravitational influences on the Earth of the inner planets:

$$\begin{aligned} s(i) &= \frac{\max_t \Delta_g E_3 (\tau_i, 0, 0, t, 0)}{\max_t \Delta_g E_3 (\tau_1, 0, 0, t, 0)} \\ &= \frac{M_i R_{Oi} (R_{O3}^2 - R_{O1}^2)(T_3 - T_1)}{M_1 R_{O1} (R_{O3}^2 - R_{Oi}^2)(T_3 - T_i)}, \quad i = 1, 2. \end{aligned} \quad (140)$$

We have the obvious value $s(1) = 1$ for Mercury ($i = 1$). We calculated [12] the value $s(2) = 89.6409$ for Venus ($i = 2$) based on the planetary numerical values [50] of the average radii of the orbits, the time periods of circulations around the Sun, and the masses of the Earth, Venus, and Mercury.

Since the values given by the expression (135) are negative for the outer planets, we used the absolute (positive) value

$$\begin{aligned} & \left| \min_t \Delta_g E_3 (\tau_i, 0, 0, t, 0) \right| \\ &= \left| \Delta_g E_3 (\tau_i, 0, 0, t_1^* (3, i), 0) \right| \\ &= 2\gamma M_3 M_i \frac{R_{O3} T_3}{(R_{Oi}^2 - R_{O3}^2)(T_i - T_3)} > 0, \\ & \quad i = 4, 5, 6, 7, 8, 9. \end{aligned} \quad (141)$$

Using the expressions (141) and (136), we obtained [12] the relative values $s(i)$ of the maximal integral energy gravitational influences on the Earth of the outer planets of the Solar System ($i = 4, 5, 6, 7, 8, 9$):

$$\begin{aligned} s(i) &= \frac{\left| \min_t \Delta_g E_3 (\tau_i, 0, 0, t, 0) \right|}{\max_t \Delta_g E_3 (\tau_1, 0, 0, t, 0)} \\ &= \frac{M_i R_{O3} (R_{O3}^2 - R_{O1}^2)(T_3 - T_1)}{M_1 R_{O1} (R_{Oi}^2 - R_{O3}^2)(T_i - T_3)}, \\ & \quad i = 4, 5, 6, 7, 8, 9. \end{aligned} \quad (142)$$

Based on the planetary numerical values [50], we calculated the following numerical values [9]: $s(4) = 2.6396$ for Mars ($i = 4$), $s(5) = 31.319$ for Jupiter ($i = 5$), $s(6) = 1.036$ for Saturn ($i = 6$), $s(7) = 0.0133$ for Uranus ($i = 7$), $s(8) = 0.003229$ for Neptune ($i = 8$), and $s(9) = 1.4495 \cdot 10^{-7}$ for Pluto ($i = 9$).

Taking into account the calculated relative values $s(i)$, we obtained [9] the following order of signification of the planets of the Solar System: Venus ($s(2) = 89.6409$), Jupiter ($s(5) = 31.319$), Mars ($s(4) = 2.6396$), Saturn ($s(6) = 1.036$), Mercury ($s(1) = 1$), Uranus ($s(7) = 0.0133$), Neptune ($s(8) = 0.003229$), and Pluto ($s(9) = 1.4495 \cdot 10^{-7}$) with respect to the established significance of the planetary maximal integral energy gravitational influences on the Earth.

We established [12] that Venus and Jupiter induce the main maximal integral energy gravitational influences on the Earth. Mars, Saturn, and Mercury induce the combined maximal integral energy gravitational influence on the Earth, which is one order of the magnitude smaller than the maximal integral energy gravitational influence of Jupiter. The maximal integral energy gravitational influences on the Earth of Uranus, Neptune, and Pluto are two, three, and seven orders of the magnitude, respectively, smaller than the maximal integral energy gravitational influence of Mercury.

4.2. The Energy Gravitational Influences on the Earth of the Moon

4.2.1. *The Evaluation of the Relative Maximal Instantaneous Energy Gravitational Influence of the Moon on the Earth in the Second Approximation of the Elliptical Orbits of the Earth and the Moon around the Combined Mass Center $C_{3,MOON}$ of the Earth and the Moon.* We shall consider the movement of the Earth τ_3 and the Moon along the elliptical orbits around the combined mass center $C_{3,MOON}$ of the Earth and the Moon. We have the following relations (see Figure 9):

$$r_{MOON} (\varphi_{MOON} (t)) = \frac{P_{MOON}}{(1 + e_{MOON} \cos \varphi_{MOON} (t))}, \quad (143)$$

$$\begin{aligned} r_E (\varphi_E (t)) &= r_E (\varphi_{MOON} (t) + \pi) \\ &= \frac{P_E}{(1 - e_E \cos (\varphi_{MOON} (t) + \pi))} \\ &= \frac{P_E}{(1 + e_E \cos \varphi_{MOON} (t))} \end{aligned} \quad (144)$$

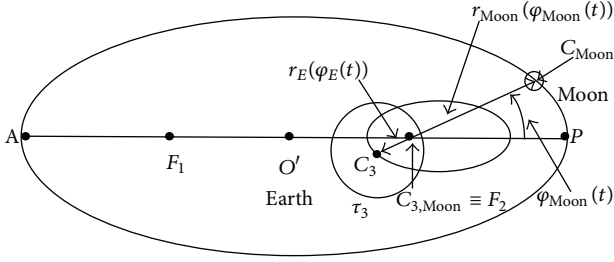


FIGURE 9: The geometric sketch of circulation of the mass center C_3 of the Earth τ_3 and the mass center C_{MOON} of the Moon around the combined mass center $C_{3,\text{MOON}}$ of the Earth-Moon system.

for the distance $r_{\text{MOON}}(\varphi_{\text{MOON}}(t))$ between the combined mass center $C_{3,\text{MOON}}$ and the mass center C_{MOON} of the Moon and for the distance $r_E(\varphi_E(t))$ between the combined mass center $C_{3,\text{MOON}}$ and the mass center C_3 of the Earth τ_3 . We have the focal parameter p_{MOON} and the eccentricity e_{MOON} of the elliptical orbit of the Moon. p_E and e_E ($e_E = e_{\text{MOON}}$) are the focal parameter and the eccentricity, respectively, of the elliptical Earth's orbit around the combined mass center $C_{3,\text{MOON}}$. We have the expression for the distance $d_{3M}(E_M)$

$$d_{3M}(E_M) = \frac{p_{\text{MOON}}}{(1 + e_{\text{MOON}} \cos \varphi_{\text{MOON}}(t))} + \frac{p_E}{(1 + e_E \cos \varphi_{\text{MOON}}(t))} - R_3 \quad (145)$$

between the mass center C_{MOON} of the Moon and the point E_M , which is the intersection of the direct line (connecting the mass center C_{MOON} of the Moon and the mass center C_3 of the Earth τ_3) with the surface of the Earth τ_3 . We have the expression for the gravitational potential $\psi_{3,\text{MOON}}(E_M)$ created by the Moon at the point E_M of the Earth τ_3 :

$$\psi_{3,\text{MOON}}(E_M) = -\gamma \frac{M_{\text{MOON}}}{d_{3M}(E_M)}. \quad (146)$$

We obtained [25, 26] from the relation (146) the expression for the partial derivative $(\partial/\partial t)\psi_{3,\text{MOON}}(E_M)$ of the gravitational potential $\psi_{3,\text{MOON}}(E_M)$ created by the Moon at the point E_M of the Earth τ_3 :

$$\begin{aligned} \frac{\partial}{\partial t} \psi_{3,\text{MOON}}(E_M) &= \frac{\gamma M_{\text{MOON}} e_{\text{MOON}} p_{\text{MOON}} \sin(\varphi_{\text{MOON}}(t))}{(p_{\text{MOON}} + p_E - R_3 (1 - e_{\text{MOON}} \cos \varphi_{\text{MOON}}(t)))^2} \\ &\times \frac{d\varphi_{\text{MOON}}(t)}{dt}. \end{aligned} \quad (147)$$

We have the expression for the distance $d_{3M}(C_3)$

$$d_{3M}(C_3) = \frac{p_{\text{MOON}}}{(1 + e_{\text{MOON}} \cos \varphi_{\text{MOON}}(t))} + \frac{p_E}{(1 + e_E \cos \varphi_{\text{MOON}}(t))} \quad (148)$$

between the mass center C_{MOON} of the Moon and the mass center C_3 of the Earth τ_3 . We have the expression for the gravitational potential $\psi_{3,\text{MOON}}(C_3)$ created by the Moon at the mass center C_3 of the Earth τ_3 :

$$\psi_{3,\text{MOON}}(C_3) = -\gamma \frac{M_{\text{MOON}}}{d_{3M}(C_3)}. \quad (149)$$

We obtained [25, 26] from the relation (149) the expression for the partial derivative:

$$\begin{aligned} \frac{\partial}{\partial t} \psi_{3,\text{MOON}}(C_3) &= \frac{\gamma M_{\text{MOON}} e_{\text{MOON}} p_{\text{MOON}} \sin(\varphi_{\text{MOON}}(t))}{(p_{\text{MOON}} + p_E)^2} \\ &\times \frac{d\varphi_{\text{MOON}}(t)}{dt}. \end{aligned} \quad (150)$$

We can obtain the focal parameter p_{MOON} of the elliptical orbit of the Moon in terms of the average distance R_{3M} (between the mass centers of the Earth and the Moon) and the eccentricity $e_{\text{MOON}} = e_E$ of the elliptical orbits of the Moon and the Earth around the combined mass center $C_{3,\text{MOON}}$ of the Earth and the Moon. Using the relation (143), we have the relation for the large semiaxis a_{MOON} of the elliptical orbit of the Moon:

$$\begin{aligned} 2a_{\text{MOON}} &= r_{\text{MOON}}(0) + r_{\text{MOON}}(\pi) \\ &= \frac{p_{\text{MOON}}}{(1 + e_{\text{MOON}})} + \frac{p_{\text{MOON}}}{(1 - e_{\text{MOON}})} \\ &= \frac{2p_{\text{MOON}}}{(1 - e_{\text{MOON}}^2)}, \end{aligned} \quad (151)$$

which gives the relation for the focal parameter p_{MOON} of the elliptical orbit of the Moon:

$$p_{\text{MOON}} = (1 - e_{\text{MOON}}^2) a_{\text{MOON}}. \quad (152)$$

We can obtain the large semiaxis a_{MOON} of the elliptical orbit of the Moon in terms of the average distance R_{3M} (between the mass centers of the Earth and the Moon) and the eccentricity e_{MOON} of the elliptical orbit of the Moon. Defining the average distance R_{3M} (between the mass centers of the Earth and the Moon) as the average arithmetic value of the large semiaxis a_{MOON} and the small semiaxis b_{MOON} of the elliptical orbit of the Moon

$$R_{3M} = \frac{(a_{\text{MOON}} + b_{\text{MOON}})}{2} \quad (153)$$

and using the definition of the eccentricity e_{MOON} of the elliptical orbit of the Moon

$$e_{\text{MOON}} = \frac{c_{\text{MOON}}}{a_{\text{MOON}}} = \frac{\sqrt{a_{\text{MOON}}^2 - b_{\text{MOON}}^2}}{a_{\text{MOON}}}, \quad (154)$$

we obtained [25, 26] the relation for the average distance R_{3M} :

$$R_{3M} = \frac{a_{\text{MOON}} \left(1 + \sqrt{1 - e_{\text{MOON}}^2}\right)}{2}, \quad (155)$$

which leads to the relation for the large semiaxis a_{MOON} :

$$a_{\text{MOON}} = \frac{2R_{3M}}{\left(1 + \sqrt{1 - e_{\text{MOON}}^2}\right)}. \quad (156)$$

Using the relations (152) and (156), we obtained [25, 26] the relation for the focal parameter p_{MOON} of the elliptical orbit of the of the Moon:

$$p_{\text{MOON}} = \frac{2R_{3M} \left(1 - e_{\text{MOON}}^2\right)}{\left(1 + \sqrt{1 - e_{\text{MOON}}^2}\right)}. \quad (157)$$

Using the relation (157) and the relations

$$p_{\text{MOON}} = p_{\text{MOON},E} \frac{M_3}{(M_3 + M_{\text{MOON}})}, \quad (158)$$

$$p_E = p_{\text{MOON},E} \frac{M_{\text{MOON}}}{(M_3 + M_{\text{MOON}})},$$

the relation (150) can be rewritten as follows [25, 26]:

$$\begin{aligned} & \frac{\partial}{\partial t} \psi_{3,\text{MOON}}(C_3) \\ &= \frac{\gamma M_{\text{MOON}} e_{\text{MOON}} \left(1 + \sqrt{1 - e_{\text{MOON}}^2}\right) \sin(\varphi_{\text{MOON}}(t))}{2R_{3M} (1 - e_{\text{MOON}}^2) \left(\frac{M_{\text{MOON}}}{M_3} + 1\right)^2} \\ & \quad \times \frac{d\varphi_{\text{MOON}}(t)}{dt}. \end{aligned} \quad (159)$$

Taking $\sin(\varphi_{\text{MOON}}(t)) = 1$ and equating evaluating $d\varphi_{\text{MOON}}(t)/dt$ to ω_{MOON} (for the corresponding hypothetical circular orbits of the Earth and the Moon), we obtained [25, 26] the characteristic maximal positive value of the partial derivative $(\partial/\partial t)\psi_{3,\text{MOON}}(C_3)$:

$$\begin{aligned} & \text{char. max.pos. } \frac{\partial}{\partial t} \psi_{3,\text{MOON}}(C_3, \text{second approximation}) \\ &= \frac{\gamma M_{\text{MOON}} e_{\text{MOON}} \left(1 + \sqrt{1 - e_{\text{MOON}}^2}\right) \omega_{\text{MOON}}}{2R_{3M} (1 - e_{\text{MOON}}^2) \left((M_{\text{MOON}}/M_3) + 1\right)^2}. \end{aligned} \quad (160)$$

To evaluate (in the second approximation) the relative power of the energy gravitational influence of the Moon on the Earth, we obtained the ratio $f_{\text{MOONM}}(C_3, \text{second approximation})$ of the maximal characteristic maximal positive value $\text{char. max.pos.}(\partial/\partial t)\psi_{3,\text{MOON}}(C_3, \text{second approximation})$ and the maximal positive value $\max(\partial/\partial t)\psi_{3M}(C_3, \text{int})$:

$$\begin{aligned} & f_{\text{MOONM}}(C_3, \text{second approximation}) \\ &= \frac{\text{char. max.pos.}(\partial/\partial t)\psi_{3,\text{MOON}}(C_3, \text{second approximation})}{\max(\partial/\partial t)\psi_{3M}(C_3, \text{int})}. \end{aligned} \quad (161)$$

The corresponding numerical value $f_{\text{MOONM}}(C_3, \text{second approximation}) = 19.44083$ was calculated [25, 26] by taking into account the following numerical values: $e_{\text{MOON}} = 0.05$, $M_{\text{MOON}} = M_3/81$, $M_M = 0.06M_3$, $T_{\text{MOON}} = 29.5306$ days, and $T_M = 88$ days.

The calculated numerical value $f_{\text{MOONM}}(C_3, \text{second approximation})$ is 19.44083 times larger than the maximal power of the energy gravitational influence (on the unit mass at the mass center C_3 of the Earth) of Mercury moving around the mass center O of the Sun along the hypothetical circular orbit.

Taking into account the calculated [25, 26] nondimensional maximal instantaneous energy gravitational influences on the unit mass of the Earth at the mass center C_3 of the Earth: $f(2, C_3) = 37.69807434$ (for Venus), $f_{\text{MOONM}}(C_3, \text{second approximation}) = 19.44083404$ (for the Moon), $f(5, C_3) = 7.41055774$ (for Jupiter), $f(1, C_3) = 1$ (for Mercury), $f(4, C_3) = 0.67441034$ (for Mars), $f(6, C_3) = 0.24601009$ (for Saturn), $f(7, C_3) = 0.00319056$ (for Uranus), $f(8, C_3) = 0.00077565$ (for Neptune), and $f(9, C_3) = 3.4813 \cdot 10^{-8}$ (for Pluto), we have the following order of significance (in the frame of the considered second approximation) of the Moon and the planets of the Solar System: Venus, Moon, Jupiter, Mercury, Mars, Saturn, Uranus, Neptune, and Pluto. The obtained numerical sequence reveals the main instantaneous energy gravitational influences on the Earth of Venus, Moon, Jupiter, Mercury, and Mars, which determine (in collection) the main combined instantaneous energy gravitational influence on the Earth (not taking into account the instantaneous energy gravitational influences of the Sun and our Galaxy).

4.2.2. The Evaluation of the Maximal Integral Energy Gravitational Influence of the Moon on the Earth in the Approximation of the Elliptical Orbits of the Earth and the Moon around the Combined Mass Center $C_{3,\text{MOON}}$ of the Earth and the Moon. We evaluated [25, 26] the maximal integral energy gravitational influence of the Moon on the Earth in the approximation of the elliptical orbits of the Earth and the Moon around the combined mass center $C_{3,\text{MOON}}$ of

the Earth and the Moon. We have the integral energy gravitational influence of the Moon on the Earth τ_3 (characterized by the mass M_3) during the time interval (t_0, t) :

$$\begin{aligned} \Delta_g E_3 (\text{Moon}, \varphi_{\text{MOON}}(t_0), t, t_0) &= \int_{t_0}^t \left(\iiint_{\tau_3} \left(\frac{\partial \psi_{3, \text{MOON}}(C_3)}{\partial t'} \right) \rho dV \right) dt' \\ &\approx M_3 \int_{t_0}^t \left(\frac{\partial \psi_{3, \text{MOON}}(C_3)}{\partial t'} \right) dt'. \end{aligned} \quad (162)$$

Substituting the expression (159) into (162) and integrating, we obtained [25, 26] the following analytical relation:

$$\begin{aligned} \Delta_g E_3 (\text{Moon}, \varphi_{\text{MOON}}(t_0), t, t_0) &= - \left(\gamma M_3 M_{\text{MOON}} e_{\text{MOON}} \left(1 + \sqrt{1 - e_{\text{MOON}}^2} \right) \right. \\ &\quad \times \left. \left(\cos \varphi_{\text{MOON}}(t) - \cos \varphi_{\text{MOON}}(t_0) \right) \right) \\ &\quad \times \left(2R_{3M} (1 - e_{\text{MOON}}^2) \left(\frac{M_{\text{MOON}}}{M_3} + 1 \right) \right)^{-1}. \end{aligned} \quad (163)$$

Considering the following phases: $\varphi_{\text{MOON}}(t) = \pi$ and $\varphi_{\text{MOON}}(t_0) = 0$, we have from relation (163) the maximal positive value of the integral energy gravitational influence of the Moon on the Earth:

$$\begin{aligned} \max_t \Delta_g E_3 (\text{Moon}, \varphi_{\text{MOON}}(t_0), t, t_0) &= \frac{\gamma M_3 M_{\text{MOON}} e_{\text{MOON}} \left(1 + \sqrt{1 - e_{\text{MOON}}^2} \right)}{R_{3M} (1 - e_{\text{MOON}}^2) \left(\frac{M_{\text{MOON}}}{M_3} + 1 \right)^2}. \end{aligned} \quad (164)$$

To evaluate the maximal integral energy gravitational influence of the Moon on the Earth, we consider the ratio $s(\text{Moon, second approximation})$ of the maximal positive value (164) and the maximal positive value (136) (of the integral energy gravitational influence of Mercury on the Earth):

$$\begin{aligned} s(\text{Moon, second approximation}) &= \frac{\max_t \Delta_g E_3 (\text{Moon}, \varphi_{\text{MOON}}(t_0), t, t_0)}{\max_t \Delta_g E_3 (\tau_1, 0, 0, t, 0)} \\ &= \left(e_{\text{MOON}} \left(1 + \sqrt{1 - e_{\text{MOON}}^2} \right) M_{\text{MOON}} \right. \\ &\quad \times \left. \left(R_{\text{O}_3}^2 - R_{\text{O}_1}^2 \right) (T_3 - T_1) \right) \\ &\quad \times \left(\left(1 - e_{\text{MOON}}^2 \right) \left(\frac{M_{\text{MOON}}}{M_3} + 1 \right)^2 M_1 R_{3M} R_{\text{O}_1} T_3 \right)^{-1}. \end{aligned} \quad (165)$$

Using the relation (165), we calculated [25, 26] the numerical value $s(\text{Moon, second approximation}) = 13.0693$ for the following numerical values: the eccentricity $e_{\text{MOON}} = 0.05$ of the elliptical orbits of the Moon and the Earth around the combined mass center $C_{3, \text{MOON}}$, the mass $M_1 = M_M = 0.06M_3$ of Mercury, the mass $M_{\text{MOON}} = M_3/81$ of the Moon, the average distance $R_{3M} = 384400$ km between the mass centers of the Earth and the Moon, the time period $T_3 = 365.3$ days of the Earth's circulation around the Sun, the time period $T_1 = T_M = 88$ days of Mercury's circulation around the Sun, the average radius $R_{\text{OM}} = R_{\text{O}_1} = 57.85 \cdot 10^6$ km of Mercury's orbit around the Sun, and the average radius $R_{\text{O}_3} = 149.6 \cdot 10^6$ km of the Earth's orbit around the Sun.

Thus, considering the aspect of the cosmic gravitational preparation of the strong earthquakes, we have demonstrated the Venusian ($s(2) = 89.6409$) and Jupiter's ($s(5) = 31.319$) energy gravitational predominance [12] in supplying of the cosmic planetary gravitational energy to the focal region of the preparing earthquakes. We have demonstrated the significant maximal integral energy gravitational influence of the Moon ($s(\text{Moon, second approximation}) = 13.0693$) [25, 26] on the Earth. Venus, Jupiter, and the Moon induce the main combined (planetary and lunar) integral energy gravitational influence on the Earth. The combined maximal integral energy gravitational influence on the Earth of Mars ($s(4) = 2.6396$), Saturn ($s(6) = 1.036$), and Mercury ($s(1) = 1$) is one order of the magnitude smaller than the maximal integral energy gravitational influence of Venus. The combined maximal integral energy gravitational influence on the Earth of Uranus ($s(7) = 0.0133$), Neptune ($s(8) = 0.003229$), and Pluto ($s(9) = 1.4495 \cdot 10^{-7}$) is two orders of the magnitude smaller (i.e., negligible) than the maximal integral energy gravitational influence of Mercury.

4.3. The Demonstration of the Reality of the Cosmic Energy Gravitational Genesis of Preparation and Triggering of Earthquakes

4.3.1. The Demonstration of the Real Cosmic Energy Gravitational Genesis of Preparation of Earthquakes. Using the formula (139), we evaluated [12, 25, 26] the numerical value $E_g(\tau_2, D_3, m_\tau)$ of the integral energy gravitational influence of Venus on the macroscopic continuum region τ (the focal region of the preparing earthquake) of mass m_τ near the surface point D_3 of the Earth during the time

$$T_g(2) = t_1^*(3, 2) = \frac{1}{2} \frac{T_2 T_3}{(T_2 - T_3)} = 291.902 \text{ days} \quad (166)$$

of the energy gravitational influence of Venus on the macroscopic continuum region τ of the Earth. Using the expression (139) for the maximal positive integral energy gravitational influence $E_g(\tau_2, D_3, m_\tau)$ of Venus ($i = 2$) on the macroscopic continuum region τ of mass m_τ near the surface point D_3 of

the Earth, we obtained the obvious estimation for the value $E_g(\tau_2, D_3, m_\tau)$:

$$\begin{aligned} E_g(\tau_2, D_3, m_\tau) &= 2\gamma m_\tau M_2 \frac{R_{O_2} T_3}{(R_{O_3}^2 - R_{O_2}^2)(T_3 - T_2)} \\ &= 2\gamma (l_\tau)^3 \rho_\tau M_2 \frac{R_{O_2} T_3}{(R_{O_3}^2 - R_{O_2}^2)(T_3 - T_2)} > 0, \end{aligned} \quad (167)$$

where the final expression for the estimation $E_g(\tau_2, D_3, m_\tau)$ is given for the focal region of the cubical form characterized by the size l_τ of the cube. Considering the following numerical values: $l_\tau = 10$ km, $\rho_\tau = 5000$ kg/m³ (the average density of the cubical focal region), and $\gamma = 6.67 \cdot 10^{-11}$ J · m/kg² (the gravitational constant) and using the following known [50] parameters of the Solar System: $T_V = T_2 = 224.7$ days, $R_{OV} = R_{O_2} = 108.1 \cdot 10^6$ km, and $M_V = M_2 = 0.82M_3$, $M_3 = 6 \cdot 10^{24}$ kg, $T_3 = 365.3$ days, we calculated [12, 25, 26] from the expression (167) the numerical value

$$E_g(\tau_2, D_3, m_\tau) = 8.619 \cdot 10^{19} \text{ J}, \quad (168)$$

which is close to the change " $\Delta W \approx 10^{20}$ J" [2] of the rotational kinetic energy of the Earth during the strongest earthquakes. The order of magnitude of the estimation (168) for the value $E_g(\tau_2, D_3, m_\tau)$ is consistent with the earlier estimation of the seismotectonic energy E_{ST} [2], which can discharge in the focal region of the strongest earthquakes:

$$E_{ST}(\tau_2, D_3, m_\tau) \leq E_g(\tau_2, D_3, m_\tau). \quad (169)$$

It was pointed out [2] that the coincidence of the values E_{ST} and ΔW is not the casual fact: it is the indication that the strongest earthquake can be considered as the energy quantum corresponding to the regular change of the rotational regime of the Earth. Using the equivalent generalized differential formulations (50), (56), and (59) of the first law of thermodynamics applied for the focal region τ of the preparing earthquake, we found strictly the equality of the orders of the magnitude of the values E_{ST} and ΔW for the strongest earthquakes. Consequently, the coincidence of the orders of the magnitude of the values E_{ST} , ΔW , and $E_g(\tau_2, D_3, m_\tau)$ is the indication that the regular changes of the rotational regime of the Earth are related to the regular discharges of the accumulated potential energy (in the different focal regions of earthquakes) supplying of the cosmic gravitational energy influences of the planets of the Solar System, the Sun, and the Moon.

Thus, based on the equivalent generalized differential formulations (50), (56), and (59) of the first law of thermodynamics used for the Earth's macroscopic continuum region τ (the focal region of the preparing earthquake), we evaluate the reality of the cosmic energy gravitational genesis of the preparation of the earthquakes.

4.3.2. *The Demonstration of the Real Cosmic Energy Gravitational Genesis of Triggering of the Preparing Earthquakes.* We evaluated [12] the relative (normalized on the maximal integral energy gravitational influence of Mercury τ_1 on the Earth) average integral energy gravitational planetary influences corresponding to the time duration $T_{MOON}/2$ of the maximal integral energy gravitational influence of the Moon on the Earth. We take into account the time durations of the maximal integral energy gravitational influences on the Earth of the inner planets (Mercury τ_1 and Venus τ_2)

$$T_g(i) = t_1^*(i, 3) = \frac{1}{2} \frac{T_i T_3}{(T_3 - T_i)}, \quad (i = 1, 2), \quad (170)$$

which are the time durations of supplying of the cosmic planetary gravitational energy from the inner planets ($i = 1, 2$) to the focal region of the preparing earthquakes. We take into account the time durations of the maximal integral energy gravitational influences on the Earth of the outer planets (Mars τ_4 , Jupiter τ_5 , Saturn τ_6 , Uranus τ_7 , Neptune τ_8 , and Pluto τ_9)

$$T_g(i) = t_1^*(3, i) = \frac{1}{2} \frac{T_i T_3}{(T_i - T_3)}, \quad (i = 4, 5, 6, 7, 8, 9) \quad (171)$$

which are the time durations of supplying of the cosmic planetary gravitational energy from the outer planets ($i = 4, 5, 6, 7, 8, 9$) to the focal region of the preparing earthquakes.

We defined [12] and calculated the relative values $s(i)$ (normalized on the maximal integral energy gravitational influence of Mercury ($i = 1$) on the Earth) of the maximal integral energy gravitational influences on the Earth of the planets of the Solar System ($i = 1, 2, 4, 5, 6, 7, 8, 9$). We evaluated [12] the relative (normalized on the maximal integral energy gravitational influence of Mercury ($i = 1$) on the Earth) average values $e(i)$

$$e(i) = s(i) \frac{0.5T_{MOON}}{T_g(i)}, \quad (i = 1, 2, 4, 5, 6, 7, 8, 9) \quad (172)$$

of the integral energy gravitational influences on the Earth of the planets of the Solar System corresponding to the time duration $T_{MOON}/2$ of the maximal integral energy gravitational influence of the Moon on the Earth.

Using the expression (170) for the time $T_g(i)$ of supplying of the cosmic planetary gravitational energy from the inner planets ($i = 1, 2$), the expression (171) for the time $T_g(i)$ of supplying of the cosmic planetary gravitational energy from the outer planets ($i = 4, 5, 6, 7, 8, 9$) and the expression (172) for $e(i)$, we calculated the following numerical values [12]: $T_g(1) = 57.96$ days and $e(1) = 0.2547$ (which is one order of magnitude smaller than $s(\text{Moon, second approximation}) = 13.0693$) for Mercury; $T_g(2) = 291.902$ days and $e(2) = 4.5342$ (which is smaller than $s(\text{Moon, second approximation}) = 13.0693$) for Venus; $T_g(4) = 390.0545$ days and $e(4) = 0.0999$ (which is significantly smaller than

$s(\text{Moon, second approximation}) = 13.0693$) for Mars; $T_g(5) = 199.4705$ days and $e(5) = 2.3182$ (which is smaller significantly than $s(\text{Moon, second approximation}) = 13.0693$) for Jupiter; $T_g(6) = 189.069$ days and $e(6) = 0.0809$ (which is significantly smaller than $s(\text{Moon, second approximation}) = 13.0693$) for Saturn; $T_g(7) = 184.8506$ days and $e(7) = 0.001066$ (which is four orders of the magnitude smaller than $s(\text{Moon, second approximation}) = 13.0693$) for Uranus; $T_g(8) = 183.7653$ days and $e(8) = 0.0002594$ (which is four-five orders of the magnitude smaller than $s(\text{Moon, second approximation}) = 13.0693$) for Neptune; $T_g(9) = 183.3905$ days and $e(9) = 1.1671 \cdot 10^{-8}$ (which is nine orders of the magnitude smaller than $s(\text{Moon, second approximation}) = 13.0693$) for Pluto.

In Section 4.2 we have demonstrated the following order of significance of the planets of the Solar System and the Moon for the cosmic gravitational preparation of the strong earthquakes: Venus ($s(2) = 89.6409$), Jupiter ($s(5) = 31.319$), the Moon ($s(\text{Moon, second approximation}) = 13.0693$), Mars ($s(4) = 2.6396$), Saturn ($s(6) = 1.036$), Mercury ($s(1) = 1$), Uranus ($s(7) = 0.0133$), Neptune ($s(8) = 0.003229$), and Pluto ($s(9) = 1.4495 \cdot 10^{-7}$). We have the different order of significance of the planets of the Solar System and the Moon related to the defined relative average values $e(i)$: the Moon ($s(\text{Moon, second approximation}) = 13.0693$), Venus ($e(2) = 4.5342$), Jupiter ($e(5) = 2.3182$), Mercury ($e(1) = 0.2547$), Mars ($e(4) = 0.0999$), Saturn ($e(6) = 0.0809$), Uranus ($e(7) = 0.001066$), Neptune ($e(8) = 0.0002594$), and Pluto ($e(9) = 1.1671 \cdot 10^{-8}$).

Taking into account the obtained [12] numerical values $e(i)$ for the planets of the Solar System and the numerical value $s(\text{Moon, second approximation}) = 13.0693$ for the Moon [25, 26], we can recognize the established [25, 26] predominant significance of the Moon (along with the minor significance of Venus, Jupiter, and Mercury) as the predominant lunar cosmic trigger mechanism of earthquakes preparing by the combined (planetary and lunar) integral energy gravitational influences on the Earth of Venus, Jupiter, the Moon, Mars, and Mercury.

It was suggested in [51] the hypothesis that the Chandler's wobble of the Earth's pole can be generated by the motion of the rigid kernel of the Earth induced by the disturbances in the Sun-Earth-Moon system. The presented results of Sections 4.1, 4.2, and 4.3 support the stated [25, 26] conclusion that the related geophysical phenomena (the small oscillatory motion of the rigid kernel of the Earth relative to the fluid kernel of the Earth [51]; the small oscillation of the Earth's pole (i.e., the Chandler's wobble of the Earth's pole); the small oscillations of the boundary of the Pacific Ocean (i.e., the seismic zone of the Pacific Ring [2]); the oscillations [42], rotations, and deformations [1, 2] of the geoblocks weakly coupled with the surrounding plastic layers in all seismic zones of the Earth and the formation of fractures related to the strong earthquakes [1-5, 9-12, 23] and the planetary cataclysms [25, 26]) are induced by the combined nonstationary cosmic energy gravitational influence on the Earth of the planets of the Solar System, the Sun, and the Moon.

4.4. The Cosmic Energy Gravitational Genesis of the Time Periodicities of the Seismotectonic Activity Induced by the Nonstationary Cosmic Energy Gravitational Influences on the Earth of the Sun, the Moon, Venus, Jupiter, and Mars

4.4.1. The Time Periodicities of the Maximal (Instantaneous and Integral) Energy Gravitational Influences on the Earth of the Sun and the Moon, Venus, Jupiter, and Mars

(1) *The Time Periodicities of the Maximal (Instantaneous and Integral) Energy Gravitational Influences on the Earth of the Sun-Moon System.* If the configuration of the Sun and the Moon is characterized at any time moment by the maximal combined (instantaneous or integral) energy gravitational influence on the Earth, then the Sun and the Moon will have the recurrence of the same configuration after different integer numbers of circulations ($j_{\text{MOON},3}$ circulations of the Moon around the Earth and $m_{3,\text{MOON}}$ circulations of the Earth around the Sun) to satisfy the following condition [12]:

$$j_{\text{MOON},3} T_{\text{MOON}} = m_{3,\text{MOON}} T_3. \quad (173)$$

Following the known method [52], we present the ratio T_3/T_{MOON} by the following mathematical fraction:

$$\begin{aligned} \frac{T_3}{T_{\text{MOON}}} &= \frac{365.3}{29.5306} = 12 + \frac{109328}{295306} \\ &= 12 + \frac{1}{2 + \frac{1}{1 + \frac{1}{2 + \frac{1}{1 + \frac{1}{2 + \frac{1}{1 + \frac{1}{8 + \frac{458}{1204}}}}}}}} \end{aligned} \quad (174)$$

Considering the different approximation of the ratio T_3/T_{MOON} , we obtained [12] the successive approximations for the time periodicities:

$$\begin{aligned} (T_{S-\text{MOON},3})_1 &= 3 \text{ years,} \\ (T_{S-\text{MOON},3})_2 &= 8 \text{ years,} \\ (T_{S-\text{MOON},3})_3 &= 19 \text{ years,} \\ (T_{S-\text{MOON},3})_4 &= 27 \text{ years,} \\ (T_{S-\text{MOON},3})_5 &= 235 \text{ years} \end{aligned} \quad (175)$$

of recurrence of the maximal (instantaneous and integral) combined energy gravitational influences of the Sun and the Moon on the Earth in the first, second, third, fourth, and fifth approximations, respectively. We can verify that the time periodicity

$$(T_{S-\text{MOON},3})_3 = (T_{S-\text{MOON},3})_1 + (T_{S-\text{MOON},3})_2 = 11 \text{ years} \quad (176)$$

may be considered approximately as the third approximation of recurrence of the maximal (instantaneous and integral) energy gravitational influences of the Sun-Moon system on the Earth.

(2) *The Time Periodicities of the Maximal (Instantaneous and Integral) Energy Gravitational Influences on the Earth of Venus.* If the configuration of the Earth and Venus is characterized at any time moment by the maximal (instantaneous or integral) energy gravitational influence on the Earth, then the Earth and Venus will have the recurrence of the same configuration (in the frame of the real elliptical orbits of the Earth and Venus) after $k_{V,3}$ circulations of Venus around the Sun and $m_{3,V}$ circulations of the Earth around the Sun to satisfy the following condition [12]:

$$k_{V,3}T_V = m_{3,V}T_3. \quad (177)$$

Following the known method [52], we present the ratio T_3/T_V by the following mathematical fraction:

$$\begin{aligned} \frac{T_3}{T_V} &= \frac{365.3}{224.7} = 1 + \frac{1406}{2247} \\ &= 1 + \frac{1}{1 + \frac{1}{1 + \frac{1}{1 + \frac{1}{2 + \frac{1}{280}}}}} \end{aligned} \quad (178)$$

Considering the different approximation of the ratio T_3/T_V , we obtained the successive approximations for the time periodicities [12]:

$$\begin{aligned} (T_{V,3})_1 &= 3 \text{ years,} \\ (T_{V,3})_2 &= 8 \text{ years} \end{aligned} \quad (179)$$

of recurrence of the maximal (instantaneous and integral) energy gravitational influences of Venus on the Earth in the first and second approximations, respectively. We can verify that the time periodicity

$$(T_{V,3})_3 = (T_{V,3})_1 + (T_{V,3})_2 = 11 \text{ years} \quad (180)$$

may be considered as the third approximation of recurrence of the maximal (instantaneous and integral) energy gravitational influences of Venus on the Earth.

(3) *The Time Periodicities of the Maximal (Instantaneous and Integral) Energy Gravitational Influences on the Earth of Jupiter.* If the configuration of the Earth and Jupiter is characterized at any time moment by the maximal (instantaneous or integral) energy gravitational influences on the Earth, then the Earth and Jupiter will have the recurrence of the same configuration (in the frame of the real elliptical orbits of the Earth and Jupiter) after $n_{J,3}$ circulations of Jupiter around the Sun and $m_{3,J}$ circulations of the Earth around the Sun to satisfy the condition [12]

$$n_{J,3}T_J = m_{3,J}T_3. \quad (181)$$

Following the known method [52], we present the ratio T_J/T_3 by the following mathematical fraction:

$$\frac{T_J}{T_3} = \frac{4332}{365.3} = 11 + \frac{1}{1 + \frac{1}{6 + \frac{1}{12 + \frac{24}{41}}}} \quad (182)$$

Considering the different approximation of the ratio T_J/T_3 , we obtained the successive approximations for the time periodicities [12]:

$$(T_{J,3})_1 = 11 \text{ years,} \quad (183)$$

$$(T_{J,3})_2 = 12 \text{ years,} \quad (184)$$

$$(T_{J,3})_3 = 83 \text{ years} \quad (185)$$

of recurrence of the maximal (instantaneous and integral) energy gravitational influences of Jupiter on the Earth in the first, second, and third approximations, respectively.

(4) *The Time Periodicities of the Maximal (Instantaneous and Integral) Energy Gravitational Influences on the Earth of Mars.* If the configuration of the Earth and Mars is characterized at any time moment by the maximal (instantaneous or integral) energy gravitational influence on the Earth, then the Earth and Mars will have the recurrence of the same configuration after $g_{MARS,3}$ circulations of Mars around the Sun and $m_{3,MARS}$ circulations of the Earth around the Sun to satisfy the following condition [12]:

$$g_{MARS,3}T_{MARS} = m_{3,MARS}T_3. \quad (186)$$

Following the known method [52], we present the ratio T_{MARS}/T_3 by the mathematical fraction:

$$\begin{aligned} \frac{T_{MARS}}{T_3} &= \frac{687.0}{365.3} = 1 + \frac{3217}{3653} \\ &= 1 + \frac{1}{1 + \frac{1}{7 + \frac{1}{2 + \frac{1}{1 + \frac{47}{59}}}}} \end{aligned} \quad (187)$$

Considering the different approximation of the ratio T_{MARS}/T_3 , we obtained the successive approximations for the time periodicities [12]:

$$(T_{MARS,3})_1 = 15 \text{ years,}$$

$$(T_{MARS,3})_2 = 32 \text{ years,} \quad (188)$$

$$(T_{MARS,3})_3 = 47 \text{ years}$$

of recurrence of the maximal (instantaneous or integral) energy gravitational influences of Mars on the Earth in the first, second, and third approximations, respectively.

4.4.2. *Empirical Time Periodicities of the Seismotectonic Activity of the Earth.* It was pointed out [1] that the sinusoidal “saw-like” form of the graphic dependence of growth and recession of the seismotectonic activation of the separate geological structure is related to the following empirical time periodicities:

$$11 \text{ years}, \quad (189)$$

$$22 \text{ years}, \quad (190)$$

$$44 \text{ years}, \quad (191)$$

$$88 \text{ years}, \quad (192)$$

$$352 \text{ years}. \quad (193)$$

It was pointed out [2] that the strongest earthquakes in the all boundary region of the Pacific Ocean are characterized by the established tendency for recurrence on average once during the following time period [53–61]:

$$T_r = 100 \pm 50 = 50 \div 150 \text{ years}. \quad (194)$$

It was pointed out [2] also that the close values for recurrence of the strongest earthquakes were established for different seismic belts of the Earth: $90 \div 140$ years for the Caucasus [62] and 150 years for the Anatolian fault zone [63]. We present the data of the monograph [2] concerning to the recurrence of the strongest earthquakes in different regions of the seismic zone of the Pacific Ring [1, 64, 65]:

$$90 \pm 40 = 50 \div 130 \text{ years—Kamchatka}, \quad (195)$$

$$130 \pm 50 = 80 \div 180 \text{ years—Japan}, \quad (196)$$

$$110 \pm 50 = 60 \div 160 \text{ years—Peru}, \quad (197)$$

$$100 \pm 50 = 50 \div 150 \text{ years—Aleutians}. \quad (198)$$

The empirical range of the time periodicities [66] was revealed:

$$250 \div 300 \text{ years} \quad (199)$$

for recurrence of the strongest earthquakes in Turkey.

The empirical range of the time periodicities [67] was revealed (as a result of analysis of Chinese earthquakes during the time $\Delta t = 2200$ years [2] of long observations):

$$240 \div 280 \text{ years} \quad (200)$$

for recurrence of the strongest earthquakes in China.

Based on the data presented in the monograph [2] concerning the recurrence of the strongest earthquakes in different regions of the Earth, Dr. A. V. Vikulin made the valid conclusion that the seismic processes have the global nature for the Earth. In the next section we shall explain the considered empirical time periodicities by the different combinations of the cosmic energy gravitational influences on the Earth of the Sun-Moon system, Venus, Jupiter, and Mars.

4.4.3. *The Time Periodicities of the Periodic Global Seismotectonic (and Volcanic) Activity and the Global Climate Variability of the Earth Induced by the Different Combinations of the Cosmic Energy Gravitational Influences of the Sun-Moon System, Venus, Jupiter, and Mars.* We have shown [12] that the periodic recurrence (characterized by the time periodicity T_{energy}) of the maximal integral energy gravitational influences on the Earth (defined by the planetary combination of the Sun-Moon system and the arbitrary combination of the planets: Venus, Mars, and Jupiter) leads (according to the generalized differential formulations (50) applied for the Earth) to the periodic recurrence of the maximal tectonic activity (characterized by the same time periodicity $T_{\text{tec}} = T_{\text{energy}}$) of the geospheres of the Earth and each geoblock of Earth. We have shown [12] that the periodic recurrence (characterized by the time periodicity $T_{\text{tec}} = T_{\text{energy}}$) of the maximal tectonic (and volcanic) activity of the geospheres of the Earth and each geoblock of the Earth (defined by the combination of the Sun-Moon system and the arbitrary combinations of the planets: Venus, Mars, and Jupiter) leads to the periodic recurrence (characterized by the time periodicity $T_{\text{tec}} = T_{\text{energy}}$) of the maximal concentration of the atmospheric greenhouse gases owing to the periodic increase (characterized by the time periodicity $T_{\text{tec}} = T_{\text{energy}}$) of the output of the greenhouse gases related to the periodic tectonic-volcanic activation of the Earth. We have shown [12] that the periodic increase (characterized by the time periodicity $T_{\text{tec}} = T_{\text{energy}}$) of the average planetary concentration of the atmospheric greenhouse gases leads (as a consequence of the greenhouse effect produced by the gravity-induced periodic tectonic-volcanic activation accompanied by increase of the atmospheric greenhouse gases) to the periodic global planetary warming related to the increase (characterized by the time periodicity $T_{\text{tec}} = T_{\text{energy}}$) of temperature of the atmosphere-ocean system of the Earth. The periodic decrease (characterized by the time periodicity $T_{\text{tec}} = T_{\text{energy}}$) of the average planetary concentration of the atmospheric greenhouse gases leads (as a consequence of the decreased greenhouse effect) to the periodic global planetary cooling [12] related to the fall (characterized by the time periodicity $T_{\text{tec}} = T_{\text{energy}}$) of temperature of the atmosphere-ocean system of the Earth. The time periodicity T_{energy} of the periodic recurrence of the maximal integral energy gravitational influences on the Earth (defined by the combination of the Sun-Moon system and the arbitrary combinations of the planets: Venus, Mars, and Jupiter) corresponds to different two time periodicities of the Earth's climate variability [12]: the first time periodicity $T_{\text{clim1}} = T_{\text{tec}} = T_{\text{energy}}$ (related to the periodic tectonic-volcanic activity of the geospheres of the Earth induced by the cosmic nonstationary combined energy gravitational influences on the Earth of the Sun-Moon system, Venus, Mars, and Jupiter) and the second time periodicity $T_{\text{clim2}} = T_{\text{endog}} = T_{\text{energy}}/2$ related to the periodic tectonic-endogenous heating (of the geospheres of the Earth, the atmosphere, and the oceans of the Earth) induced by the periodic continuum deformation (characterized by the time periodicity T_{energy}) owing to the periodic cosmic nonstationary combined energy gravitational influences (characterized by the time periodicity T_{energy}) on the Earth of the Sun-Moon system, Venus, Mars, and Jupiter.

Using the equivalent generalized differential formulations (50), (56), and (59) of the first law of thermodynamics [12] applied for the Earth and the evaluated successive approximations for the time periodicities of the periodic recurrence of the maximal (instantaneous and integral) energy gravitational influences on the Earth of the Sun-Moon system, Venus, Jupiter, and Mars, we founded [12] the sets of the global seismotectonic and volcanic periodicities T_{tec} (of the periodic global gravity-induced seismotectonic and volcanic activities) and the global climatic periodicities T_{clim1} (of the periodic global gravity-induced climate variability and the global variability of the quantities of the fresh water and glacial ice resources):

$$\begin{aligned} T_{\text{tec}} &= T_{\text{clim1}} = T_{\text{energy}} \\ &= (T_{\text{S-MOON},3})_i^{l_o} \times (T_{\text{V},3})_j^{l_2} \times (T_{\text{MARS},3})_k^{l_4} \times (T_{\text{J},3})_n^{l_5}, \end{aligned} \quad (201)$$

determined by the multiplications of various successive time periodicities related to the different combinations of the following integer numbers: $i = 1, 2, 3, 4, 5$; $j = 1, 2$; $k = 1, 2, 3$; $n = 1, 2, 3$; $l_o = 0, 1$; $l_2 = 0, 1$; $l_4 = 0, 1$; $l_5 = 0, 1$. The global seismotectonic and volcanic periodicities T_{tec} and the global climatic periodicities T_{clim1} are related to the periodic recurrence of the maximal combined integral energy gravitational influences on the Earth induced by the different combinations of the cosmic nonstationary energy gravitational influences of the Sun-Moon system, Venus, Jupiter, and Mars.

By comparing the combined time periodicities (obtained from the expression (201)) with the empirical time periodicities of the seismotectonic activity of the Earth submitted in Section 4.4.2, we established [12] that the empirical time periodicities (of the seismotectonic activity of the Earth) may be satisfactory approximated by the expression (201) with the different combinations of the various integer numbers.

The calculated time periodicity 24 years (given by 3×8 years determined by the Sun-Moon system and Venus) is close to empirical time periodicity 22 years given by (190). The calculated average time periodicity 34.5 years (of the evaluated time range $33 \div 36 = 3 \times (11 \div 12)$ years [12, 25, 26] of the Earth's periodic seismotectonic and volcanic activity and the global climate variability determined by the combined cosmic nonstationary energy gravitational influence on the Earth of the Sun-Moon system, Venus, and Jupiter) is very close to the empirical time periodicity 35 years [68] of the seismotectonic activity of various regions of the seismic belts around the Pacific Ocean (the Pacific Ring). The calculated time periodicity 45 years (given by 3×15 years determined by the Sun-Moon system, Venus, and Mars) is close to the empirical time periodicity 44 years given by (191).

The empirical time periodicity 88 years (given by (192)) is equal to the same time periodicity 88 years (given by 8×11 years determined by the Sun-Moon system, Venus, and Jupiter). Since the ratio $88 \text{ years} / T_{\text{MARS}} = 46.786$ is close to 47, we concluded [25, 26] that the time periodicity 88 years is determined also by Mars.

The calculated time periodicities $88 \div 96$ years (given by $8 \times (11 \div 12)$ years determined by the Sun-Moon system, Venus, and Jupiter) get into the four empirical ranges of the time periodicities: $T_r = 100 \pm 50$ years (given by (194)), 90 ± 40 years (given by (195)), 130 ± 50 years (given by (196)), 110 ± 50 years (given by (197)), and 100 ± 50 years given by (198). The calculated time periodicity 96 years (given by 3×32 years determined by the Sun-Moon system, Venus, and Mars) gets into the four empirical ranges of the time periodicities: $T_r = 100 \pm 50$ years (given by (194)), 90 ± 40 years (given by (195)), 130 ± 50 years (given by (196)), 110 ± 50 years (given by (197)), and 100 ± 50 years given by (198). The calculated range $99 \div 108$ years (given by $3 \times 3 \times (11 \div 12)$ years determined by the Sun-Moon system, Venus, and Jupiter) gets into the empirical ranges of the time periodicities: $T_r = 100 \pm 50$ years given by (194), 90 ± 40 years (given by (195)), 130 ± 50 years (given by (196)), 110 ± 50 years (given by (197)), and 100 ± 50 years given by (198). The calculated time periodicity 120 years (given by 8×15 years determined by the Sun-Moon system, Venus, and Mars) gets into the four empirical ranges of the time periodicities: $T_r = 100 \pm 50$ years (given by (194)), 90 ± 40 years (given by (195)), 130 ± 50 years (given by (196)), 110 ± 50 years (given by (197)), and 100 ± 50 years given by (198). The calculated time periodicity 135 years (given by $3 \times 3 \times 15$ years determined by the Sun-Moon system, Venus, and Mars) gets into the empirical range $T_r = 100 \pm 50$ years given by (194). The calculated time periodicity 152 years (given by $152 = 19 \times 8$ determined by the Sun-Moon system and Venus) gets into the empirical range 130 ± 50 years (given by (196)) and gets into the empirical range 110 ± 50 years given by (197). The calculated range $165 \div 180$ years (given by $15 \times (11 \div 12)$ years determined by the Sun-Moon system, Mars, and Jupiter) gets into the empirical range 130 ± 50 years given by (196). The calculated time periodicity 249 years (given by $249 = 3 \times 83$ years determined by the Sun-Moon system, Venus, and Jupiter) is near the lower value of the empirical range $250 \div 300$ years (given by (199)) and gets into the empirical range $240 \div 280$ years given by (200). The calculated time periodicity 285 years (given by 19×15 years determined by the Sun-Moon system and Mars) is close to the upper value of the empirical range $240 \div 280$ years given by (200). The calculated time periodicity 285 years (given by 19×15 years determined by the Sun-Moon system and Mars) gets into the empirical range $250 \div 300$ years given by (199). The calculated range of the time periodicities $264 \div 288$ years (given by $3 \times 8 \times (11 \div 12)$ years determined by the Sun-Moon system, Venus, and Jupiter) gets approximately into the empirical range $240 \div 280$ years given by (200). The calculated time periodicity 352 years (given by 32×11 years determined by the Sun-Moon system, Mars, and Jupiter) is equal to the empirical time periodicity 352 years given by (193).

4.5. Cosmic Energy Gravitational Genesis of the Chinese 2008 Earthquakes. It was forecasted in advance the single Chinese Haicheng 1975 earthquake using the warning omens. The nearest (to the Haicheng 1975 earthquake) Chinese Luhuo 1973 and Tang Shan 1976 earthquakes were not forecasted using the warning omens. The modern Chinese Bachu 2003,

TABLE 1: The time periods T_1 (given in years) of recurrence of the strongest Japanese earthquakes [2] and the obtained [12, 25, 26] corresponding time periodicities (given in years) determined by the following cosmic combinations.

Region	Magnitude M of the strongest Japanese earthquakes	Date of the strongest Japanese earthquakes	The time periods T_1 (given in years) of recurrence of the strongest Japanese earthquakes	Corresponding time periodicities (given in years) determined by the following cosmic combination
Tokyo region	7.9	1.01.1605		
	8.2	31.12.1703	98	$88 \div 96 = 8 \times (11 \div 12)$ —Sun-Moon-Venus-Jupiter-Mars $96 = 3 \times 32$ —Sun-Moon-Venus-Mars
	8.2	1.09.1923	220	$209 \div 228 = 19 \times (11 \div 12)$ —Sun-Moon-Jupiter
Southwest from Tokyo	8.6	20.09.1498		
	7.9	31.01.1605	107	$96 = 3 \times 32$ —Sun-Moon-Venus-Mars $120 = 8 \times 15$ —Sun-Moon-Venus-Mars
	8.4	28.10.1707	102	$96 = 3 \times 32$ —Sun-Moon-Venus-Mars $120 = 8 \times 15$ —Sun-Moon-Venus-Mars
	8.4	23.12.1854	147	$152 = 19 \times 8$ —Sun-Moon-Venus
	8.0	7.12.1944	90	$88 \div 96 = 8 \times (11 \div 12)$ —Sun-Moon-Venus-Jupiter

Ruichang 2005, and Yanjin 2006 earthquakes were not forecasted also using the warning omens. Using the results of previous sections and the presented set of the Chinese earthquakes (Luhuo 1973, Haicheng 1975, and Tang Shan 1976; Bachu 2003, Ruichang 2005, and Yanjin 2006), we predicted (Simonenko, 2007) the nearest (to the Yanjin 2006 earthquake) Chinese 2008 earthquakes by considering the following arguments.

The difference equal to 3 years between the times of the Luhuo 1973 and Tang Shan 1976 earthquakes means that the Tang Shan 1976 earthquake may be induced by the integral energy gravitational influence of the Sun-Moon system or Venus (characterized by the same time periodicity 3 years of recurrence of the maximal integral energy gravitational influence on the Earth in the first approximation) or by the combined integral energy gravitational influence on the Earth of the Sun-Moon system and Venus. If the Tang Shan 1976 earthquake was induced by the integral energy gravitational influence of the Sun-Moon system then the Bachu 2003 earthquake can be explained by the recurrence of the integral energy gravitational influence of the Sun-Moon system (characterized by the time periodicity 27 years of recurrence of the maximal integral energy gravitational influence on the Earth in the fourth approximation):

$$1976 + 27 = 2003\text{—Bachu 2003 earthquake.} \quad (202)$$

The Tang Shan 1976 earthquake can be induced by the participation of the integral energy gravitational influence of Venus (characterized by the time periodicity 8 years of recurrence of the maximal integral energy gravitational influence on the Earth in the second approximation) since it is easily to explain the Ruichang 2005 earthquake by the recurrence of the maximal integral energy gravitational influence of Venus on the Earth. Considering [12]

$$1973 + i_V 8 = 2005, \quad (203)$$

which should be solved for integer number i_V , we obtained [12] the integer number $i_V = 4$ confirming the Venusian genesis of the Tang Shan 1976 and the Ruichang 2005 earthquakes:

$$1973 + 4 \times 8 = 2005\text{—Ruichang 2005 earthquake.} \quad (204)$$

Taking into account the Chinese Yanjin 2006 earthquake (explained [12] by the sum $1973 + 3 \times 11$) and considering the Venusian genesis of the Tang Shan 1976 earthquake, we obtained the time of the Chinese 2008 earthquake from the following inequality [12]:

$$0 < 1976 + j_V 8 - 2006 < (T_{V,3})_1 = 3, \quad (205)$$

which should be solved for integer number j_V . The obtained solution $j_V = 4$ founded the time of the several (owing to the participation of Mars characterized by the time periodicity 32 years of recurrence of the maximal integral energy gravitational influence on the Earth in the second approximation) distinct Chinese 2008 earthquakes [12]:

$$1976 + 4 \times 8 = 2008. \quad (206)$$

The occurrence of two large earthquakes in 2008 in the areas surrounding Yutian (Xinjiang) and Wenchuan (Sichuan) confirmed the proposed [12, 25, 26] cosmic energy gravitational genesis of the strong Chinese earthquakes.

4.6. Cosmic Energy Gravitational Genesis of the Strongest Japanese Earthquakes near the Tokyo Region. We have shown [12, 25, 26] the cosmic energy gravitational genesis of the strongest ($M \geq 7.9$) Japanese earthquakes near Tokyo region and southwest from Tokyo. To confirm the proposed cosmic energy gravitational genesis of the strongest ($M \geq 7.9$) Japanese earthquakes, we present in Table 1 the time periods T_1 (given in years) of recurrence of the strongest Japanese earthquakes [2] and the obtained [12, 25, 26] corresponding time periodicities (given in years) determined by the following planetary combinations.

Taking into account the time periodicity 83 years (given by (185)) and the year 1927 AD of Jupiter's opposition with the Earth, respectively, and the time periodicity 88 years = 8×11 years (determined by the Sun-Moon system, Venus, Jupiter, and Mars) and the year 1923 AD of the last strongest Japanese earthquake in the Tokyo region, we predicted [25, 26] "the time range

$$2010 \div 2011 \text{ AD } (1927 + 83 \div 1923 + 88) \quad (207)$$

of the next sufficiently strong Japanese earthquake near the Tokyo region".

The powerful 6.6-magnitude (on Richter scale) Japanese earthquake (that occurred on 14 March, 2010) near Tokyo (with the epicenter in the Fukushima Prefecture) gets into the predicted time range 2010 \div 2011 AD [25, 26]. The powerful 6.8-magnitude (on Richter scale) Japanese earthquake (that occurred on 11 March, 2011) near Tokyo gets also into the predicted time range 2010 \div 2011 AD [25, 26]. The occurrence of the strong Japanese earthquakes on 14 March, 2010, and on 11 March, 2011, confirmed the previous predictions [1, 25, 26] and the proposed cosmic energy gravitational genesis [12, 25, 26] of the strongest Japanese earthquakes.

5. Summary of Main Results and Conclusion

We have developed in this article the fundamentals of the thermohydrogravodynamic theory intended for the long-term deterministic predictions of the strong earthquakes. The deterministic thermohydrogravodynamic theory is based on the established generalized formulation [11, 12] of the first law of thermodynamics for moving rotating deforming compressible heat-conducting stratified macroscopic continuum region τ subjected to the nonstationary Newtonian gravitational field.

Using the classical continuum-mechanical theoretical approach [29, 33], we have presented in Section 2.1 the generalized expression [24, 31] for the macroscopic kinetic energy of a small continuum region. The generalized expression [24, 31] is the generalization of the classical expression [28, 29] in classical nonequilibrium thermodynamics for the macroscopic kinetic energy per unit mass of a small macroscopic continuum region (considered in a stratified three-dimensional shear flow) by taking into account the irreversible shear component of the hydrodynamic velocity field related to the rate of strain tensor e_{ij} . The macroscopic kinetic energy (of the small macroscopic continuum region) is presented as a sum of the macroscopic translational kinetic energy and three Galilean invariants: the classical macroscopic internal rotational kinetic energy [28, 29], the established macroscopic internal shear kinetic energy [24, 31], and the established macroscopic internal kinetic energy of shear-rotational coupling [24, 31] with a small correction. The generalized formula (20) for the macroscopic kinetic energy per unit mass ε_k and its particular form (31) for homogeneous continuum regions of spherical and cubical shapes generalize the classical de Groot and Mazur expression (2) in classical nonequilibrium thermodynamics [28, 29] by taking into account the established [24, 31] macroscopic internal shear

kinetic energy per unit mass ε_s , which expresses the kinetic energy of irreversible dissipative shear motion, and also the established [24, 31] macroscopic internal kinetic energy of shear-rotational coupling per unit mass $\varepsilon_{s,r}^{\text{coup}}$, which expresses the kinetic energy of local coupling between irreversible dissipative shear and reversible rigid-like rotational macroscopic fluid motions. The generalized expression (20) confirms the postulate [35] that the velocity shear ($e_{ij} \neq 0$) represents an additional energy source.

Based on the postulates of thermodynamics [27, 28], continuum mechanics [29, 30] and hydrodynamics [33, 38], we have presented in Section 2.2 the equivalent generalized differential formulations (50), (56), and (59) (given for the Galilean frame of reference) of the first law of thermodynamics [11, 12] for nonequilibrium shear-rotational states of the deformed finite one-component individual continuum region (characterized by the symmetric stress tensor \mathbf{T}) moving in the nonstationary Newtonian gravitational field. The equivalent generalized differential formulations (50), (56), and (59) are valid for moving rotating deforming compressible heat-conducting stratified macroscopic continuum region τ subjected to the nonstationary Newtonian gravity. The generalized differential formulation (56)

$$dU_\tau + dK_\tau + d\pi_\tau = \delta Q + \delta A_{\text{np},\partial\tau} + dG \quad (208)$$

generalizes the classical [27, 32] formulations (39) and (40):

$$dU = \delta Q - pdV, \quad (d\varepsilon \equiv dU \equiv dU_\tau, -\delta W = -pdV) \quad (209)$$

by taking into account (along with the classical infinitesimal change of heat δQ and the classical infinitesimal change of the internal energy $dU_\tau \equiv dU$) the infinitesimal increment of the macroscopic kinetic energy dK_τ , the infinitesimal increment of the gravitational potential energy $d\pi_\tau$, the generalized expression [11, 12, 24] for the infinitesimal work $\delta A_{\text{np},\partial\tau}$ done on the continuum region τ by the surroundings of τ , and the additional [11, 12] infinitesimal amount dG of energy added (or lost) as the result of the Newtonian nonstationary energy gravitational influence on the continuum region τ during the infinitesimal time interval dt . The presented (in Section 2.3) generalized expression [11, 12] for infinitesimal work $\delta A_{\text{np},\partial\tau}$ (done on the continuum region τ by the surroundings of τ) generalizes the classical [27] expression $\delta A_{\text{np},\partial\tau} = -\delta W = -pdV$ by taking into account (for Newtonian continuum) the infinitesimal work δA_c (given by expression (68)) of the acoustic forces and the infinitesimal work δA_s (given by expression (69)) of the viscous forces acting during the infinitesimal time interval dt on the boundary surface $\partial\tau$ of the individual continuum region τ .

Based on the equivalent generalized differential formulations (50), (56), and (59) of the first law of thermodynamics and the obtained expression (74) for the gravitational energy power $W_{\text{gr}}(\tau)$, we have presented in Section 2.4 the established [11, 12] gravitational energy mechanism of the gravitational energy supply into the continuum region τ owing to the local time increase of the potential ψ of the gravitational field inside the continuum region τ subjected to the nonstationary Newtonian gravitational field. The revealed gravitational

mechanism [11, 12] of the gravitational energy supply into the continuum region τ is consistent with the empirical findings [1, 3–5, 9, 10] related to the anomalous variations of the gravitational field before the strong earthquakes. Based on the equivalent generalized differential formulations (50), (56), and (59) of the first law of thermodynamics, we have presented the evidence [12, 25] about the significant increase of the energy flux $\delta F_{vis,c}$ (given by expression (76)) of the geoaoustic energy from the focal region τ before the earthquake in a good agreement with the results of the detailed experimental studies [43].

We have presented in Section 3 the evidence [12, 25] of the cosmic energy gravitational genesis of earthquakes. Using the evolution equation (73) (deduced from the generalized differential formulation (50) of the first law of thermodynamics) of the total mechanical energy of the macroscopic continuum region τ (of the compressible viscous Newtonian continuum), we have presented in Section 3.1 the thermodynamic foundation of the classical deformational (shear) model [1] of the earthquake focal region for the quasi-uniform medium of the Earth's crust characterized by practically constant viscosity. Based on the generalized differential formulation (50) of the first law of thermodynamics for the macroscopic continuum region τ , we have presented in Section 3.1 the generalized thermohydrogravodynamic shear-rotational model [11, 12] of the earthquake focal region by taking into account the classical macroscopic rotational kinetic energy [28, 29], the macroscopic nonequilibrium kinetic energies [24, 31], and the external cosmic energy gravitational influences on the focal region of the preparing earthquakes. We have presented in Section 3.2 the evidence [11, 12] of the physical adequacy of the rotational model [2] of the earthquake focal region for the seismic zone of the Pacific Ring.

We have presented in Section 4 the fundamentals of the cosmic geophysics [12, 25, 26]. We have presented in Section 4.1 the consideration of the energy gravitational influences on the Earth of the inner planets and the outer planets of the Solar System. We have presented in Section 4.1.1 the relation (96) for the energy gravitational influences (on the Earth) of the inner and the outer planets in the second approximation of the elliptical orbits of the planets of the Solar System. We have presented in Section 4.1.2 the evaluation of the relative maximal planetary instantaneous energy gravitational influences on the Earth in the approximation of the circular orbits of the planets of the Solar System. Considering the maximal positive value $\max(\partial/\partial t)\psi_{31}(C_3, \text{int})$ (of the partial derivative $(\partial/\partial t)\psi_{31}(C_3, \text{int})$ of the gravitational potential $\psi_{31}(C_3, \text{int})$ created by Mercury at the mass center C_3 of the Earth) as a scale of the instantaneous energy gravitational influence of the planets of the Solar System on the Earth (in the considered first approximation of the circular orbits of the planets), we have presented in Section 4.1.2 the following numerical sequence of the nondimensional relative maximal powers of the planetary energy gravitational influences (on the unit mass of the Earth at the mass center C_3 of the Earth): $f(2, C_3) = 37.69807434$ (for Venus), $f(5, C_3) = 7.41055774$ (for Jupiter), $f(1, C_3) = 1$ (for Mercury), $f(4, C_3) = 0.67441034$ (for Mars), $f(6, C_3) = 0.24601009$ (for Saturn), $f(7, C_3) = 0.00319056$ (for Uranus),

$f(8, C_3) = 0.00077565$ (for Neptune), and $f(9, C_3) = 3.4813 \cdot 10^{-8}$ (for Pluto). Considering the maximal positive value $\max(\partial/\partial t)\psi_{3M}(D_3, \text{int})$ (of the partial derivative $(\partial/\partial t)\psi_{3M}(D_3, \text{int})$ of the gravitational potential $\psi_{3M}(D_3, \text{int})$ created by Mercury at the surface point D_3 of the Earth) as a scale of the energy gravitational influence of the planets of the Solar System on the Earth (in the considered first approximation of the circular orbits of the planets), we have presented in Section 4.1.2 the following numerical sequence (corrected slightly the previous numerical values [12]) of the nondimensional relative maximal powers of the planetary energy gravitational influences (on the unit mass of the Earth at the surface point D_3 of the Earth): $f(2, D_3) = 37.70428085$ (for Venus), $f(5, D_3) = 7.40926122$ (for Jupiter), $f(1, D_3) = 1$ (for Mercury), $f(4, D_3) = 0.67420160$ (for Mars), $f(6, D_3) = 0.24596865$ (for Saturn), $f(7, D_3) = 0.00319004$ (for Uranus), $f(8, D_3) = 0.00077552$ (for Neptune), and $f(9, D_3) = 3.4807 \cdot 10^{-8}$ (for Pluto). We have recognized [25, 26] that the revealed small difference of the combined planetary maximal energy gravitational influences at the surface point D_3 and at the mass center C_3 of the Earth can explain the following related geophysical phenomena: the small oscillatory motion of the rigid kernel of the Earth relative to the fluid kernel of the Earth; the small oscillation of the Earth's pole (i.e., the Chandler's wobble of the Earth's pole); the small oscillations of the boundary of the Pacific Ocean (i.e., the seismic zone of the Pacific Ring); the oscillations, rotations, and deformations of the geoblocks weakly coupled with the surrounding plastic layers in all seismic zones of the Earth and the formation of fractures related to the strong earthquakes and the planetary cataclysms. We have presented in Section 4.1.3 the evaluation of the relative maximal planetary integral energy gravitational influences on the Earth in the approximation of the circular orbits of the planets of the Solar System. Considering the maximal positive integral energy gravitational influence $\max_t \Delta_g E_3(\tau_1, 0, 0, t, 0)$ of Mercury (given by the expression (136)) on the Earth as a scale of the integral energy gravitational influence of the planets of the Solar System on the Earth (in the considered first approximation of the circular orbits of the planets), we have presented in Section 4.1.3 the following order of signification (with respect to the established planetary maximal integral energy gravitational influences on the Earth) of the planets of the Solar System: Venus ($s(2) = 89.6409$), Jupiter ($s(5) = 31.319$), Mars ($s(4) = 2.6396$), Saturn ($s(6) = 1.036$), Mercury ($s(1) = 1$), Uranus ($s(7) = 0.0133$), Neptune ($s(8) = 0.003229$), and Pluto ($s(9) = 1.4495 \cdot 10^{-7}$), which gives the predominant combined planetary integral energy gravitational influence on the Earth of Venus and Jupiter.

We have presented in Section 4.2 the consideration of the lunar energy gravitational influences on the Earth. We have presented in Section 4.2.1 the evaluation of the relative maximal instantaneous energy gravitational influence of the Moon on the Earth in the second approximation of the elliptical orbits of the Earth and the Moon around the combined mass center $C_{3,MOON}$ of the Earth and the Moon. Considering the maximal positive value $\max(\partial/\partial t)\psi_{31}(C_3, \text{int})$ (of the partial derivative $(\partial/\partial t)\psi_{31}(C_3, \text{int})$ of the gravitational potential

$\psi_{31}(C_3, \text{int})$ created by Mercury at the mass center C_3 of the Earth) as a scale for evaluation of the maximal instantaneous energy gravitational influence of the Moon on the Earth, we have presented the nondimensional numerical value $f_{\text{MOONM}}(C_3, \text{second approximation}) = 19.44083$, which means that the power of the maximal energy gravitational influence of the Moon (on the unit mass of the Earth at the mass center C_3 of the Earth) is 19.44083 times larger than the maximal power of the energy gravitational influence (on the unit mass at the mass center C_3 of the Earth) of Mercury moving around the mass center O of the Sun along the hypothetical circular orbit. Taking into account the calculated [25, 26] nondimensional maximal instantaneous energy gravitational influences on the unit mass of the Earth at the mass center C_3 of the Earth, we established the following order of significance (with respect to the established planetary and lunar maximal instantaneous energy gravitational influences on the Earth) of the Moon and the planets of the Solar System: Venus, the Moon, Jupiter, Mercury, Mars, Saturn, Uranus, Neptune, and Pluto, which reveals the main instantaneous energy gravitational influences on the Earth of Venus, the Moon, Jupiter, Mercury, and Mars determining (in collection) the main combined instantaneous energy gravitational influence on the Earth (not taking into account the instantaneous energy gravitational influences of the Sun and our Galaxy).

We have presented in Section 4.2.2 the evaluation of the maximal integral energy gravitational influence of the Moon on the Earth in the approximation of the elliptical orbits of the Earth and the Moon around the combined mass center $C_{3,\text{MOON}}$. Considering the maximal positive integral energy gravitational influence $\max_t \Delta_g E_3(\tau_1, 0, 0, t, 0)$ of Mercury (given by the expression (136)) on the Earth as a scale for evaluation of the maximal integral energy gravitational influence of the Moon on the Earth (in the considered first approximation of the circular orbits of the planets and in the approximation of the elliptical orbits of the Earth and the Moon around the combined mass center $C_{3,\text{MOON}}$), we established that the maximal positive integral energy gravitational influence of the Moon on the Earth is $s(\text{Moon, second approximation}) = 13.0693$ times larger than the maximal positive integral energy gravitational influence of Mercury on the Earth. Considering the aspect of the cosmic gravitational preparation of the strong earthquakes, we established the Venusian ($s(2) = 89.6409$ [12]), Jupiter's ($s(5) = 31.319$ [12]), and the Moon's ($s(\text{Moon, second approximation}) = 13.0693$ [25, 26]) energy gravitational predominance in supplying of the cosmic planetary and lunar gravitational energy to the focal region of the preparing earthquakes. By considering the energy gravitational influence on the Earth's macroscopic continuum region τ of Venus, we have presented in Section 4.3.1 the evidence (based on the equivalent generalized differential formulations (50), (56), and (59) of the first law of thermodynamics used for the macroscopic continuum region τ considered as the focal region of the preparing earthquake) of the real cosmic energy gravitational genesis of preparation of earthquakes. Using the expression (167) for the maximal positive integral energy gravitational influence $E_g(\tau_2, D_3, m_\tau)$ of Venus on the macroscopic continuum region τ of mass m_τ near the surface point D_3 of the Earth, we have presented in Section 4.3.1

the evidence [12] that the regular changes of the rotational regime of the Earth [2] are related to the regular discharges of the accumulated potential energy (in the focal region of earthquakes) supplying of the cosmic energy gravitational influences of the planets of the Solar System, the Sun, and the Moon. We have presented in Section 4.3.2 the evidence of the cosmic energy gravitational genesis of triggering of the preparing earthquakes. By considering the calculated relative average values $e(i)$ of the integral energy gravitational influences (corresponding to the time duration $T_{\text{MOON}}/2$ of the maximal integral energy gravitational influence of the Moon on the Earth) on the Earth of the planets of the Solar System and the Moon [12, 25]: $s(\text{Moon, second approximation}) = 13.0693$ (for the Moon), $e(2) = 4.5342$ (for Venus), $e(5) = 2.3182$ (for Jupiter), $e(1) = 0.2547$ (for Mercury), $e(4) = 0.0999$ (for Mars), $e(6) = 0.0809$ (for Saturn), $e(7) = 0.001066$ (for Uranus), $e(8) = 0.0002594$ (for Neptune), and $e(9) = 1.1671 \cdot 10^{-8}$ (for Pluto), we established [25] the exceptional predominant significance of the cosmic energy gravitational influence of the Moon (along with the established [12] minor significance of Venus, Jupiter, and Mercury) as the predominant cosmic trigger mechanism of discharge (on the final stage of the preparation of the earthquakes) of the accumulated potential energy (in the focal region of earthquakes) supplying of the cosmic gravitational energy influences of the planets of the Solar System and the Moon. The considered results of Sections 4.1, 4.2, and 4.3 have demonstrated the cosmic energy gravitational genesis (related to the combined nonstationary cosmic energy gravitational influence of the planets of the Solar System, the Sun, and the Moon) of the following correlated geophysical phenomena: the small oscillations [2] of the boundary of the Pacific Ocean (i.e., the seismic zone of the Pacific Ring); the small oscillatory motion of the rigid kernel of the Earth relative to the fluid kernel of the Earth [51]; the Chandler's wobble of the Earth's pole; the oscillations [42], rotations, and deformations [1, 2] of the geoblocks weakly coupled with the surrounding plastic layers in all seismic zones of the Earth; the formation of the planetary fractures related to the strong earthquakes [1, 3–5, 9, 10, 23] and the planetary cataclysms [25, 26].

We have demonstrated in Section 4.4 the cosmic energy gravitational genesis [12] of the time periodicities of the global seismotectonic activity of the Earth induced by the nonstationary cosmic energy gravitational influences on the Earth of the Sun-Moon system, Venus, Jupiter, and Mars. We have presented in Section 4.4.1 the time periodicities [12] of the maximal (instantaneous and integral) energy gravitational influences on the Earth of the Sun and the Moon, Venus, Jupiter, and Mars. We have presented in Section 4.4.1 (1) the successive approximations of the following time periodicities: $(T_{S-\text{MOON},3})_1 = 3$ years, $(T_{S-\text{MOON},3})_2 = 8$ years, $(T_{S-\text{MOON},3})_3 = 11$ years and $(T_{S-\text{MOON},3})_3 = 19$ years, $(T_{S-\text{MOON},3})_4 = 27$ years, and $(T_{S-\text{MOON},3})_5 = 235$ years of recurrence of the maximal (instantaneous and integral) combined energy gravitational influences of the Sun-Moon system on the Earth in the first, second, third, fourth, and fifth approximations, respectively. We have presented in Section 4.4.1 (2) the successive approximations of the following time periodicities: $(T_{V,3})_1 = 3$ years, $(T_{V,3})_2 = 8$ years, and

$(T_{V,3})_3 = 11$ years of recurrence of the maximal (instantaneous and integral) energy gravitational influences of Venus on the Earth in the first, second, and third approximations, respectively. We have presented in Section 4.4.1 (3) the successive approximations of the following time periodicities: $(T_{J,3})_1 = 11$ years, $(T_{J,3})_2 = 12$ years, and $(T_{J,3})_3 = 83$ years of recurrence of the maximal (instantaneous and integral) energy gravitational influences of Jupiter on the Earth in the first, second, and third approximations, respectively. We have presented in Section 4.4.1 (4) the successive approximations of the following time periodicities: $(T_{MARS,3})_1 = 15$ years, $(T_{MARS,3})_2 = 32$ years, and $(T_{MARS,3})_3 = 47$ years of recurrence of the maximal (instantaneous or integral) energy gravitational influences of Mars on the Earth in the first, second, and third approximations, respectively. We have presented in Section 4.4.2 the empirical time periodicities [1, 2, 53–67] of the seismotectonic activity for different regions of the Earth.

Based on the equivalent generalized differential formulations (50), (56), and (59) of the first law of thermodynamics [12, 25] used for the Earth and using the evaluated (in Section 4.4.1) successive approximations for the time periodicities of the periodic recurrence of the maximal energy gravitational influences on the Earth of the Sun-Moon system, Venus, Mars, and Jupiter, we have presented in Section 4.4.3 the following sets of the global seismotectonic and volcanic periodicities T_{tec} and the global climatic periodicities T_{clim1} of the Earth:

$$\begin{aligned} T_{tec} &= T_{clim1} = T_{energy} \\ &= (T_{S-MOON,3})_i^{l_0} \times (T_{V,3})_j^{l_2} \times (T_{MARS,3})_k^{l_4} \times (T_{J,3})_n^{l_5}, \end{aligned} \quad (210)$$

determined by the successive global periodicities T_{energy} (defined by the multiplications of various successive time periodicities related to the different combinations of the following integer numbers: $i = 1, 2, 3, 4, 5$; $j = 1, 2$; $k = 1, 2, 3$; $n = 1, 2, 3$; $l_0 = 0, 1$; $l_2 = 0, 1$; $l_4 = 0, 1$; $l_5 = 0, 1$) of recurrence of the maximal combined energy gravitational influences on the Earth of the different combined combinations of the cosmic nonstationary energy gravitational influences on the Earth of the Sun-Moon system, Venus, Mars, and Jupiter. We have shown that the considered empirical time periodicities [1, 2, 53–67] of the seismotectonic activity may be satisfactory approximated by the different combined combinations of the cosmic nonstationary energy gravitational influences on the Earth of the Sun-Moon system, Venus, Mars, and Jupiter.

We have presented in Section 4.5 the evidence of the cosmic energy gravitational genesis of the Chinese 2008 earthquakes. Using the established time periodicities [12] of the maximal (instantaneous and integral) energy gravitational influences on the Earth of the Sun-Moon system, Venus, Mars, and Jupiter, and considering the presented set of the Chinese earthquakes (Luhuo 1973, Haicheng 1975, and Tang Shan 1976; Bachu 2003, Ruichang 2005, and Yanjin 2006), we predicted [12] the nearest year (2008) of the next Chinese 2008 earthquakes. The proposed cosmic energy gravitational genesis of the predicted [12] strong Chinese 2008 earthquakes

was confirmed by the occurrence of two large earthquakes in 2008 in the areas surrounding Yutian (Xinjiang) and Wenchuan (Sichuan). The proposed cosmic energy gravitational genesis of the predicted [12] strong Chinese 2008 earthquakes was also confirmed by the noticeable gravity variations [9] (derived from regional gravity monitoring data in China from 1998 to 2005) before the occurrence of two large earthquakes in 2008 in the areas surrounding Yutian (Xinjiang) and Wenchuan (Sichuan). According to the equivalent generalized differential formulations (50), (56), and (59) of the first law of thermodynamics [12, 25] and the presented results of Section 2.4, the noticeable gravity variations (mentioned in articles [1, 3–5, 9, 13]) are related to supply of the gravitational energy into the focal region before the occurrence of earthquake. According to the equivalent generalized differential formulations (50), (56), and (59) of the first law of thermodynamics [12, 25], the noticeable gravity variations in the focal region is the necessary (but not sufficient) condition for preparation of earthquake. A recent research [10] by Zhan and his colleagues confirmed this conclusion demonstrating that significant gravity changes were observed before all nine large earthquakes in China from 2001 to 2008. It is clear that the presented equivalent generalized differential formulations (50), (56), and (59) of the first law of thermodynamics [12, 25] can give the mathematical basis to “remove the subjective nature in the determination of the timeframe of a forecasted earthquake” [9]. This conclusion is in agreement with the demonstrated (in Section 4.6) cosmic energy gravitational genesis of the strongest Japanese earthquakes near the Tokyo region. “The time range 2010 ÷ 2011 AD of the next sufficiently strong Japanese earthquake near the Tokyo region” [25, 26] was predicted based on the established time periodicities $(T_{J,3})_3 = 83$ years (determined by Jupiter) and 88 years = 8×11 years (determined by the Sun-Moon system, Venus, Jupiter, and Mars) and taking into account the year 1923 AD of the strongest Japanese earthquake near the Tokyo region. The proposed [12, 25, 26] cosmic energy gravitational genesis of the strongest Japanese earthquakes was confirmed by occurrence of the strong Japanese earthquakes on 14 March, 2010, and on 11 March, 2011.

The time periodicity 88 years (of the global seismotectonic and volcanic activity and the global climate variability related to recurrence of the maximal combined energy gravitational influences on the Earth of the Sun-Moon system, Venus, Mars, and Jupiter [12, 25, 26]) is in good agreement with the estimated (based on the spectral Fourier analysis) climatic time periodicity 88 years [69] obtained from the studies of sediments from Siberian and Mongolian lakes. This good agreement (of the independent experimental seismotectonic [1] and the climatic [69] periodicity 88 years with the global seismotectonic, volcanic, and climatic periodicity 88 years [12, 25, 26]) is the additional confirmation of the validity of the thermohydrogravodynamic theory [11, 12, 25, 26] of the seismotectonic, volcanic, and climatic activity of the Earth.

The founded generalized differential formulations (50), (56), and (59) of the first law of thermodynamics [12, 25] can be used as the thermohydrogravodynamic basis for rapid development of the urgent technologies of the long-term deterministic predictions of the strong earthquakes in order

to sustain the stable evolutionary development, the survival, greatness, and cosmic dignity of the humankind in the present and forthcoming epochs of the critical surrounding cosmic, seismotectonic, volcanic, and climatic conditions of the human existence on the Earth.

Acknowledgments

The author thanks the Academic Editor Dr. Umberta Tinivella with gratitude for the editorial corrections to improve the final text of the article. The author thanks a reviewer for bringing to the author's attention the additional interesting information, which was used with gratitude for the correction of the article. The author thanks Prof. V. A. Abramov and Dr. Sergey V. Smirnov for helpful discussions and Dr. Yuri Panarin and Amrtatjuti V. Sereda for the editorship of the first version of the article in English.

References

- [1] V. A. Abramov, "Forecasting of disastrous earthquakes," *Proceedings of the Vladivostok Professor's Club*, no. 1, pp. 64–77, 1997 (Russian).
- [2] A. V. Vikulin, *Physics of Wave Seismic Process*, The Kamchatsky State Pedagogical University Press, Petropavlovsk-Kamchatsky, Russia, 2003, In Russian.
- [3] B. F. Chao and R. S. Gross, "Changes in the Earth's rotation and low-degree gravitational field induced by earthquakes," *Geophysical Journal of the Royal Astronomical Society*, vol. 91, no. 3, pp. 569–596, 1987.
- [4] B. F. Chao and R. S. Gross, "Changes in the Earth's rotational energy induced by earthquakes," *Geophysical Journal International*, vol. 122, no. 3, pp. 776–783, 1995.
- [5] B. Fong Chao, R. S. Gross, and D.-N. Dong, "Changes in global gravitational energy induced by earthquakes," *Geophysical Journal International*, vol. 122, no. 3, pp. 784–789, 1995.
- [6] F. Machado, "Geological evidence for a pulsating gravitation," *Nature*, vol. 214, no. 5095, pp. 1317–1318, 1967.
- [7] R. H. Rapp, "Gravitational potential of the Earth determined from a combination of satellite, observed, and model anomalies," *Journal of Geophysical Research*, vol. 73, no. 20, pp. 6555–6562, 1968.
- [8] V. Sgrigna and L. Conti, "A deterministic approach to earthquake prediction," *International Journal of Geophysics*, vol. 2012, Article ID 406278, 20 pages, 2012.
- [9] Y. Zhu and F. B. Zhan, "Medium-term earthquake forecast using gravity monitoring data: evidence from the Yutian and Wenchuan earthquakes in China," *International Journal of Geophysics*, vol. 2012, Article ID 307517, 6 pages, 2012.
- [10] F. B. Zhan, Y. Zhu, J. Ning, J. Zhou, W. Liang, and Y. Xu, "Gravity changes before large earthquakes in China: 1998–2005," *Geo-Spatial Information Science*, vol. 14, no. 1, pp. 1–9, 2011.
- [11] S. V. Simonenko, "Statistical thermohydrodynamics of irreversible strike-slip-rotational processes," in *Rotational Processes in Geology and Physics*, pp. 225–251, KomKniga, Moscow, Russia, 2007, In Russian.
- [12] S. V. Simonenko, *Thermohydrogravidynamics of the Solar System*, Institute of Technology and Business Press, Nakhodka, Russia, 2007.
- [13] S. I. Zubkov, *Catalogue of Earthquakes' Precursors. Gravitational Precursors*, Moscow, Russia, 1988.
- [14] T. Matuzawa, "On the possibility of gravitational waves in soil and allied problems," *Japanese Journal of Astronomy and Geophysics*, vol. 3, pp. 161–177, 1925.
- [15] C. Lomnitz and H. Castanos, "Earthquake hazard in the valley of Mexico: entropy, structure, complexity," in *Earthquake Source Asymmetry, Structural Media and Rotation Effects*, pp. 347–364, Springer, New York, NY, USA, 2006.
- [16] C. Lomnitz, "Some observations of gravity waves in the 1960 Chile earthquake," *Bulletin of the Seismological Society of America*, vol. 59, no. 2, pp. 669–670, 1970.
- [17] C. Lomnitz, "Mexico 1985: the case for gravity waves," *Geophysical Journal International*, vol. 102, no. 3, pp. 569–572, 1990.
- [18] C. F. Richter, *Elementary Seismology*, W.H. Freeman, San Francisco, Calif, USA, 1958.
- [19] A. V. Vikulin, "Geodynamics and gravitation (cosmic factors)," in *Proceedings of the 3rd Tectonophysic Conference on Thectonophysic and Pressing Questions of the Earth's Sciences*, vol. 1, pp. 57–61, UIPE, RAS, Moscow, Russia, 2012, In Russian.
- [20] A. V. Vikulin, "Geodynamics and gravitation," in *Proceedings of the All-Russian Conference and of Youth School on Modern Geodynamics: Modern Geodynamics of Central Asia and Dangerous Natural Processes: The Results of Investigation Obtained on the Quantitative Basis*, pp. 26–28, IEC, SB RAS, Irkutsk, Russia, 2012, In Russian.
- [21] A. V. Vikulin, *Seismicity, Volcanism and Geodynamics. The Selected Works*, The Kamchatsky State University Press, Petropavlovsk-Kamchatsky, Russia, 2011, In Russian.
- [22] A. V. Vikulin, "Angular momentum's geodynamics, gravitational waves and the superfluidity of the geological environment," in *Proceedings on Seismicity, Volcanism and Geodynamics*, pp. 384–394, The Kamchatsky State University Press, Petropavlovsk-Kamchatsky, Russia, 2011, In Russian.
- [23] R. Console, K. Yamaoka, and J. Zhuang, "Implementation of short- and medium-term earthquake forecasts," *International Journal of Geophysics*, vol. 2012, Article ID 217923, 2 pages, 2012.
- [24] S. V. Simonenko, *Non-Equilibrium Statistical Thermohydrodynamics of Turbulence*, Nauka, Moscow, Russia, 2006.
- [25] S. V. Simonenko, *Fundamentals of the Thermohydrogravidynamic Theory of Cosmic Genesis of the Planetary Cataclysms*, Institute of Technology and Business Press, Nakhodka, Russia, 2009.
- [26] S. V. Simonenko, *Fundamentals of the Thermohydrogravidynamic Theory of Cosmic Genesis of the Planetary Cataclysms*, Institute of Technology and Business Press, Nakhodka, Russia, 2nd edition, 2010.
- [27] J. W. Gibbs, "Graphical methods in the thermodynamics of fluids," in *Transactions of the Connecticut Academy*, vol. 2, pp. 309–342, 1873.
- [28] S. R. De Groot and P. Mazur, *Non-Equilibrium Thermodynamics*, North-Holland, Amsterdam, The Netherlands, 1962.
- [29] I. Gyarmati, *Non-Equilibrium Thermodynamics. Field Theory and Variational Principles*, Springer, 1970.
- [30] A. Sommerfeld, *Vorlesungen Über Theoretische Physic. Bd. 21. Mechanik der Deformierbaren Medien*, 2. Neubearb, Aufl, Leipzig, Germany, 1949.
- [31] S. V. Simonenko, "The macroscopic non-equilibrium kinetic energies of a small fluid particle," *Journal of Non-Equilibrium Thermodynamics*, vol. 29, no. 2, pp. 107–123, 2004.

- [32] L. D. Landau and E. M. Lifshitz, *Theoretical Physics*, vol. 5 of *Statistical Physics*, Nauka, Moscow, Russia, 1976, In Russian.
- [33] G. K. Batchelor, *An Introduction to Fluid Dynamics*, Cambridge University Press, Cambridge, UK, 1967.
- [34] H. Helmholtz, "About integrals of hydrodynamic equations related with vortical motions," *Crelle's Journal*, vol. 55, p. 25, 1858.
- [35] D. J. Evans, H. J. M. Hanley, and S. Hess, "Non-newtonian phenomena in simple fluids," *Physics Today*, vol. 37, no. 1, pp. 26–33, 1984.
- [36] I. Prigogine and I. Stengers, *Order Out of Chaos: Man's New Dialogue with Nature*, Bantam Books, Toronto, Canada, 1984.
- [37] G. Nicolis and I. Prigogine, *Exploring Complexity. An Introduction*, Freeman, New York, NY, USA, 1989.
- [38] L. D. Landau and E. M. Lifshitz, *Theoretical Physics*, vol. 6 of *Hydrodynamics*, Nauka, Moscow, Russia, 1988, In Russian.
- [39] J. Verhoogen, F. J. Turner, L. E. Weiss et al., *The Earth. An Introduction to Physical Geology*, Holt, Rinehart and Winston, New York, NY, USA, 1970.
- [40] B. Rangelov, S. Dimitrova, D. Gospodinov et al., "Fractal properties of the mediterranean seismotectonic model for seismic hazard assessment," *Annual, Geology and Geophysics*, vol. 46, part 1, pp. 397–401, 2003.
- [41] S. V. Simonenko, *Non-Equilibrium Statistical Thermohydrodynamics*, vol. 2 of *Towards the Foundation of the Theory of the Non-Equilibrium Dissipative Small-Scale Turbulence and the Tolerance Theory Related with the Quality Control*, The Pacific State University of Economics Press, Vladivostok, Russia, 2005.
- [42] G. I. Dolgikh, *The Investigations of the Wave Fields of the Ocean and Lithosphere By Laser-Interference Methods*, Dalnauka, Vladivostok, Russia, 2000, In Russian.
- [43] G. I. Dolgikh, A. V. Kuptsov, I. A. Larionov et al., "Deformation and acoustic precursors of earthquakes," *Doklady Earth Sciences*, vol. 413, no. 1, pp. 281–285, 2007 (Russian).
- [44] L. I. Sedov, *Mechanics of Continuous Medium*, vol. 2, Nauka, Moscow, Russia, 1994, In Russian.
- [45] S. Shamsi and F. D. Stacey, "Dislocation models and seismomagnetic calculation for California 1906 and Alaska 1964 earthquakes," *Bulletin of the Seismological Society of America*, vol. 59, no. 4, pp. 1435–1448, 1969.
- [46] V. S. Mount and J. Suppe, "State of stress near the San Andreas fault: implications for wrench tectonics," *Geology*, vol. 15, no. 12, pp. 1143–1146, 1987.
- [47] Z. Guo, "Significance of a ground and block rotation in the earthquake prediction," *Northwestern Seismological Journal*, vol. 10, no. 1, pp. 82–85, 1988.
- [48] A. V. Vikulin and I. V. Melekestcev, "Vortexes and life," in *Rotational Processes in Geology and Physics*, pp. 39–101, KomKniga, Moscow, Russia, 2007, In Russian.
- [49] T. Yu. Tveritinova and A. V. Vikulin, "Wave rotational-elastic tectonics of the planets," in *Rotational Processes in Geology and Physics*, pp. 271–278, KomKniga, Moscow, Russia, 2007, In Russian.
- [50] A. V. Zhirmunsky and V. I. Kuzmin, *Critical Levels in the Development of Natural Systems*, Nauka, Leningrad, Russia, 1990, In Russian.
- [51] Y. N. Avsjuk, *Tidal Forces and Natural Processes*, UIPE RAS, Moscow, Russia, 1996, In Russian.
- [52] Y. I. Perelman, *Entertaining Astronomy, State Publishing Office of the Technical-Theoretical Literature*, Moscow, Russia, 1956, In Russian.
- [53] S. A. Fedotov, "Regularities of the distribution of strong earthquakes in Kamchatka, the Kuril Islands, and Northeastern Japan," *Trudy Institut Fiziki Zemli. Akademii Nauk SSSR*, vol. 36, no. 203, pp. 63–93, 1965 (Russian).
- [54] C. Davison, *Great Earthquakes*, Thomas Murby, London, UK, 1936.
- [55] D. H. Christensen and L. J. Ruff, "Rupture process of the March 3, 1985 Chilean earthquake," *Geophysical Research Letters*, vol. 13, no. 8, pp. 721–724, 1986.
- [56] S. E. Barrientos and E. Kausel, "Genesis y proceso de ruptura del terremoto del 3 demarzo de 1985," *Revista de Geofísica*, vol. 46, no. 1, pp. 3–18, 1990.
- [57] K. H. Jacob, "Estimates of long-term probabilities for future great earthquakes in the Aleutians," *Geophysical Research Letters*, vol. 11, no. 4, pp. 295–298, 1984.
- [58] K. Shimazaki and T. Nakata, "Time-predictable recurrence model for large earthquakes," *Geophysical Research Letters*, vol. 7, no. 4, pp. 279–282, 1980.
- [59] S. Suyehiro, "Earthquake prediction efforts in Japan," in *Atti della Conferenza Internazionale sulle Zone Sismiche dell'Area Mediterranea, Matera, Italy, 16-18 November 1981*, pp. 41–44, Potenza, Italy, 1984.
- [60] R. H. Clark, R. R. Dibble, H. E. Fyfe, G. J. Lensen, and R. P. Suggate, "Tectonic and earthquake risk zoning," *Transactions of the Royal Society of New Zealand*, vol. 1, no. 10, pp. 113–126, 1965.
- [61] A. R. Johnston, "Earthquake fault Line hazards with special reference to Wellington," *New Zealand Engineering*, vol. 20, no. 8, pp. 320–322, 1965.
- [62] G. P. Tamrazyan, "About periodicity of seismic activity during the last one and half-two thousand years (as an example for Armenia)," *Izvestiya Akademii Nauk SSSR, Fizika Zemli*, no. 1, pp. 76–85, 1962 (Russian).
- [63] N. N. Ambraseys, "Some characteristic features of the Anatolian fault zone," *Tectonophysics*, vol. 9, no. 2-3, pp. 143–165, 1970.
- [64] A. V. Vikulin, "Seismicity and the Earth's rotation," *Computing Technologies*, vol. 1, no. 3, pp. 124–130, 1992 (Russian).
- [65] A. V. Vikulin, "On the nature of Australian earthquakes," *Volcanology and Seismology*, no. 2, pp. 99–108, 1994 (Russian).
- [66] I. V. Kyrillov, "On the periodicity of destructive earthquakes at the Caucasus and in Turkey," *Doklady Akademii Nauk SSSR*, vol. 115, no. 4, pp. 771–773, 1957 (Russian).
- [67] H. H. Turner, "On Mr Leath's intersects," *Monthly Notices of the Royal Astronomical Society*, vol. 46, supplement 1, no. 6, 1925.
- [68] S. Hattory, "Migration and periodicity of seismic activity in the world," *Bulletin of the International Institute of Seismology*, vol. 15, pp. 33–47, 1977.
- [69] I. Kalugin and A. Darin, "High resolution geochemical signal of paleoclimate in the bottom sediments based on scanning x-ray fluorescence analysis on synchrotron radiation (XRF SR)," in *Abstracts of the 2nd Russia-China Symposium on Marine Science: Marine Environmental and Resources in 21st Century*, p. 70, FEB RAS, Vladivostok, Russia, October 2012.

Research Article

Metrological Analysis of Geopotential Gravity Field for Harbor Waterside Management and Water Quality Control

Oswaldo Faggioni,^{1,2,3} Maurizio Soldani,¹ and Davide Andrea Leoncini^{1,2}

¹ OGS (Istituto Nazionale di Oceanografia e di Geofisica Sperimentale), ST-COPS, Via Carducci 120, 19126 La Spezia, Italy

² Università degli Studi di Genova, DITEN, Via all'Opera Pia 11A, 16145 Genova, Italy

³ Istituto Nazionale di Geofisica e Vulcanologia, Sez. Roma 2, Via di Vigna Murata 605, 00143 Roma, Italy

Correspondence should be addressed to Oswaldo Faggioni; ofaggioni@ogs.trieste.it

Received 24 January 2013; Accepted 22 April 2013

Academic Editor: Michela Giustiniani

Copyright © 2013 Oswaldo Faggioni et al. This is an open access article distributed under the Creative Commons Attribution License, which permits unrestricted use, distribution, and reproduction in any medium, provided the original work is properly cited.

Sea level oscillations are the superposition of many contributions. In particular, tide is a sea level up-down water motion basically depending on three different phenomena: the Earth-Moon-Sun gravitational relationship, the water surface fluid reaction to atmospheric meteorological dynamic, and the Newtonian vertical adjustment of the sea surface due to atmospheric pressure variations. The first tide component (astrotide) is periodic and well known in all points of the Earth surface; the second one is directly related to the meteorological phenomenon, and then it is foreseeable; the Newtonian component, on the contrary, is not readily predictable by a general hydrostatic law, because the J factor that represents the Newtonian transfer (from the atmospheric weight to the consequent sea level) is variable in each harbor area. The analysis of the gravity field permits to forecast the sea level variation due to meteorological tide events, and its metrological analysis highlights a compensation in the inverse hydrobarometric factor to be taken into account to correctly compensate atmospheric pressure variations in semibinding basins. This phenomenon has several consequences in Harbor Waterside management and in water quality control as shown by the reported case studies and introduces a new reference parameter: the so-called Water 1000.

“Dedicated to the memory of Ilaria Sanvenero”

The topic of this article should have been part of a degree thesis by Ilaria, a brilliant physics student at the University of Pisa. She left us at the age of twenty-two.

Here, we wish to remember Ilaria by paying public homage to her brief but precious work.

1. Introduction

During the last three years, the metrological observation of tide waves highlighted a phenomenon of seawater level fluctuations in port/coastal basins, strictly connected to Climate Global Change (CGC), caused by weight variations of the above atmosphere district (gravity field variations) that produce a Newtonian compensation by sea level imbalance also two time greater than the one produced by astronomical tides; moreover, the time duration range of these phenomena is 24–120 h.

This phenomenon is the first measured example, not extraordinary, of the direct effect of CGC on human life: in fact, metrological observations pointed out a constant increment of amplitude variation and pressure with a consequential anomalous seawater level variation in port basins (superhigh and superlow tides) with several consequences on human activities.

The phenomenon has also significant effects on the quality of port waters. From the point of view of port water quality control (WQC), the mass of seawater represents the solvent in which the pollutants components are dissolved.

TABLE 1: Main astronomic tide components, periods, and radian frequencies (table from [15]).

Harmonic	Period (h)	Radian frequency (rad/s)
O_1	25.819.341	$6.7597744E - 5$
Π_1	24.132.140	$7.2323884E - 5$
P_1	24.065.890	$7.2522945E - 5$
S_1	24.000.000	$7.2722052E - 5$
K_1	23.934.469	$7.2921158E - 5$
J_1	23.096.474	$7.5560361E - 5$
$2N_2$	12.905.374	$1.3524049E - 4$
η_2	12.871.757	$1.3559370E - 4$
N_2	12.658.348	$1.3787969E - 4$
ν_2	12.626.004	$1.3823290E - 4$
M_2	12.420.601	$1.4051890E - 4$
L_2	12.191.620	$1.4315810E - 4$
T_2	12.016.449	$1.4524500E - 4$
S_2	12.000.000	$1.4544410E - 4$
R_2	11.983595	$1.4564320E - 4$
K_2	11.967.234	$1.4584231E - 4$
M_4	6.210.300	$2.8103780E - 4$
MS_4	61.033.392	$2.8596300E - 4$

The density of this solution depends on the amount of the solute (pollutants) and on the mass of the solvent (seawater). In high pressure conditions, the mass of water can be greatly decreased, and then the solution seawater pollutant may increase its density significantly also without any increment of the solute (chemical and physical pollutants). Obviously, in the case of low atmospheric pressure, the opposite occurs (increment of the mass of water and consequent decrement of the density of the pollutants without diminution of their mass in the solution). In order to have a correct and comparable series of measures for WQC, it is therefore necessary to introduce a reference level called Water 1000 (W1000) in order to normalize the density values of the pollutants measured at any atmospheric pressure to those corresponding to an atmospheric pressure of about 1000 hPa. This is possible by means of a parameter (J) that connects the pressure variation atmospheric to the variation of mass of port water.

The capability of prediction of harbor water level permits moreover to improve the effectiveness of safety in port navigation and security provided by underwater port protection systems.

Indeed, port basins usually host key infrastructures and are at the same time strategic points for maritime transportation: for these reasons, ports should be able to protect themselves and their infrastructures from damage, destruction, or disruption by natural disasters, deliberate acts of terrorism, negligence, and so forth.

The paper is composed of four sections. After a short introduction in Section 2, there are reported theoretical considerations on gravity field and its metrological analysis, in particular, Section 2.3 discusses the safety and security issues in which the phenomenon is involved and points out the HWSM and WQC consequences due to the analyzed

phenomenon. Section 3 reports two different case studies in different geographical areas with several interesting aspects addressed in the paper, and then conclusions and possible future works follow.

The purposes of this work are to develop a quantitative method for the forecasting of the flow times and amplitude of meteorological tides (meteotides), based on the joined use of barometers, hydrometers, and clocks, describe a preliminary law of meteo-tide parameters studying the meteotides as adjustment of the geodetic surface (free sea surface), and present the first results on HWSM and WQC based on meteo-tide forecasting.

2. Materials and Methods

2.1. The Tide Phenomenon and Its Components. The term “tide” derives from the German “*tiet*” which means “time”: indeed, this term is used commonly to indicate the phenomenon of rise and fall of sea level [1] caused by the combined effects of periodic gravitational forces exerted by the Moon, the Sun, and the rotation of the Earth. In general, this definition is correct only at a first analysis: in fact, this definition concerns only the astronomical component of this kind of phenomenon (primary contributes) without taking into account other gravitational forces (secondary contributes) usually aperiodic.

The astronomical component can be easily described by a Fourier analysis, both in its elementary (fundamental) components and in the composed harmonics resulting from interference among the fundamental waves themselves. The harmonic sinusoidal tide components have specific amplitude depending on the site of observation and are characterized by typical and recurrent frequencies (see Table 1).

The Rete Mareografica Nazionale (RMN), managed by the Istituto Superiore per la Protezione e la Ricerca Ambientale (ISPRA)—Servizio Mareografico Nazionale (SMN), provides a coverage of the Italian coasts that effectively monitors sea level fluctuations. The harmonic analysis of these data underlines both the presence of the fundamental tide components and the composed ones (also named overtides) that cover an important role in the sea level fluctuations of shallow water (M_4 and MS_4 ; see Table 1).

Together with these contributions (primary contributions), there are some sea level fluctuations not related to the classical tide concept but due to other climatic agents such as wind action (i.e., storm surges) [2], pressure variations of thermal origin (e.g., alternation night-day), local morphology of the environment (i.e., seiches and coastal trapped wave), and aperiodic low-frequency sea level fluctuations (due to meteorological pressure variations) representing the background level on which astronomic components overlap (secondary contributions) [3–7].

All the secondary contributions—except sea level fluctuations due to meteorological pressure variations—have been widely analyzed in the literature and are characterized by phenomena which are easy to note and to forecast. The paper focuses the attention to the forecasting of the sea level fluctuations due to meteorological pressure variations because of its novelty.

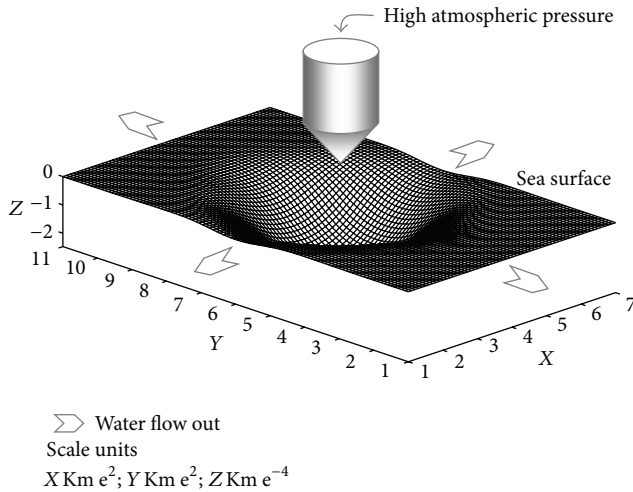


FIGURE 1: Picture of the geodetic phenomenon of sea level deformation due to atmosphere weight (image from [15]).

These fluctuations depend in a variable way on the transit of atmospheric fronts or, in general, on the atmosphere meteorological dynamics over the considered sea basin [8] and hence cannot be predicted by harmonic analysis [9–14].

When a high-pressure air front moves on a free water surface, it originates an additional weight on it. The isostatic reaction of free water surface is a concave adjustment with respect to the starting surface (see Figure 1) to compensate, in the local atmosphere-water column, the increase in atmosphere weight with a water outflow (low meteo-tide).

On the contrary, when a perturbed front produces a drop in atmosphere weight, the isostatic compensation adjustment will be realized in a bump produced by a flow of incoming tide (high meteo-tide).

The time between the pressure imbalance and its Newtonian compensation is called “tide inertness”.

2.2. Metrological Analysis of the Geopotential Gravity Field. Starting from these considerations a local atmospheric variation produces a meteo-tides flow that consists in an adjustment of the free sea surface. When the sea level is in isostatic equilibrium with atmosphere weight, tide fluctuations concern only astronomic components. When an atmospheric weight variation occurs, the sea surface reacts by a low-frequency fluctuation reaching a new equilibrium state.

Such adjustment is characterized by a delay time due to the different dynamic responses of atmosphere compared with seawater. This delay cannot be evaluated with a theoretical law on the basis of barometric measurements. Meteo-tide flow and reflow times, in fact, feel the effects of many local factors: the most important being coast and bottom morphology and, secondly, the currents, the wind, and seawater density.

On the contrary, if a gravimetric anomaly signal is detectable, the force producing the beginning of a meteo-tide event will be technically measurable before the beginning of the sea surface compensation related to the barometric

variations. The weight change of the mass which induces the change of atmospheric pressure at sea level is due, in first approximation, to three types of contributions. The contribution of the first order is the density of the volume of the considered atmosphere (the mass of air present in the local column of atmosphere) which in turn also depends on chemical-physical characteristics of the mixture of air considered (essentially humidity) and on its meteorological dynamic state (down force kinetic—principle of Bernoulli), respectively, second and third order. However, regardless of the causes of inducing phenomenon, an atmospheric weight increment always induces a Newtonian adjustment in the sea surface. For this evidence, the metrological approach, correlating atmospheric weight variations to the inverse geodetical sea level variations, is fully consistent with the quantitative definition of the relationship between the phenomena. When the cause (high pressure) generating such adjustment stops, the sea surface is in geopotential unbalanced conditions and produces a gravimetric anomaly inducing a Newtonian water flow to compensate this imbalance (returning to the sea surface geometry preceding the increase of pressure), as a propagating tide wave. Then, using a barometer near the meteo-mareographic station provides an essential preliminary datum, since such instrument (if sensitive to the phenomenon) is able to measure the Newtonian signal of geodetic imbalance when it occurs. If a tide gauge is joined to the barometer, the sea level measurement and the meteo-tide wave arrival time can be achieved. The difference between barometric maximum time and meteo-tide wave arrival time (i.e., the delay between the Newtonian generating cause and the geodetic reaction) is the meteo-tide time of flow (or reflux). A reasoned statistic of these measurements is able to provide the law of meteo-tide delay based on the entity of the Newtonian generating push. Such law, characteristic of every harbor, will become the barometric measure predictors of meteo-tide delay time. Another critical aspect of this phenomenon is represented by its persistence on the local region. Indeed while astronomical tides have an influence time period in the order of some hours, a meteo-tide event could affect the area also for some days.

This phenomenon is well known in the literature [16–18] and is called Inverted Barometer (IB) effect. The simplest approximated correction that could be done consists in considering a purely local response of the sea surface to atmospheric pressure at the measurement point. The inverse barometer correction can be easily computed from the dry troposphere correction [19]:

$$IB [mm] = -9.948 * (\Delta R_{dry} [m bars] - 1013.3). \quad (1)$$

To 1 hPa of variation of atmospheric pressure corresponds a linear response of the sea level of about 1 cm. This simplified condition, which represents the state of the art in meteo-tide analysis, is true in offshore areas where there are no physical constraints. Vice versa in port basins or in coastal areas, the presence of natural and manmade structural constraints such as rocks, cliffs, pier, and dock structures forces the exciting free volume of water to reflow outside the basin. This isostatic reaction implies a significant modification to the IB effect

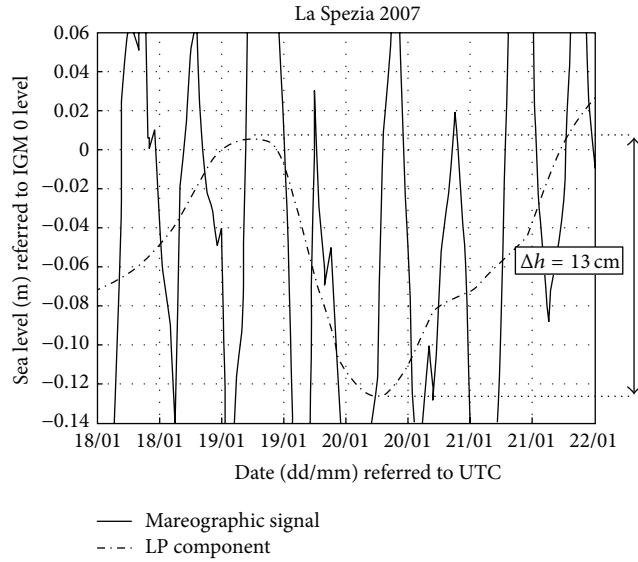


FIGURE 2: The mareographic signal recorded by La Spezia Newtonian Meteo-tide Station between 18.01.2007 and 22.01.2007 and its low pass component, $F_c = 10^{-5}$ Hz (image from [15]).

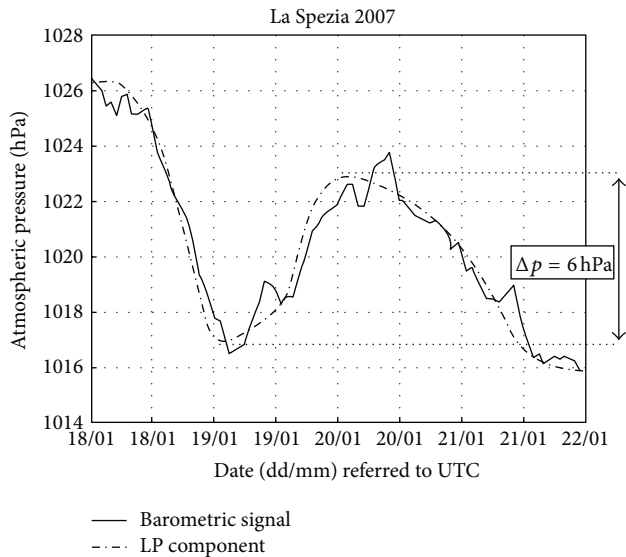


FIGURE 3: The barometric signal recorded by La Spezia Newtonian Meteo-tide Station between 18.01.2007 and 22.01.2007 and its low pass component, $F_c = 10^{-5}$ Hz (image from [15]).

introducing a new forecasting parameter in port areas: the inverse hydrobarometric factor (J) [3, 15, 19].

2.2.1. The Hydrobarometric Factor (J) as Atmospheric Pressure—Port Water Sea Level Transfer Factor. The starting point to perform a meteo-tide forecasting analysis in port basins is to detect a statistic relationship between atmospheric pressure and sea level variations. By this way, the low-frequency components of barometric and mareographic signals grabbed during several events and occurred in last years have been compared. The cut off frequency F_c has been

determined in order to separate low-frequency band (meteo-tide due to Newtonian phenomena) from high-frequency band (astronomical tide and sea wave phenomena) and is equal to 10^{-5} Hz.

In particular, the J factor was calculated for each studied event, according to the following formula:

$$J = \left| \frac{\Delta h}{\Delta p} \right| \quad (2)$$

in which Δh represents the low pass component variation of the sea level and Δp the low pass component variation of the atmospheric pressure. To explain the developed method to calculate J , we analyze the event from 18.01.2007 to 22.01.2007 in the La Spezia harbor (see Figures 2 and 3). During the analyzed event, the atmospheric pressure increased to 6 hPa ($\Delta p = 6$ hPa) while the port water sea level decreased by 13 cm ($\Delta h = -13$ cm).

By this way, the phenomenon could be characterized by a J factor computed as follow:

$$J = \left| \frac{\Delta h}{\Delta p} \right| \approx \frac{13 \text{ cm}}{6 \text{ hPa}} \approx 2.2 \frac{\text{cm}}{\text{hPa}}. \quad (3)$$

This means that every increase of 1 hPa in atmospheric pressure was followed by a decrease in sea level of about 2.2 cm. The computation of the J factor was repeated for several significant events occurred during 2007 in the La Spezia harbor obtaining a J factor value for each event. So, it was possible to calculate an estimated \hat{J} value by an extensive statistic of J factor:

$$\hat{J} \approx 2 \frac{\text{cm}}{\text{hPa}}. \quad (4)$$

A correct estimation of the key parameter \hat{J} allows the conversion of an atmospheric pressure variation into an expected sea level increase/decrease in the considered basin:

$$\Delta \tilde{h} = -\hat{J} * \Delta p, \quad (5)$$

where $\Delta \tilde{h}$ is the sea level expected variation, \hat{J} is the estimated hydrobarometric factor, and Δp is the measured pressure variation.

These results indicate an opposite trend sea level variation of about 2 cm for any atmospheric pressure variation of 1 hPa in the Port of La Spezia. The described forecasting method error (difference between the expected sea level and the observed one) did not exceed 5 cm in the Port of La Spezia during 2007.

The same statistical analysis performed during last years in other Italian ports (see Table 2) shows that \hat{J} ranges from 1.6 cm/hPa to greater than 2 cm/hPa (depending on the port), while it values about 1 cm/hPa in the offshore areas according to the IB effect law.

2.2.2. Meteotide Inertness. Geometrical comparison between low-frequency components of the two signals shows that a time $\Delta t \approx 10$ h elapses between atmospheric pressure minimum time (19/01 00:00) and corresponding sea level

TABLE 2: Inverse hydro-barometric factor (J) estimation in different Italian ports—one year observation.

Gulf	J (cm/hPa)
La Spezia	1.9
Genova	1.8
Marina di Carrara	1.7
Piombino	1.8
Civitavecchia	1.6
Livorno	1.9
Ancona	1.8
Bari	1.6
Ravenna	2.2

maximum time (19/01 10:00; meteomareographic flux). Such delay could be also identified between atmospheric pressure maximum time (19/01 22:00) and sea level minimum time (20/01 08:00; meteomareographic reflux): variation of atmospheric pressure and consequent opposite variation of sea level shifted each other by nearly 10 h. This delay represents, for these events, the inertness of water mass moving in reply to Newtonian pulse generated by variation of atmospheric pressure. In general, the same temporal analysis performed in Italian ports shows an inertness range from 10 h to 18 h.

2.2.3. Meteotide Forecasting in Port Basins and Its Consequences. Starting from these considerations, it is interesting to notice that the amplitudes of maxima meteo-tide waves (briefly named meteotides) are sensitively greater than astronomical tide waves (astrotides). This phenomenon is typical in several Italian ports (see Table 2), where the merchant and military harbor structures are subject, under unexceptional meteorological conditions, to low-frequency meteo-tide flows showing an amplitude even four times greater than normal astrotide amplitudes (i.e., Port of Ravenna). Therefore, the importance of forecasting the meteo-tide flows is remarkable for safety and security reasons and should be taken into account in HWSM rules and in HWQ controls.

Moreover, with the increase of occurrences of local atmospheric variations due to the Climate Global Change (CGC), also the occurrences of this phenomenon have increased (i.e., in Marina di Carrara, Livorno, Piombino, and Civitavecchia harbors; see Figures 4(a), 4(b), 4(c), and 4(d)) producing a direct impact on port and coastal ecosystems including human activities. The phenomenon is detectable in all coast sectors we are monitoring (North Tyrrhenian Sea, see Figure 5).

2.3. Effects of Newtonian Meteotide in Port Environment. The knowledge and prediction capability of the hydrobarometric tide waves dynamics produce a relevant increase in local safety and security HWSM and HWQ controls and in sea structure port design. As reported in the previous paragraphs, the flow times and amplitudes of meteotides unlike the astrotides are not easily predictable because of the stochastic nature of the atmospheric dynamics and because of the complex correlation between atmospheric pressure variation

and consequent sea surface adjustment (related to temporal phase displacement and amplitude variations).

However, the advent of numerical modelling and the use of air-wave-ocean coupled systems have been improving a lot the forecasting skills of atmospheric pressure [20–28].

Independently by the accuracy and reliability of these methods, port authorities could obtain a forecasting of the sea level of the first order considering the pressure measured at the current time and considering the inertness of the sea volume. By this way, they obtain forecasting capabilities of a certain (because it has been measured) sea level variation. Moreover, using a numerical model able to forecast the atmospheric pressure variations, it is possible to introduce a second order forecasting longer in the delay time but uncertain and with lesser reliability.

Only taking into account the concept reported in Sections 1 and 2, it is possible to provide an effective parameter in environmental HWSM (in particular regarding nautical traffic) and in HWQ controls. The knowledge of such phenomenon makes it possible to define the resistive capacity of the harbor/basin to environmental impact. Moreover, it makes it possible to plan human activities in the harbor waters according to the stress condition of the area. As an example, if a dredging operation or any other intrusive action in shallow waters should be performed in an harbor basin, the statistical knowledge of the seasonal period of maximum water exchange and the ability to forecast the exchange times will be decisive in minimization of environmental impact. Indeed they can provide some crucial indications on the best time for works execution.

2.3.1. Safety Aspects. The capability of prediction of real harbor water surface level permits to improve the effectiveness of safety in the port navigation and water quality control and in sea structure port design and implementation. A first evidence related to port navigation safety is represented by the Moby Rider ship. The complete analysis is reported in Section 3.

The environmental water quality in port areas is often monitored with many chemical-physical controls, especially in the harbors in which, in addition to the normal human and port activities (not particularly high pollution values without considering accidental events), there are also industrial activities. The density of the pollutants, for both chemical and physical aspects (e.g. increase of temperature due to industrial cooling waters downloaded into the sea), does not depend only on the introduced solute but also on the quantity of solvent (seawater) present in the harbor during the same flow. Meteobaric tides have a role more important than astronomic tides in the formation of the port watery solution because beyond their amplitude, they are often very persistent for several days. So, for the same quantity of introduced solute, they govern the final density of the solution (adding or extracting solvent). For the same quantity of pollutants introduced in the sea basin, a sampling without correlation to the reading of the meteobaric tide amplitude can overestimate or underestimate the environmental waters quality. The meteobaric tides forecasting furnishes the real quantity of

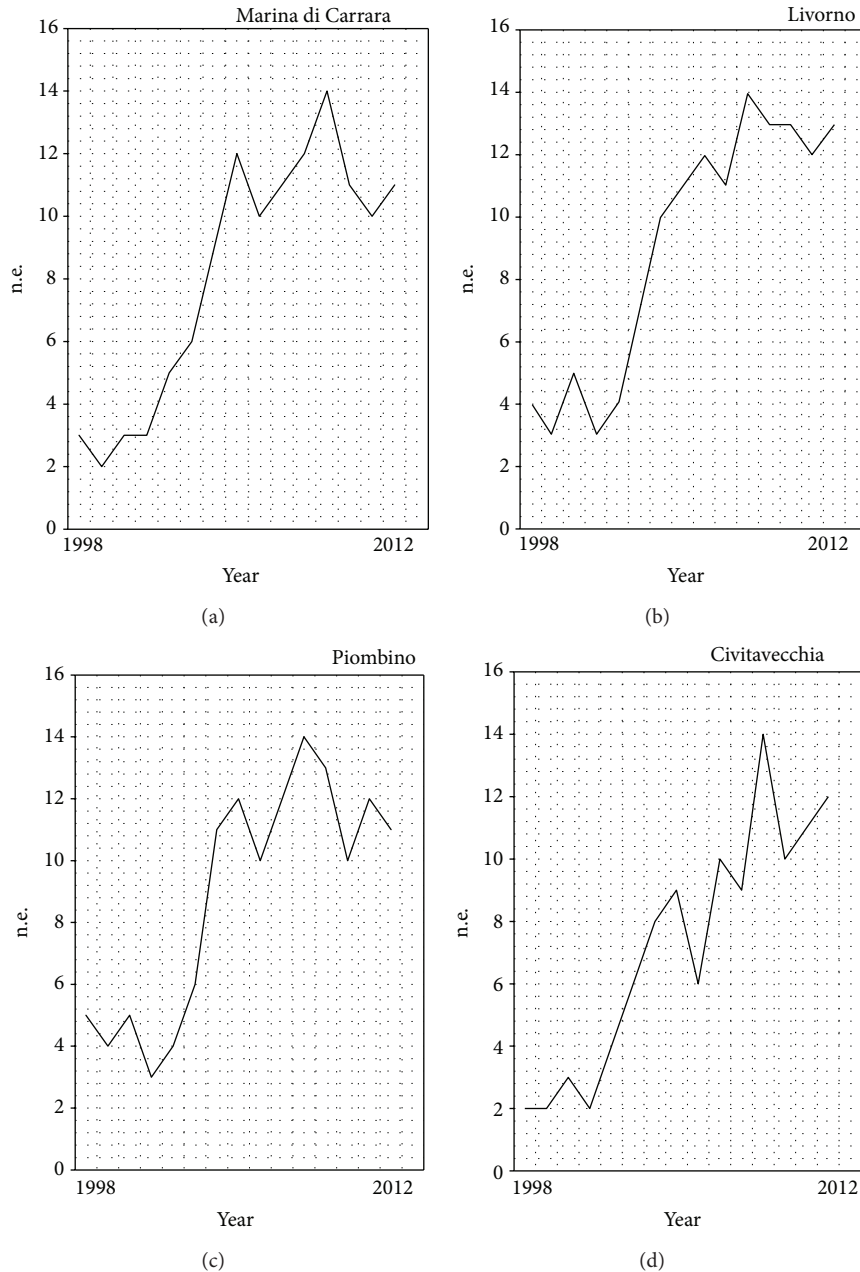


FIGURE 4: Occurrences from 1998 to 2012 of Newtonian meteorites events in Marina di Carrara, Livorno, Piombino, and Civitavecchia (n.e. number of events).

solvent present in the harbor (seawater) during sampling and therefore the possibility to set the environmental surveys to the normalized water (W1000—port sea level at 1013 hPa of atmospheric pressure) making them comparable among them.

2.3.2. The W1000 Concept. The duration and the amplitude of the port hydrobarometric tidal waves can interfere significantly on the port water quality altering the solute-solvent mass ratio. Defining with X a hypothetical pollutant, the water quality with respect to the mentioned pollutant is the

concentration of X in the water solution of the port where the solvent is represented by the seawater. The concentration of the solution is thus a function of the mass of solute X and of the mass of seawater. The result is that there is no univocal relationship between the quantity of pollutant dissolved and the quality of the solution.

In conditions of persistent high pressure, the harbor basins of Table 2 are emptied of water also in an intense and long-lasting way (usually equal to a few percentage points and sometimes more), and then the concentration of the solution is altered by the decrease of solvent and not by the increase of pollutant.

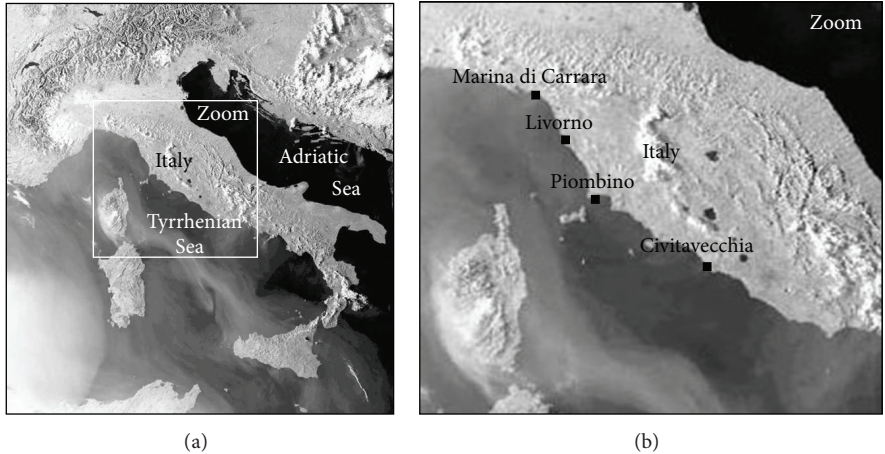


FIGURE 5: North Tyrrhenian Sea map with analyzed harbor localizations.

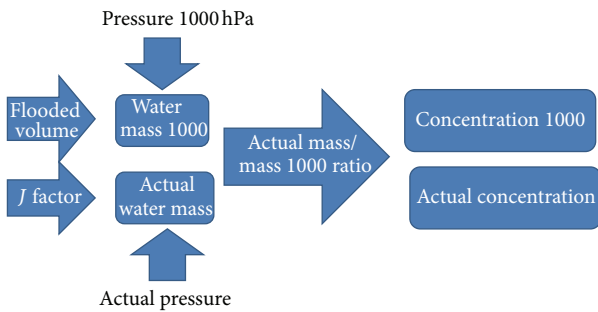


FIGURE 6: W1000 and actual concentration computation (algorithmic scheme).

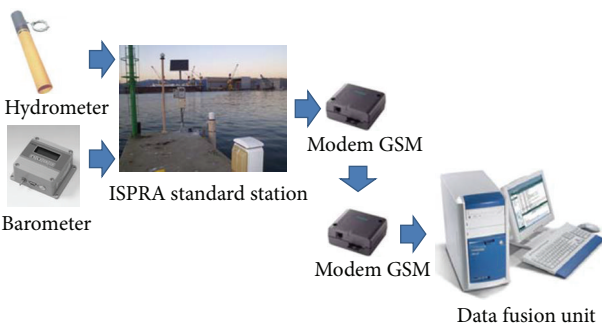


FIGURE 7: ISPRA standard meteorographic station (La Spezia ISPRA station schematic).

This environmental dependence of the concentration of the solution alters the information on the intensity of the anthropic pressure on the environment itself and above all makes metrologically not comparable successive measurements because the only density measurement of the chemical solution does not inform about the amount of solvent. Obviously, in conditions of persistent high atmospheric pressures, the measurements of the quality of port water tend to be overestimated (compared to the quantity of pollutant). Vice versa in conditions of low atmospheric pressures and thus



FIGURE 8: Port of Bari and in particular the port entrance (Image from Google Maps).

superfilling, the measurements of port waters environmental quality will lead to an underestimation of the amount of the pollutant in the solution.

This serious drawback (fatal from a metrological point of view) makes random the comparison between successive measurements of harbor water quality (worse in the control of the mass of solvent). To overcome this problem it is possible to introduce the W1000 concept.

By means of the *J* factor, it is possible to estimate the mass of water in the port under investigation (for which you know the volume of flooded) at any atmospheric pressure conditions at the time of measurement. By this way, it is possible to calculate the percentage ratio of the change in mass of solvent from the atmospheric conditions of measurement to those of W1000, and it is possible to compensate the concentration of the solution with respect to the mass changing of solvent. The port water quality samples will then give two answers: the overall concentration and the W1000 concentration (see Figure 6).

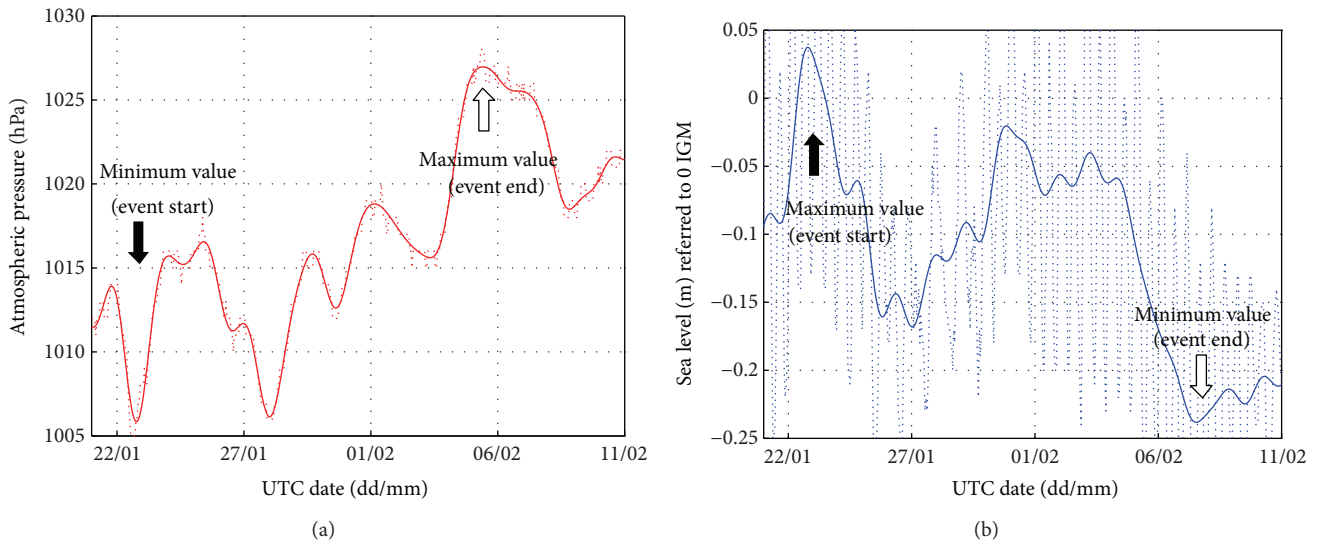


FIGURE 9: Port of Bari atmospheric pressure and sea level during February 2010 meteo-tide event (dotted line: high frequency, continue line: low frequency, $F_c = 10^{-5}$ Hz).

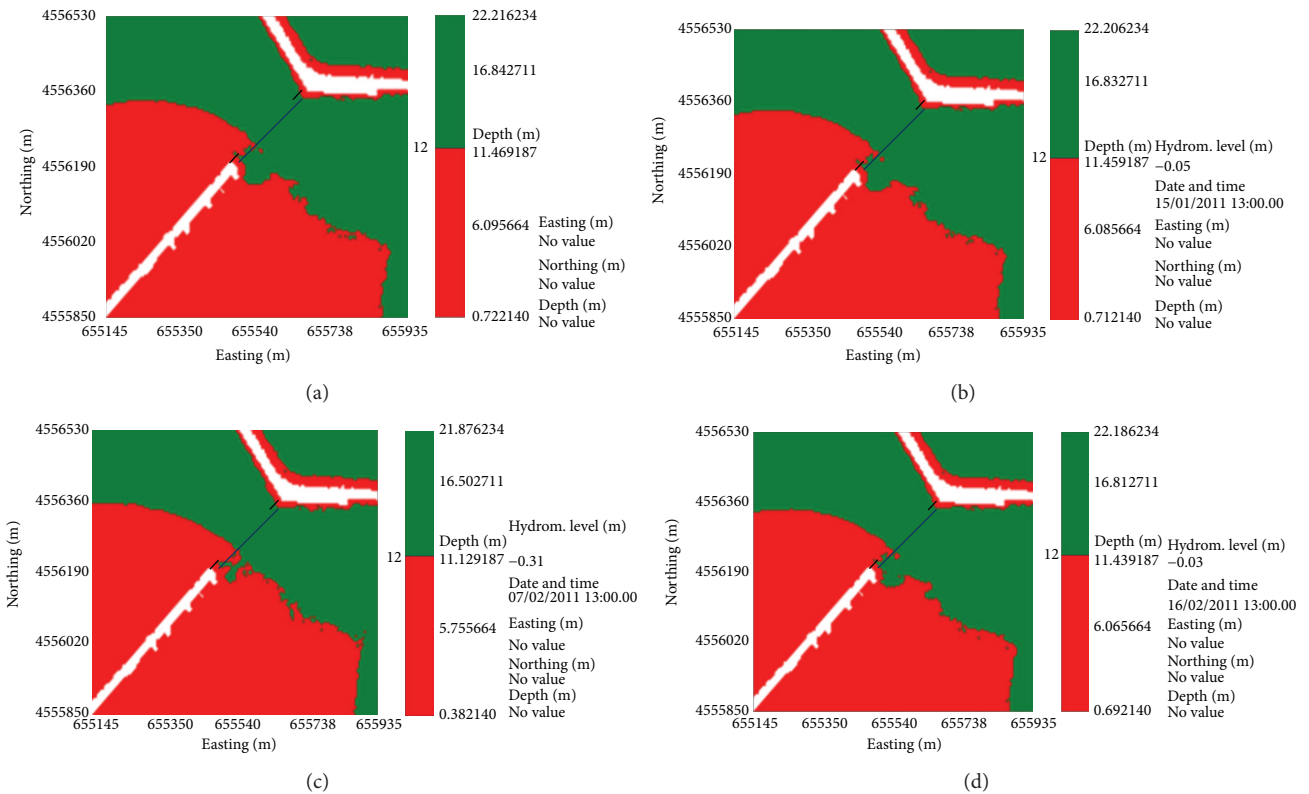


FIGURE 10: Dynamic bathymetry of Port of Bari. The blue line represents the acoustic subsystem while the two black lines represent the magnetic subsystem. Red areas are zones with water depth under 12 m (not controllable with acoustic subsystem configured with operative quote of 12 m) while green areas are zones with water depth above 12 m. (a) represent the static analysis of the area, (b) the area before the event, (c) during the event, and (d) after the event.

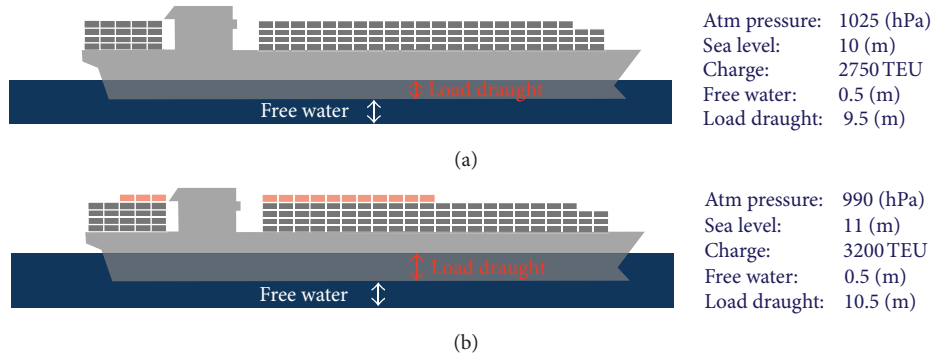


FIGURE 11: Difference of payload in TEU during two different atmospheric pressure situations.



FIGURE 12: Port of Livorno and in particular S. Stefano basin locations (image from Google Maps).

The atmospheric pressure is not the only environmental factor that affect measurements of harbor water quality control. Other factors (secondary contributions with respect to the ones produced by atmospheric pressure because they produce sea level variations of low intensity) include but are not limited to various water sources such as precipitation or evaporation phenomena and river and dispersed freshwater inputs. Nevertheless, these kinds of factors can be interesting for high definition analysis but irrelevant for the HWSM.

However, the W1000 problem is solved from a geodetic point of view by the definition of the J factor at first approximation and with secondary contribution only in higher approximations.

3. Results and Discussion

Every port in Table 2 has been equipped with an ISPRA meteomareographic station. The standard configuration includes one microwave hydrometer, one digital barometer, one GPS module, and one GSM module for data transmission (see Figure 7).

Using a standard station, it is possible to estimate the atmospheric air mass variation on the observed area and then to identify a meteo-tide event.

3.1. Port of Bari. The first example is a generic observation of a specific meteo-tide event and their possible consequences in Port of Bari (see Figure 8). In particular in February 2010, considering only the effect of meteo-tide (low frequency signal), an atmospheric pressure variation of about 21 hPa produced a diminution of sea level of about 28 cm (see Figure 9, white arrow). Simulating the event, it is interesting to notice that the sea level variation in 07/02/2011 at 13:00 (date of the maximum sea level variation) is of -0.33 m (see Figure 10(c)). The astronomic tide from tide tables in the same time is of about -0.05 m while the meteo-tide is of about -0.28 m (as previously seen). This highlights the right considerations on meteo-tide effect. Starting from these considerations, it is also possible to compute the inverse hydrobarometric J factor for the analyzed event:

$$J = \left| \frac{\Delta h}{\Delta p} \right| \approx \frac{28 \text{ cm}}{21 \text{ hPa}} \approx 1.3 \frac{\text{cm}}{\text{hPa}}. \quad (6)$$

Another interesting aspects to point out is that the effect of the sea level variation takes place one hour later compared to the pressure variation beginning (identified by the black arrows in Figure 9), but the delay increases until becoming equal to some days (see white arrow in Figure 9).

Once analyzed one example of meteo-tide occurrence and its effects on the basin water volume, it could be interesting to investigate some possible issues caused by this phenomenon.

To avoid intrusion in Bari harbour, it is possible to displace an acoustic/electromagnetic barrier on the sea bottom in the port entrance. The water depth in quite condition in the specific area is of about 12 meters so the acoustic active subsystem could be configured with a maximum range of 12 m. By this way, if the sea level grows, it could be possible for a diver to enter the area without being detected passing at a sea floor distance greater than 12 m. Vice versa if the sea level falls down, the reverberation noise produced by the reflection caused by the sea surface could increase making blind the

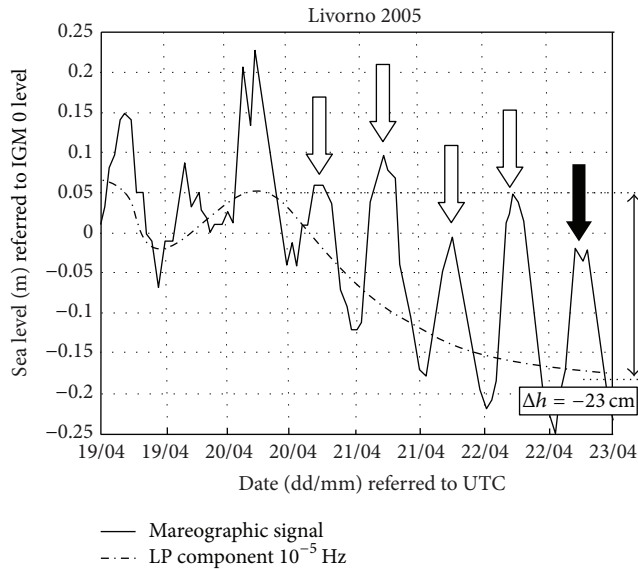


FIGURE 13: Sea level variations in Port of Livorno (original signal and its low pass component in dotted line) (image from [15]).

acoustic subsystem. In this scenario, the task performed by the acoustic subsystem could be developed by the magnetic subsystem that should be able to reconfigure itself to close a possible acoustic gap. An example of the above situation could be revealed analyzing the sea level variation produced by the meteo-tide event analyzed previously in the entrance zone during the phenomenon. Analyzing the bathymetry of the zone, it is possible to identify a region in which the acoustic subsystem could be placed without contraindication and in which with the integration with two segments of magnetic subsystem the barrier could provide a complete protection (see Figure 10(a)). In quiet conditions, the acoustic subsystem could work properly, and the gap near the docks is covered by the magnetic subsystem (see Figure 10(b)).

During the occurrence of the phenomenon under investigation, the acoustic subsystem could not provide a complete protection of its competence area, and the system should be reconfigured to close this gap (see Figure 10(c)). After the event, the situation goes back, and the zone returns completely controlled (see Figure 10(d)).

Another interesting aspect related to non compensation of sea level variation can be analysed considering water quality control. If a water quality sample has been taken during a low atmospheric pressure event (more or less -40 hPa) in which the sea level variation is, for example, $+1 \text{ m}$ ($+70 \text{ cm}$ due to meteo-tide and $+30 \text{ cm}$ due to astronomic tide) in a basin with a medium sea level of about 10 m considering a constant quantity of solute, the solvent will increase by about 10%. Vice versa if the sample has been taken during a high atmospheric pressure event (more or less $+40 \text{ hPa}$) and the sea level variation is about 1 m considering a constant quantity of solute, the solvent will decrease by about 10%. The result is that in the first case it could be possible not to identify an anomaly situation while in the second case it could be possible to indicate as an alert a normal situation.

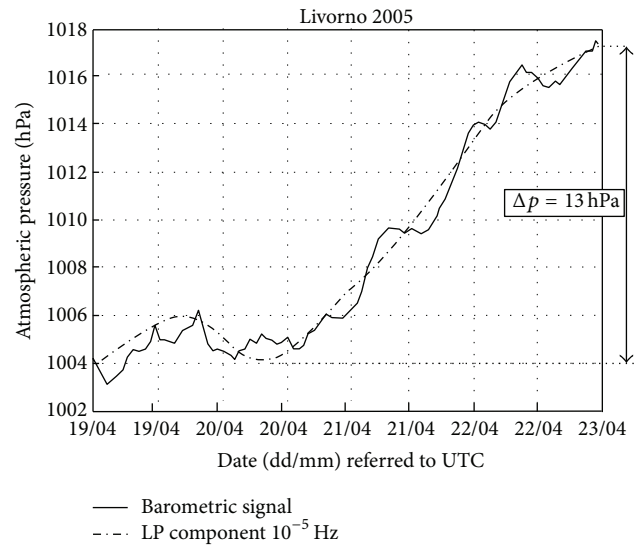


FIGURE 14: Atmospheric pressure variations in Port of Livorno (original signal and its low pass component in dotted line) (image from [15]).

A possible solution could be to report all the analyses to a standard pressure value following the W1000 concept (see Section 2.3.2). Moreover, with meteo-tide forecasting, it is possible to regulate the discharge of waters from industry (i.e., hot water from ENEL—Italian electric energy provider company—establishments), allowing a major water discharge when the sea level is high and limiting the discharge when the quantity of water in sea basin is low.

The last example of consequence due to not considering meteo-tide events in the right way could be performed analyzing the cargo capacity of a panamax cargo ship. If we consider the same variation of the last example with a sea level variation of about 1 m , it is possible to increase the payload of a panamax of about 450 TEU (*twenty-foot equivalent unit*) equal to more or less an increase of about 17% of the entire load of the cargo (see Figure 11). At the same, time a free water of about 0.5 could not be sufficient to guarantee a safety navigation for the ship without taking into account meteo-tide events and its different inverse hydrobarometric factor in constrained areas.

3.2. Port of Livorno. A significant example of harbor water-side management for safety in ship traffic based on meteo-tide forecasting is represented by the refloating operation of the Moby Rider ship. In April 19–22, 2005, in S. Stefano basin (Livorno port, see Figure 12), the Italian ship Moby Raider stranded for several technical reasons. The Port Authority launched the refloating procedure based on forecasting of astronomical tide highs.

The refloating operation has not succeeded for four attempts (see white arrows in Figure 13) because the action of increase of atmospheric pressure had tide negative effects absolutely higher than the positive effects due to tide astronomical highs. Before starting with the fifth attempt, the atmospheric pressure in Livorno stops its increasing (see

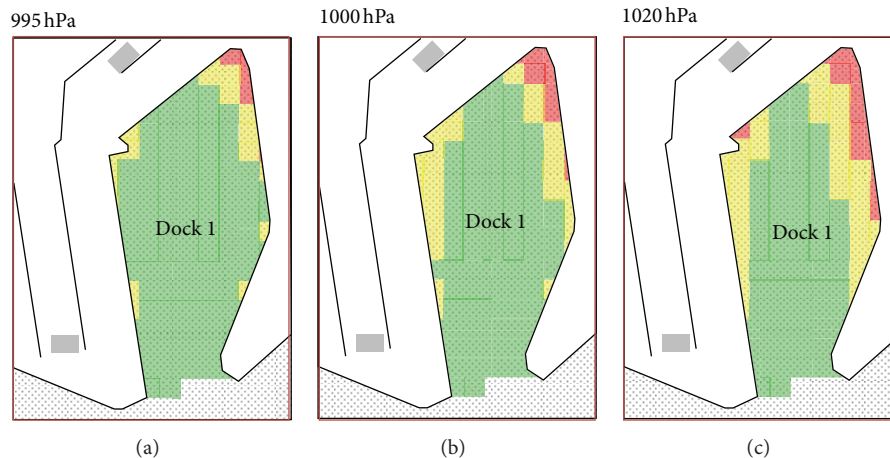


FIGURE 15: Bathymetric map of a dock in the Port of Livorno depending on the atmospheric pressure (995 hPa, 1000 hPa, and 1020 hPa); the three colours (green, yellow, and red) indicate three water depth ranges (very deep, deep, and not deep) (image from [15]).

Figure 14). Accordingly, with this phenomenon, the sea level stops to decrease. Under these conditions (without meteo-tide variations), the refloating was obtained (see black arrow in Figure 13). The refloating operation has had a positive outcome only because the pressure increment has stopped. With the forecasting of the meteo-tide, the refloating operation should be performed at the first attempt executing the operation only at the end of the phenomenon. Moreover, the forecasting could be used to avoid strand events.

3.2.1. Optimization of a Dock Performance. The knowledge of \hat{J} is also very useful in HWSM to forecast the water depth in the approaches and stationing ships knowing only the expected atmospheric pressure. The effects of the pressure variation on the water depth were applied to a dock in the Port of Livorno (see Figure 15). Water depth goes down about 50 cm consequently due to an atmospheric pressure increase from 995 to 1020 hPa, and consequently, J for this event is nearly 2 cm/hPa; then, the pressure variation changes the bathymetry of the basin, as displayed in Figure 15. A pressure variation could be converted, through \hat{J} , into an expected sea level variation and then into a new bathymetric map. In the design phase of maritime works, it is necessary to introduce the \hat{J} factor in order to define the height of the marine protection works.

4. Conclusions

The paper highlights the importance of metrological analysis of geopotential gravity fields for HWSM and HWQ pointing out safety and security aspects. In the experimental result in Section 2, different areas and situations have been investigated. The above results encourage the research in this field to increase the forecasting capabilities of the system based on meteo-tide analysis. An interesting future work to be addressed could be the constitution of a network of meteomareographic stations able to increase the prediction capability of the system.

Acknowledgment

The authors would like to thank ISPRA-SMN for the data provided and for the disponibility of its operators.

References

- [1] I. Vilibić, G. Beg Paklar, V. Dadić, D. Ivanković, and S. Čupić, "Qualitative analysis of old and new sea level measuring techniques and their data consistency," *IEEE Journal of Oceanic Engineering*, vol. 32, no. 2, pp. 428–435, 2007.
- [2] D. S. Rosen and L. Raskin, "Wind and wave effects on sea level measurements," in *Proceedings of the ESEAS-RI Workshop on Sea Level Observation and Interpretation*, Valletta, Malta, November 2004.
- [3] O. Faggioni, G. Arena, M. Bencivenga et al., "The Newtonian approach in meteorological tide waves forecasting: preliminary observations in the East Ligurian harbours," *Annals of Geophysics*, vol. 49, no. 6, pp. 1177–1187, 2006.
- [4] M. Crépon, "Influence de la pression atmosphérique sur le niveau moyen de la Méditerranée Occidentale et sur le flux à travers le Détroit de Gibraltar," *Cahiers Océanographiques*, vol. 17, pp. 15–32, 1965.
- [5] F. Mosetti, "Oscillazioni del livello medio marino a Venezia in rapporto con le oscillazioni di pressione atmosferica," *Bollettino di Geofisica Teorica ed Applicata*, vol. 11, no. 43–44, pp. 264–277, 1969.
- [6] C. Stocchino and V. Scotto, "Il livello marino e la pressione atmosferica nel porto di Genova," *Bulletin de l'Institut Océanographique de Monaco*, vol. 69, no. 1399, pp. 1–10, 1970.
- [7] C. Garrett and B. Toulany, "Sea level variability due to meteorological forcing in the northeast Gulf of St. Lawrence," *Journal of Geophysical Research*, vol. 87, no. C3, pp. 1968–1978, 1982.
- [8] P. Picco, R. Bozzano, M. E. Schiano et al., "Marine observing system from fixed platform in the Ligurian Sea," *Bollettino di Geofisica Teorica ed Applicata*, vol. 48, no. 3, pp. 227–239, 2007.
- [9] J. S. Allen and D. W. Denbo, "Statistical characteristics of the large-scale response of coastal sea level to atmospheric forcing," *Journal of Physical Oceanography*, vol. 14, pp. 1079–1094, 1984.

- [10] C. Garrett and F. Majaess, "Non-isostatic response of sea-level to atmospheric pressure in the Eastern Mediterranean," *Journal of Physical Oceanography*, vol. 14, pp. 656–665, 1984.
- [11] A. A. H. El-Gindy and F. M. Eid, "Long term variations of monthly mean sea level and its relation to atmospheric pressure in the Mediterranean Sea," *International Hydrographic Review*, vol. 67, no. 1, pp. 147–159, 1990.
- [12] M. N. Tsimplis, "The response of sea level to atmospheric forcing in the Mediterranean," *Journal of Coastal Research*, vol. 11, no. 4, pp. 1309–1321, 1995.
- [13] M. N. Tsimplis and G. N. Vlahakis, "Meteorological forcing and sea level variability in the Aegean Sea," *Journal of Geophysical Research*, vol. 99, no. C5, pp. 9879–9890, 1994.
- [14] P. Y. Le Traon and P. Gauzelin, "Response of the Mediterranean mean sea level to atmospheric pressure forcing," *Journal of Geophysical Research*, vol. 102, no. C1, pp. 973–984, 1997.
- [15] O. Faggioni, M. Soldani, G. L. Piangiamore et al., "Harbour water management for port structures and sea bottom design, coast proximity navigation management, water quality control," in *Proceedings of Mediterranean Days of Coastal and Port Engineering*, Palermo, Italy, October 2008.
- [16] C. Wunsch and D. Stammer, "Atmospheric loading and the oceanic "Inverted barometer" effect," *Reviews of Geophysics*, vol. 35, no. 1, pp. 79–107, 1997.
- [17] J. Willebrand, S. Philander, and R. Pacanowski, "The oceanic response to large-scale atmospheric disturbances," *Journal of Physical Oceanography*, vol. 10, pp. 411–429, 1980.
- [18] R. M. Ponte and P. Gaspar, "Regional analysis of the inverted barometer effect over the global ocean using TOPEX/POSEIDON data and model results," *Journal of Geophysical Research*, vol. 104, no. C7, pp. 15587–15601, 1999.
- [19] *Aviso and PoDaac User Handbook—IGDR and GDR Jason-1 Product, SMM-MU-M5-OP-13184-CN*, 4.1 edition, 2008.
- [20] G. B. Brassington, "Ocean prediction issues related to weather and climate prediction," in *Proceedings of the 15th Session of the Commission for Atmospheric Sciences*, Seoul, Republic of Korea, November 2009.
- [21] I. Moon, "Impact of a coupled ocean wave-tide-circulation system on coastal modeling," *Ocean Modelling*, vol. 8, no. 3, pp. 203–236, 2005.
- [22] P. Lynch, "The origins of computer weather prediction and climate modeling," *Journal of Computational Physics*, vol. 227, no. 7, pp. 3431–3444, 2008.
- [23] P. Lynch, "Weather prediction by numerical process," in *The Emergence of Numerical Weather Prediction*, pp. 1–27, Cambridge University Press, 2006.
- [24] American Institute of Physics, *Atmospheric General Circulation Modeling*, 2008.
- [25] H. Hughes, *Model Output Statistics Forecast Guidance*, United States Air Force Environmental Technical Applications Center, 1976.
- [26] D. L. Best and S. P. Pryor, *Air Weather Service Model Output Statistics Systems*, Air Force Global Weather Central, 1983.
- [27] D. J. Stensrud, *Parameterization Schemes: Keys to Understanding Numerical Weather Prediction Models*, Cambridge University Press, 2007.
- [28] T. N. Krishnamurti, "Numerical weather prediction," *Annual Review of Fluid Mechanics*, vol. 27, no. 1, pp. 195–224, 1995.

Research Article

Relationship of Worldwide Rocket Launch Crashes with Geophysical Parameters

N. Romanova,¹ N. Crosby,² and V. Pilipenko³

¹ *Institute of Physics of the Earth, Russian Academy of Sciences, Gruzinskaya Street 10-1, Moscow 123995, Russia*

² *Belgian Institute for Space Aeronomy, Ringlaan 3 Avenue Circulaire, Brussels 1180, Belgium*

³ *Space Research Institute (IKI), Russian Academy of Sciences, Profsoyuznaya Street 84/32, Moscow 117997, Russia*

Correspondence should be addressed to N. Romanova; runatka@mail.ru

Received 7 November 2012; Revised 14 February 2013; Accepted 8 April 2013

Academic Editor: Umberta Tinivella

Copyright © 2013 N. Romanova et al. This is an open access article distributed under the Creative Commons Attribution License, which permits unrestricted use, distribution, and reproduction in any medium, provided the original work is properly cited.

A statistical comparison of launch crashes at different worldwide space ports with geophysical factors has been performed. A comprehensive database has been compiled, which includes 50 years of information from the beginning of the space age in 1957 about launch crashes occurring world-wide. Special attention has been paid to statistics concerning launches at the largest space ports: Plesetsk, Baikonur, Cape Canaveral, and Vandenberg. In search of a possible influence of geophysical factors on launch failures, such parameters as the vehicle type, local time, season, sunspot number, high-energy electron fluxes, and solar proton events have been examined. Also, we have analyzed correlations with the geomagnetic indices as indirect indicators of the space weather condition. Regularities found in this study suggest that further detailed studies of space weather effects on launcher systems, especially in the high-latitude regions, should be performed.

1. Introduction

Since the beginning of the space era in 1957 more than 5000 space vehicles have been launched from different space ports in the world. Details of world-wide space ports (latitude/longitude, operational period, total number of launches, and launch crashes) are listed in Table 1, and their locations are shown in Figure 1. However, 384 of these launches were reported to have failed through 2008. The total number of launches and crashes at the major space ports from 1957 till 2008 is shown in Figure 2.

Launch crashes are commonly attributed to engineering faults in the rocket equipment and/or control system during launch. Specifically, the reason behind launch crashes can be due to a wide range of reasons: construction errors of the rocket launcher and launch complex systems; breakdown in the preparation process; human factor. Crashes during the prime stage phase of launch (up to an altitude of ~100 km) are mainly caused by combustion instability, ignition failure, turbopump overheating, insufficient control gain, staging electrical disconnect, and so forth. Any such failure results

in enormous financial losses for the space industry and insurance companies [1]. A possible influence of geophysical factors (meteorological or space environment) on rocket systems may be questioned. Even though the number of critical situations during takeoff and space flight related to the space weather is probably not very high as compared with general statistics, even a single event causes a huge financial loss.

There is ever growing evidence that the dynamic space environment may have hazardous effect on high-technology systems in general, and on electronic equipment of near-Earth orbiting satellites in particular [2, 3]. Clouds of low-energy electrons may produce differential charging of spacecraft surfaces and cause electrical discharges in control systems, whereas penetrating radiation and high-energy electrons can produce volume charging and destructive electrical discharges [4–7]. The effects of space weather on ground technology infrastructure [8] and aviation [9] are actively examined. According to an estimate of the US Aircraft Insurance Group, the space weather impact was responsible for ~\$ 0,5 billion revenue loss in 1996–2000 [10, 11]. However, the possible impact of space weather on rocket launches has not

TABLE 1: Main world space ports.

Space port	State owned	Lat.°	Long.°	Period of operation	# of launches	# of crashes
(1) Plesetsk	USSR/Russia	63N	41E	1966–present	1558	66
(2) Baikonur	USSR/Russia	46N	62E	1957–present	1288	109
(3) Cape Canaveral	USA	28N	80W	1957–present	638	62
(4) Vandenberg AFB	USA	34N	120W	1959–present	586	50
(5) Centre Spatial Guyanais, Kourou	Guyane Francaise	05N	52W	1968–present	189	14
(6) Kapustin Jar	USSR/Russia	48N	45E	1961–1999	100	16
(7) Xichang Space Center	China	28N	102E	1984–present	47	4
(8) Tanegashima	Japan	30N	130E	1975–present	44	2
(9) Naval Missile Facility, Point Arguello	USA	34N	120W	1986–present	44	12
(10) Wallops Flight Facility	USA	38N	75W	1960–present	42	3
(11) Jiuquan	China	40N	100E	1970–present	42	5
(12) Kagoshima	Japan	31N	130E	1966–2006	35	8
(13) Taiyuan	China	37N	112E	1988–2006	23	2
(14) Sea Launch, Platform Odyssey	USA, Russia, Ukraine, Norway	0	154W	1999–present	24	2
Others		—	—	1957–present	229	29

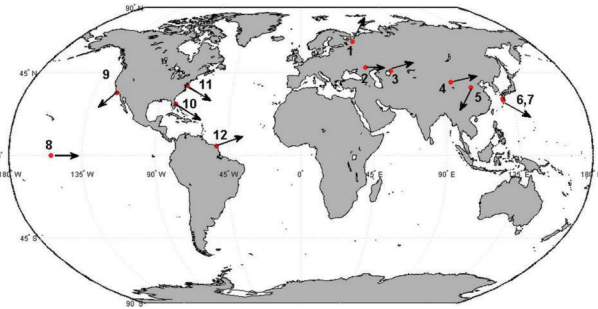


FIGURE 1: World map locations of main space sites. Arrows indicate the main direction of rocket trajectory after launch. The key worldwide spaceports are as follows: (1) Plesetsk, (2) Kapustin Jar, (3) Baykonur, (4) Jiuquan Space Center, (5) Taiyuan Satellite Launch Center, (6) Tanegashima Space Center, (7) Kagoshima Space Center, (8) Sea Launch, (9) Vandenberg, (10) Cape Canaveral, (11) Wallops space factory, and (12) Centre Spatial Guyanais (Kourou).

been thoroughly examined yet. So, it is still uncertain whether the rocket community should introduce some procedures for mitigating the space weather adverse influence on rocket launches.

Cases of space vehicle failures during magnetic storms have been noticed by Romanova et al. [12], who analyzed the statistics of launchers at the Plesetsk site for the period 1966–2005. They found that the relative number of launch crashes was nearly 2 times higher at summertime than during other seasons and statistically increased during elevated geomagnetic activity. The reason of this effect and its statistical validation needs further studies.

In this paper, we examine statistically all world-wide launch crashes occurring at all major space sites from 1957 to 2008. Though the number of available space weather and geophysical parameters is very limited, we believe that examination of even basic indirect parameters could be worthwhile to outline directions of further more detailed studies. If

crashes do not depend on geophysical/space environment, then the corresponding geophysical parameters during failure events should have random distributions. The randomness of pertinent geophysical parameters will be evaluated in this study. The data used are described in Section 2. Section 3 presents general statistical properties of the launch failures, including their seasonal and diurnal variations, and dependence on vehicle type. In Section 4, the dependence of failures on solar and geomagnetic activity at various launching sites is analyzed, and, in Section 5, the results of the study are discussed and main conclusions are given.

2. Spacecraft Launch Databases

For this study, we have compiled a complete spacecraft launch database based on information available from the following resources:

- (1) History of Spaceflight website by J. McDowell (<http://www.planet4589.org/space/>);
- (2) Encyclopedia “Cosmonautics” (Chronicle of accidents and catastrophes) by A. Zheleznyakov (<http://www.cosmoworld.ru/>);
- (3) Vehicle Launch Log from Encyclopedia Astronautica (<http://www.astronautix.com/data/>);
- (4) Southwest’s Source for Space and Astronomy Information (<http://www.spacearchive.info/>);
- (5) SPACEWARN monthly Bulletin of the NASA National Space Science Data Center (<http://nssdc.gsfc.nasa.gov/spacewarn/>).

This merged database contains information about successful launches as well as failures and is available for the scientific community via the Internet (<http://geomagnet.ifz.ru/>). The database contains information about launch times, launching sites or platforms, vehicle types, and successfulness of launches. For failed launches we tried to find a more

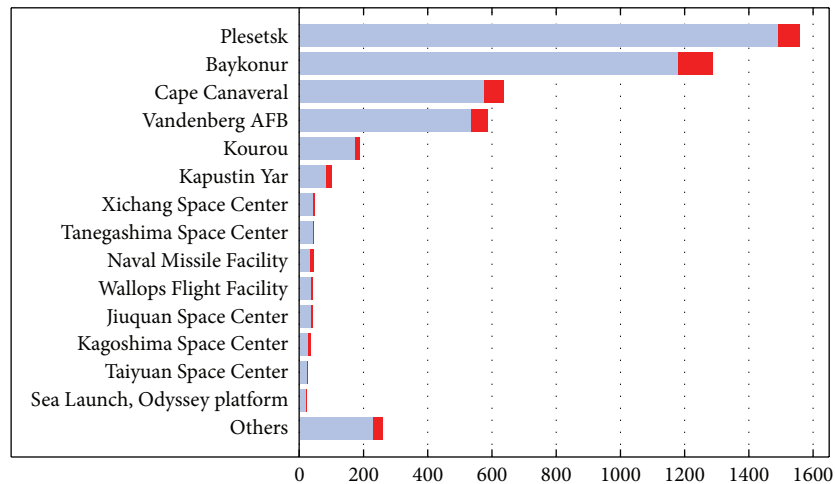


FIGURE 2: Number of launches from the most-used space ports in the world from 1957 till 2008. Red mark denotes crashes.

detailed description of the problem from other additional resources (news, space agency official bulletins, etc.). In our analysis, an event has been classified as “launch crash” if the reason by which the spacecraft did not reach its planned orbit cannot be explained neither by rocket destruction nor the malfunction of the launcher’s control system. The compiled database comprises the 50-year period, from 1957 to 2008. The statistical analysis of failed events has been made for the major sites: Cape Canaveral, Pleseetsk, Baykonur, and Vandenberg. For other launch sites the statistics is not large enough for statistically significant results. Emergencies at the launch pad before the actual takeoff (e.g., explosion during prelaunch preparation, fuel fire, loss of launcher engine thrust, etc.) have been excluded from the analysis. The launches of all manned missions (e.g., NASA Shuttle from Canaveral) are not included, because of limited statistics and specifics of the prelaunch operation. Thus, only the failures which occurred in the high-altitude atmosphere or ionosphere during the takeoff or initial phase of the mission are included. The major part of the failures occurred at altitudes ranging from 15 to 100 km; however, it is not possible to give a more precise distribution of failure rate along the altitude because of lack of information.

The long-term databases of direct measurements of radiation in space (e.g., fluxes of precipitated high-energy particles) at low altitudes are not available, therefore, for statistical analysis we use, as indirect measures of the space weather, various solar and geomagnetic indices: sunspot number (Wolf’s number) R ; planetary geomagnetic index K_p characterizing the midlatitude geomagnetic activity; AE index measuring the intensity of auroral disturbances; D_{st} index characterizing the ring current intensity. Additionally, we use the solar proton flux intensity J with energies $E > 1, 2, 4,$ and 10 MeV measured by interplanetary monitors IMP5-8; the high-energy electron fluxes ($E = 50$ keV–2 MeV) from geostationary satellites LANL and GOES.

The parameters R , K_p , and J have been taken from the OMNI database (<http://omniweb.gsfc.nasa.gov/>); geomagnetic indices D_{st} and AE have been provided by the World

Data Center for Geomagnetism (<http://wdc.kugi.kyoto-u.ac.jp/aedir/index.html>). Additionally, the index P characterizing the total power input by auroral particles precipitating into the Northern polar region, measured by NOAA satellites (<http://www.swpc.noaa.gov/pmap/>), has been used.

3. General Properties of Crash Probability and Analysis Methods

Yearly distributions of the number of launches, crash launches, and relative number of crashes for all world-wide launching sites from 1957 till 2007 are shown in Figure 3. These plots show that the number of failures was very high at the beginning of the space era (1957–1961), then slowly decreased till 1975 and since then has remained nearly at the same level. As a measure of failure rate we use the crash probability, that is, the relative number of crashes normalized by a number of launches throughout a certain period. The failure rate for each launching site varies from 4% to 10% and decreases in general with the growth of launch number. For the whole period of operation the largest rate of failures occurred at Kapustin Yar (16%), thereafter at Cape Canaveral (10%), Baikonur (8.5%), Vandenberg (8.5%), Kourou (7%), and the lowest rate of failures was at Pleseetsk (4%).

We will estimate the dependence/independence of an accident occurrence and a parameter under the study with the following statistical approach. To come up with a measure of their dependence, we will use the χ^2 test [13]. In this particular case, one of the two variables is the Boolean indicator of whether or not an incident happened, and the other variable is a parameter. Our null hypothesis is the assumption that this parameter and launch failures are independent. Given marginal frequencies of a particular parameter and launch failures, we can calculate (based on that independence assumption) the theoretical frequencies of failures for each parameter value. Next, we compare these theoretical frequencies with the actual frequencies observed. The χ^2 test is used to decide if the deviation of the observed

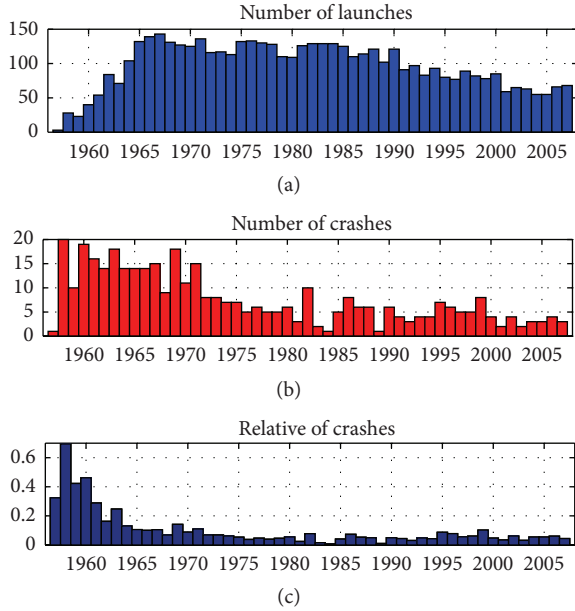


FIGURE 3: Yearly distributions of the number of launches, launch failures, and relative number of crashes for all world-wide launches from 1957 till 2007. Relative number of crashes is the number of crashes per year normalized by the number of total launches that year.

frequencies from the theoretical ones is large enough to reject the null hypothesis. Two random variables are considered independent if the observed frequencies are close to the expected theoretical frequencies. The Pearson χ^2 -criterion checks whether the summary deviations of the failure rate from the expected rate are within the tail α of the event distribution, where the apriori significance level α has been chosen to be 0.05. Additionally, we estimate the attained level of significance (P -value), which is the probability to get a larger statistical criterion than for a given sample. The larger is P -value, the higher is the probability that null-hypothesis is correct. If the P value is smaller than the chosen apriori significance level α , the null hypothesis must be rejected.

The statistical analysis of the failure rate dependence on various technical and geophysical parameters, launcher type, season, magnetic activity, and so forth, has been performed in a similar way. We have applied also the method of superposed epoch analysis which gives the possibility to estimate relatively short-period variations around the moment of a failure.

3.1. Statistics of Failures for Different Types of Launchers. Since the onset of the space era, more than 60 types of launch vehicles have been used [14]. For the statistical analysis, we select only those launchers that are widely used (not less than 100 launches). Differences between modifications of the same type of launchers have been neglected (e.g., all launch vehicles Ariane-1, Ariane-2, and so forth, have been considered as just Ariane, the rocket Kosmos assumes Kosmos-11 K65, Kosmos-65S3, etc.). The comparison of the failure rate for various types of launchers is shown Figure 4.

We will estimate dependence/independence of the accident occurrence on a launcher type. In this case, one of two

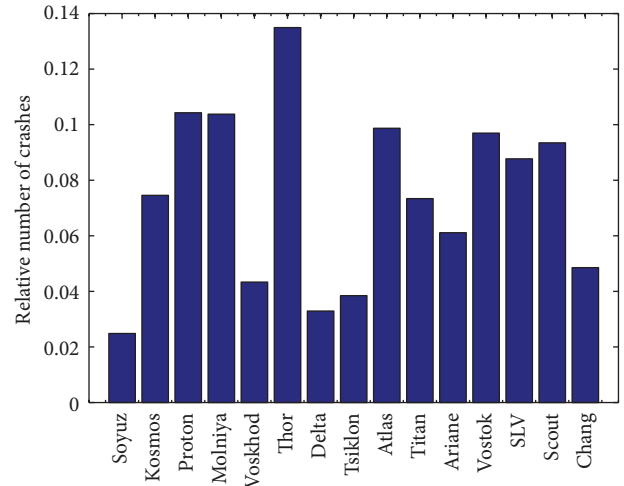


FIGURE 4: Relative number of crashes (the number of crashes normalized on a number of launches) for various types of launchers.

statistical variables is the Boolean indicator of whether or not an incident happened, and the other variable is the launcher type. From 4333 launches under examination 295 (6.8%) of them failed. If a failure rate does not depend on a type of launcher, then in each group this rate must be 6.8%. However, Pearson χ^2 -criterion indicates a relation between the failure rate and launcher type. However, this criterion does not show which particular group of launchers is more vulnerable to failures. Attained level of significance $P < 10^{-5}$, while $\chi^2 = 120$, hence, the null hypothesis must be rejected. Soyuz and Thor launchers have the largest deviation from the expected 6.8% failure rate: the failure rate for Soyuz is only 2.5%, and that for Thor is as high as 13%. Proton and Kosmos vehicles also have failure rates nearly 2 times higher than the average one.

We have verified the same null hypothesis for all launchers excluding Soyuz and Thor. For this subgroup, the attained level of significance is less than the apriori chosen $\alpha = 0.05$, which means that there are no statistical distinctions between failure risks for the remaining launcher types. Further, this sub-group has been compared with other groups of launchers, where the failure rate dependence on a type might be expected. The obtained χ^2 -criterion value turns out to be larger than the critical value, thus, it may be concluded that the four preselected launcher groups (Proton, Kosmos, Soyuz, and Thor) indeed differ from other launcher types. Then, we perform a similar exclusive analysis for each of the four groups taking into account the Bonferroni correction factor [15]. The Bonferroni correction is a safeguard against multiple tests of statistical significance on the same data falsely giving an appearance of significance purely by chance. If it is desired that the significance level for the whole family of tests should be α , then the Bonferroni correction would be to test each of the individual tests at a significance level of α/n , where n is the number of hypotheses to be tested. As a result, we found that for Proton and Kosmos launchers the deviations in the failure rate are statistically insignificant from others. For Soyuz and Thor, the deviations have been proven

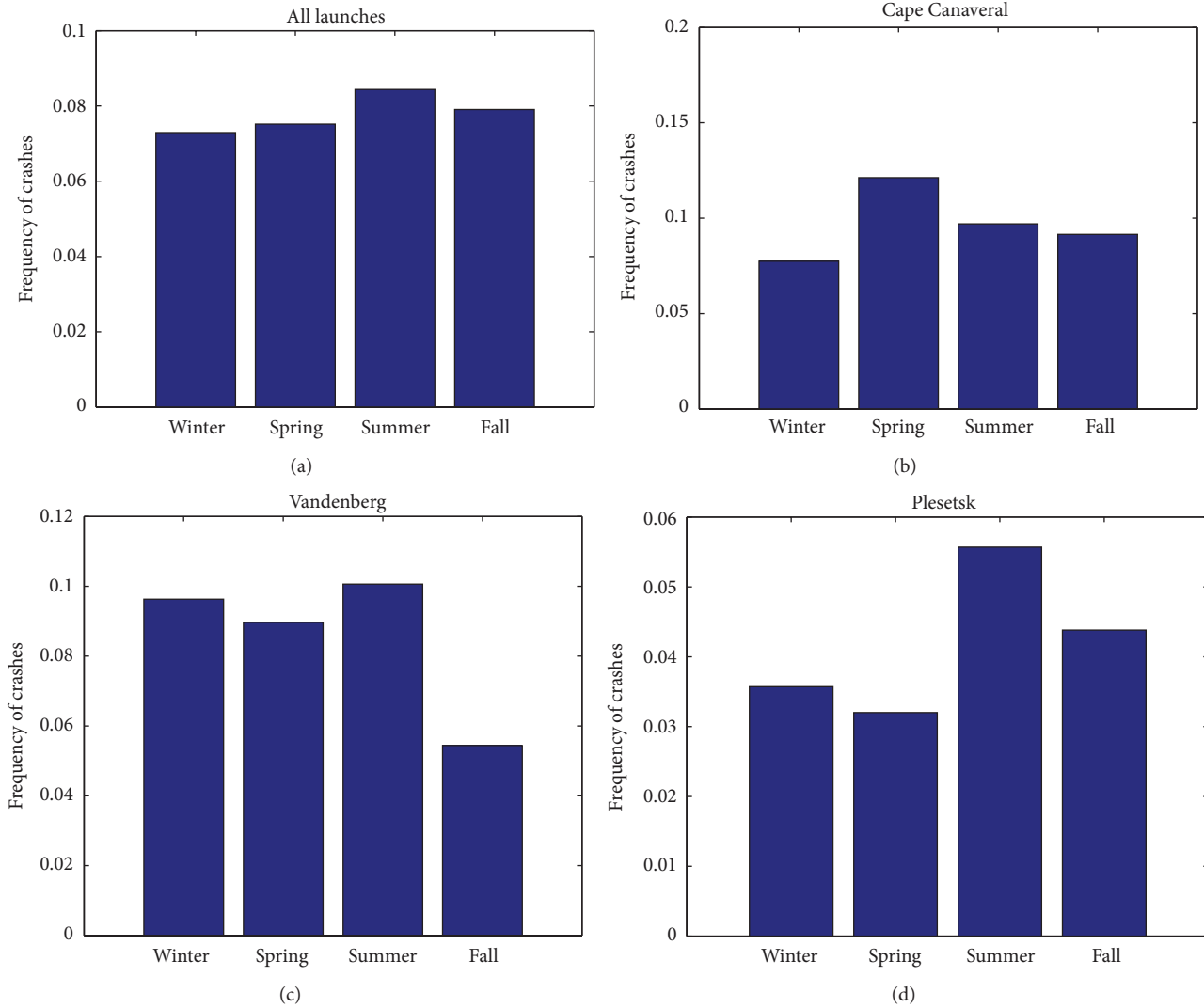


FIGURE 5: The season distribution of relative launch crashes (the relative number of crashes normalized on a number of launches throughout a certain season): (a) world-wide, (b) Cape Canaveral, (c) Vandenberg, and (d) Plesetsk.

to be statistically significant, so these thrusters are to be considered as most reliable and most risky, correspondingly.

3.2. Seasonal and Daily Variations of the Launch Crash Probability

3.2.1. Seasonal Effects. For the examination of seasonal dependence, all launches have been grouped into the winter period (December–February), spring (March–May), summer (June–August), and autumn (September–November). During the 50 years of operation, the seasonal probability distribution of all world-wide launch crashes (Figure 5(a)) is found to be very uniform for all four seasons with a slight increase in summer.

The seasonal dependence of the world-wide failure rate has been validated with the χ^2 -criterion, where a null hypothesis implies that the failure rate does not depend on the season

under the confidence level $\alpha = 0.05$. The statistical analysis proves the absence of any seasonal effect: the significance level $P = 0.9$, and $\chi^2 = 1.3$.

However, for some individual space ports the seasonal dependence has anomalies. For example, the frequency of crashes at Cape Canaveral seems to be higher in spring than during other seasons (Figure 5(b)). The accident rate at Vandenberg (Figure 5(c)) seems to decrease in autumn as compared with other seasons. At Plesetsk (Figure 5(d)) in summertime, the percentage of emergencies increases ~ 1.5 times as compared to other seasons. The seasonal distribution for Baikonur turns out to be flat and is not shown.

The statistical analysis with the use of the χ^2 -criterion reveals that both the spring peak at Cape Canaveral and autumn minimum at Vandenberg are statistically insignificant ($P = 0.6$, $\chi^2 = 1.8$ for Cape Canaveral, and $P = 0.5$, $\chi^2 = 2.5$ for Vandenberg). Thus, the visual impression

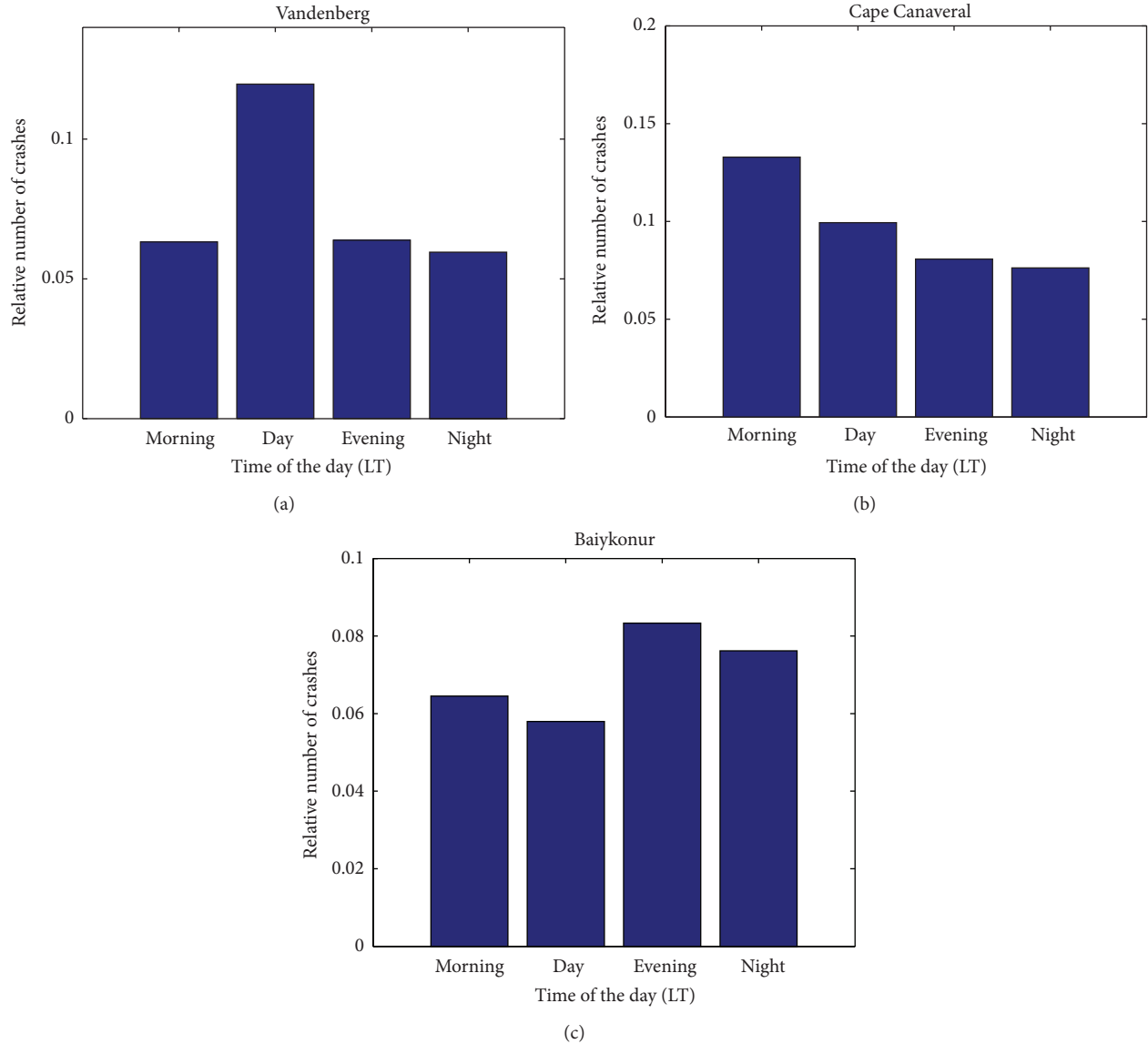


FIGURE 6: The daily distributions of relative launch crashes at the main space ports: (a) Vandenberg (UT -8 hr), (b) Cape Canaveral (UT -05 hr), and (c) Baikonur (UT $+05$ hr) depending on LT sector: morning (LT = 06–11), afternoon (LT = 12–17), evening (LT = 18–23), and night (LT = 23–05).

is not supported by the statistical validation, so the seasonal peaks at these launching sites are statistically insignificant.

The statistical validation with the χ^2 -criterion shows that the summer maximum at Plesetsk turns out to be near the limits of statistical fluctuations. The probability of the first order error is rather high, ~ 0.4 , thus, the increase of take-off failures at Plesetsk in the summer time is very near to the statistical dispersion, or just slightly above it ($P = 0.2$, $\chi^2 = 4$). Thus, no launching site shows a statistically convincing dependence of the launch failures on a season.

3.2.2. Daily Variations. We have tried to evaluate the diurnal distribution of launch failures, though the time of launch is

not known for all events. These daily time distributions of launch crashes at different sites (Vandenberg, Cape Canaveral, and Baikonur) are shown in Figure 6. The events are binned according to their local time (LT) into the following subsets: “morning” (LT = 06–11), “afternoon” (LT = 12–17), “evening” (LT = 18–23), and “night” (LT = 23–05).

It is natural to suppose that the failure rate is to be the same at all local times. However, interesting local peculiarities can be revealed at space ports Canaveral and Vandenberg. The failure rate at Canaveral (Figure 6(b)) has a weak increase in the morning hours, but the χ^2 -criterion shows that this increase is not statistically significant ($P = 0.3$, $\chi^2 = 3.5$). At Vandenberg (Figure 6(a)) during the daytime, the failure rate increases ~ 2 times as compared to the rest of the day. This

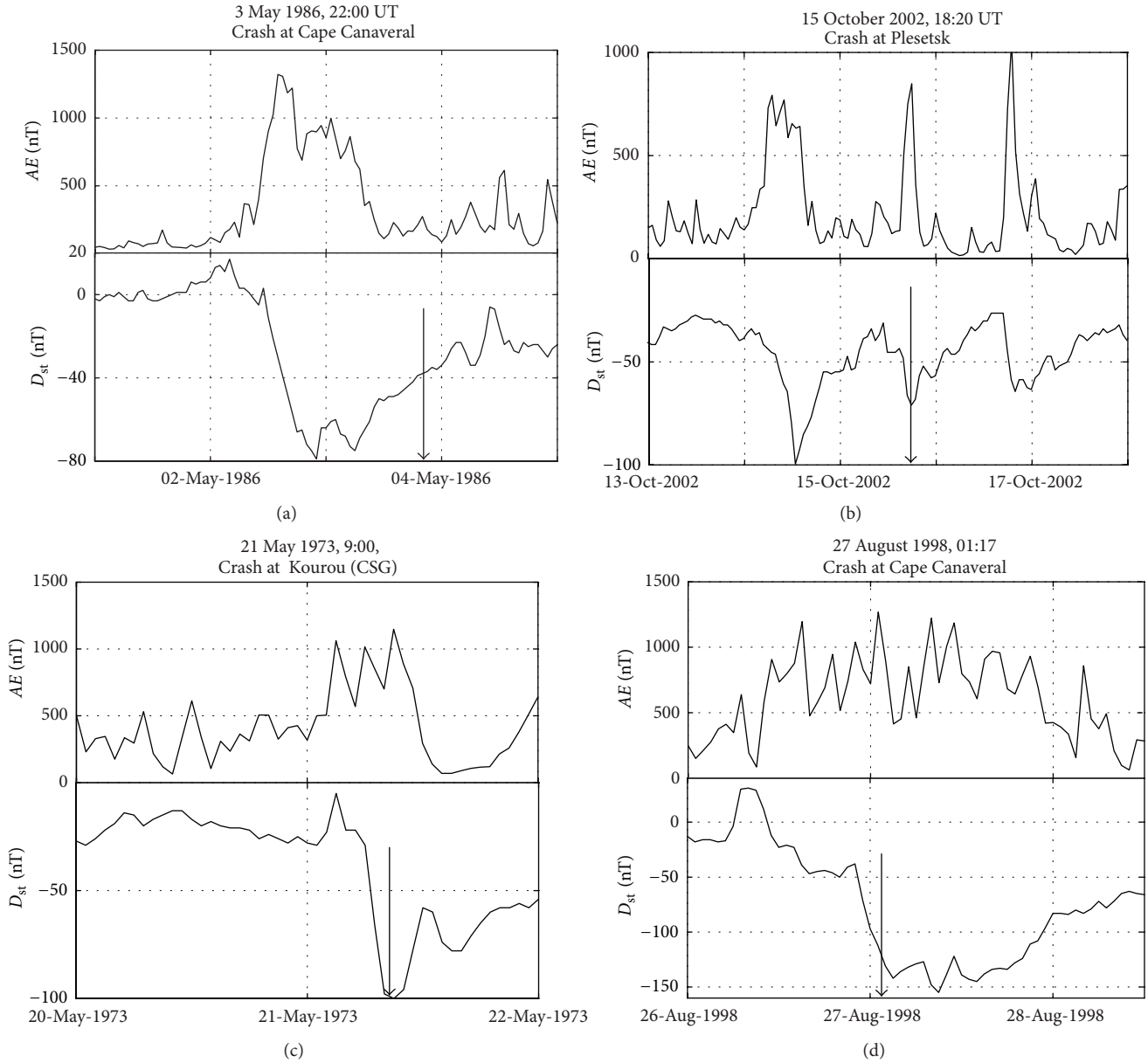


FIGURE 7: Examples of launch failures during magnetic storms: (a) rocket Delta at Cape Canaveral on May 02, 1986, (b) rocket Soyuz at Plesetsk on October 15, 2002, (c) rocket Diamant B at Kourou on May 21, 1973, and (d) rocket Delta at Cape Canaveral on August 27, 1998.

increase turns out to be statistically significant according to the χ^2 -criterion ($P = 0.039$, $\chi^2 = 8.31$). We are not aware of any reasonable explanation for this fact.

4. Launch Crashes, Solar, and Geomagnetic Activity

4.1. Example of Launches during Severe Space Weather. A possible relation of launch failures with space weather conditions may result from the fact that ~40% of failures occurred when during the day before the launch the indices indicated geomagnetic disturbances: $D_{st} < -50$ nT and $AE > 500$ nT. More than half of failures (56%) occurred when $K_p > 3$ the

day before launch. Nearly 10% of failures occurred during main and ~20% during recovery phase of magnetic storm. However, a relationship between the space weather and take-off failures, if it exists, is not straightforward. During periods of strong space weather disturbances, as characterized by geomagnetic indices, evidence has been found of both successful launches and failures. Figure 7 shows several examples of launch failures during times of disturbed space weather.

The rocket Delta 3914 failure on May 3, 1986 (Figure 7(a)), which prevented the placement into orbit the GOES-G satellite, occurred just after an intense substorm ($AE \sim 1300$ nT) during moderate, but long-lasting magnetic storm ($D_{st} \sim -80$ nT). The engine of the third stage accidentally turned on too early because of errors in the electronic system.

On October 15, 2002 (Figure 7(b)) at Plesetsk the space laboratory Foton-M was launched by the middle-range rocket Sojuz-U. Approximately 30 sec after takeoff, the 400 tons rocket exploded because of an unknown technical error, causing a forest fire and casualties. This crash occurred during a moderate magnetic storm ($D_{st} \sim -70$ nT, $AE \sim 800$ nT). The actual cause of the crash has not been identified.

On May 21, 1973 (Figure 7(c)) during the main phase of a strong magnetic storm ($D_{st} \sim -100$ nT), the rocket Diamant-B crashed by an unknown reason at the Kourou launching site.

On August 27, 1998 (Figure 7(d)) the rocket Delta-8930 carrying the Galaxy satellite lost radio contact with Canaveral 80 sec after takeoff and fell down into the ocean. This crash occurred during the main phase of a strong magnetic storm ($D_{st} \sim -150$ nT, $AE \sim 1200$ nT). On the preceding day, August 26, during the solar proton event, the flux of protons with $E > 10$ MeV reached $J \sim 670$ ($\text{cm} \cdot \text{s} \cdot \text{str}$)⁻¹ and was still highly elevated during the crash.

There are many other examples of launch failures during the main and recovery phases of magnetic storms (not shown): launch failures at Plesetsk on March 28, 1995 and October 15, 1986—a day after a magnetic storm onset; at Baikonur on March 25, 1966, November 25, 2002, July 22, 1971, and December 9, 1982—less than a day after a moderate magnetic storm onset; at Jiquian Space Centre on July 28, 1979; at Centre Spatial Guyanais on September 10, 1982—at the recovery phase of a strong magnetic storm, and so forth.

On the other hand, on July 15, 2000 a strong geomagnetic storm occurred: D_{st} index reached as low as -295 nT, and other geomagnetic indices were very high $AE \sim 1800$ nT, $K_p \sim 9$ [16]. On this date, there were severe accidents onboard various spacecraft, for example, total loss of ASCA satellite, temporary problems with GOES-8,10, ACE, WIND, SOHO, YOHKOH, TRACE, and others [17]. Nonetheless, from the Plesetsk the rocket Kosmos-11K65 M was successfully launched during this period.

4.2. Dependence of the Launch Failures on Solar Activity. The comparison of solar activity, as characterized by yearly averaged Wolf number $\langle R \rangle$, and yearly distributions of the relative number of crashes (i.e., yearly number of failures normalized by the yearly number of launches) for all worldwide launches from 1957 till 2007 is shown in Figure 8. A surprisingly high (~ 0.36) positive correlation of the relative number of crashes with the average annual level of solar activity can be seen for the entire period from 1957–2007.

However, a careful analysis shows that this high correlation is due mainly to the beginning of the space age: from 1957 till 1975, when the correlation coefficient of the crash probability with $\langle R \rangle$ is high, ~ 0.69 , whereas the significance level of this correlation is $P = 0.0015$. Since the magnitude of P is less than $\alpha = 0.05$, this correlation is statistically significant.

For later time intervals, the correlation decreases, and, for the interval 1978–2007, the correlation coefficient becomes -0.26 . The relevant significance level is $P = 0.2$, which means that the correlation is lacking. We suggest that this

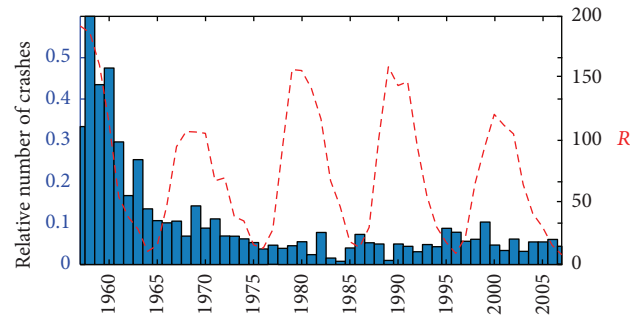


FIGURE 8: The comparison of yearly distributions solar activity, as characterized by sunspot number $\langle R \rangle$ (red curve) and the relative number of crashes for all launches from 1957 till 1975 (blue histogram).

dependence is due to the fact that the beginning of the space age coincided with the solar maximum in 1957, and that in the following years the decrease of failures is mainly attributed to improvements of technology and skill of personnel. Later on, when the failure rate was stabilized at most launching sites, no indications on the solar activity dependence can be seen.

4.3. Geomagnetic Activity Effect. The indices of geomagnetic and auroral activity have been analyzed for the time period around every launch crash. The statistical null hypothesis assumes that the time of launch is random in respect to geomagnetic activity, so launches are to have the Poisson distribution in respect to the geomagnetic indices. Thus, the probability of the launch occurrence during a particular value of geomagnetic index is determined by the intrinsic index distribution only. Indeed, the general statistical distribution of geomagnetic indices and distribution of indices during the failures have turned out to be similar. However, because the index distributions are not normal (rather power law), one cannot apply the parametric methods (e.g., dispersion analysis) [13] for the validation of the relationships between the geomagnetic activity and the failure rate. Only if there is a distinction between the statistical distributions of indices during the events and general statistics, may one assume the possibility of the failure being related to geomagnetic activity.

Because the level of energetic particle fluxes in the terrestrial magnetosphere is considerably determined by the prehistory of the magnetospheric disturbance evolution, we use the maximum value of the geomagnetic indices $K_p^{(\max)}$, $AE^{(\max)}$, and $D_{st}^{(\max)}$ during a 24-hour period before a takeoff as a measure of space weather conditions.

In Table 2, the attained levels of significance (χ^2 -criterion) are summarized for each geomagnetic index. As a measure of failure probability, the relative number of failures normalized by the number of launches during an analyzed period has been taken. The relative number of world-wide crashes under a given level of $AE^{(\max)}$ index (Figure 9(a)) and $K_p^{(\max)}$ index (Figure 9(b)) is about the same, $\sim 9\%$, for any interval of the index. Despite the visual impression that there seems to be an enhanced failure rate during moderately

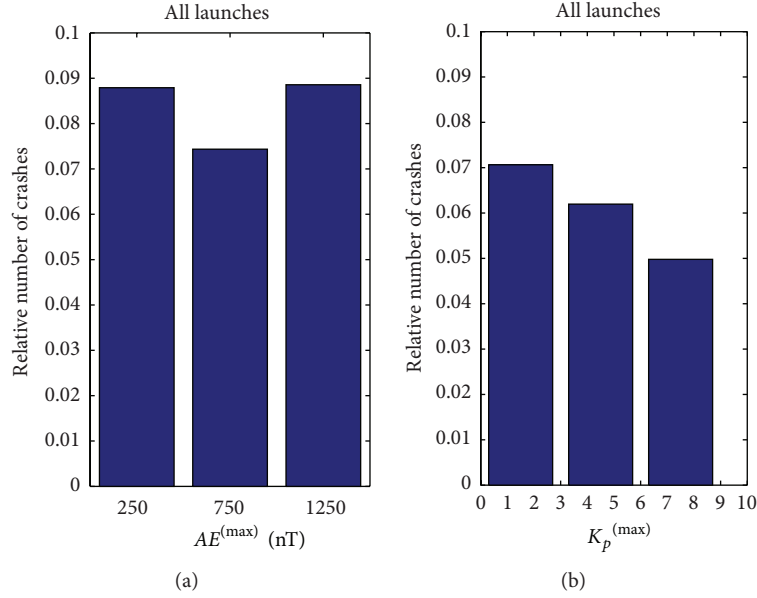


FIGURE 9: Relative number of crashes for different levels of geomagnetic indices (for maximum value for the previous day) of K_p (a) and AE (b).

disturbed storms, $AE^{(\max)} > 500$ nT, the analysis does not reveal a statistically significant distinction between the general sample and the distribution during launch failures. Both for $K_p^{(\max)}$ (Figure 9(b)) and $D_{st}^{(\max)}$ (not shown) the dependence of launch failure on magnetic activity level is statistically insignificant.

Though the total failure rate does not depend on geomagnetic activity, such dependence could be revealed for a particular launch site, because geophysical factors are strongly latitude dependent. Therefore, a possible dependence of the launch failure on geomagnetic activity has been statistically analyzed for each rocket site. The results of the estimated dependence of failures on geomagnetic activity are summarized in Table 2 for the midlatitude sites, Baikonur, Cape Canaveral, and Vandenberg, and the high-latitude Plesetsk site. The detailed analysis for each site is presented below.

4.3.1. Midlatitude Sites: Baikonur, Cape Canaveral, and Vandenberg. The histograms of the relative number of crashes at Baikonur for various intervals of $K_p^{(\max)}$ and $AE^{(\max)}$ values are given in Figure 10. The failure probability is pretty much the same for all levels of $AE^{(\max)}$ and $K_p^{(\max)}$ values. Some deviations at extreme magnitudes of $AE^{(\max)}$ and $K_p^{(\max)}$ indices are not statistically significant (Table 2). Neither does the analysis of failure rate on D_{st} index reveals any statistically significant relations (not shown). Thus, the failure probability at Baikonur does not depend on geomagnetic activity.

The failure probability at Cape Canaveral increases with the growth in the geomagnetic activity, characterized by $K_p^{(\max)}$ (Figure 11(a)) and $AE^{(\max)}$ (Figure 11(b)) indices. The increase of the failure rate at very high values, $K_p^{(\max)} > 6$ and $AE^{(\max)} > 1000$, is statistically significant. Nonetheless, we cannot prove this conclusion with a great confidence,

TABLE 2: The attained levels of significance (P -values) for relationships between launch failures at various launch sites and geomagnetic activity (italic data indicate the occurrence of statistically significant relationships if apriori significance level α has been chosen to be 0.05).

Launching site	Geomagnetic indices			
	K_p	D_{st}	AE	P
Total	0.31	0.82	0.32	—
Baikonur	0.47	0.22	0.9	—
Canaveral	<i>0.04</i>	0.38	<i>0.02</i>	<i>0.03</i>
Vandenberg	0.73	0.052	<i>0.04</i>	—
Plesetsk	0.27	0.76	0.8	<i>0.04</i>

“—”: relationship with the index was not checked (χ^2 -criterion).

because the sample number at high level of geomagnetic disturbances is not representative, only 7 events.

Therefore, the power of any statistical criterion is not very high, $\sim 55\%$, so the probability to reject wrongly the null hypothesis is high. Rather surprisingly, the statistical-ly significant relationships between the launch failures at Cape Canaveral with the auroral power index $P^{(\max)}$ have been revealed: the risk of failure increases for $P^{(\max)} > 125$ GW. However, a similar distribution in respect to the D_{st} index does not reveal any statistically significant effects (not shown). Thus, a statistically nonnegligible correlation between failure rate at Cape Canaveral and geomagnetic activity manifests itself only for indices mostly corresponding to the auroral and the middle latitude activity (AE , P , and K_p), but not to the near-equatorial disturbances (D_{st}).

A similar situation is observed at Vandenberg. The relative number of failures at this launch site shows a peak at high $AE^{(\max)}$ indices, 1000–1500 nT (Figure 12(a)), and

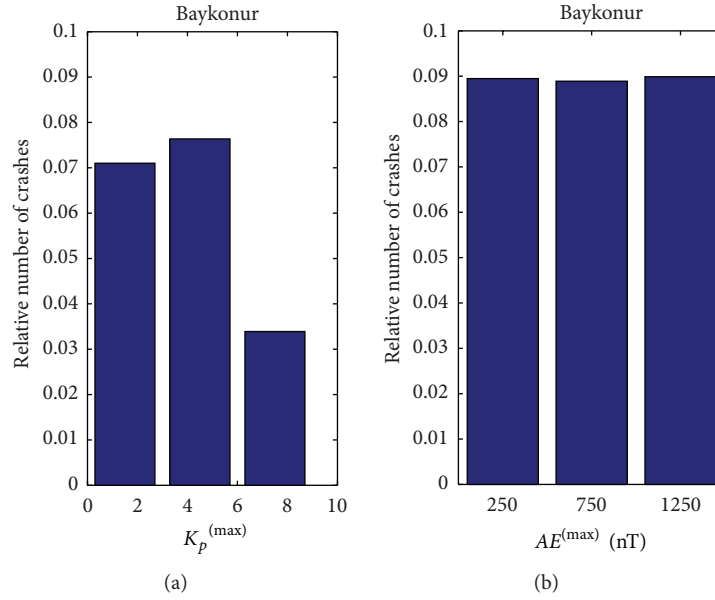


FIGURE 10: Relative number of crashes for different levels of geomagnetic indices K_p (a) and AE (b) at Baykonur.

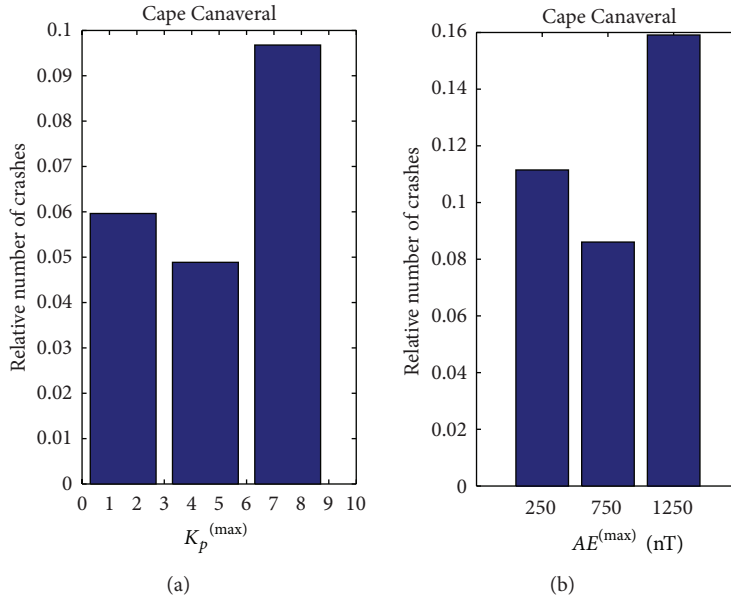


FIGURE 11: Relative number of crashes for different level of geomagnetic indices K_p (a) and AE (b) at Cape Canaveral.

this peak turns out to be statistically significant. However, other indices, K_p (not shown) and D_{st} (Figure 12(b)), do not demonstrate any dependence of the launch failures on the geomagnetic activity. At the same time, the increase of the failures at Vandenberg at high $AE^{(max)}$ is due to 5 events only.

4.3.2. *High-Latitude Space Port: Plesetsk.* The annual mean number of crashes at the high-latitude space port Plesetsk before 1993 varied from 1 to 3 with the average number

of launches being about 50 per year (Figure 13). While the number of launches at Plesetsk is the highest as compared with other launching sites, the general accident rate here is the lowest among all the launching sites (e.g., 2 times less than at Baikonur). From 1966 to 1975, the percentage of crashes steadily decreased, and, up to 1976, the percentage of crashes reached ~2% per year. Since 1993, the number of launches per year decreased (<20), but at the same time the number of crashes practically remained the same, which resulted in the growth of the relative number of accident risk.

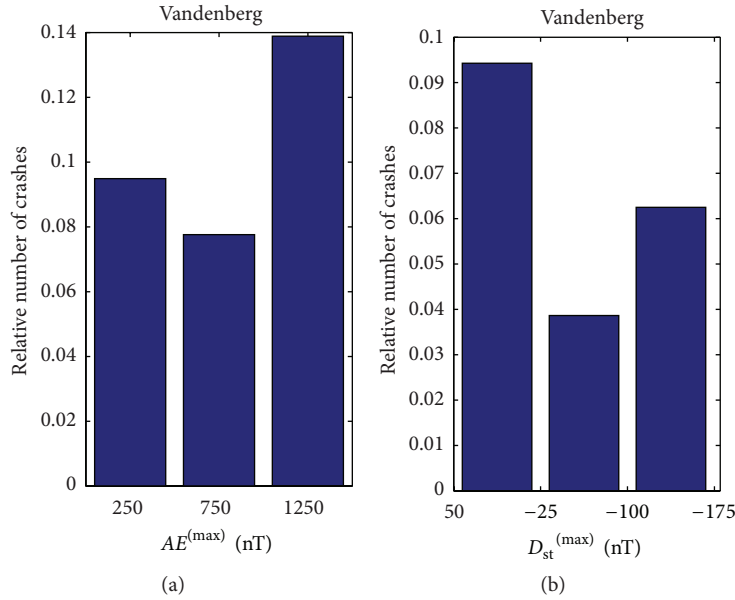


FIGURE 12: Relative number of crashes for different levels of geomagnetic indices AE (a) and D_{st} (b) at Vandenberg.

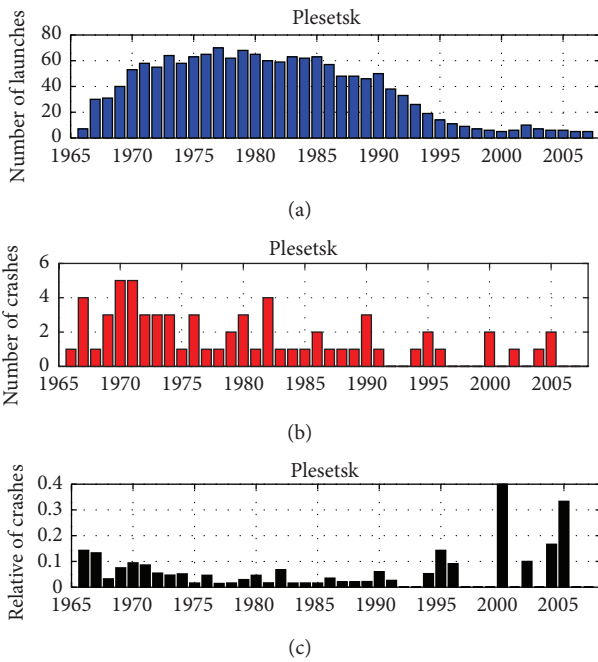


FIGURE 13: The yearly mean number of launches, crashes, and relative number of crashes (upper to lower panel) at the high-latitude space port Plesetsk from 1966 till 2007.

The relative percentage of emergencies (probability of crash) for Plesetsk is rather stable in time despite the fact that the number of launches has decreased and performance of rockets and take-off facilities has improved. We suggest that the reason for this feature may partly be due to the high-latitude location of Plesetsk. The initial trajectories of rockets launched from Plesetsk go through the auroral zone, where geomagnetic activity effects are major.

Comparison of each launch failure with the geomagnetic activity has shown that ~60% of failures took place when the hourly AE index exceeded 400 nT. The distribution of the relative number of launch failures in respect to geomagnetic indices D_{st} , AE , and K_p is shown in Figures 14(a), 14(b), and 14(c). Additionally, a similar histogram has been produced for the auroral P index, characterizing total power input by auroral particles to the northern polar region (Figure 14(d)). The statistical analysis of the failure rate dependence on various indices, D_{st} (Figure 14(a)), K_p (Figure 14(b)), AE (Figure 14(c)), and auroral particle index P (Figure 14(d)), rejects the null hypothesis about the independence of launch failures on these indices. Thus, there is a tendency of a failure rate increase at Plesetsk at higher levels of geomagnetic activity and auroral particle precipitation.

However, the power of statistical conclusions due to limited statistics is not high, so there is still a chance to reject incorrectly the null hypothesis. Separating the geomagnetic activity into two intervals, quiet ($AE \leq 400$ nT, $K_p \leq 3$, $D_{st} \geq -50$ nT) and disturbed ($AE > 400$ nT, $K_p > 3$, $D_{st} < -50$ nT), we found no statistically significant distinctions between quiet and disturbed conditions. If the geomagnetic activity can influence the launch failure rate, then there probably must be a threshold level for such an impact. Because of limited statistics, we cannot estimate reliably this threshold, but may suggest that it should be $AE \sim 1000$ nT.

4.4. The Relationship of Launch Failures with High-Energy Particle Fluxes

4.4.1. Launch Crashes and Solar Proton Events. A launch failure may be caused in principle by the burst of solar proton events. Effect of energetic particle events on rocket functioning depends on the type of orbit. Boscher et al. [18] estimated that the risk of failure for ARIANE 5 launch into

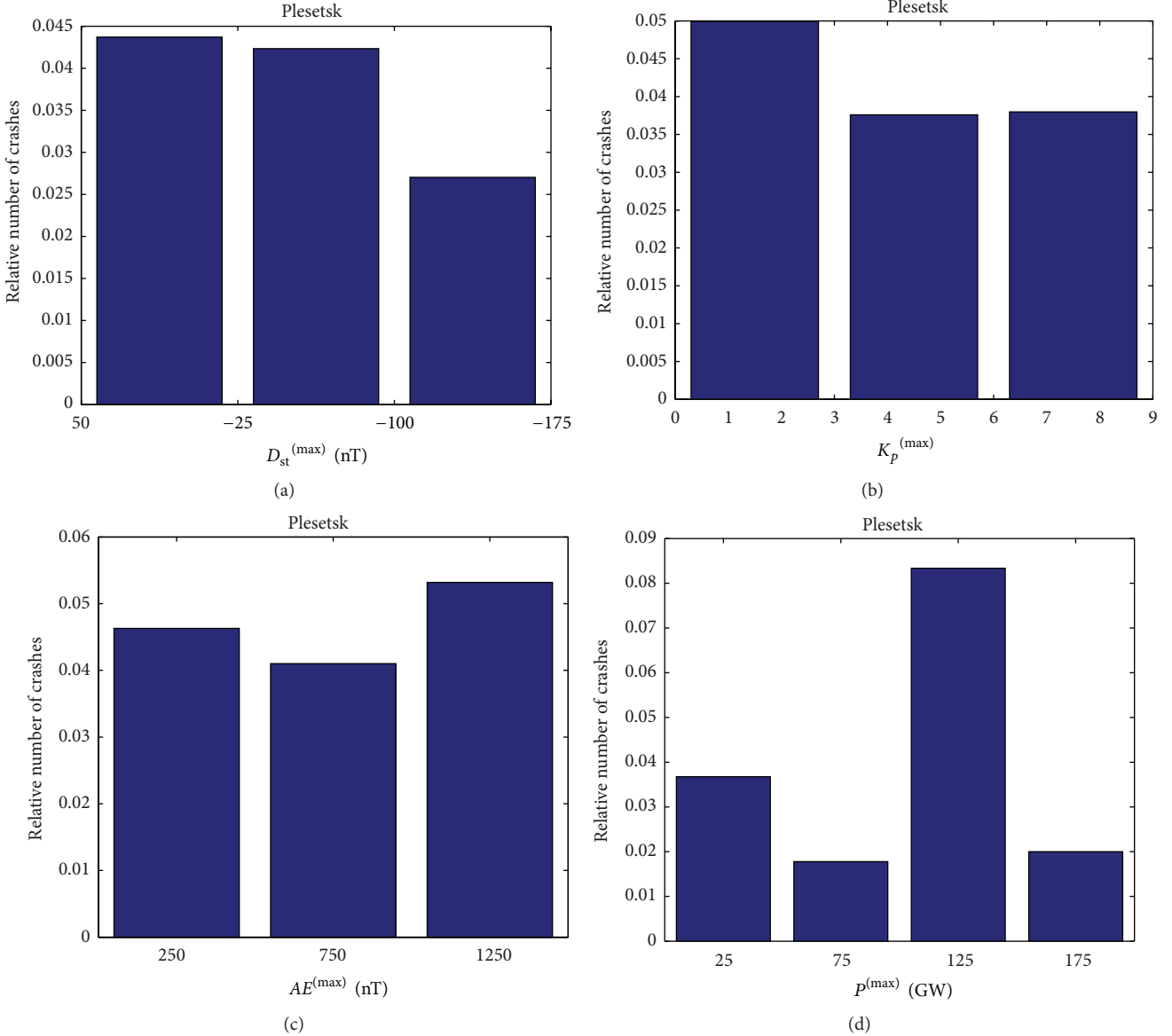


FIGURE 14: Relative number of crashes for different levels of geomagnetic indices at Plesetsk: (a) D_{st} ; (b) K_p ; (c) AE ; (d) auroral power index P .

geostationary orbit is insignificant, but it is increased by a factor of 200 for the launch into sun-synchronous orbit, and by a factor of 10 for a launch into geostationary transfer orbit. However, the overall probability of failure still was estimated to be below the target values (typically 0.02) with a possible exception of launch during a solar energetic proton event.

We have verified statistically the possibility of the hazardous impact of solar proton events on launches with the superposed epoch method. In this method, the instant of a launch failure has been taken as a zero reference moment, and variations of particle fluxes have been averaged according to this moment. The proton flux rate with $E > 4$ MeV measured by IMP averaged over all failed launch events at Cape Canaveral and Baykonour in the 5 days interval around the moment of launch is shown in Figure 15. Though the superposed epoch method demonstrates the occurrence of

the intensity peak 1 day before the launch at Cape Canaveral (Figure 15(a)) and the same day at Baykonour (Figure 15(b)), a statistical analysis does not prove a correspondence between these peaks and launch failures. The averaged superposed plots for all successful launches do not deviate noticeably from the plot for failed launches (dashed line). Moreover, the magnitudes of these peaks are less than the root mean squared deviation for given samples.

In no proton energy channels (from 1 MeV to 60 MeV), any statistically significant effect was observed. This dependence is rather flat and does not show any increase of solar proton intensity during or just before the failure. The same result was obtained for Plesetsk, Vandenberg, and for all crashes in total (not shown). Thus, we may conclude that there are no statistically reliable relationships between solar proton flux intensities and the studied launch failures.

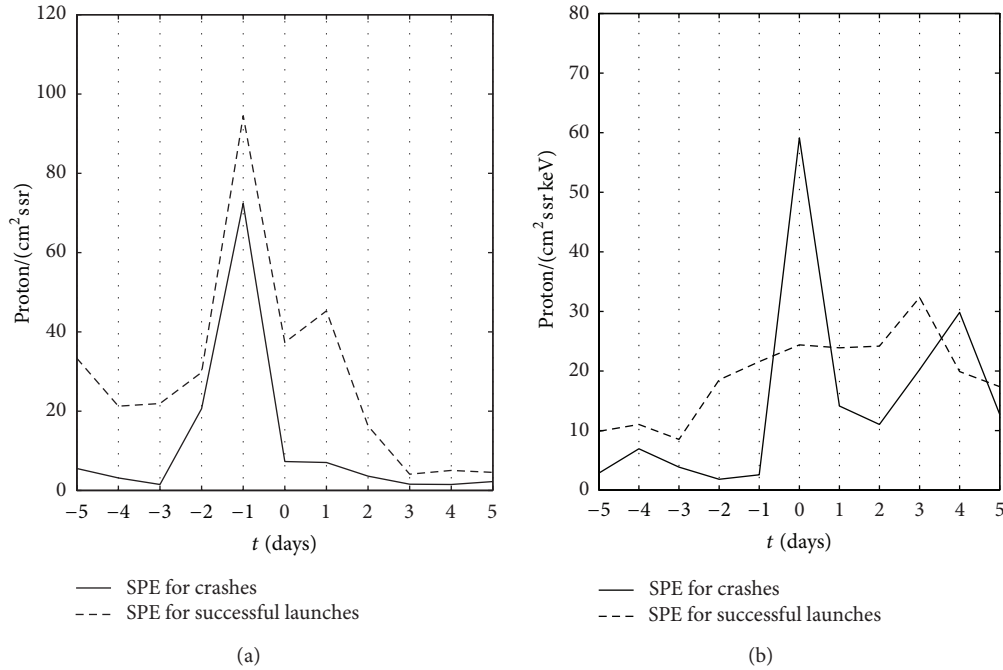


FIGURE 15: The proton flux rate with $E > 4$ MeV averaged over crash events in the 5 days interval around the moment of launch: (a) Cape Canaveral; (b) Baikonur.

4.4.2. Launch Crashes at Site Plesetsk and High-Energy Electron Fluxes. The fluxes of magnetospheric electrons with relativistic energies are known to enhance up to 2-3 orders of magnitude at the recovery phase of magnetic storms. Therefore, it might be supposed that the precipitation of relativistic electrons could exert a hazardous impact on rockets launched from high-latitude site, such as Plesetsk. To validate this possibility, we have correlated the high-energy electron fluxes at geostationary orbit with launch crashes at high-latitude site Plesetsk. However, this study, similar to the high-energy protons, has not revealed a statistically reliable correlation (not shown). Although from the total number of 263 at Plesetsk site during a period (since 1990) with available magnetospheric electron data only 14 failed. Probably, such a low statistics is not sufficient for statistically reliable estimates.

5. Discussion and Conclusions

The statistical comparison of launch crashes at different space ports with geophysical factors is performed using a big database, that includes information about all rocket launches occurring in the world in the time interval from 1957 to 2007. Attention is given to the largest space ports: Plesetsk, Baykonur, Cape Canaveral and Vandenberg. The main results of this study are as follows.

- (i) The accident rate is found to be different for various types of launchers. The failure rate for “Soyuz” is least and is highest for “Thor.”
- (ii) There are no statistically reliable seasonal effect in the launch failure probability at any sites. The earlier noticed increase of the failure rate at Plesetsk ~ 1.5

times in the summertime [12] is not supported by the χ^2 -criterion.

- (iii) For most sites, the failure risk does not depend on the time of the day. Only at Vandenberg, the failure rate is statistically higher during the day time by an unknown reason.
- (iv) Solar activity, as characterized by the sunspot number $\langle R \rangle$, does not influence the launch failure. There is no statistically significant influence of solar proton events on failure risk.
- (v) Statistically non-negligible relationships between the failure rate and geomagnetic and auroral activity, as characterized by indices AE , P , and K_p , have been revealed at Cape Canaveral, Vandenberg, and Plesetsk.

However, additional validation with the use of nonparametric criterion (χ^2) and splitting of all the events into disturbed/quiet conditions does not reveal any statistically significant distinctions in the failure probability. Because of rather limited statistics, especially during extreme values of the space weather parameters, the statistical power of estimates is not very high, about 50–60%. Thus, though the tendency of the geomagnetic activity impact on launches at Plesetsk, Cape Canaveral, and Vandenberg is statistically significant, it cannot be confirmed with a high accuracy.

A possible mechanism of space weather impact on rocket launches may be related to various factors. At higher altitudes, high-energy particle precipitation could influence the functioning of the electronic control systems of the launcher. For example, energetic or relativistic electrons can produce

charging of elements of a rocket in a similar way as of magnetospheric satellites [6]. The intense electric currents during auroral disturbances in the region of the launch trajectory may influence the elements of the launch control system.

The possible mechanism of an indirect space weather impact on rocket launches may be related to disturbances in atmospheric electricity. At the moment of takeoff, a rocket can obtain a substantial spatial charge and considerable electric potential (from 10^3 up to 10^5 V/m for various journey legs) [19]. Increase of electric field intensity can be accompanied by discharges. Electrification of the vehicle depends on electrical conditions in the atmosphere and presence of thunderstorm structures. Also, along the take-off trajectory the high-altitude atmospheric discharges well above thunderclouds, accompanied by bursts of accelerated relativistic electrons and γ -rays [20], may be of potential hazards to space missions during the ascent and descent phases.

Interaction of the charged launcher and its engine waste with the conducting ionosphere can result in unexpected effects which are not clearly understood yet. Special experiments (e.g., "Waterhole") showed that injection of combustion materials into the ionospheric plasma results in a fast "sweep" of plasma and generation of intense electrical and magnetic impulses, excitation of turbulence, and stimulation of electron precipitation [6, 21, 22]. It is possible that these effects adversely affect rocket electronic systems.

The results presented in this paper suggest that a more thorough study of space weather effects on launcher systems, especially in the high-latitude regions, should be continued in order to improve the knowledge about the relationship between rocket launch crashes and geophysical parameters. Though the possible number of critical situations during launch and space flight related to the space weather is not very high as compared with general statistics, even a single event can cause huge financial losses. Even a relatively small number of crashes during geomagnetic disturbances are worthy to pay attention to and the problem of the influence of space weather upon launch vehicles and its onboard equipment should be studied in a greater detail. In view of the high costs associated with delaying launch, and possibly missing launch windows, only a nowcast could provide a sufficiently reliable service. Thus, space weather real-time monitoring and prediction could become an important issue in the optimization of launch procedures.

Acknowledgments

This study was supported by INTAS YSF Grant 05-109-4661 (NR) and Program 22 of the Russian Academy of Sciences (VP).

References

- [1] R. B. Horne, Benefits of a space weather programme, ESA Space Weather Programme Study, BAS Contract 300738, ESA ITT AO/1-3353/99/NL/SB, 2001.
- [2] D. N. Baker, J. H. Allen, S. G. Kanekal, and G. D. Reeves, "Disturbed space environment may have been related to pager satellite failure," *Eos, Transactions American Geophysical Union*, vol. 79, no. 40, pp. 477–483, 1998.
- [3] D. N. Baker, "The occurrence of operational anomalies in spacecraft and their relationship to space weather," *IEEE Transactions on Plasma Science*, vol. 28, no. 6, pp. 2007–2016, 2000.
- [4] D. F. Webb and J. H. Allen, "Spacecraft and ground anomalies related to the October–November 2003 solar activity," *Space Weather*, vol. 2, no. 3, 2004.
- [5] N. Iucci, A. E. Levitin, A. V. Belov et al., "Space weather conditions and spacecraft anomalies in different orbits," *Space Weather*, vol. 3, no. 1, 2005.
- [6] V. Pilipenko, N. Yagova, N. Romanova, and J. Allen, "Statistical relationships between satellite anomalies at geostationary orbit and high-energy particles," *Advances in Space Research*, vol. 37, no. 6, pp. 1192–1205, 2006.
- [7] N. V. Romanova, V. A. Pilipenko, N. V. Yagova, and A. V. Belov, "Statistical correlation of the rate of failures on geosynchronous satellites with fluxes of energetic electrons and protons," *Cosmic Research*, vol. 43, no. 3, pp. 186–193, 2005.
- [8] D. H. Boteler, R. J. Pirjola, and H. Nevanlinna, "The effects of geomagnetic disturbances on electrical systems at the Earth's surface," *Advances in Space Research*, vol. 22, no. 1, pp. 17–27, 1998.
- [9] E. G. Stassinopoulos, C. A. Stauffer, and G. J. Brucker, "A systematic global mapping of the radiation field at aviation altitudes," *Space Weather*, vol. 1, no. 1, 2003.
- [10] G. Siscoe, "The space-weather enterprise: past, present, and future," *Journal of Atmospheric and Solar-Terrestrial Physics*, vol. 62, no. 14, pp. 1223–1232, 2000.
- [11] C. Kunstadter, "Space insurance experience and outlook: a statistical review of volatility," in *Presentation at the Federal Aviation Administration's Commercial Space Transportation Advisory Committee (FAA COMSTAC '05)*, 2005.
- [12] N. V. Romanova, V. A. Chizhenkov, and V. A. Pilipenko, "Possible relation of emergencies during spacecraft launches from the Plesetsk site to high-latitude geomagnetic disturbances," *Geomagnetism and Aeronomy*, vol. 49, no. 1, pp. 104–109, 2009.
- [13] R. L. Plackett, "Karl Pearson and the Chi-Squared test," *International Statistical Review*, vol. 51, no. 1, pp. 59–72, 1983.
- [14] C. Behrens, "Space launch vehicles: government activities, commercial competition, and satellite exports," Tech. Rep., Congressional Research Service, Washington, DC, USA, 2006.
- [15] E. Paulson, "On the comparison of several experimental categories with a control," *Annals of Mathematical Statistics*, vol. 23, pp. 239–246, 1952.
- [16] R. Tripathi and A. Mishra, "Occurrence of severe geomagnetic storms and their association with solar-interplanetary features," in *Proceedings of the ILWS Workshop on Solar Influence on the Heliosphere and Earth's Environment*, Goa, India, February 2006.
- [17] J. H. Allen, "Historical and recent solar activity and geomagnetic storms affecting spacecraft operations," in *Proceedings of the Government Microcircuit and Applications Conference (GOMAC '02)*, Monterey, Calif, USA, March 2002.
- [18] D. Boscher, J. L. Bougeret, J. Breton, P. Lantos, J. Y. Prado, and M. Romero, *Space Weather Final Report from the French Evaluation Group on Needs*, European Space Agency, ESTEC, Noordwijk, The Netherlands, 1999.

- [19] D. S. Hazen, W. P. Roeder, B. F. Boyd, J. B. Lorens, and T. L. Wilde, "Weather impact on launch operations at the eastern range and kennedy space center," in *Proceedings of the 6th Conference on Aviation Weather Systems*, pp. 270–275, January 1995.
- [20] T. Neubert, M. Rycroft, T. Farges et al., "Recent results from studies of electric discharges in the mesosphere," *Surveys in Geophysics*, vol. 29, no. 2, pp. 71–137, 2008.
- [21] M. C. Kelley, U. V. Fehleson, G. Holmgren, R. Bostrom, P. M. Kintner, and E. Kudeki, "Generation and propagation of an electromagnetic pulse in the Trigger experiment and its possible role in electron acceleration," *Journal of Geophysical Research*, vol. 85, pp. 5055–5060, 1980.
- [22] A. W. Yau and B. A. Whalen, "Auroral perturbation experiments," *Advances in Space Research*, vol. 8, no. 1, pp. 67–77, 1988.

Review Article

Removing Regional Trends in Microgravity in Complex Environments: Testing on 3D Model and Field Investigations in the Eastern Dead Sea Coast (Jordan)

A. Al-Zoubi,¹ L. Eppelbaum,² A. Abueladas,¹ M. Ezersky,³ and E. Akkawi¹

¹ Al-Balqa Applied University, Salt 19117, Jordan

² Department of Geophysical, Atmospheric and Planetary Sciences, Tel Aviv University, Ramat Aviv, Tel Aviv 69978, Israel

³ Geophysical Institute of Israel, P.O. Box 182, Lod 71100, Israel

Correspondence should be addressed to L. Eppelbaum; levap@post.tau.ac.il

Received 29 September 2012; Accepted 18 January 2013

Academic Editor: Umberta Tinivella

Copyright © 2013 A. Al-Zoubi et al. This is an open access article distributed under the Creative Commons Attribution License, which permits unrestricted use, distribution, and reproduction in any medium, provided the original work is properly cited.

Microgravity investigations are now recognized as a powerful tool for subsurface imaging and especially for the localization of underground karsts. However numerous natural (geological), technical, and environmental factors interfere with microgravity survey processing and interpretation. One of natural factors that causes the most disturbance in complex geological environments is the influence of regional trends. In the Dead Sea coastal areas the influence of regional trends can exceed residual gravity effects by some tenfold. Many widely applied methods are unable to remove regional trends with sufficient accuracy. We tested number of transformation methods (including computing gravity field derivatives, self-adjusting and adaptive filtering, Fourier series, wavelet, and other procedures) on a 3D model (complicated by randomly distributed noise), and field investigations were carried out in Ghor Al-Haditha (the eastern side of the Dead Sea in Jordan). We show that the most effective methods for regional trend removal (at least for the theoretical and field cases here) are the bilinear saddle and local polynomial regressions. Application of these methods made it possible to detect the anomalous gravity effect from buried targets in the theoretical model and to extract the local gravity anomaly at the Ghor Al-Haditha site. The local anomaly was utilized for 3D gravity modeling to construct a physical-geological model (PGM).

1. Introduction

The development of new modern gravimetric and variometric (gradientometric) equipment, which makes it possible to record small previously inaccessible anomalies, has enhanced observational methodology as well as new gravity data processing methods and interpretation. These advances have triggered the rapid rise in the number of microgravity methodology applications in environmental and economic minerals geophysics.

Microgravity is now recognized as an effective tool for the analysis of a whole range of geological subsurface inhomogeneities, the monitoring of volcanic activity, and prospecting for useful minerals (e.g., [1–34]).

At the same time different kinds of noise of different origin complicate analysis of microgravity data. For removing

(elimination) the noise components numerous procedures and methodologies were developed. We will analyze in this paper a problem of regional trend removing under complex geological-geophysical environments. Such a problem is highly essential by delineation of weak anomalies from buried karst terranes in the Dead Sea Basin where regional horizontal gravity gradients may exceed values of 10 mGal/km.

2. A Brief Review of Microgravity Investigations in Subsurface Studies

Colley [2] apparently was the first to apply the gravity method for cave delineation. Despite the fact that the accuracy of gravity observations at that time was not sufficiently precise, he presented some examples of typical negative gravity anomalies in large caverns in Iraq.

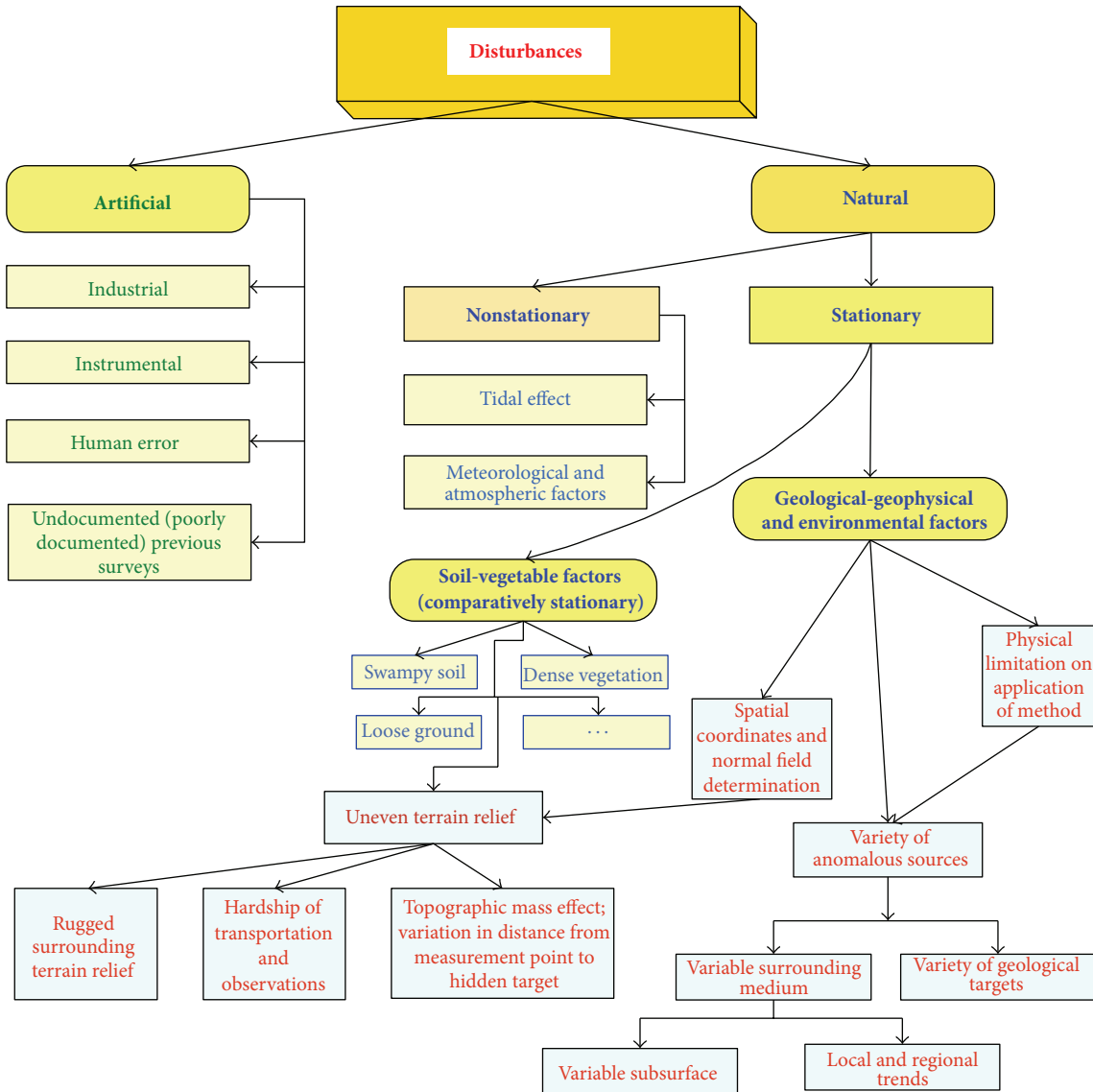


FIGURE 1: Noise affecting microgravity investigations (adapted from [45]).

Fajkiewicz [4] examined the vertical gravity gradient (W_{zz}) over underground galleries. He was probably the first to note a significant difference between the physically measured W_{zz} and this value obtained by transformation. Interesting examples of microgravity anomalies from archaeological targets are presented in Bližkovský [5]. Butler [7] showed that microgravity measurements could be used to detect and delineate the main components of complex underground cavity systems. He computed the second and third derivatives of the gravity potential and polynomial surface to develop the initial physical-geological models (PGMs). Butler [8] surveyed gravity and gravity-gradient determination concepts and their corresponding interpretative microgravity procedures.

A nonconventional attempt to use microgravity observations for weight determination of stockpiled ore was

reported by Sjoström and Butler [35] who estimated the mass of many chromite and other ore bodies noninvasively.

Crawford [12] employed microgravity to detect sinkhole collapses under highways in the USA. Elawadi et al. [36] showed that the application of well-known neural network procedures could increase the assessment effectiveness of the depth and radius of subsurface cavities revealed by microgravity data. Rybakov et al.'s [15] work triggered the use of microgravity to find sinkholes in the complex geological conditions of the Dead Sea coastal plain.

Types of noise (disturbances) arising in microgravity investigations were studied in detail in Debeglia and Dupont [37]. Styles et al. [18] discussed the key problems related to the removal of noise components in microgravity in complex environments.

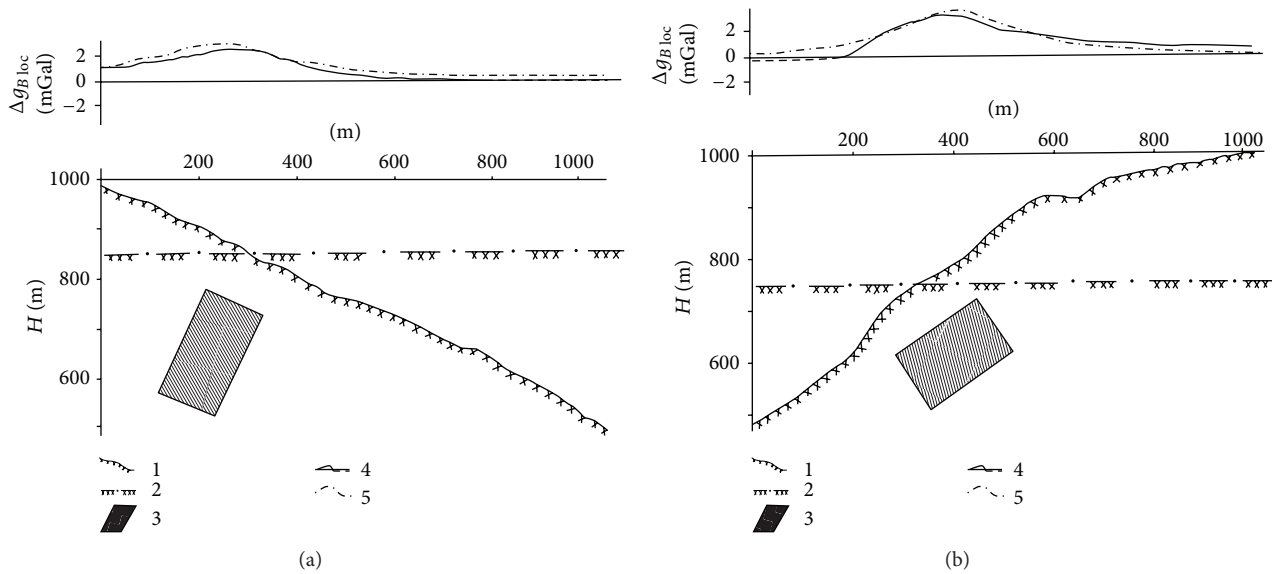


FIGURE 2: Negative effect of gravitational anomalies from a local anomalous body observed on inclined and horizontal profiles (after [46], with modifications). (a) Smooth slope, (b) complicated slope. (1) Inclined profile; (2) horizontal profile; (3) anomalous body with a positive contrast density $\Delta\sigma = 1500 \text{ kg/m}^3$; anomaly Δg_B from the same body after topographic mass attraction correction: (4) on an inclined profile, (5) on a horizontal profile.

The need for additional computation of the surrounding terrain relief by 3D gravity modeling in ore deposits occurring in the very complex topography of the Greater Caucasus was discussed in Eppelbaum and Khesin [17].

Abad et al. [23] carried out an assessment of a buried rainwater cistern in a Carthusian monastery (Valencia, Spain) by 2D microgravity modeling. Microgravity monitoring is one of the most widely used geophysical techniques for predicting volcanic activity; for instance, Carbone and Greco [38] described in detail their microgravity monitoring of Mt. Etna.

Advanced methods in magnetic prospecting can be adapted to quantitative analysis of microgravity anomalies in complex environments [25]. Eppelbaum et al. [1] described various transformation methods to identify buried sinkholes including 3D gravity modeling to develop a PGM of Nahal Never South in the western Dead Sea coast.

Deroussi et al. [27] applied precise gravity investigations for delineating cavities and large fractured zones by planning road construction in lava flow after recent volcano eruption in Réunion island. Microgravity combined with absolute gravity measurements has also been used to study water storage variations in a karst aquifer on the Larzac Plateau (France) [39]. Castiello et al. [40] reported a microgravity study of an ancient underground cavity in the complex urban environment of Naples.

Types of noise associated with microgravity studies of shallow karst cavities in areas of developed infrastructure are presented in detail in Leucci and Georgi [30]. Porzucek [41] discusses the advantages and disadvantages of using the Euler deconvolution in microgravity studies. A new method for the simultaneous, nonlinear inversion of gravity changes and

surface deformation using bodies with a free geometry was proposed by Camacho et al. [31].

The importance of gravity field observations at different levels as well as the precise calculation of topographic effects in intermediate and distant zones was analyzed in Eppelbaum [32]. Dolgal and Sharkhimullin [42] suggested using a “localization function” to enhance the quality of PGMs and reduce the ambiguity of the results in high-precise gravity.

Kaufmann et al. [43] successfully employed microgravity to identify subsurface voids in the Unicorn cave in the Harz Mountains (Germany). Hajian et al. [33] applied locally linear neurofuzzy microgravity modeling to the three most common shapes of subsurface cavities: sphere, vertical cylinder, and horizontal cylinder. The authors showed that their method can estimate cavity parameters more accurately than least-squares minimization or multilayer perceptron methods.

Panisova et al. [44] fruitfully applied a new modification of close range photogrammetry for calculation of building corrections in the microgravity survey for karst delineation in the area of historical edifice (Slovakia).

3. Different Kinds of Noise in Microgravity Surveys

A microgravity survey is the geophysical method most affected by corrections and reductions caused by different kinds of noise (disturbances). A chart showing the different types of noise typical to microgravity studies is presented in Figure 1.

These types of noise are described in more detail below.

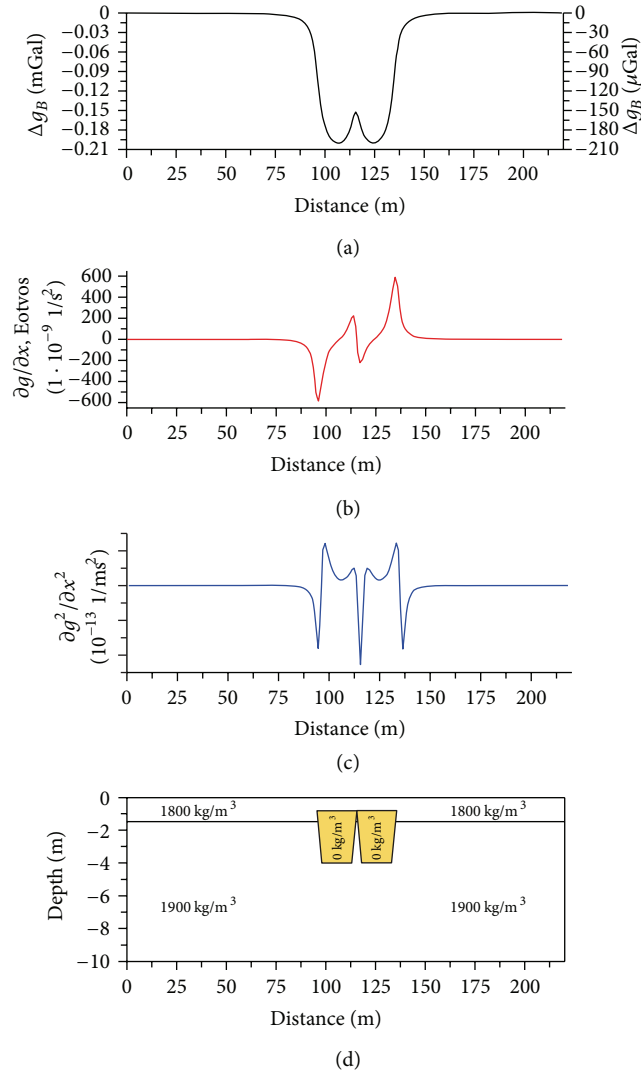


FIGURE 3: Computation of the horizontal derivatives of the gravity field for two proximal sinkhole models. (a) Computed gravity curve (level of computation: 0.3 m), (b) first horizontal derivative of gravity field Δg_x , (c) second horizontal derivative Δg_{xx} , and (d) physical-geological model (after [1]).

3.1. Artificial (Man-Made) Noise. The *industrial* component of noise mainly comes from surface and underground constructions, garbage dumps, transportation and communications lines, and so forth. The *instrumental* component is associated with the technical properties of gravimeters (e.g., shift zero) and gradientometers. *Human error*, obviously, can accompany geophysical observations at any time. Finally, *undocumented (poorly documented)* results of previous surveys can distort preliminary PAM development.

3.2. Natural Disturbances. *Nonstationary* noise includes, for instance, known tidal effects. *Meteorological conditions* (rain, lightning, snow, hurricanes, etc.) can also affect gravimeter readings. Corrections for the *atmosphere* deserve special attention in microgravity investigations, since the air layer

attraction is different at various levels over and below the m.s.l. *Soil-vegetation factors* associated with certain soil types (e.g., swampy soil or loose ground in deserts) and dense vegetation, which sometimes hampers movement along the profile, also need to be taken into account.

3.3. Geological-Geophysical and Environmental Factors. These constitute the most important physical-geological disturbances. The application of any geophysical method depends primarily on the existence of physical properties contrast between the objects under study and the surrounding medium. The *physical limitation of method application* assesses the measurable density contrast properties between the anomalous targets and the host media.

3.4. Spatial Coordinates and Normal Gravity Field Determination. *Spatial coordinates and normal gravity field determination* are also crucial to precise gravity studies and any inaccuracies here may lead to significant errors in subsequent analyses.

3.5. Uneven Terrain Relief. *Uneven terrain relief* can hamper the movement of equipment and restrict gravity data acquisition. Physically, the gravity field is affected by the form and density of the topographic features composing the relief, as well as *variations in the distance from the point of measurement to the hidden target* [32]. Calculations for the *surrounding terrain relief* (sometimes for radii up to 200 km) are also of great importance [47, 48].

3.6. Earthquake Damage. *Earthquake damage zones* are widely spread over the Eastern Mediterranean, especially in the regions near the Dead Sea Transform (DST) Zone [49]. These zones may significantly complicate microgravity data analysis.

3.7. The Variety of Anomalous Sources. *The variety of anomalous sources* is composed of two factors: *the variable surrounding medium* and *the variety of anomalous targets*. Both these factors are crucial and greatly complicate the interpretation of magnetic data.

3.8. Variable Subsurface. *Variable subsurface* can make it difficult to determine the correct densities of bodies occurring close to the earth's surface.

3.9. Local and Regional Trends. *Local and regional trends* (linear, parabolic, or other types) often mask the target gravity effects considerably (e.g., [46–48, 50]). Sometimes regional gravity trend effects may exceed local desired anomalies by some tenfold.

Let us consider the last disturbing factor in detail. The correct removal (elimination) of regional trends is not a trivial task (e.g., [47]). Below we present two examples showing disturbing trend effects in detailed gravity investigations. Figure 2 shows two cases of nonhorizontal gravity observations with the presence of an anomalous body. The distorting effect of a nonhorizontal observation line occurs

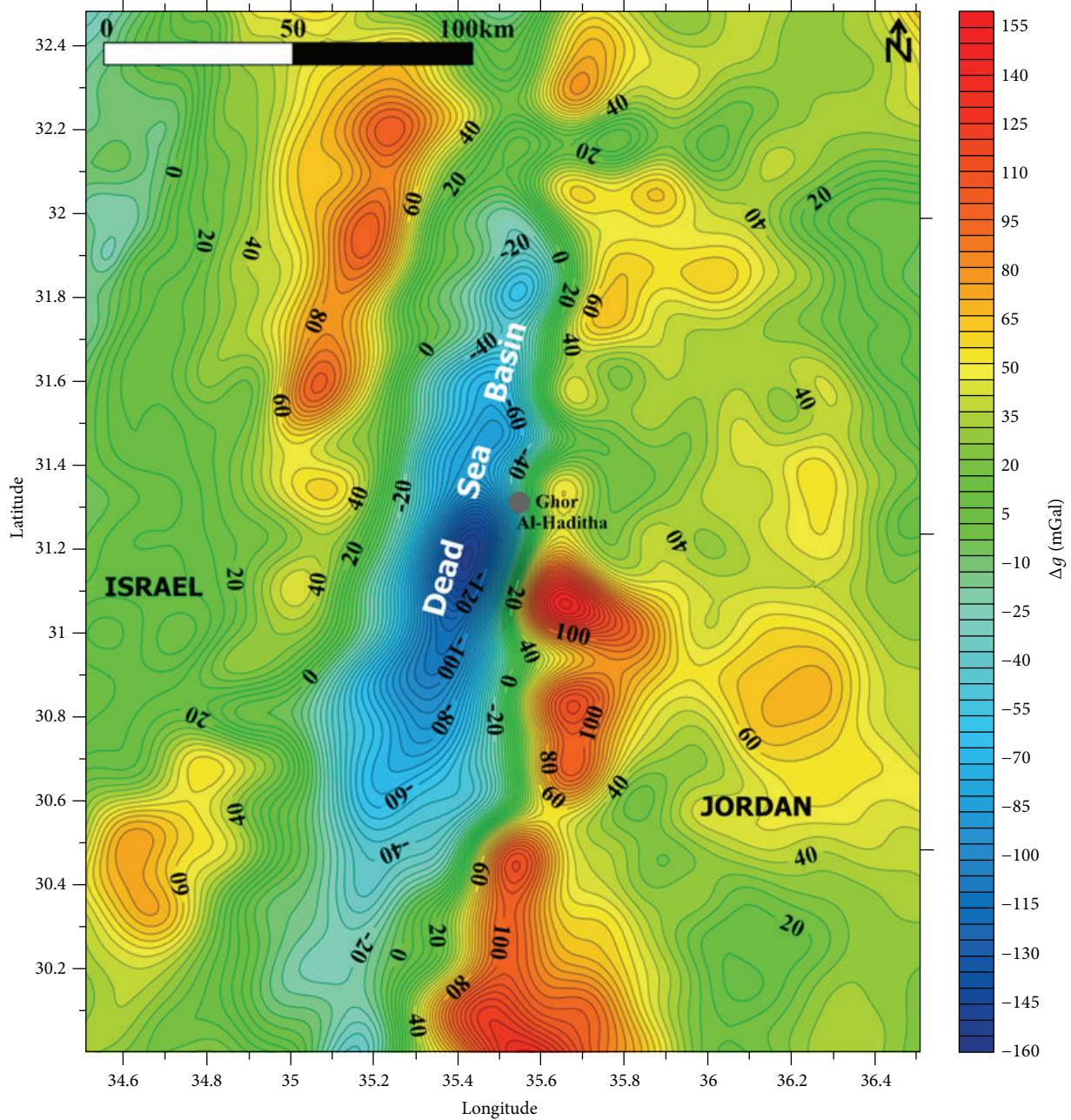


FIGURE 4: Areal map of the investigated site.

when the target object differs from the host medium by a contrast density and produces an anomalous vertical gradient. Comparing the Δg_B anomalies from the local body observed on the inclined and horizontal relief indicates that the gravity effects in these situations are different (Figure 2). Despite the fact that all the necessary corrections were applied to the observations on the inclined relief, the computed Bouguer anomaly is characterized by small negative values (minimum) in the downward direction of the relief, whereas the anomaly on the horizontal profile has no negative values (this kind of noise is described in Section 3.5). Thus, applying all conventional corrections does not eliminate this trend

because the observation point for the anomalous object was different [46]. Hence a special methodology is required for gravimetric quantitative anomaly interpretation in conditions of inclined relief [32].

Sometimes even simple computing of the first and second derivatives of the gravity field Δg_x and Δg_{xx} (second and third derivatives of the gravity potential, resp.) is enough to locate local bodies against a disturbing field background. One such example is presented in Figure 3 where the Bouguer gravity Δg_B is practically impossible to interpret, whereas the calculation of Δg_{Bx} was informative regarding the geometry of two closely occurring sinkholes. Finally, the behavior

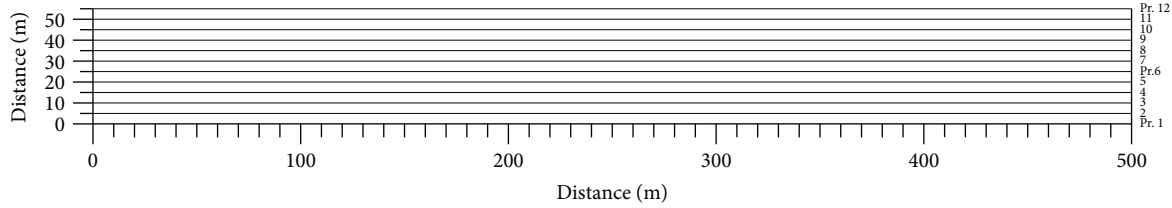


FIGURE 5: Scheme of gravity field 3D computation for the model example.

of the graph Δg_{Bxx} clearly reflects the location of the vertical boundaries of two closely occurring objects with a small negative interval (surrounding medium) between them.

The area under study—Ghor Al-Haditha—is situated in the eastern coastal plain of the Dead Sea (Jordan) in conditions of very complex regional gravity pattern (Figure 4). The satellite gravity data shown in this figure were obtained from the World Gravity DB as retracked from Geosat and ERS-1 altimetry [51]. These observations were made with regular global 1-minute grids that can differentiate these data from previous odd surface and airborne gravity measurements. This complex gravity field distribution in the vicinity of the area under study is caused mainly by the strong negative effect of the low density sedimentary associations and salt layers accumulated in the DST and also several other factors.

4. Computation of the 3D Gravity Effect from Models of Sinkholes and the Dead Sea Transform

To test methods of regional trend elimination, two theoretical PGMs—sinkhole PGM and DST PGM—were developed. The computed gravity effects from these PGMs were also artificially complicated by randomly distributed noise.

4.1. Computation of the 3D Gravity Effect from the Sinkhole PGM. To calculate the 3D gravity field, 12 parallel profiles with a distance between them of 5 m were applied (Figure 5). For the PGM a two layer ($\sigma_1 = 2000 \text{ kg/m}^3$ and $\sigma_2 = 2100 \text{ kg/m}^3$, resp.) PGM with two types of ellipsoidal sinkholes was constructed (Figure 6). The center of the first large sinkhole was located at a depth of -60 m below the earth's surface in the second layer, with a contrast density of -900 kg/m^3 . The center of the second small sinkhole was located at a depth of -20 m below the earth's surface in the first layer, with a contrast density of -2000 kg/m^3 . Profile 6 was selected as the central one, and the left and right ends of sinkhole 1 were defined as -30 and $+30 \text{ m}$, and for sinkhole 2 as -12 and $+12 \text{ m}$, respectively. For the 3D gravity field modeling of this and the following examples, mainly the GSFC program [17] software was employed. The number of computation points along the sinkholes PGM was chosen to be 200, that is, every 2.5 m.

The compiled gravity map for the 12 profiles for the sinkhole PGM is shown in Figure 7. As can be seen from this

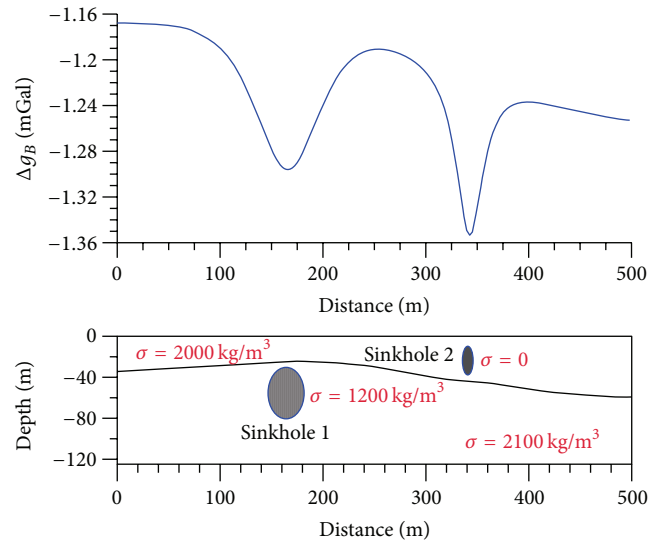


FIGURE 6: Gravity field anomalies along profile 6 from models of sinkholes.

map, the anomaly from sinkhole 2 is narrower than sinkhole 1 but is characterized by comparatively high amplitude.

4.2. Computation of the 3D Gravity Effect from the DST. The simplified PGM of the DST for its deepest part (Figure 8) was constructed from data presented in Ginzburg and Ben-Avraham [52], Weber et al. [53], and the authors' computations. The location of the sinkhole 500 m profile in the upper right section of the model is shown. The PGM of the DST was computed as the same for all 12 profiles. The computed gravity effect from the DST was added to the gravity field to account for the sinkhole PGM (Figure 9). As can be seen from this figure, the anomaly from sinkhole 2 can be visually detected, but the anomaly from sinkhole 1 is practically undetectable against the regional trend produced by the DST.

4.3. Noise Added by Random Number Generation. Given that the geological medium is usually more complex than presented in the models in Figures 6 and 8 we used a random number generator to introduce a noise factor into the calculations. Algorithms developed by Bichara et al. [6] and Wichura [54] were applied. The parameters of this randomly distributed noise—the mean values and the standard deviations along 12 profiles—are listed in Table 1. In other words,

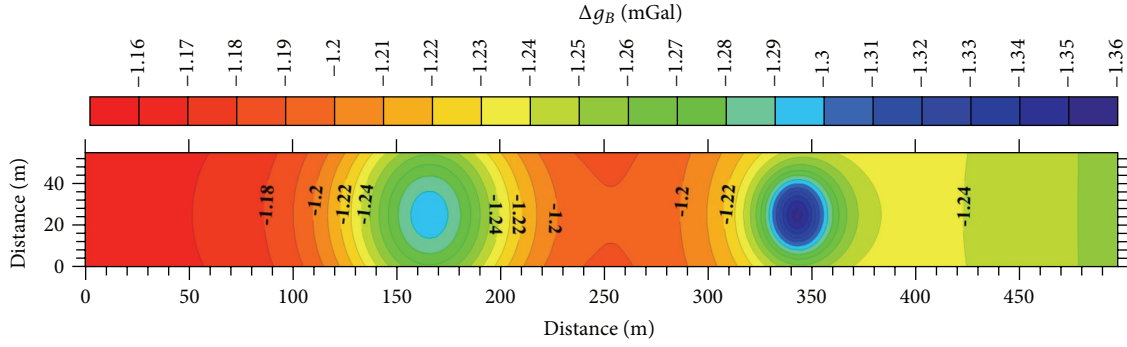


FIGURE 7: Compiled gravity map for 12 profiles.

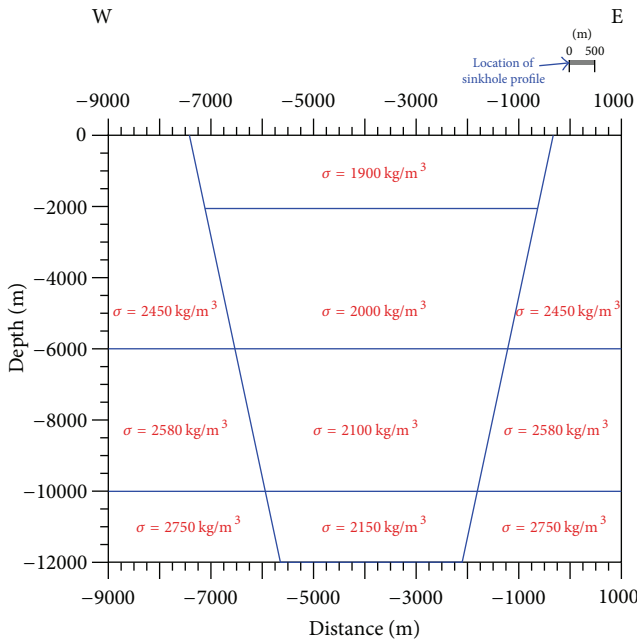


FIGURE 8: Simplified density-geological model of the Dead Sea Transform.

the randomly distributed nonrecurrent noise was added to 200 computation points for each of 12 profiles.

Figure 10 shows a gravity map compiled on the basis of randomly distributed noise (from Table 1). The combined gravity effects from (1) the sinkhole PGM, (2) the DST PGM, and (3) randomly distributed noise were used to compute the integrated gravity map that sums the effects of these three factors (Figure 11). It should be noted that in the map (Figure 11) there are no visual signatures of the negative anomalies from sinkholes 1 and 2.

4.4. Results of the Different Algorithms to Eliminate Regional Trends. To remove the regional trends, different algorithms and methods were applied: the first and second derivatives, self-adjusting and adaptive filtering, Fourier series, wavelet

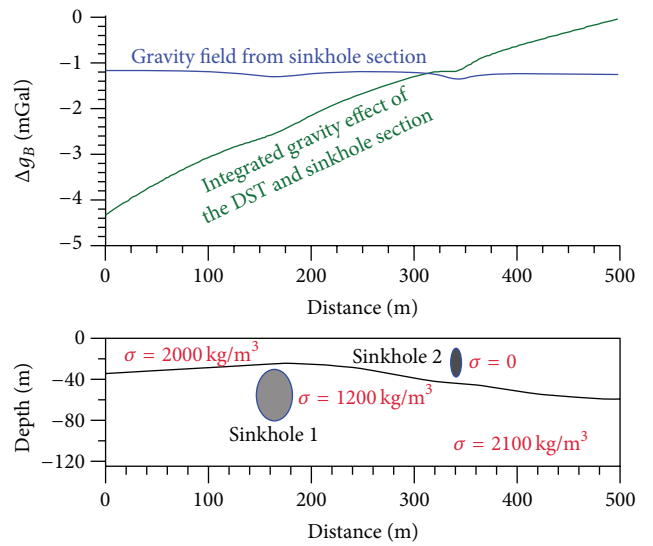


FIGURE 9: Combined gravity field along profile 6 from models of sinkholes and effect of the DST.

TABLE 1: Inserted randomly distributed noise.

Profile number	Mean value	Standard deviation
1	0.150	0.040
2	0.160	0.030
3	0.140	0.035
4	0.130	0.038
5	0.170	0.029
6	0.120	0.033
7	0.150	0.038
8	0.140	0.032
9	0.110	0.024
10	0.160	0.031
11	0.125	0.025
12	0.15	0.028

decomposition, principal component analysis, inverse probability, and other methods were applied (altogether more than 30 different procedures).

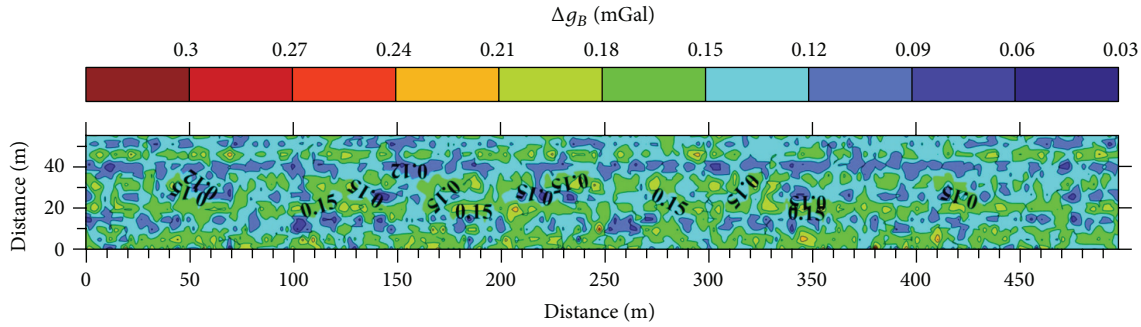


FIGURE 10: Compiled gravity map of the random noise for 12 profiles.

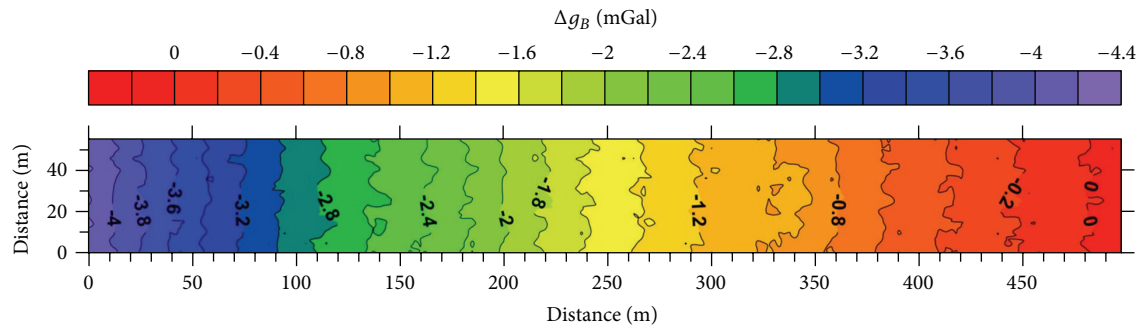


FIGURE 11: Compiled gravity map for 12 profiles with combined effect from: (1) the DST, (2) sinkholes, and (3) random noise.

Examples of applications of (1) the entropy parameter using a moving window with self-adapting size, (2) gradient sounding, and (3) power estimation by the Morlet transformation are presented in Figures 12(a), 12(b), and 12(c), respectively. Computing the entropy with the moving window (Figure 12(a)) revealed a clear ring anomaly from sinkhole 2; the anomaly from sinkhole 1 was difficult to locate. At the same time the boundary effect at the map edges (Figure 12(a)) complicated image reading. The results of gradient sounding (Figure 12(b)) suggested the presence of an anomaly from sinkhole 2. A power estimation based on a Morlet transformation (Figure 12(c)) very clearly indicates the location of sinkhole 2. However, a superposition of computed gravity anomalies and noise effects gives a false weak anomaly (located at 105–108 m) of sinkhole 1.

Regression analysis is now considered one of the most powerful methods for removing trends of different kinds (e.g., [55–57]). Two regression methods were selected. Figure 13 shows the residual gravity map after subtracting a bilinear saddle ($F(x, y) = a + bx + cy + dxy$) regression. The negative gravity anomaly from sinkhole 1 in the area of 160 m (see Figures 6 and 9) is clearly detected, whereas the negative anomaly from sinkhole 2 in the area of 340 m is small and could not be reliably detected.

The gravity map after subtracting a local polynomial regression ($F(x, y) = a + bx + cy + dxy + ex^2 + fy^2$) is presented in Figure 14. Here the negative anomaly from sinkhole 1 was weak and was difficult to detect, but the

anomaly from sinkhole 2 was unmistakable. These findings suggest that there are advantages to using a combination of methods.

5. Removing Regional Gravity Trend in the Area of Ghor Al-Haditha, on the Eastern Coastal Plain of the Dead Sea (Jordan)

The Ghor Al-Haditha area is located south-east of the northern Dead Sea basin (see Figure 4). Alluvial fan deposits from Wadi Ibn Hammad cover the southern part of this area. Borehole sections indicate that the geological material of the shallow subsurface consists of laminated sand interbedded with layers of calcareous silts and possibly clay or marl. The sinkholes at the eastern coast of the Dead Sea can be dated to the mid-1980s [58].

The observed gravity map (Figure 15) shows the strong influence of the negative gravity effect due to the DST (and possibly other geological factors). Computing the first and second derivatives, self-adjusting filtering, gradient directional filtering, Fourier series, principal component analysis, and other methods were less successful than the bilinear saddle and local polynomial regressions.

Figure 16 displays results of the gradient sounding. After regional trend removal two local anomalies were found: one complex in the center of the area and the other near the western border. Clearly, however, this type of analysis is only valid for target qualitative delineation.

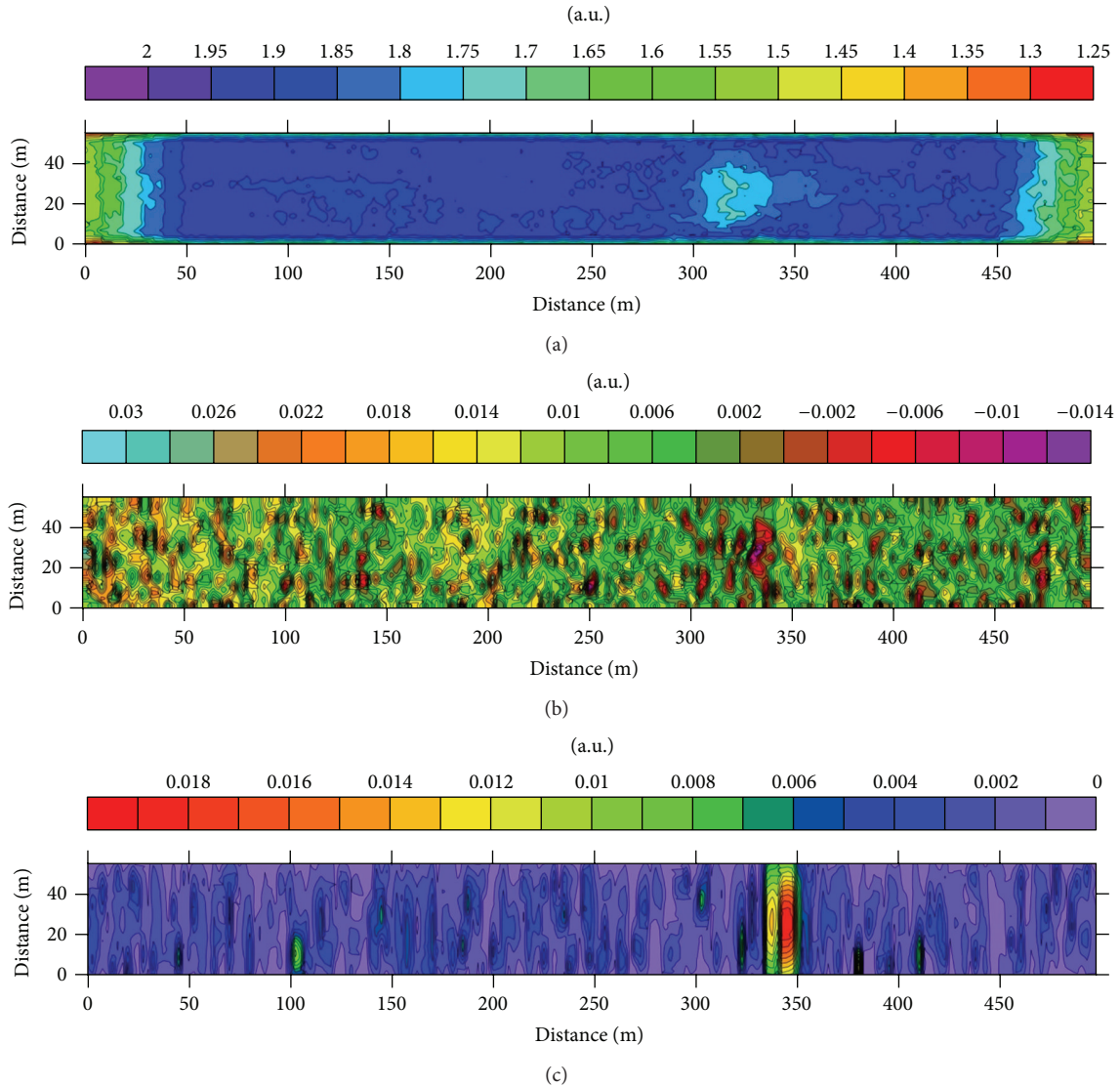


FIGURE 12: Results of three different methodologies: (a) entropy computation using a moving window with self-adapting size, (b) gradient sounding, and (c) power estimation by Morlet transformation.

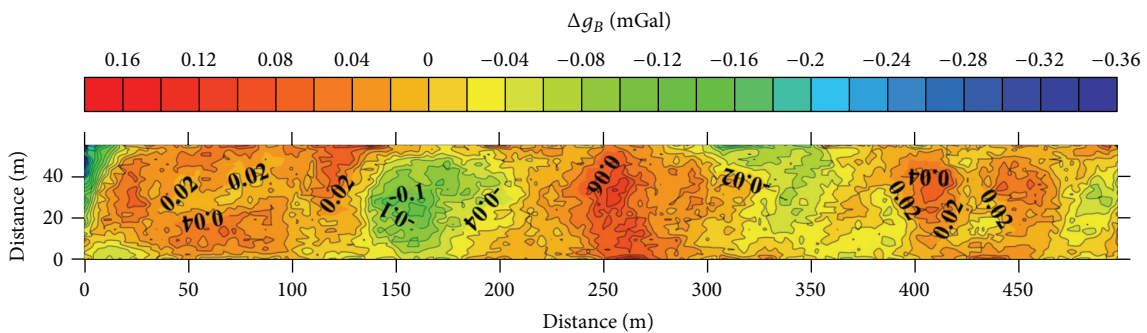


FIGURE 13: Residual gravity map after subtracting bilinear saddle regression.

A visual comparison of the residual maps (Figures 17 and 18, resp.) shows the great similarity between the two regression methods. A negative anomaly in the center of the map with amplitude of 0.6-0.7 mGal is very visible. An

important advantage of the residual maps is that these maps can be used both for qualitative and quantitative analysis.

The gravity profiles are constructed along the same line (A-B in Figure 17) and (A'-B' in Figure 18) demonstrate

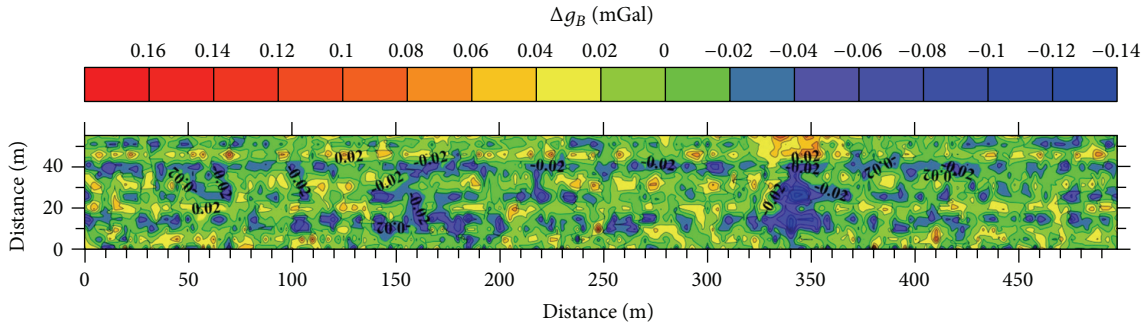


FIGURE 14: Residual gravity map after subtracting local polynomial.

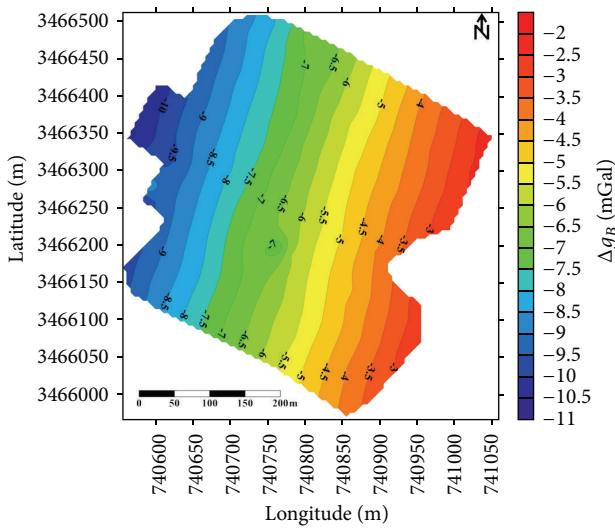


FIGURE 15: Bouguer gravity map of the Ghor Al-Haditha area (Jordan).

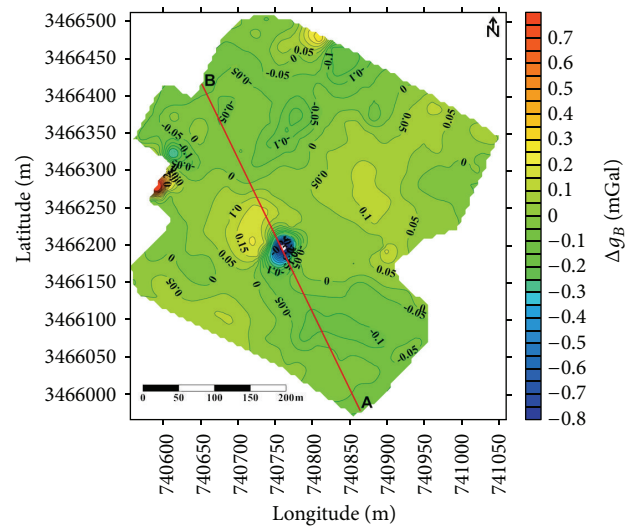


FIGURE 17: Residual gravity map of the Ghor Al-Haditha area after subtracting bilinear saddle regression.

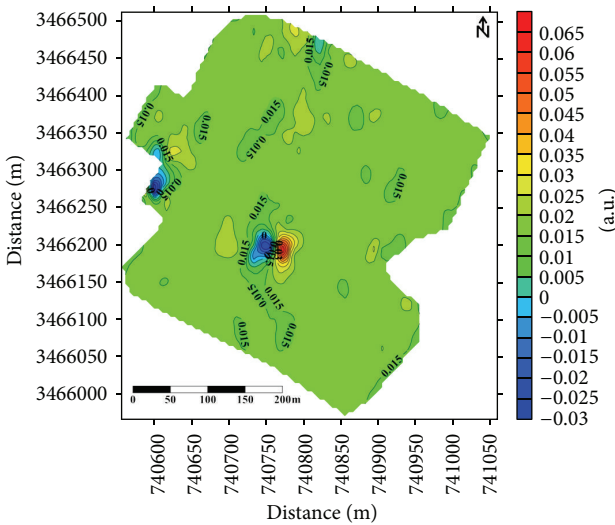


FIGURE 16: Results of gradient sounding.

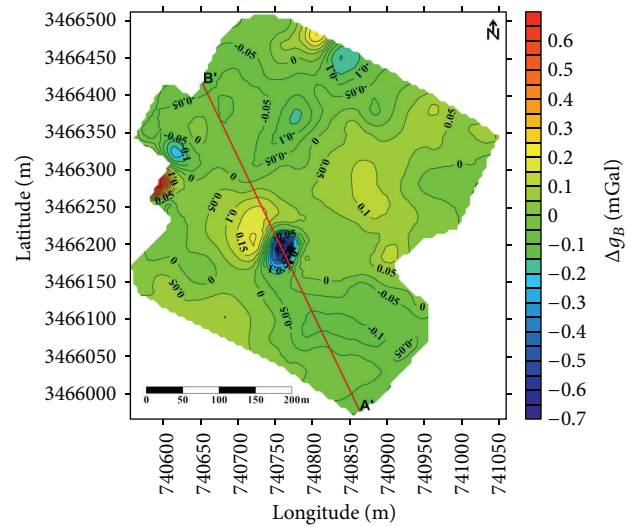


FIGURE 18: Residual gravity map of the Ghor Al-Haditha area after subtracting local polynomial.

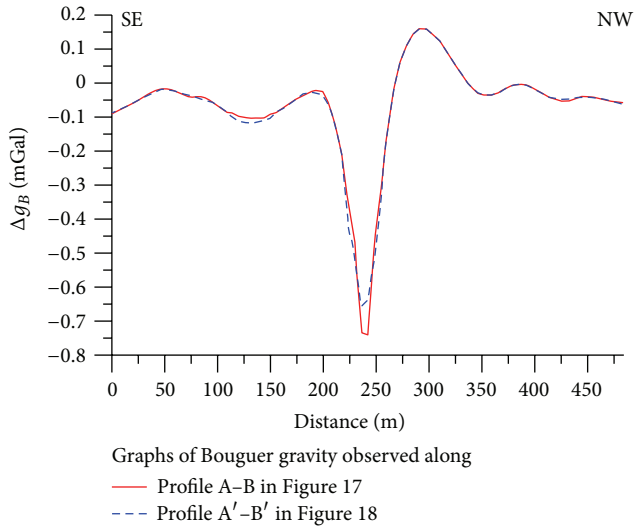


FIGURE 19: Comparison of gravity curves constructed along profile A-B for Figure 17 (after subtracting the bilinear saddle regression) and A'-B' for Figure 18 (after subtracting the local polynomial).

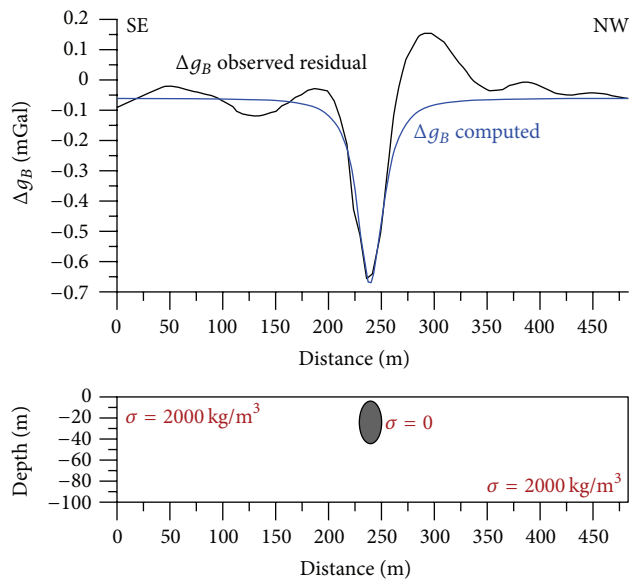


FIGURE 20: An initial physical-geological model along profile A'-B' developed on the basis of 3D gravity field modeling.

(Figure 19) that there are some small differences, mainly in the amplitude value from the anomalous object with a negative density contrast.

3D modeling indicates that such a gravity anomaly may have been produced by a sinkhole (similar to model 2 in Figure 6, but enlarged roughly twice) with its upper edge occurring at a depth of 4 m below the earth's surface (Figure 20). The location of this sinkhole and its size are consistent with the available geological data [59]. The disparity between the observed and computed Δg_B in the right part of the profile may have been caused by the presence of an additional small underground cavity with an irregular shape.

6. Conclusion

The different kinds of noise affecting microgravity investigations amply illustrate the need for careful calculation of each of these disturbing factors. In particular, the influence of regional trends often masks the target local microgravity anomalies. The 3D theoretical PGM of sinkholes combined with the gravity effect from the DST (producing a strong regional trend) as well as the randomly distributed noise (introducing some geological medium complexity) was constructed. Comparison of different methodologies to remove regional trends revealed that the most effective algorithms are the bilinear saddle and local polynomial regressions. The use of these methods to analyze gravity data observed in the complex geological environments of the Ghor Al-Haditha site (eastern coastline of the Dead Sea, Jordan) successfully removed the regional gradient and localized the negative anomaly possibly produced by a subsurface sinkhole. The 3D gravity field modeling led to identification of the parameters of this PGM.

Acknowledgments

The authors would like to thank anonymous reviewers, who thoroughly reviewed this paper, and their critical comments and valuable suggestions were very helpful in preparing this paper. This publication was made possible through support provided by the U.S. Agency for International Development (USAID) and the MERC Program under terms of Award No. M27-050.

References

- [1] L. V. Eppelbaum, M. G. Ezersky, A. S. Al-Zoubi, V. I. Goldshmidt, and A. Legchenko, "Study of the factors affecting the karst volume assessment in the Dead Sea sinkhole problem using microgravity field analysis and 3-D modeling," *Advances in Geosciences*, vol. 19, pp. 97–115, 2008.
- [2] G. C. Colley, "The detection of caves by gravity measurements," *Geophysical Prospecting*, vol. 11, no. 1, pp. 1–9, 1963.
- [3] Arzi, "Microgravimetry for engineering applications," *Geophysical Prospecting*, vol. 23, no. 3, pp. 408–425, 1975.
- [4] Z. J. Fajkiewicz, "Gravity vertical gradient measurements for the detection of small geologic and anthropogenic forms," *Geophysics*, vol. 41, no. 5, pp. 1016–1030, 1976.
- [5] M. Blížkovský, "Processing and applications in microgravity surveys," *Geophysical Prospecting*, vol. 27, no. 4, pp. 848–861, 1979.
- [6] M. Bichara, J. C. Erling, and J. Lakshmanan, "Technique de mesure et d'interpretation minimisant les erreurs de mesure en microgravimetrie," *Geophysical Prospecting*, vol. 29, pp. 782–789, 1981.
- [7] D. K. Butler, "Interval gravity-gradient determination concepts," *Geophysics*, vol. 49, no. 6, pp. 828–832, 1984.
- [8] D. K. Butler, "Microgravimetric and gravity-gradient techniques for detection of subsurface cavities," *Geophysics*, vol. 49, no. 7, pp. 1084–1096, 1984.
- [9] B. E. Khesin, V. V. Alexeyev, and L. V. Eppelbaum, "Investigation of geophysical fields in pyrite deposits under mountainous

- conditions," *Journal of Applied Geophysics*, vol. 30, no. 3, pp. 187–204, 1993.
- [10] D. Patterson, J. C. Davey, A. H. Cooper, and J. K. Ferris, "The investigation of dissolution subsidence incorporating microgravity geophysics at Ripon, Yorkshire," *Quarterly Journal of Engineering Geology*, vol. 28, no. 1, pp. 83–94, 1995.
- [11] D. E. Yule, M. K. Sharp, and D. K. Butler, "Microgravity investigations of foundation conditions," *Geophysics*, vol. 63, no. 1, pp. 95–103, 1998.
- [12] N. C. Crawford, "Microgravity investigations of sinkhole collapses under highway," in *Proceedings of the 1st SAGEEP Conference*, vol. 1, pp. 1–13, St. Louis, Mo, USA, 2000.
- [13] M. Beres, M. Luetscher, and R. Olivier, "Integration of ground-penetrating radar and microgravimetric methods to map shallow caves," *Journal of Applied Geophysics*, vol. 46, no. 4, pp. 249–262, 2001.
- [14] D. K. Butler, "Potential fields methods for location of unexploded ordnance," *Leading Edge*, vol. 20, no. 8, pp. 890–895, 2001.
- [15] M. Rybakov, V. Goldshmidt, L. Fleischer, and Y. Rotstein, "Cave detection and 4-D monitoring: a microgravity case history near the Dead Sea," *Leading Edge*, vol. 20, no. 8, pp. 896–900, 2001.
- [16] T. Hunt, M. Sugihara, T. Sato, and T. Takemura, "Measurement and use of the vertical gravity gradient in correcting repeat microgravity measurements for the effects of ground subsidence in geothermal systems," *Geothermics*, vol. 31, no. 5, pp. 525–543, 2002.
- [17] L. V. Eppelbaum and B. E. Khesin, "Advanced 3D modelling of gravity field unmasks reserves of a pyrite-polymetallic deposit: a case study from the Greater Caucasus," *First Break*, vol. 22, no. 11, pp. 53–56, 2004.
- [18] P. Styles, S. Toon, E. Thomas, and M. Skittrall, "Microgravity as a tool for the detection, characterization and prediction of geohazard posed by abandoned mining cavities," *First Break*, vol. 24, no. 5, pp. 51–60, 2006.
- [19] D. K. Butler, Ed., *Near-Surface Geophysics*, no. 13 of Investigations in Geophysics, Society of Exploration Geophysicists, 2005.
- [20] J. S. da Silva and F. J. F. Ferreira, "Gravimetry applied to water resources and risk management in karst areas: a case study in Parana state, Brazil," in *Proceedings of the Transactions of the 23th FIG Congress*, p. 14, Munich, Germany, 2006.
- [21] M. W. Branston and P. Styles, "Site characterization and assessment using the microgravity technique: a case history," *Near Surface Geophysics*, vol. 4, no. 6, pp. 377–385, 2006.
- [22] N. Debeglia, A. Bitri, and P. Thierry, "Karst investigations using microgravity and MASW; application to Orléans, France," *Near Surface Geophysics*, vol. 4, no. 4, pp. 215–225, 2006.
- [23] I. R. Abad, F. G. García, I. R. Abad et al., "Non-destructive assessment of a buried rainwater cistern at the Carthusian Monastery "Vall de Crist" (Spain, 14th century) derived by microgravimetric 2D modelling," *Journal of Cultural Heritage*, vol. 8, no. 2, pp. 197–201, 2007.
- [24] C. C. Bradley, M. Y. Ali, I. Shawky, A. Levannier, and M. A. Dawoud, "Microgravity investigation of an aquifer storage and recovery site in Abu Dhabi," *First Break*, vol. 25, no. 11, pp. 63–69, 2007.
- [25] L. V. Eppelbaum, "Revealing of subterranean karst using modern analysis of potential and quasi-potential fields," in *Proceedings of the SAGEEP Conference*, vol. 20, pp. 797–810, Denver, Colo, USA, 2007.
- [26] T. Mochales, A. M. Casas, E. L. Pueyo et al., "Detection of underground cavities by combining gravity, magnetic and ground penetrating radar surveys: a case study from the Zaragoza area, NE Spain," *Environmental Geology*, vol. 53, no. 5, pp. 1067–1077, 2008.
- [27] S. Deroussi, M. Diament, J. B. Feret, T. Nebut, and T. Staudacher, "Localization of cavities in a thick lava flow by microgravimetry," *Journal of Volcanology and Geothermal Research*, vol. 184, no. 1-2, pp. 193–198, 2009.
- [28] M. Ezersky, A. Legchenko, C. Camerlynck et al., "The Dead Sea sinkhole hazard—new findings based on a multidisciplinary geophysical study," *Zeitschrift fur Geomorphologie*, vol. 54, no. 2, pp. 69–90, 2010.
- [29] F. Greco, G. Currenti, C. Del Negro et al., "Spatiotemporal gravity variations to look deep into the Southern flank of Etna volcano," *Journal of Geophysical Research B*, vol. 115, no. 11, Article ID B11411, 2010.
- [30] G. Leucci and L. de Giorgi, "Microgravimetric and ground penetrating radar geophysical methods to map the shallow karstic cavities network in a coastal area (Marina Di Capilungo, Lecce, Italy)," *Exploration Geophysics*, vol. 41, no. 2, pp. 178–188, 2010.
- [31] A. G. Camacho, P. J. González, J. Fernández, and G. Berrino, "Simultaneous inversion of surface deformation and gravity changes by means of extended bodies with a free geometry: application to deforming calderas," *Journal of Geophysical Research*, vol. 116, no. B10, 2011.
- [32] L. V. Eppelbaum, "Review of environmental and geological microgravity applications and feasibility of their implementation at archaeological sites in Israel," *International Journal of Geophysics*, vol. 2011, Article ID 927080, 9 pages, 2011.
- [33] A. Hajian, H. Zomorrodian, P. Styles, F. Greco, and C. Lucas, "Depth estimation of cavities from microgravity data using a new approach: the local linear model tree (LOLIMOT)," *Near Surface Geophysics*, vol. 10, pp. 221–234, 2012.
- [34] L. V. Eppelbaum, "Application of microgravity at archaeological sites in Israel: some estimation derived from 3D modeling and quantitative analysis of gravity field," in *Proceedings of the Symposium on the Application of Geophysics to Engineering and Environmental Problems Conference (SAGEEP)*, vol. 22, pp. 434–446, Fort Wort, Tex, USA, 2009.
- [35] K. J. Sjostrom and D. K. Butler, "Noninvasive weight determination of stockpiled ore through microgravity measurements," Report of the US Army Corps of Engineers, Paper GL-96-24, 1996.
- [36] E. Elawadi, A. Salem, and K. Ushijima, "Detection of cavities and tunnels from gravity data using a neural network," *Exploration Geophysics*, vol. 32, no. 4, pp. 204–208, 2001.
- [37] N. Debeglia and F. Dupont, "Some critical factors for engineering and environmental microgravity investigations," *Journal of Applied Geophysics*, vol. 50, no. 4, pp. 435–454, 2002.
- [38] D. Carbone and F. Greco, "Review of microgravity observations at Mt. Etna: a powerful tool to monitor and study active volcanoes," *Pure and Applied Geophysics*, vol. 164, no. 1, pp. 1–22, 2007.
- [39] T. Jacob, J. Chery, R. Bayer et al., "Time-lapse surface to depth gravity measurements on a karst system reveal the dominant role of the epikarst as a water storage entity," *Geophysical Journal International*, vol. 177, no. 2, pp. 347–360, 2009.
- [40] G. Castiello, G. Florio, M. Grimaldi, and M. Fedi, "Enhanced methods for interpreting microgravity anomalies in urban areas," *First Break*, vol. 28, no. 8, pp. 93–98, 2010.

- [41] S. Porzucek, "Some Applicability problems of Euler deconvolution to the interpretation of the results of microgravity survey," in *Proceedings of the Transactions of the Near Surface EAGE Conference*, P55, pp. 1–5, Zurich, Switzerland, 2010.
- [42] A. C. Dolgal and A. F. Sharkhimullin, "Increasing accuracy of monogenic gravity anomaly interpretation," *Geoinformatics*, vol. 4, pp. 49–56, 2011 (Russian).
- [43] G. Kaufmann, D. Romanov, and R. Nielbock, "Cave detection using multiple geophysical methods: unicorn cave, Harz Mountains, Germany," *Geophysics*, vol. 76, no. 3, pp. B71–B77, 2011.
- [44] J. Panisova, R. Pašteka, J. Papco, and M. Fraštia, "The calculation of building corrections in microgravity surveys using close range photogrammetry," *Near Surface Geophysics*, vol. 10, pp. 391–399, 2012.
- [45] L. V. Eppelbaum, "Archaeological geophysics in Israel: past, present and future," *Advances in Geosciences*, vol. 24, pp. 45–68, 2010.
- [46] B. E. Khesin, V. V. Alexeyev, and L. V. Eppelbaum, *Interpretation of Geophysical Fields in Complicated Environments*, Advanced Approaches in Geophysics, Kluwer Academic, Dordrecht, The Netherlands, 1996.
- [47] W. M. Telford, L. P. Geldart, and R. E. Sheriff, *Applied Geophysics*, Cambridge University Press, Cambridge, UK, 1990.
- [48] L. V. Eppelbaum and B. E. Khesin, *Geophysical Studies in the Caucasus*, Springer, Heidelberg, Germany, 2012.
- [49] L. V. Eppelbaum, B. E. Khesin, and S. E. Itkis, "Archaeological geophysics in arid environments: examples from Israel," *Journal of Arid Environments*, vol. 74, no. 7, pp. 849–860, 2010.
- [50] D. S. Parasnis, *Principles of Applied Geophysics*, Chapman & Hall, London, UK, 4th edition, 1986.
- [51] D. T. Sandwell and W. H. F. Smith, "Global marine gravity from retracked Geosat and ERS-1 altimetry: ridge segmentation versus spreading rate," *Journal of Geophysical Research B*, vol. 114, no. 1, Article ID B01411, 2009.
- [52] A. Ginzburg and Z. Ben-Avraham, "A seismic refraction study of the north basin of the Dead Sea, Israel," *Geophysical Research Letters*, vol. 24, no. 16, pp. 2063–2066, 1997.
- [53] M. Weber, K. Abu-Ayyash, A. Abueladas et al., "Anatomy of the Dead Sea transform from lithospheric to microscopic scale," *Reviews of Geophysics*, vol. 47, no. 2, 2010.
- [54] M. J. Wichura, "Algorithm AS 241: the percentage points of the normal distribution," *Applied Statistics*, vol. 37, no. 3, pp. 477–484, 1988.
- [55] S. Shatterjee and A. S. Sadi, *Regression Analysis by Example*, John Wiley & Sons, New York, NY, USA, 1996.
- [56] J. O. Rawlings, S. G. Pantula, and D. A. Dickey, *Applied Regression Analysis: A Research Tool*, Springer, New York, NY, USA, 2nd edition, 1998.
- [57] M. H. Bingham and J. M. Fry, *Regression: Linear Models in Statistics*, Undergraduate Math Series, Springer, London, UK, 2010.
- [58] S. A. Taqieddin, N. S. Abderahman, and M. Atallah, "Sinkhole hazards along the eastern Dead Sea shoreline area, Jordan: a geological and geotechnical consideration," *Environmental Geology*, vol. 39, no. 11, pp. 1237–1253, 2000.
- [59] A. Al-Zoubi, A. Abueadas, A. Akkawwi, L. Eppelbaum, E. Levi, and M. Ezersky, "Use of microgravity survey in the Dead Sea areas affected by the sinkholes hazard," in *Proceedings of the Transactions of the 8th EUG Meeting, Geophysical Research Abstracts*, vol. 14 of EGU2012-1982, Vienna, Austria, 2012.

Research Article

3D Imaging of Dead Sea Area Using Weighted Multipath Summation: A Case Study

Shemer Keydar,¹ Benjamin Medvedev,^{1,2} Abdallah Al-Zoubi,³
Michael Ezersky,¹ and Emad Akkawi³

¹ Project Department, The Geophysical Institute of Israel, Lod 71100, Israel

² Schlumberger, Via dell'Unione Europea, 4 San Donato Milanese, Milan, Italy

³ Engineering Faculty, Al-Balqa' Applied University, Salt 19117, Jordan

Correspondence should be addressed to Shemer Keydar; shemer@gii.co.il

Received 4 November 2012; Revised 27 January 2013; Accepted 28 January 2013

Academic Editor: Umberta Tinivella

Copyright © 2013 Shemer Keydar et al. This is an open access article distributed under the Creative Commons Attribution License, which permits unrestricted use, distribution, and reproduction in any medium, provided the original work is properly cited.

The formation of sinkholes along the Dead Sea is caused by the rapid decline of the Dead Sea level, as a possible result of human extensive activity. According to one of the geological models, the sinkholes in several sites are clustered along a narrow coastal strip developing along lineaments representing faults in NNW direction. In order to understand the relationship between a developing sinkhole and its tectonic environment, a high-resolution (HR) three-dimensional (3D) seismic reflection survey was carried out at the western shoreline of the Dead Sea. A recently developed 3D imaging approach was applied to this 3D dataset. Imaging of subsurface is performed by a spatial summation of seismic waves along time surfaces using recently proposed multipath summation with proper weights. The multipath summation is performed by stacking the target waves along all possible time surfaces having a common apex at the given point. This approach does not require any explicit information on parameters since the involved multipath summation is performed for all possible parameters values within a wide specified range. The results from processed 3D time volume show subhorizontal coherent reflectors at approximate depth of 50–80 m which incline on closer location to the exposed sinkhole and suggest a possible linkage between revealed fault and the sinkholes.

1. Introduction

During the last thirty years, hundreds of sinkholes have appeared along the Dead Sea (DS) shoreline in both Israel and Jordan (Figure 1) [1–3]. The process began in the southern part of the DS coast and slowly spread northward along the western coast. The eastern coast which is usually steeper has been less affected at the flat-lying region close to the Lisan Peninsula. The sinkholes have already caused considerable damage to infrastructure, and there is obvious potential for further collapses beneath main highways and other infrastructure.

In order to understand the relationship between a developing sinkhole and its tectonic environment, a numerous number of high resolution seismic reflection surveys were carried out using common midpoint (CMP) technique [3, 5, 6]. The high-resolution seismic reflection method is

intended for the study faults and conduits in the shallow subsurface (down to 100–200 m deep), which could bring the fresh water to the salt layer presumably from below. The conventional processing technique, the so-called common midpoint (CMP) method, essentially consists of a “stack” (summation) of properly corrected traces thus increasing the signal-to-noise ratio. However, in the shallow subsurface, the conventional CMP method causes a loss of information because of the problem of “stretching” of data caused by NMO time correction formula. That is why a new 2D and 3D free stretch imaging approach had been applied in the framework of the MERC project M27-050 in order to examine tectonic hypothesis connecting the sinkholes with tectonic faults [7–9]. This approach involves zero-offset common shot point (CSP) stacking and diffraction imaging method [9]. On the basis of those methods in combination with a new weighted multipath summation technique [10, 11], a package

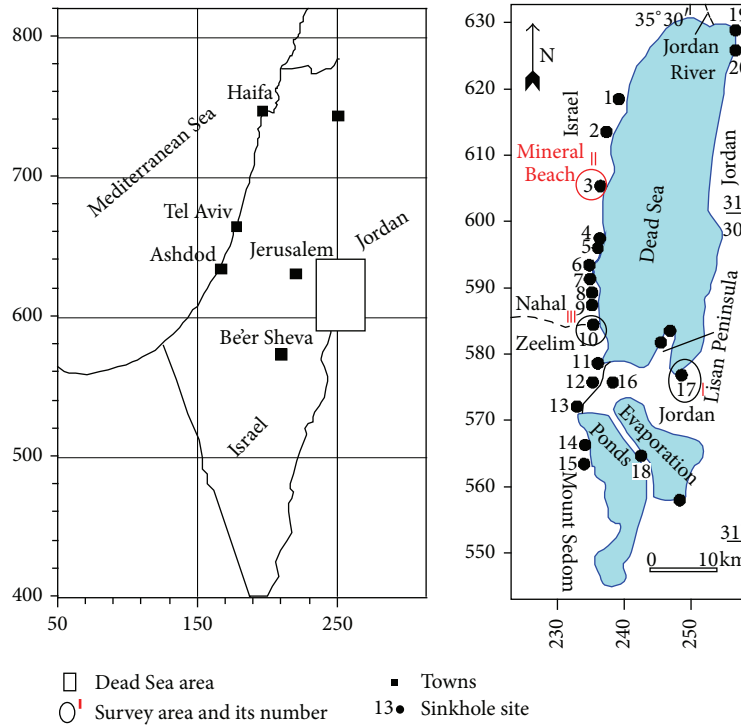


FIGURE 1: Sinkhole sites along the Dead Sea shore: (1) Palms, (2) Samar Spring, (3) Mineral Beach, (4) Ein Gedi and Nahal Arugot, (5) Yesha, (6) Zeruya, (7) Nahal Hever northern, (8) Nahal Hever southern, (9) Asa'el, (10) Nahal Zeelim, (11) Mezada, (12) Rahaf, (13) Mor, (14) Ein Boqeq, (15) Newe Zohar, (16) Lisan Peninsula, (17) Ghor Al-Haditha, (18) Dam-2. I-III: sites under investigation. (coordinates are in km, new Israel Mercator grid).

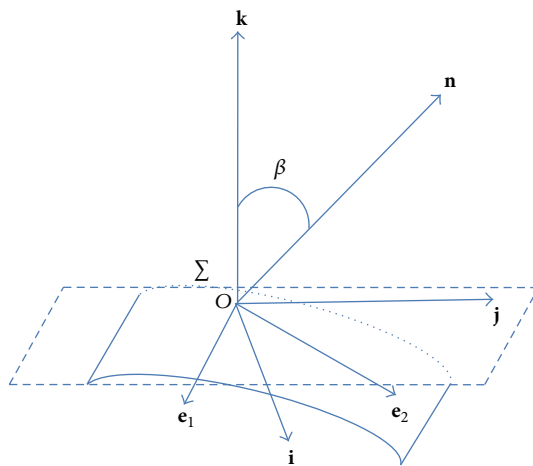


FIGURE 2: Scheme of wavefront arriving at a Common Shot Point.

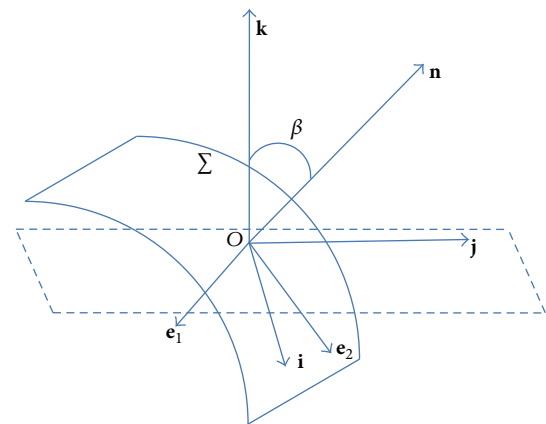


FIGURE 3: The same as Figure 2 in case of one direction is normal to vector k .

of programs was written. The CSP stack and diffraction method are complementary to each other and reveal useful information about the subsurface. The diffraction method serves as a tool for detection of faults and voids, while the CSP stacking contains information about the structure of the subsurface. These methods were applied along the Dead Sea's

shorelines. We have carried out several new seismic surveys along line crossing the sinkhole lineaments and reinterpreted a number of previous reflection sections. The 2D imaging technique has been presented in [7]. This paper examines the new 3D imaging approach and its application to 3D data that was acquired at the western shoreline of the Dead Sea. The results of the imaging allow better understanding between

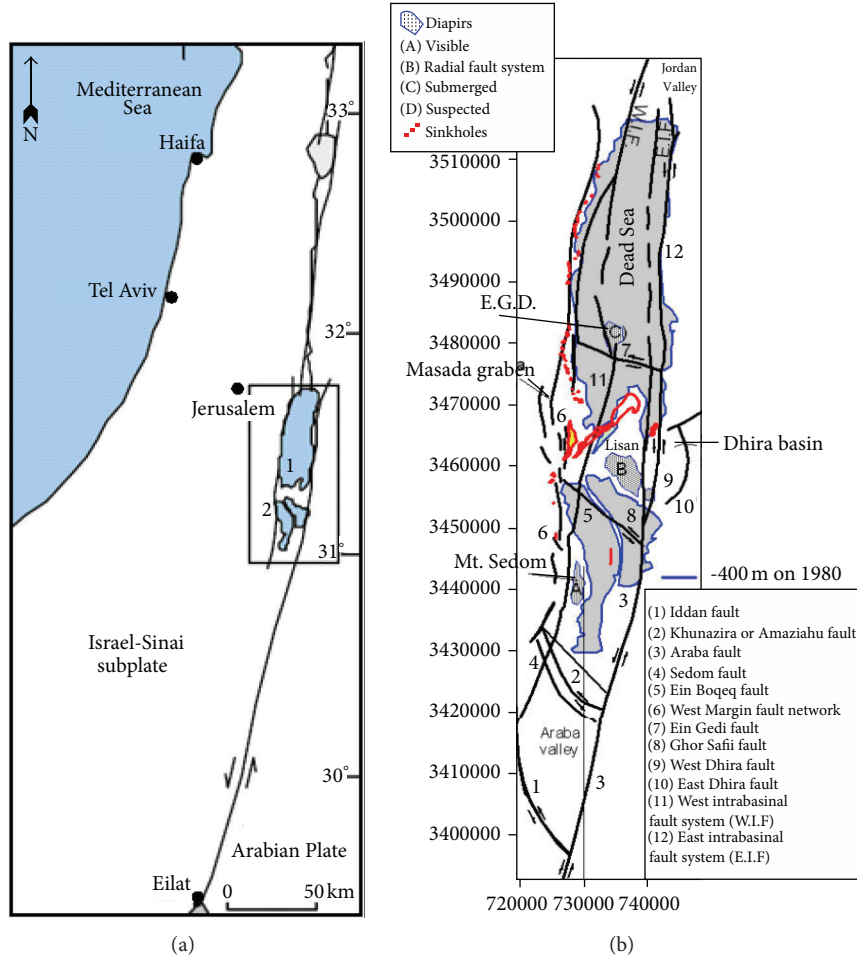


FIGURE 4: Dead Sea tectonic setting: (a) Dead Sea transform; (b) faults through the DS area [4].

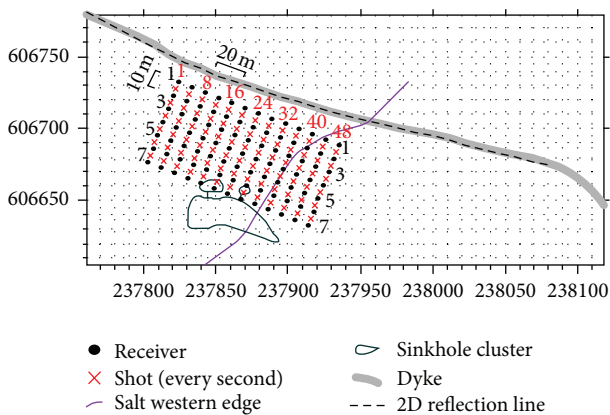


FIGURE 5: The geometry of 3D seismic survey.

a developing sinkhole and its tectonic environment. We give here a short description of 3D zero-offset stacking and multipath weighted summation. For a more comprehensively discussion of the methods, one can read in the relevant papers.

2. The 3D Zero Offset Stacking Method

The basis of the 3D zero-offset stacking method is a new normal moveout (NMO) time correction formula for three-dimensional media as function on wavefront parameters [11, 12]. One of these parameters on which the proposed time correction formula is based is the emergence angle β , defined as the acute angle between the wavefront normal and the normal to the acquisition plane at the CSP. Let us consider a central ray and its associated wavefront arriving at a common shot point (CSP) (Figure 2).

An ellipsoidal wavefront emerges at the CSP location O . It has two independent vectors e_1 and e_2 tangent to the wavefront and the normal n . The emergence angle β is the angle between n and the normal to the acquisition plane, k . Additional fundamental parameters on which the time correction formula is based are the curvatures of the wavefront. It is well known from the differential geometry of surfaces that at each point of the wavefront two principal curvatures can be defined, being the eigenvalues of the 2×2 matrix of second derivatives. These curvatures are the minimal and maximal curvatures and are related to the mean and Gaussian curvatures. The principal curvatures are associated

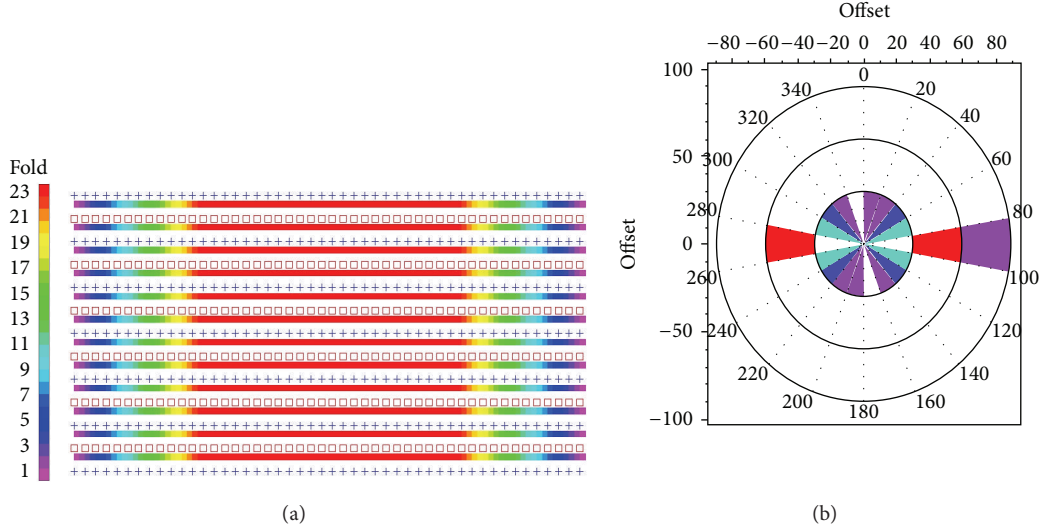


FIGURE 6: Fold scheme. (a) The shots locations are marked by “+” and receivers locations are marked by squares, (b) fold as function of azimuth.

to two perpendicular principal directions, which together with the wavefront normal form a rectangular system of axes. The curvature of the wavefront is completely described by the two principal curvatures and the angle the principal directions make with the general coordinate system. This is denoted in Figure 2 as \mathbf{i} , \mathbf{j} , and \mathbf{k} . The principal curvatures can be expressed in terms of principal radii of curvature, which play an important role in the traveltime correction expressions derived in this paper. Figure 3 illustrates the case where one of the principal directions is normal to \mathbf{k} . Based on those principles and eikonal equation only, the following 3D travel-time correction formula for an arbitrary system of coordinates was obtained:

$$\begin{aligned}
 t &= \frac{1}{V} (a_{31}x + a_{32}y) + \frac{1}{2VR_1} (a_{11}x + a_{12}y)^2 \\
 &+ \frac{1}{2VR_2} (a_{21}x + a_{22}y)^2 + \dots, \\
 a_{31} &= \sin \beta \sin \phi, & a_{32} &= -\sin \beta \cos \phi, \\
 a_{11} &= \cos \phi, & a_{12} &= \sin \phi, \\
 a_{21} &= -\cos \beta \sin \phi, & a_{22} &= \cos \beta \cos \phi,
 \end{aligned} \tag{1}$$

where β is the emergence angle of the wavefront at point O , ϕ azimuth angle, defined as the angle between the axis $O\tilde{X}$ and the principal direction of the wavefront at point O , \tilde{x} and \tilde{y} are the offsets along the axis $O\tilde{X}$ and $O\tilde{Y}$. For a given source receiver, gather the moveout equations that express the moveout correction with respect to a zero-offset trace by five parameters measured at the central point. The parameters are principal radii of the wavefront R_1 , R_2 , the azimuth angle ϕ , the emergence angle β , and the reference velocity V .

In the following, we give a short description of the weighted multipath summation.

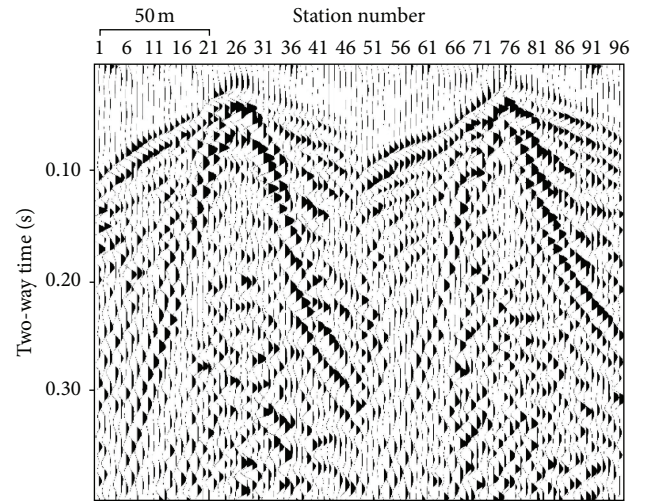


FIGURE 7: Typical common shot gathering including 96 channels.

3. Multipath Summation

The summation of 3D stacking is performed along time surfaces defined by (1). The summation can be implemented using either of the two approaches. In the first conventional approach, the target waves are stacked along the time surfaces defined by wavefront parameters and velocity. These optimal parameters usually are estimated using optimization problem which consists of finding parameters which maximize some correlation functional. We use an alternative, more formal recently proposed multipath summation with a proper weighting [10, 13–15]. The weighted multipath summation allows us to replace the complex optimization problem of estimating the optimal parameters, by summation along all possible surfaces that are created from small variations

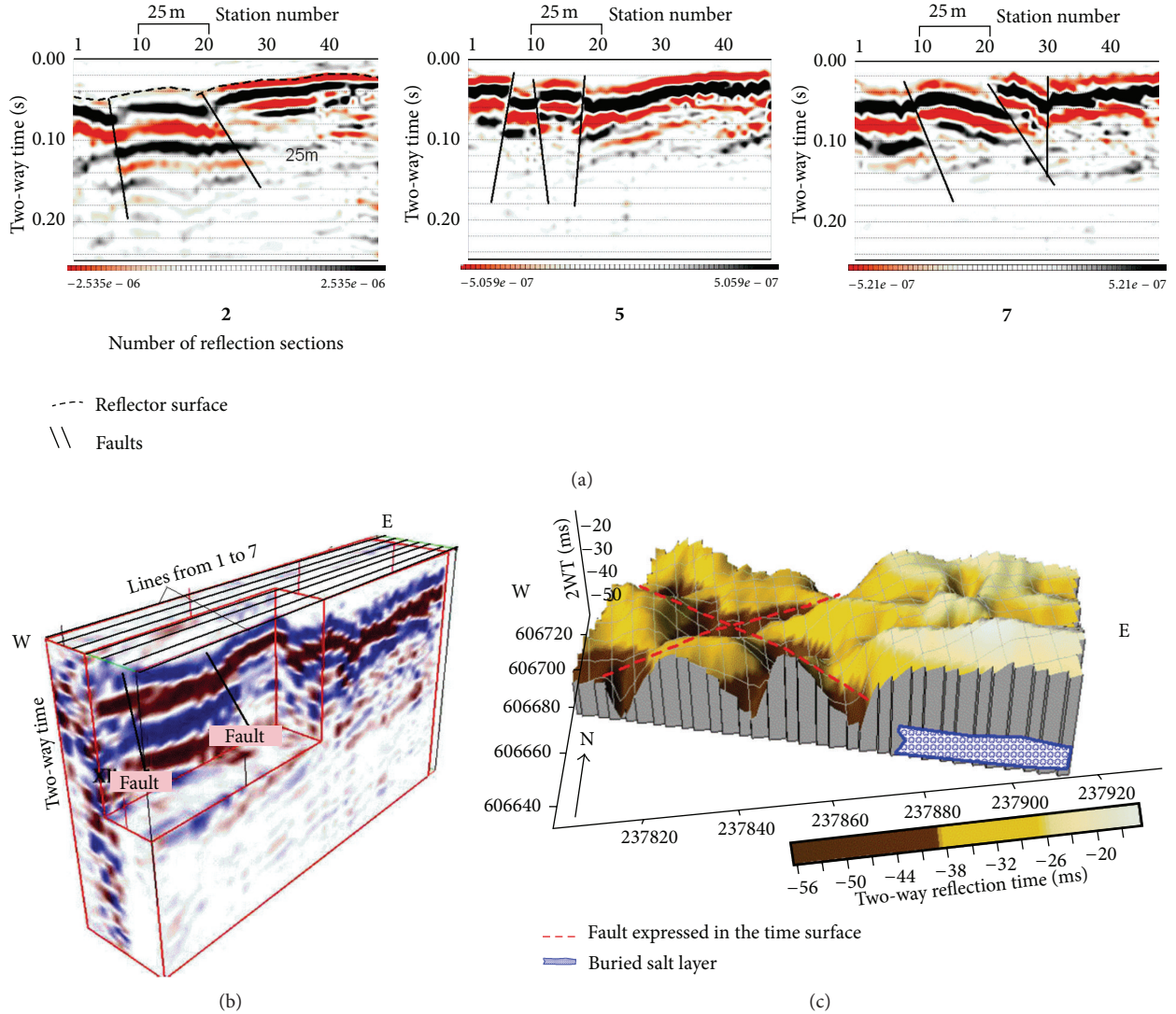


FIGURE 8: Typical two-way time sections (a) constructed from 3D time cube obtained using 3D imaging approach (b); two-way time map of reflector in the 3D presentation (c).

of those parameters. The weighted multipath summation (WMPS) can be described by the following expressions:

$$I_{\text{WMPS}} = \frac{\sum_P I_P W(I_P)}{\sum_P W(I_P)}, \quad (2)$$

$$I_P = \sum_P \sum_S \sum_R U_{SR}(T_{SR}(P)),$$

where $W(I_P) = \exp(\lambda I_P)$ is an “optimal” weighting function and λ is an undimensional large number. I_P is the image obtained for fixed parameters P , namely, for radii of curvatures azimuth and emergence angles. $U_{SR}(T_{SR})$ is a seismic trace for a given source-receiver pair. T_{SR} is travel time from shot S to receiver R . The summation (2) with the proper weight $W(I_P)$ is performed for all possible parameter values within a specified range. The image defined by I_P means that for every point to be imaged, seismic amplitudes are stacked

together along all possible time surfaces defined by (1). The constructive and destructive interference of the amplitudes contributed by each time surface produces an image close to that obtained by stacking with the “correct” parameter [16].

4. Case Study

4.1. Dead Sea Area—Brief Tectonic Setting. Dead Sea (DS) is a pull apart basin or strike-slip one undergone to NW-SE compression and NE-SW tensile stress (Figure 4(a)). DS consists of two basins: the northern one (deeper) (denoted by 1 in Figure 4(a)) and the southern one (shallower) (denoted by 2 in Figure 4(a)). And it is extended in approximately N-S direction.

Numerous faults have been detected through DS area (Figure 4(b)) and have mainly extended in the same direction

[4, 17, 18]. The Dead Sea is located nowadays at elevation of -426 m below the sea level (b.s.l).

4.2. Study Site. Mineral beach study site (Figure 1) is located between the Dead Sea shoreline at the east and route number 90 (the main road along the western DS shore) at the west. The area is characterized by N-S normal faults [6]. Around Mineral Beach, sinkholes develop in both mudflat (southern boreholes Mn-2, Mn-5) and alluvial fan (northern borehole Mn-4) areas. Boreholes show that salt layer at the northern part of the area is located at 10 m deeper (-434 m elevation) than that at the southern one (-424 m). At the northern part of the area, salt is overlain by sandy-gravel sediments, whereas the southern part is composed of DS mud (clay) overlaying the salt.

The field acquisition covers 120 m by 60 m and consists of seven receiver lines in a 10 m interval between them. Shooting was carried out using six shot lines (288 shots in total) and each shot includes 96 channels in 2.5 m interval between them. The distance between shot lines is 10 m (Figure 5).

We used truck mounted accelerated weight (Digipulse) as an energy source and single 10 Hz geophone per station. In order to image the new developing fault in details, the survey was designed with a full azimuth cover for offsets less than 30 m (Figure 6).

The data was recorded using 0.5 msec sample rate and 0.5 sec record length. Typical common shot gathers are seen on Figure 7.

The data was processed using the new 3D stacking algorithm. The range of variation of parameters in (2) was as follows: radii of curvature from 3 to 600 meter, emergence angle from -5 to $+5$ degree, and velocity from 300 m/s to 1000 m/s. The value of λ was 900. The results from processed 3D imaging are presented in Figure 8(a) as a time sections along reflection lines and in Figure 8(b) as a 3D cube time section.

A time map of the first reflector is presented in Figure 8(c). On all the figures, are clearly seen subhorizontal coherent reflectors at approximate depth of 50–80 m, which incline on closer location to the exposed sinkhole. In addition, faults are seen on all sections (Figure 8(a) sections denoted by 2, 5, and 7). These faults are clearly seen on reflector presented in Figure 8(c). The results are consistent with the results that were obtained from a previous 2D study [3] at the same site. This work provides the first 3D HR imaging on the edge of a sinkhole and nearby fault. The results of the seismic interpretation of 3D image suggest a possible linkage between revealed fault sinkholes and field observation.

5. Conclusions

In order to understand the relationship between a developing sinkhole and its tectonic environment, a high-resolution (HR) three-dimensional (3D) seismic reflection survey was carried out at the western shoreline of the Dead Sea. The 3D image of the subsurface was obtained by the use of a recently developed 3D imaging approach. The core of this approach is a new 3D NMO time correction surface formula. Imaging of

subsurface is performed by a spatial summation of seismic waves along these time surfaces using recently proposed multipath summation with proper weights. The multipath summation is performed by stacking the target waves along all possible time surfaces having a common apex at the given point. This approach does not require any explicit information on parameters since the involved multipath summation is performed for all possible parameters values within a wide specified range. The results from processed 3D time volume show subhorizontal coherent reflectors at approximate depth of 50–80 m which incline on closer location to the exposed sinkhole and suggest a possible linkage between revealed fault and the sinkholes.

Acknowledgments

This study has been performed within the framework of MERC project M27-050 fund sponsored by the USAID. Thanks are due to the support of the Israel Ministry of Infrastructure. The authors are also grateful to the Geophysical Institute of Israel for permission to publish this paper.

References

- [1] Y. Arkin and A. Gilat, "Dead Sea sinkholes: an ever-developing hazard," *Environmental Geology*, vol. 39, no. 7, pp. 711–722, 2000.
- [2] A. Frumkin and E. Raz, "Collapse and subsidence associated with salt karstification along the Dead Sea," *Carbonates and Evaporites*, vol. 16, no. 2, pp. 117–130, 2001.
- [3] Y. Yechieli, M. Abelson, A. Bein, O. Crouvi, and V. Shtivelman, "Sinkhole "swarms" along the Dead Sea coast: reflection of disturbance of lake and adjacent groundwater systems," *Bulletin of the Geological Society of America*, vol. 118, no. 9–10, pp. 1075–1087, 2006.
- [4] Z. Ben-Avraham, "Geophysical framework of the Dead Sea: structure and Tectonics," in *The Dead Sea: the Lake and Its Setting*, T. M. Niemi, Z. Ben-Avraham, and J. Gat, Eds., pp. 22–35, Oxford University Press, Oxford, UK, 1997.
- [5] M. Abelson, G. Baer, V. Shtivelman et al., "Collapse-sinkholes and radar interferometry reveal neotectonics concealed within the Dead Sea basin," *Geophysical Research Letters*, vol. 30, no. 10, pp. 52–1, 2003.
- [6] M. Abelson, Y. Yechieli, O. Crouvi et al., "Evolution of the Dead Sea sinkholes," *Special Paper of the Geological Society of America*, no. 401, pp. 241–253, 2006.
- [7] S. Keydar, B. Medvedev, M. Ezerky, and L. Sobolevsky, "Imaging shallow subsurface of Dead Sea area by Common Shot Point stacking and diffraction method using weighted multipath summation," *Journal of Civil Engineering and Science*, vol. 1, no. 2, pp. 75–79, 2012.
- [8] S. Keydar, L. Bodet, C. Camerlynck et al., "A new approach for shallow subsurface imaging and its application to the Dead Sea sinkhole problem," in *Proceedings of the 73rd EAGE Conference and Exhibition*, pp. 1–4, Vienna, Austria, April 2011.
- [9] S. Keydar, B. Medvedev, A. Al-Zoubi, and M. Ezerky, "Another look of imaging of shallow subsurface: real examples from the Dead Sea sinkhole development areas," in *EGU General Assembly*, vol. 14 of *Geophysical Research Abstracts*, vol. 14, p. 1432, Vienna, Austria, April 2012.

- [10] S. Keydar, "Homeomorphic imaging using path integrals," in *Proceedings of the 66th EAGE Conference & Exhibition*, pp. 7–10, Paris, France, June 2004.
- [11] S. Keydar and M. Mikenberg, "Prestack time migration using the Kirchhoff sum along a new approximation of the reflection travel time curve," in *Proceedings of the 72nd European Association of Geoscientists and Engineers Conference and Exhibition (EUROPEC '10)*, pp. 4916–4920, Barcelona, Spain, June 2010.
- [12] S. Keydar and M. Mikenberg, "A new time correction formula in three-dimensional media as a function of wavefront attributes," *Journal of Seismic Exploration*, vol. 17, no. 4, pp. 349–369, 2008.
- [13] S. Keydar and V. Shtivelman, "Imaging zero-offset sections using multipath summation," *First Break*, vol. 23, pp. 21–24, 2005.
- [14] E. Landa, S. Fomel, and T. J. Moser, "Path-integral seismic imaging," *Geophysical Prospecting*, vol. 54, no. 5, pp. 491–503, 2006.
- [15] J. Schleicher and J. C. Costa, "Migration velocity analysis by double path-integral migration," *Geophysics*, vol. 74, no. 6, pp. WCA225–WCA231, 2009.
- [16] V. Shtivelman, S. Keydar, and M. Mikenberg, "Imaging near-surface inhomogeneities using weighted multipath summation," *Near Surface Geophysics*, vol. 7, no. 3, pp. 171–177, 2009.
- [17] A. Al-Zoubi and U. S. Ten Brink, "Salt diapirs in the Dead Sea basin and their relationship to Quaternary extensional tectonics," *Marine and Petroleum Geology*, vol. 18, no. 7, pp. 779–797, 2001.
- [18] A. Frumkin, M. Ezersky, A. Al-Zoubi, E. Akkawi, and A.-R. Abueladas, "The Dead Sea hazard: geophysical assessment of salt dissolution and collapse," *Geomorphology*, vol. 134, pp. 102–117, 2011.

Research Article

Environmental Geophysical Study of the Groundwater Mineralization in a Plot of the Cotonou Littoral Zone (South Benin)

Yalo Nicaise,¹ Descloitres Marc,² Alassane Abdoukarim,¹
Mama Daouda,¹ and Boukari Moussa¹

¹Laboratory of Applied Hydrology, Faculty of Sciences and Techniques, University of Abomey-Calavi, 01BP526 Cotonou, Benin

²LTHE, IRD, BP 53, 38041 Grenoble Cedex 9, France

Correspondence should be addressed to Yalo Nicaise, yalonicaise@yahoo.fr

Received 23 August 2012; Revised 3 October 2012; Accepted 15 October 2012

Academic Editor: Michela Giustiniani

Copyright © 2012 Yalo Nicaise et al. This is an open access article distributed under the Creative Commons Attribution License, which permits unrestricted use, distribution, and reproduction in any medium, provided the original work is properly cited.

Geophysical investigations comprising electrical resistivity and electromagnetic conductivities methods were deployed in a 350 m² sector, strewn with 11 wells. Within the framework of an environmental study on a small scale in the south of Benin, the water conductivity of these wells was measured to determine in a direct way mineralization of the coastal water table in the littoral zone. This environmental study aimed to prospect by the geophysical methods the space extension of the water table mineralization obtained by direct measurements of water conductivity in the well and the depth of the fresh water/salted water interface in the coastal aquifer. Electromagnetic measurements of conductivities made it possible to chart a gradient of mineralization in the northwest direction. The logs of vertical electric soundings showed a deepening of the fresh water/salted water interface in the southern part and its rupture in the northern part. The electrical resistivities of the interface are sensitive to the degree of its mineralization. It has been observed that the geophysical methods in electrical and electromagnetic prospectation are a great contribution to the environmental study of the water table mineralization in the littoral zone for a sustainable management of the water resource.

1. Introduction

The zone in the south of the town of Cotonou (economic capital of Benin), lying between the Atlantic Ocean in the south and the most populated city of the country in the north, has vocation to develop and know an economic advancement on the tourist level. This development, thus, will imply an increase in the exploitation of the subsoil water resource a priori of the coastal groundwater aquifer. The knowledge of the extension of the saline water intrusion and depth of the fresh water/salted water interface contributes to the decision making for the safeguard of the environment for the users of the water resource. The saline water intrusion in the aquifers of several coastal zones had like consequences of the acute environmental problems [1]. The deterioration of the fresh water quality in the coastal zone due to the normal sea water infiltration affects the intensive but delicately

balanced life of the narrow coastal band [2]. Thus, the cartography of the saline water intrusion will contribute to the maintenance of this delicate balance on the environmental level.

Within the last decade, classic hydrogeological information has been increasingly complemented with subsurface geophysical information that allows obtaining more accurate images of aquifer systems [3–8]. This type of studies has led to the development of the hydrogeophysics discipline [9], in which geophysical methods are used for mapping aquifer subsurface features, estimating properties of the aquifer system, and monitoring distinct dynamic processes, such as seepage in the vadose zone, fluid flow direction, seawater intrusion, and pollutant migration [10]. The surface geophysical methods are noninvasive and constitute profitable solutions of replacement to obtain information on the underground water pollution [2]. The great contrast of

resistivity between the saturated with salted water formation and that saturated with fresh water was used by a great number of researchers for the study of the saline water intrusion in the coastal sectors [11–14]. Van Dam and Meulankamp [11] estimated the salinity of subsoil water in the western part of The Netherlands by using the method of the resistivities. Their interpretations of the resistivities were near to analytical measurements of the salinity of subsoil waters. The electromagnetic method makes it possible to chart in a noninvasive way the side variations in subsurface of electrical conductivity [15]. The determination of the resistivities by electromagnetic methods can have consequence of the values of resistivities lower than those obtained by measurements of the vertical electric surveys [16]. The principal results obtained during this study will show the contribution of geophysics in the cartography of the saline water invasion in littoral zone aquifer. Knowing that frequent and intensive pumpings in the period of pluviometrical deficit cause a lowering of the tablecloth level and a possible increase towards the grounds of salted level [17–19], this study will contribute to an integrated and balanced management of uncontaminated zones with an aim of preserving the environment.

2. Geological and Hydrogeological Setting

2.1. Study Site. The littoral environment of Benin is a zone of interface between the tableland at the north and the Atlantic Ocean at the south. The littoral zone in the south of Cotonou is characterized by a subequatorial climate. Pluviometry in this sector is on average 1200 mm per annum [20]. The variations during the year result in a bimodal regime which make it possible to distinguish a great rainy season from mid-March to mid-July followed by a small rainy season from mid-September to mid-November intercalated, respectively, by small and a great dry season. The average temperature in littoral zone is approximately 27°C. Within the framework of the study on a small scale, sector of 350 m² was selected in the littoral zone. The selected sector is between the latitudes north in 701700N and 702050N UTM coordinates then of longitudes in UTM 424850^E and 425200^E coordinates. The very little inhabited study site, crossed by the road of fishing, is reserved for the tourist development in the next years (see Figure 1). This development will imply an increase in the demand for groundwater.

2.2. Geology. From the geomorphologic point of view, the littoral is as a whole made up of three sandy bars intersected with muddy levels. These sandy bars consist of accumulations of marine granular sediments, current or inherited of last quaternary transgressions [21]. We distinguish from north to south three generations of sandy bars [22]: the intern bars of yellow sand, the median gray sand bars, and the current and subactual brown gray sand bars. The intern bars of yellow sand are separated of the median gray sand bars by the Outobo lagoon. The median gray sand bars are separated of the subactual brown gray sand bars by the coastal lagoon (see Figure 2). These various sand bars were studied by various authors such as Tastet [23], Lang

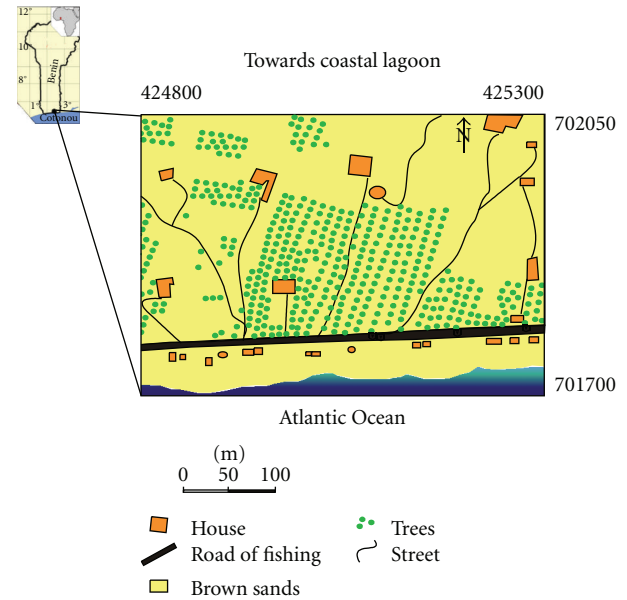


FIGURE 1: Study site map.

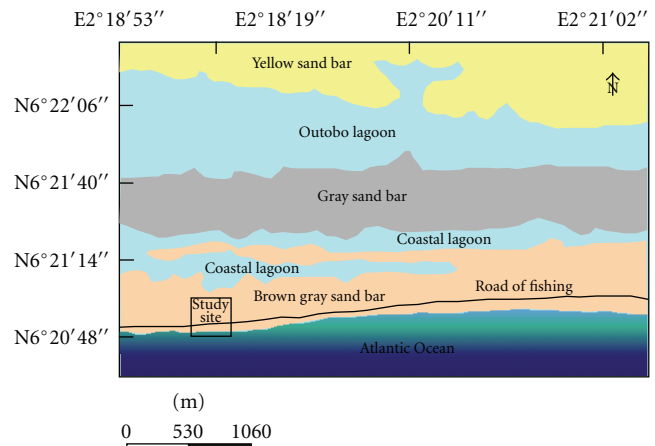


FIGURE 2: Map of sand bars in littoral plain.

et al. [22, 24], and Kaki et al. [25]. The littoral zone, target of this study, is limited to the current and subactual gray brown sand bar. The deposits of the littoral environment of Benin form a transgressed quaternary sedimentary stacking on the formations of the field of the tablelands [21]. The stratigraphy of the recent Quaternary deposits in the littoral environment of the south of Benin was variously approached by authors such as Lang and Paradis [26], Lang et al. [24], and Marsden [27]. The zone of this study is focused on brown gray sand bars.

2.3. Hydrogeology. In the littoral zone, two aquifers with relatively less potentialities are distinguished: the aquifer of Quaternary and Terminal Continental and that of Paleocene [28]. On the level of the littoral plain, the aquifers are thus superimposed (from bottom to top) the sand aquifer of the Cretaceous; the limestone aquifer of Paleocene; the sand

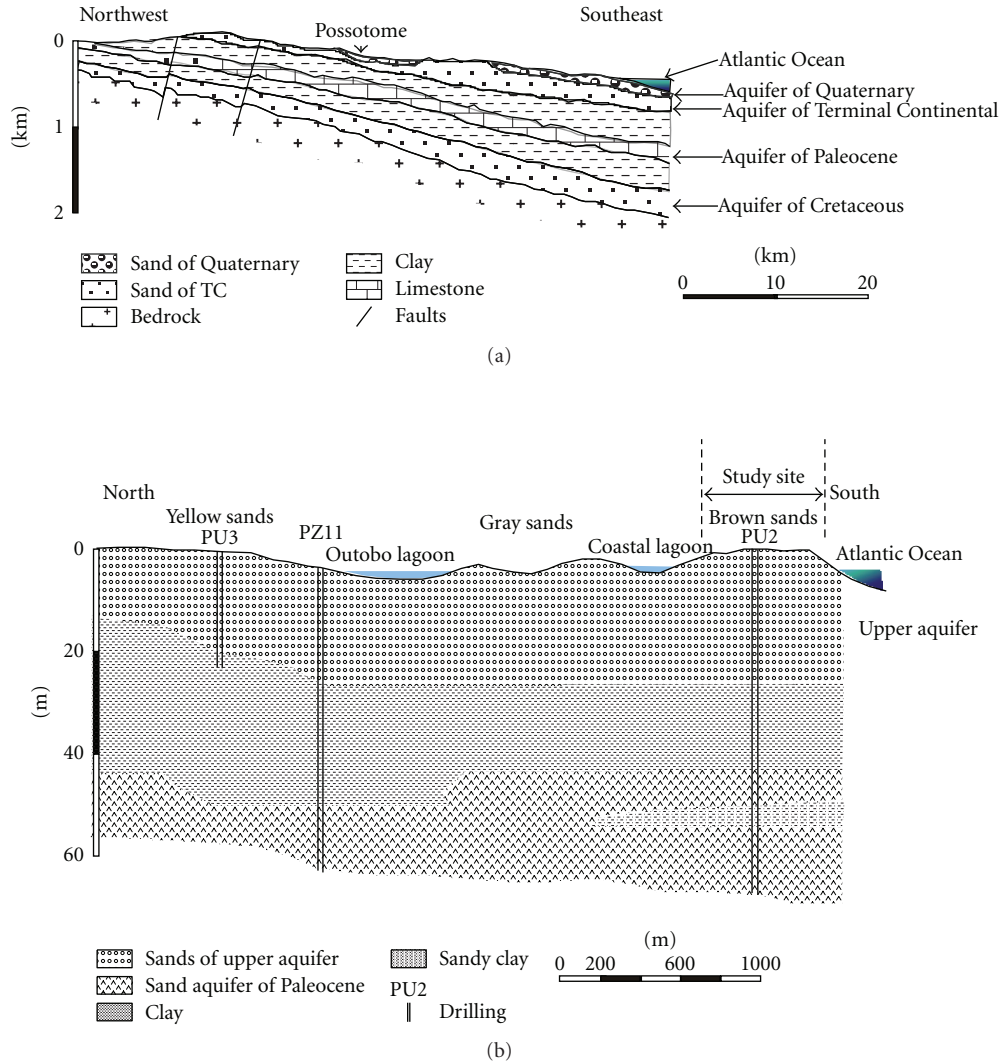


FIGURE 3: (a) Hydrogeological section of littoral plain. (b) Hydrogeological section of upper aquifer.

aquifer of the Terminal Continental (higher Miocene-Pliocene), and the littoral or alluvial sand aquifer of the Quaternary (see Figure 3(a)). The sandy bars contain an aquifer exploited by wells with flows between 1 and 15 m³/h. The permeability of sands is raised enough, between 10⁻² and 10⁻⁴ m/s. The depth of water level varies from 2,5 m to 3,5 m with an annual beat of the order of meter. Fresh water duckweed floats on salted water: water of the Ocean in the south, water of the brackish lagoons in north (Figure 2). In practice, the fresh water can be exploited by wells or not very deep drillings far away from the offshore bar limits.

The PU2 drilling data well in the study zone between the Atlantic Ocean and the coastal lagoon show that the upper sand aquifer thickness does not exceed 30 m (Figure 3(b)). This upper aquifer is collected by wells and drillings, with depth less than 30 m, in which the water level is between 1 m and 9 m. The water flow is between 1 and 15 m³ h. The PU2 drillings only collect deeper aquifers of Paleocene (PU2.2) and Cretaceous (PU2.1).

3. Material and Methods of Data Acquisition

Two principal types of geophysical surveys were carried out on the Beninian littoral sector with an aim of charting the salt water intrusion in the surface aquifer. It is the electromagnetic method to measure the side variation of electric conductivity in the sandy aquifer and the method of the vertical electric soundings to estimate in certain points of high conductivity the depth of the fresh water/salted water interface. It was shown that DC resistivity and loop-loop electromagnetic data interpreted together can also help overcome model ambiguities [29].

Another method of direct measurement of the conductivity of water in the wells was used to come in support to the geophysical methods. In our study, the results of geophysical surveys are compared with direct measurement.

3.1. Direct Measurements of Conductivity of Water in the Wells.

The direct measurements campaign has been done on mid-May 2011 when the great dry season ended and the great

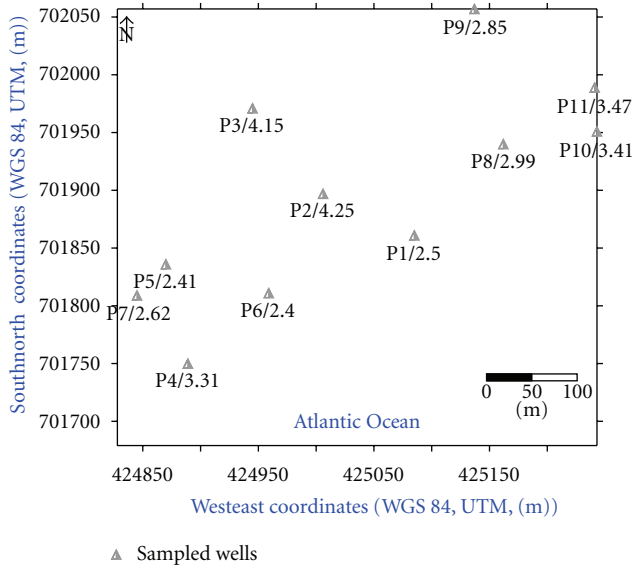


FIGURE 4: Chart of wells points distribution.

rain season begun. Direct measurements of the conductivity of the wells were taken in situ on 11 wells distributed in a random way on the surface of the studied sector (Figure 4). Measurements of conductivity were carried out using the probe of HARIBO conductivimeter. The total fluctuations of the chemical load of water can be represented by the determination of the electric conductivity of the water which is a linear function of the dissolved ions [30]. The values of conductivities vary between 271 and 826 $\mu\text{Sm} \cdot \text{cm}^{-1}$.

3.2. Electromagnetic Prospection. There is a huge scientific literature on near-surface electromagnetic geophysics [29]. Electromagnetic conductivimeter (EM) is a tool of diagnosis and very useful cartography for the study of the salted grounds as in [31] and [32]. The equipment used is a EM34 of Geonics Ltd. Canada with a choice of spacing of 10 m between the coils. Measurements were carried out in mode “vertical dipole” (horizontal coplanar coils). The mode “vertical dipole” was selected for the faster insurance of its coplanarity and its greater depth of investigation. Six profiles of approximately 350 m each, that is, more than 2 km of electromagnetic shaping, were carried out. The profiles have a northern-southern orientation and are spaced of 50 m (Figure 5). The EM34 provides information to a few tens of meters of depth and functions at the multiple frequencies in the range 100 hertz–50 kHz, but the resolution of depth remains modest.

3.3. Vertical Electric Soundings. The device used for the vertical electric soundings (VESs) is of the Wenner type. This method makes it possible to obtain, according to the depth, the apparent resistivity of a certain volume of ground [33, 34]. Field data were interpreted through the following steps: (a) matching the field curve with the standard curves of the auxiliary method [27], (b) preparing an initial geoelectrical model (thicknesses and corresponding resistivities) for a

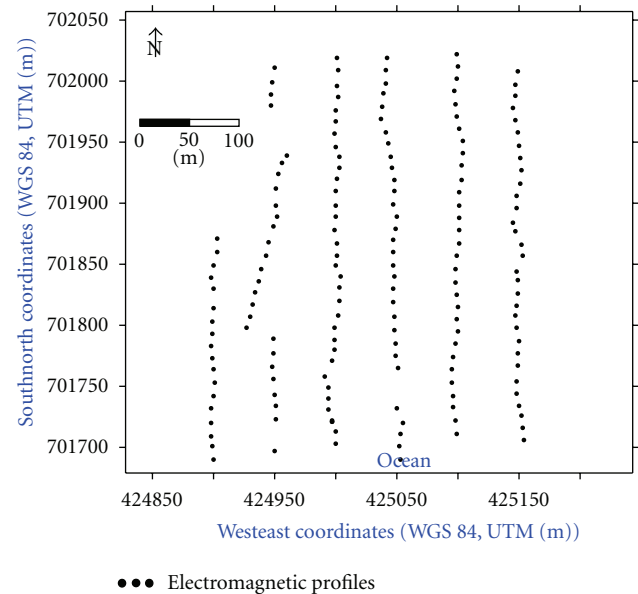


FIGURE 5: Chart of electromagnetic profiles.

limited number of layers depending on the geological background as well as the borehole information in the study area [35], and (c) entering the initial geoelectrical model into the [36] geoelectric modeling package. Each VES is subjected to 1D-forward modeling, in which the iterative procedure of [37] was applied. Iterations were carried out to reach the best fit between the smoothed field curve and the calculated one [38]. Being given that the values of the resistivity connect will be decreasing according to the degree of salinization [39], the objective is to determine the depth of the brackish water, that is, at which depth is fresh water/salted water interface. Five vertical electrical soundings were carried out in the sector of 350 m². The choice of the site of the soundings was guided by the results of electromagnetic measurements of conductivity. Indeed, the soundings were located in the zones of different electromagnetic conductivities (Figure 8). Vertical electrical sounding VES1 is located in a zone with high conductivity bordering the 60 mSm/m. This zone is near to the ocean. Vertical electrical sounding VES2 is located in a zone with normal conductivity of approximately 46 mSm/m and a distance of more than 50 m at north of shore line. Vertical electrical sounding VES3 is located in a zone of low conductivity. This conductivity is around of 36 mSm/m. The VES3 is more than 150 m at north of shore line. The VES3 is at the west of VES2. Vertical electrical sounding VES4 is located in a zone of very low conductivity at the north of studied area. There the conductivity is around of 28 mSm/m at more than 250 m of shore line. As a zone of very low electromagnetic conductivity was detected in the western south of the zone of study, a vertical electrical sounding SEV5 was established there. This sounding was established with 50 m from the shore and at the west of SEV2 in a zone where electromagnetic conductivity in lower than 20 mS/m. The electromagnetic chart of conductivity was thus used as indicator for the establishment of the vertical electric surveys. These vertical electric surveys were established

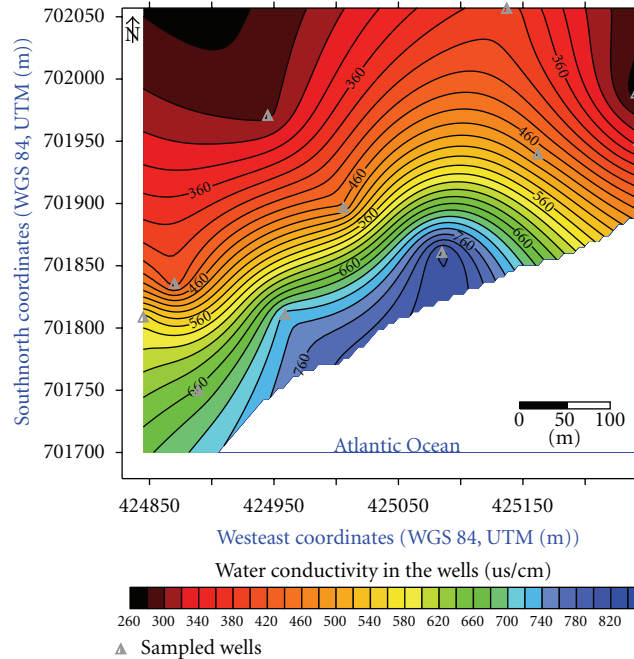


FIGURE 6: Chart of water conductivity.

from south towards north according to the variation of electromagnetic conductivity. Each log of vertical electrical sounding underwent an inversion in the IPI2Win software. This inversion provides a model of geoelectrical distinct grounds. The most conducting grounds are regarded as those containing the brackish or salted water according to their resistivity. In fact, when the resistivity of the conducting ground lies between 0.5 and $5 \Omega\text{m}$, it is supposed to contain salted water (Figure 11). When the conductivity of the conducting ground is slightly higher than $5 \Omega\text{m}$, it is supposed to contain brackish water. For our study, the grounds with resistivities ranging between 5 and $6 \Omega\text{m}$ were regarded as those containing of brackish water. It is in these grounds that the fresh water/salted water interface is.

The southnorth section passing by these vertical electric soundings made it possible to build the fresh water/salted water interface level (Figure 10).

4. Results and Discussion

4.1. Results. The values of electric conductivities of water in the wells vary between 271 and $826 \mu\text{S}\cdot\text{cm}^{-1}$. These values made it possible to build the chart of conductivities of the mineralization of the water of the wells (Figure 6).

The chart of conductivities of mineralization of water in the wells shows that the water table presents significant variations of mineralization. Electric conductivity is generally high in the south and oscillates between $600 \mu\text{S}\cdot\text{cm}^{-1}$ and $820 \mu\text{S}\cdot\text{cm}^{-1}$, while in north it is generally low and oscillate between $400 \mu\text{S}\cdot\text{cm}^{-1}$ and $260 \mu\text{S}\cdot\text{cm}^{-1}$ (Figure 6). Because of the high number and the good distribution of wells for this reduced sector, the zones presenting similar conductivities could be well delimited in classes. The various classes which

allow pronouncing about the degree of mineralization are as follows [40]:

- (i) conductivity $< 100 \mu\text{S}\cdot\text{cm}^{-1}$ very weak mineralization;
- (ii) $100 < \text{conductivity} < 200 \mu\text{S}\cdot\text{cm}^{-1}$ weak mineralization;
- (iii) $200 < \text{conductivity} < 333 \mu\text{S}\cdot\text{cm}^{-1}$ medium mineralization;
- (iv) $333 < \text{conductivity} < 666 \mu\text{S}\cdot\text{cm}^{-1}$ accentuated mineralization;
- (v) $666 < \text{conductivity} < 1000 \mu\text{S}\cdot\text{cm}^{-1}$ significant mineralization;
- (vi) conductivity $> 1000 \mu\text{S}\cdot\text{cm}^{-1}$ high mineralization.

In all the littoral zone of the studied sector, the mineralization of the water table thus varies from significant value to a medium value passing by an accentuated mineralization value. Water with high mineralization is in southern seashore in contact with the ocean. In the south of the studied sector, any well does not have listed because of the high mineralization of water. The lack of wells in the southeastern part of the studied zone is marked by the break off data interpolation on the chart of mineralization conductivities. The chart of mineralization conductivities presents in consequence a gradient of mineralization with south-east-north-west direction. This gradient of mineralization shows a deepening of the brackish water which marks the fresh water/salted water interface as one moves away from the shore.

The chart of electromagnetic conductivities distribution shows a strong variation as well in the eastwest direction as in the southnorth direction. This rate of variation is estimated

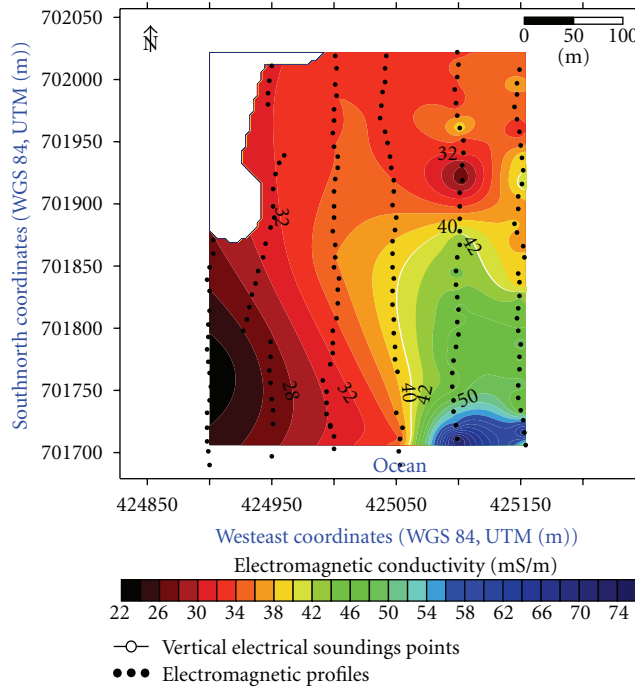


FIGURE 7: Chart of electromagnetic conductivity.

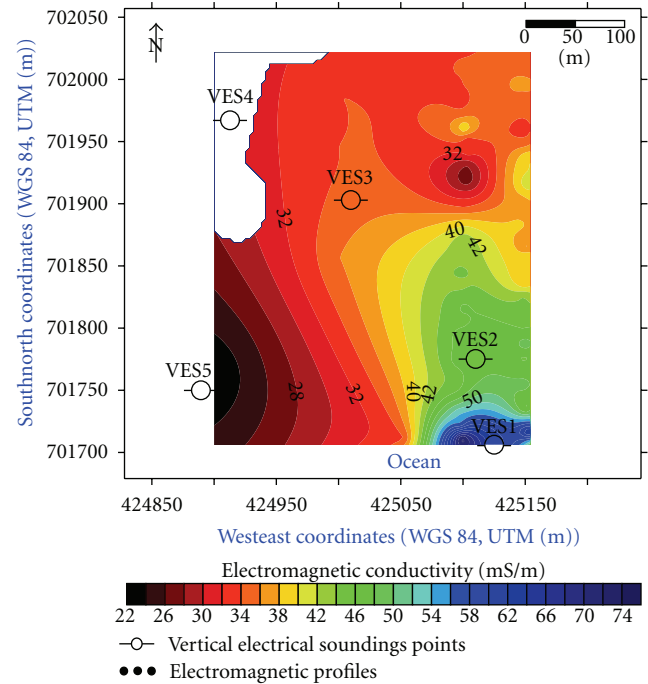


FIGURE 8: VES localization on chart of electromagnetic conductivity.

at approximately $(74 - 30)/200 = 0,22$, per meter in E-W direction and $(74 - 22)/200 = 0,26$ per meter in the S-N direction (Figure 7). This rate of variation is representative of the electromagnetic gradient of conductivity. The resulting direction of this gradient orientation would rather be south-east towards the northwest (Figure 7). The chart of electromagnetic conductivities presents a number of low conductivities anomalies. For instance, in the north of the conducting zone, a small resistant anomaly of 30 mS/m can be due to the influence of the disturbing magnetic effects related to the roof of the houses. These effects will be ignored during interpretation of the chart. In general, the chart of electromagnetic conductivities presents a reduction of conductivity as one moves away from the shore except for the western part studied zone. Nevertheless, it can be retained that the gradient of electromagnetic conductivity remains in conformity with that of the mineralization of water of well.

The vertical electrical soundings were located in the zones of different electromagnetic conductivities (Figure 8).

The log of vertical electric sounding VES1 presents its conducting ground of resistivity 5,04 Ωm at a depth of 1,02 m (Figure 9(a)). This low depth of the fresh water/salted water interface is due to the proximity of the shore.

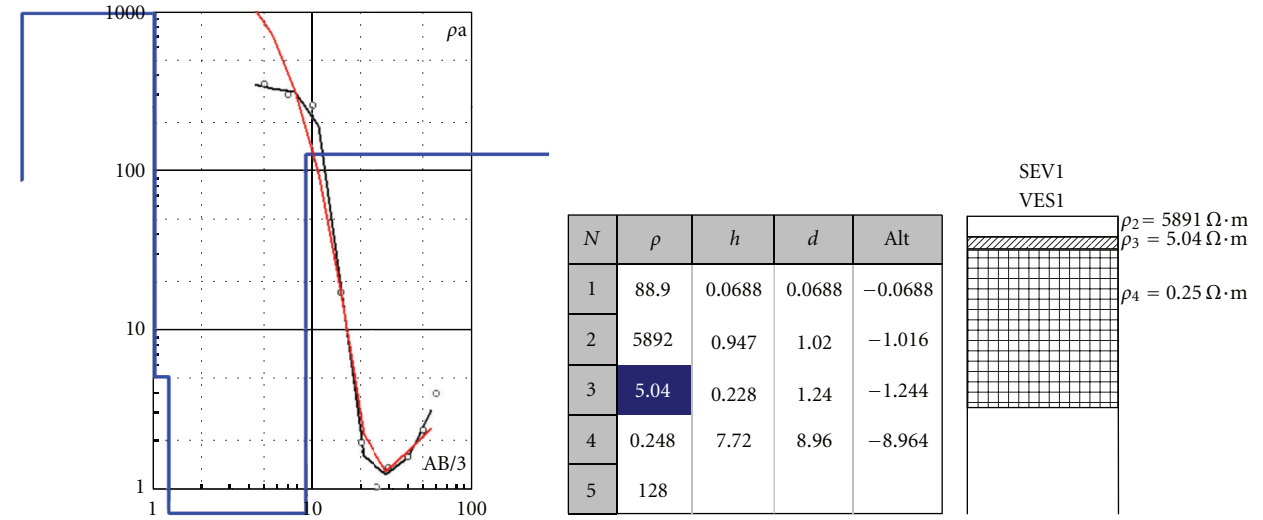
The log of vertical electric sounding VES2 presents its conducting ground of 5,04 Ωm resistivity at a depth of 4,75 m (Figure 9(b)). The fresh water/salted water interface is thus a little deeper at 70 m from shore.

The log of vertical electric sounding VES3 presents a ground of 5,83 Ωm resistivity at a depth of 11,6 m (Figure 9(c)). This significant depth of the fresh water/salted water interface is noticed at 200 m from shore in the center of the studied zone.

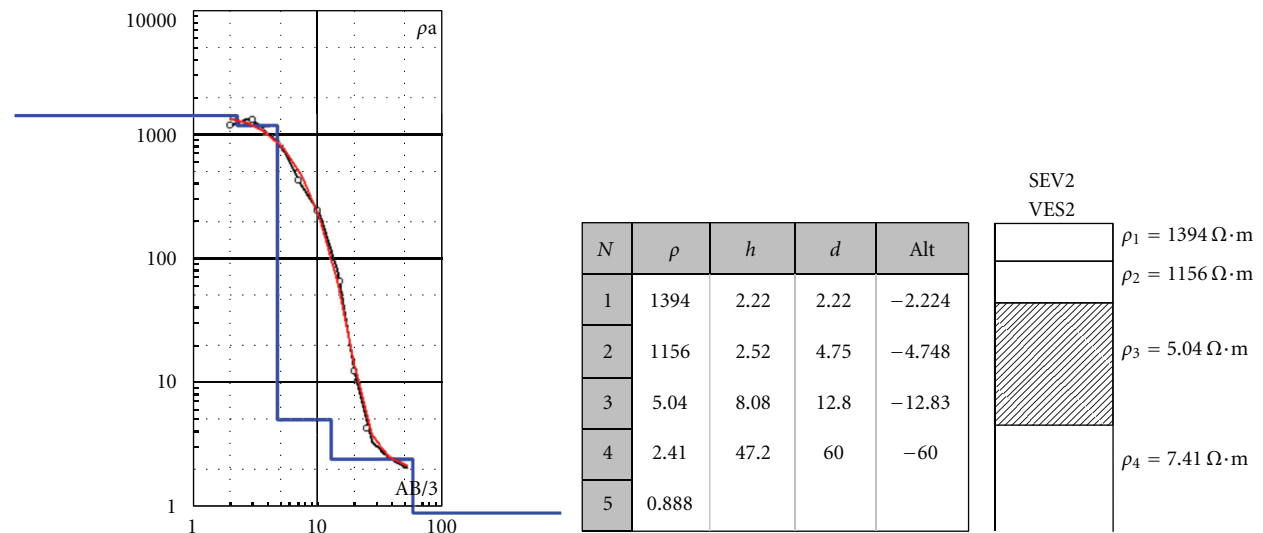
The log of vertical electric sounding VES4 presents a ground of 5,95 Ωm resistivity at a depth of 9,79 m (Figure 9(d)). This light increase of the fresh water/salted water interface is in the northern part of the zone of study. This zone is furthest away from the shore approximately to 250 m and marks the end of the deepening of the fresh water/salted water interface.

The northwestern Southeastern vertical section, taking into account the logs of the four vertical electrical soundings, delimits the deepening slope of the fresh water/salted water interface according to the distance from the shore (Figure 10). The deepening slope of this interface remains constant to approximately 5% up to 200 m from the shore where a change of incline takes place.

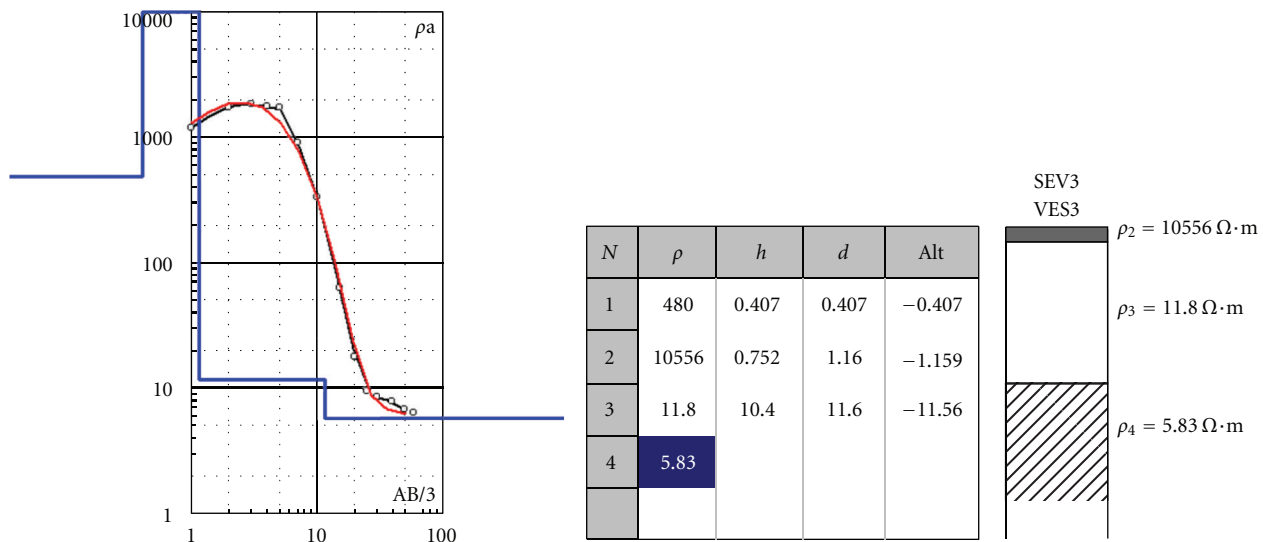
4.2. Discussion. Comparing the electromagnetic conductivity chart with that of mineralization, it is possible to note that the orientation of electromagnetic conductivity gradient is in general in conformity with that of mineralization. Nevertheless, a lack of conformity is noted about a small anomaly and especially in the southeastern part of the studied zone. For 10 m spacing between the EM34 loops, the depth of investigation is lower than 10 m. Thus, the zones, in which the depth of the fresh water/salted water interface borders exceeds the 10 m depth, are badly charted by this device. That can explain the anomaly in the center of the studied zone where the interface plunges to more than 10 m of depth. This device is also sensitive to the surface and very near surface disturbances which could be the cause of the anomaly in the south-east of the studied zone. All things considered, the electromagnetic prospecting appears as a tool able to chart the mineralization of the ground water to low



(a)

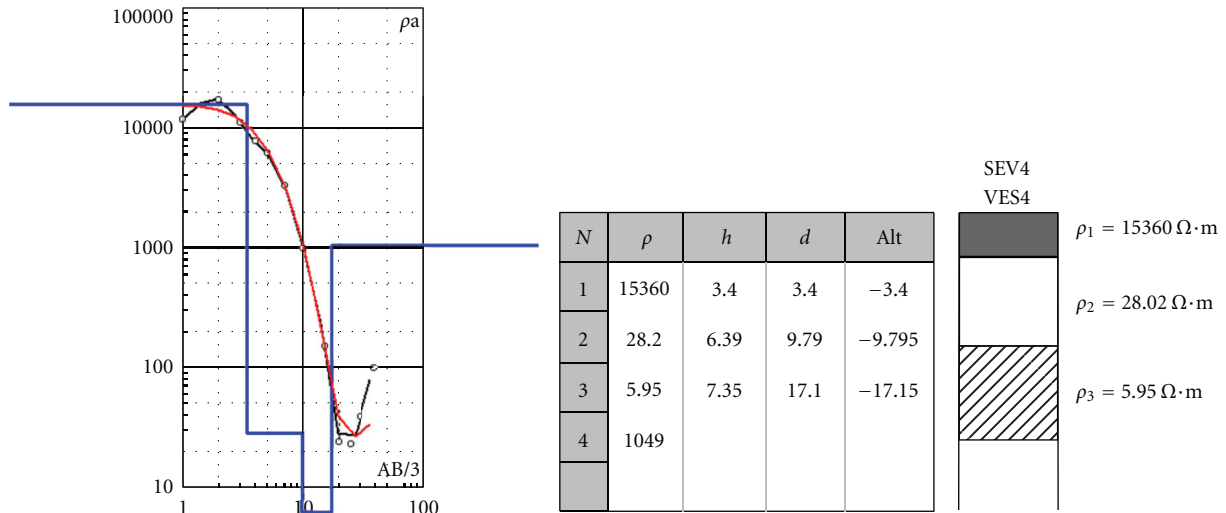


(b)

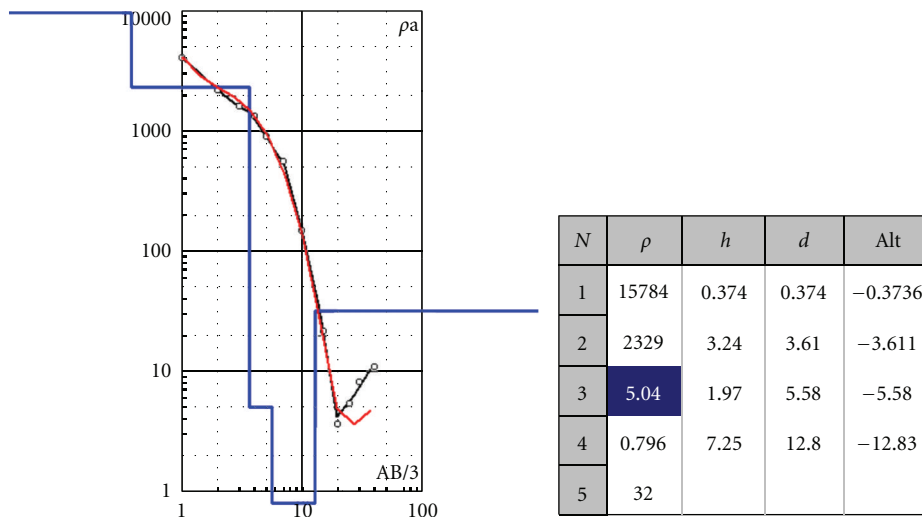


(c)

FIGURE 9: Continued.



(d)



— Model layers
 ~ Measured log of survey
 ~ Calculated log of survey

(e)

FIGURE 9: (a) VES1 log and model layers. (b) VES2 log and model layers. (c) VES3 log and model layers. (d) VES4 log and model layers. (e) VES5 log and model layers.

depth in the zones where the electromagnetic disturbances are negligible.

Comparing the deepening slope of the fresh water/salted water interface with the gradient of mineralization, it should be noted that in the south where the interface is close to surface, mineralization is high. Moreover, the weakest variations of the gradient of mineralization in the northern part of the studied zone shows the tendency towards the stability of mineralization when the slope of the interface ceases dipping. The deepening of the interface thus implies a reduction of the mineralization. Moreover, in the southwest where the resistivity of the interface is equal to 5,04 Ωm for vertical electric sounding VES5, mineralization has a conductivity of

680 μSm/cm. In the center for the vertical electric sounding VES3 where the resistivity of the interface is equal to 5,83 Ωm, mineralization has a conductivity of 460 μSm/cm. In north for the vertical electric sounding VES4 where the resistivity of the interface is equal to 5,95 Ωm, mineralization has a conductivity of 330 μSm/cm. Thus, on the qualitative level, the low values of resistivities of the interface correspond to a significant mineralization, the medium values of resistivities of the interface correspond to an accentuated mineralization, and the high values of resistivities of the interface correspond to a medium mineralization. The electrical resistivity of the fresh water/salted water interface is thus sensitive to the degree of its mineralization.

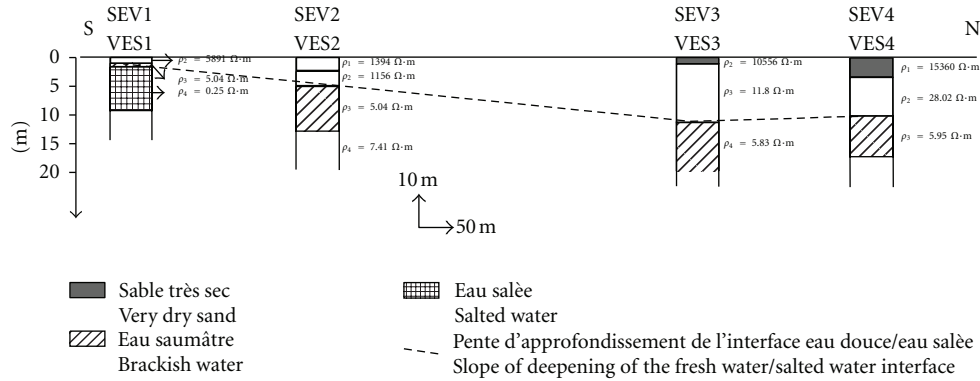


FIGURE 10: Geoelectrical section on the fresh water/salted water interface.

	$\rho_a (\Omega m)$					
	10^{-1}	10^0	10^1	10^2	10^3	10^4
Dry sand						
Sand saturated with fresh water				50	500	
Sand saturated with salt water	0.5	5				
Clay		2	20			
Silty sand				50		
Sandstone				50		
Porous limestone					500	
Massive limestone					500	
Granite, basalt						

FIGURE 11: Range of rocks resistivity.

Comparing the deepening slope of the fresh water/salted water interface with the gradient of electromagnetic conductivity, it can be noted that the slope and the gradient have a strong variation in the south of studied zone and a soft variation in north. Moreover, in the northern part of the zone where the change of incline is carried out, conductivities remain rather stable. Strong electromagnetic conductivities in the south, where the interface is close to surface, decrease gradually with the deepening of the interface in north. Nevertheless, in the southwestern part where the fresh water/salted water interface is still close to surface, electromagnetic conductivities remain high. This electromagnetic anomaly is partly due to the nature of the surface grounds located at the top of the interface. Indeed, at southwest, the log of vertical electrical sounding VES5 presents at the top of the fresh water/salted water interface, the most resistant ground (15784 Ωm) of the studied zone (Figure 9(e)). Thus, although being able to chart the deepening slope of the fresh water/salted water interface, the electromagnetic gradient can be disturbed by the presence of resistant surface grounds.

5. Conclusion

The coupling of the geophysical methods of electromagnetic conductivities and vertical electrical soundings made it

possible to chart the mineralization of ground water in the coastal aquifer on the one hand and to detect the depth and the dip of the fresh water/salted water interface in the studied zone on the other hand. The vertical electrical soundings showed that the dip of the fresh water/salted water interface is in the order of 5% in the southern part of the studied zone, and in the northern part, a change of incline takes place. The variations of the resistivities of the interface are sensitive to the variations of its mineralization. Nevertheless the electromagnetic method is able to define the gradient of mineralization but remains sensitive to the environmental disturbances and to the resistant grounds on the surface.

The geophysical methods in electrical prospecting are thus adequate for the cartography of the mineralization of the ground water in coastal zone. On the environmental level, they can be used in the zones where drilling of the wells is difficult, even impossible or useless, in order to delimit the zones where the water resource is sustainability exploitable.

Acknowledgments

The authors thank, on one hand, the Laboratory of Applied Hydrology (LHA) of the University of Abomey-Calavi in Benin for the facilitation during chemical analysis of the water samples and, on the other hand, the Institute of Research and Development (IRD) of France for the provision of the geophysical material of prospecting.

References

- [1] K. Choudhury, D. K. Saha, and P. Chakraborty, "Geophysical study for saline water intrusion in a coastal alluvial terrain," *Journal of Applied Geophysics*, vol. 46, no. 3, pp. 189–200, 2001.
- [2] R. K. Frohlich and D. W. Urish, "The use of geoelectrics and test wells for the assessment of groundwater quality of a coastal industrial site," *Journal of Applied Geophysics*, vol. 50, no. 3, pp. 261–278, 2002.
- [3] W. Schwinn and B. Tezkan, *1D Joint Inversion of Radiomagnetotelluric (RMT) And Transient Electromagnetic (TEM) Data; An Application for Groundwater Prospection in Denmark*, Aarhus, Denmark, 3rd edition, 1997.
- [4] M. J. Unsworth, X. Lu, and M. Don Watts, "CSAMT exploration at Sellafield: characterization of a potential radioactive

- waste disposal site," *Geophysics*, vol. 65, no. 4, pp. 1070–1079, 2000.
- [5] S. Krivochieva and M. Chouteau, "Integrating TDEM and MT methods for characterization and delineation of the Santa Catarina aquifer (Chalco Sub-Basin, Mexico)," *Journal of Applied Geophysics*, vol. 52, no. 1, pp. 23–43, 2003.
- [6] U. Kafri and M. Goldman, "The use of the time domain electromagnetic method to delineate saline groundwater in granular and carbonate aquifers and to evaluate their porosity," *Journal of Applied Geophysics*, vol. 57, no. 3, pp. 167–178, 2005.
- [7] L. B. Pedersen, M. Bastani, and L. Dynesius, "Groundwater exploration using combined controlled-source and radiomagnetotelluric techniques," *Geophysics*, vol. 70, no. 1, pp. G8–G15, 2005.
- [8] R. Mota and F. M. dos Santos, "2D sections of porosity and water saturation percent from combined resistivity and seismic surveys for hydrogeologic studies," *Leading Edge*, vol. 25, no. 6, pp. 735–737, 2006.
- [9] Y. Rubin and S. Hubbard, "Hydrogeophysics," *Water Science and Technology*, vol. 50, p. 521, 2005.
- [10] E. Falgàs, J. Ledo, B. Benjumea et al., "Integrating hydrogeological and geophysical methods for the characterization of a deltaic aquifer system," *Surveys in Geophysics*, vol. 32, pp. 857–873, 2011.
- [11] J. C. Van Dam and J. J. Meulankamp, "Some results of the geoelectrical resistivity method in ground water investigations in the Netherlands," *Geophysical Prospecting*, pp. 92–115, 1967.
- [12] A. A. R. Zohdy, "The use of Schlumberger and equatorial soundings on ground water investigation near El Paso Tx," *Geophysics*, vol. 34, no. 5, pp. 713–728, 1969.
- [13] A. Ginsberg and A. Levanton, "Determination of saltwater interface by electrical resistivity sounding," *Hydrological Science Bulletin*, vol. 21, pp. 561–568, 1976.
- [14] R. K. Frohlich, P. J. Barosh, and T. Boving, "Investigating changes of electrical characteristics of the saturated zone affected by hazardous organic waste," *Journal of Applied Geophysics*, vol. 64, no. 1-2, pp. 25–36, 2008.
- [15] R. Rubin and S. S. Hubbard, Eds., *Hydrogeophysics*, Springer, Amsterdam, The Netherlands, 2005.
- [16] R. K. Frohlich, D. W. Urish, J. Fuller, and M. O'Reilly, "Use of geoelectrical methods in groundwater pollution surveys in a coastal environment," *Journal of Applied Geophysics*, vol. 32, no. 2-3, pp. 139–154, 1994.
- [17] J. Handled and V. Meens, "The water soft-water/salted water interface in French Flanders," *Bulletin de la Societe Geologique de France*, vol. 7, no. 6, pp. 1281–1291, 1984.
- [18] J. Mania, S. Imerzoukene, and J. M. Brailon, "Saline pollution of the east Algerian coastal aquifer," *Hydrogeologie*, vol. 3, pp. 213–226, 1985.
- [19] J. C. Grillot and M. Razack, "Space-time Evolution of an alluvial aquifer under the effect of an exceptional multiannual dryness," *Journal of Hydrology*, vol. 82, pp. 155–173, 1985.
- [20] T. Mathias, *Climatic variability, the man and the coastal ecosystems dynamics of Benin [Thesis of doctorate]*, University of Abomey-Calavi, Cotonou, Benin, 2008.
- [21] R. A. Laibi, "Evaluation quaternaire et dynamique actuelle des cordons barriers de l'estuaire du Mono-couffo dans le littoral du Bénin (Golfe de Guinée, Afrique de l'Ouest) [Thèse de Doctorat], Université du Littoral Côte Opale, Dunkirk, France, 2001.
- [22] L. M. Oyédé, *Dynamique sédimentaire actuelle et messages enregistrés dans les séquences quaternaires et néogène du domaine margino-littoral du Bénin (Afrique de l'Ouest) [Thèse de doctorat nouveau régime]*, Université de Bourgogne et Université nationale du Bénin, 1991.
- [23] J. P. Tastet, "Les formations sédimentaires Quaternaires à Actuelles du littoral du Togo et de la République Populaire du Bénin," *Supplément du Bulletin AFEQ*, no. 50, pp. 155–167, 1977.
- [24] J. Lang, G. Paradis, and L. M. et Oyédé, "Le domaine margino-littoral du Bénin (Golfe de Guinée Afrique de l'Ouest) : âge holocène et mise en place des sables jaunes," *Journal of Africa Earth Sciences*, vol. 7, no. 5-6, pp. 829–833, 1988.
- [25] C. Kaki, L. M. Oyédé, and S. et Yessoufou, "Dynamique sédimentaire et environnement côtier du littoral béninois à l'Est de l'embouchure du fleuve Mono," *Journal de la Recherche Scientifique de l'Université du Bénin*, vol. 5, no. 2, pp. 247–261, 2001.
- [26] J. Lang and G. et Paradis, "Le Quaternaire margino-littoral béninois (Afrique de l'Ouest). Synthèse des datations de carbone 14," in *Paleoecology of Africa*, J. A. et Coetze, E. M. Van Zinderen, and A. A. Baker, Eds., vol. 16, pp. 65–67, Balkema, Rotterdam, The Netherlands, 1984.
- [27] D. Marsden, "The automatic fitting of a resistivity sounding by a geometrical progression of depth," *Geophysical Prospecting*, vol. 21, no. 2, pp. 266–280, 1973.
- [28] M. Boukari, "Reactualization of hydrodynamic knowledge relating to the Coastal Sedimentary Basin of the Benin," Support to the Water Stock Management Report (WSMR), Cotonou, Benin, 2002.
- [29] M. E. Everett, "Theoretical Developments in electromagnetic induction geophysics with selected applications in the near surface," *Surveys in Geophysics*, vol. 33, pp. 29–63, 2012.
- [30] M. Meybeck, "Chemical composition of the not polluted brooks of France," *Sciences Géologiques*, vol. 39, pp. 3–77, 1986.
- [31] S. M. Lesch, J. D. Rhoades, L. J. Lund, and D. L. Corwin, "Mapping soil salinity using calibrated electromagnetic measurements," *Soil Science Society of America Journal*, vol. 56, no. 2, pp. 540–548, 1992.
- [32] M. E. Cannon, R. C. McKenzie, and G. Lachapelle, "Soil salinity mapping with electromagnetic induction and satellite-based navigation methods," *Canadian Journal of Soil Science*, vol. 74, no. 3, pp. 335–343, 1994.
- [33] D. P. Ghosh, "Inverse filter coefficient for the computation of apparent resistivity standard curves for horizontally stratified earth," *Geophys Prospect*, vol. 19, pp. 769–775, 1971.
- [34] B. Banerjee, B. J. Sengupta, and B. P. Pal, "Apparent resistivity of a multilayered earth with a layer having exponentiality varying conductivity," *Geophysical Prospecting*, vol. 28, no. 3, pp. 435–452, 1980.
- [35] D. Patella, "A numerical computation procedure for the direct interpretation of geoelectrical soundings," *Geophysical Prospecting*, vol. 23, no. 2, pp. 335–362, 1975.
- [36] V. Velpen, *Resist: A computer processing package for dc resistivity interpretation for the IBM PC and compatibles [M.S. thesis]*, ITC, Delft, The Netherlands, 1988.
- [37] A. A. R. Zohdy, "A new method for the automatic interpretation of Schlumberger and Wenner sounding curves," *Geophysics*, vol. 54, no. 2, pp. 245–253, 1989.
- [38] M. H. Khalil, "Magnetic, geo-electric, and groundwater and soil quality analysis over a landfill from a lead smelter, Cairo, Egypt," *Journal of Applied Geophysics*, vol. 86, pp. 156–159, 2012.
- [39] M. Boughriba, A. Melloul, Y. Zarhloule, and A. Ouardi, "Spatial extension of salinization in groundwater and conceptual model of the brackish springs in the Triffa plain (northeastern Morocco)," *Comptes Rendus—Geoscience*, vol. 338, no. 11, pp. 768–774, 2006.
- [40] J. Rodier, *L'analyse de l'Eau*, Dunod, 8th edition, 1996.